The electron density: experimental determination and theoretical analysis

Smith, Gary Thomas

The Electron Density:
Experimental Determination and Theoretical Analysis.

Garry Thomas Smith,
Trevelyan College.

Thesis submitted for the degree of Doctor of Philosophy,
Department of Chemistry,
University of Durham,
1997.

Abstract

Two related lines of research in experimental electron density determination are reported in this thesis. In the first case, the well-proven and popular multipole modeling technique is applied to three high resolution, single-crystal X-ray diffraction data sets. The preliminary part of this thesis (Chapters 2-5) deals with the theoretical aspects of the multipole model, and also some of the theoretical and practical aspects of data collection and reduction. Chapter 6 reports an experimental charge density determination of a nitrogen ylide. Chapter 7 contains details of the treatment of data from a large, pendant-arm macrocyclic complex of nickel, while Chapter 8 reports the characteristics of the experimentally determined charge density for a substituted acetylene molecule which exhibits interesting intramolecular interactions. The charge densities for all three cases are analysed using Bader's Theory of Atoms in Molecules.

The latter part of this thesis deals with more novel ways of treating experimental data. Chapter 9 gives a thorough review of the literature on the application of Maximum Entropy techniques to image reconstruction in general and charge density determination in particular, followed in Chapter 10 by an application to diffraction data from the cubic phase of acetylene. The novel approach of removing core scattering from the data is developed and gives improved results.

Chapter 11 reviews some aspects of fermion density matrices and their relationship to electron density functions and X-ray scattering, followed in Chapter 12 by results from the density matrix refinement method applied to diffraction data from formamide. Particular emphasis is placed upon basis set effects, idempotency and various N-representable approximations to the experimentally determined density matrix.

Declaration

The work reported in this thesis was carried out primarily at the University of Durham between October 1993 and June 1996, augmented by additional work carried out variously at the University of Glasgow, University of Wales, College of Cardiff and University of Massachusetts at Amherst while on academically related visits. It has not been submitted, either in full or in part, for any degree or other award in this or any other University. It is the original work of the author unless indicated otherwise, either contextually or specifically.

Acknowledgements

Firstly, I would like to thank my supervisor, Professor Judith Howard for providing me with the facilities to conduct this research, and more specifically the opportunities to travel to the major meetings in the field, irrespective of their geographical location.

The continued interest of Drs. Paul Mallinson and Sean Howard, and their expertise in the areas of multipole modeling and density matrix methods respectively are much appreciated, as is their willingness to engage in excessively time-consuming technical discussions on the subjects.

Dr. Keith Henderson's knowledge and experience of Bayesian philosophy and the foundations of maximum entropy theory has proved to be invaluable to me.

Finally, the help and encouragement of all my friends and family is gratefully appreciated.

Contents

Chapter 1

Introduction

1.1 In the Beginning ...

X-rays and their diffraction is a very old "modern" science. The first ever Nobel Prize in Physics[1] was awarded to Wilhelm Conrad Röntgen in 1901 for his discovery and characterization of the then called "Röntgenrays". 1914 saw Max Theodor Felix von Laue become a Nobel Laureate for his discovery of the diffraction of "Röntgenrays" by a crystal. The significance of this work was twofold; it confirmed that X-rays displayed wave character and that a crystal is a symmetrical three-dimensional array of atoms that can act as a diffraction grating.

Even before von Laue had received his prize, work was already afoot to utilize the diffraction phenomenon in elucidation of crystal structure. Debye was prominent in his assertion that the X-rays were being scattered by electrons. He states[2]

> "It seems to me that experimental study of the scattered radiation, in particular from light atoms, should get more attention, since along this way it should be possible to determine the arrangement of the electrons in the atom."

Debye and Scherrer attempted to determine the ionic charges in LiF[3], follwed by a similar study by Bragg on NaCl[4]. Bragg also endeavoured to use diffraction data to obtain an experimental description of the covalent bonding in diamond by calculating the diffracted intensities which would result from localized two-electron bonds in accord with the Lewis model[5].

It is thus apparent that, right from the start, X-ray diffraction was recognized not only as a tool for molecular structure determination in the sense of atomic positions but also for the determination of the more fundamental electronic structure. Despite this fact, the work now done in X-ray diffraction is almost exclusively to gain information of the former kind.

1.2 Why do the Experiment?

Well, the answer to this question depends upon the viewpoint of the scientist being asked. Experimental electron density determination is an interdisciplinary topic of research. We are hoping to gain an experimental description of what is a quantum-mechanically well defined situation. The practical aspects of data collection and diffraction physics are undoubtedly well covered by crystallography but the quantitative analysis of the electron distributions so obtained is the realm of theoretical chemistry.

Chemical Crystallographers may become involved in charge-density research initially as a by-line to their occupation of solving crystal structures and become drawn in or they may become involved deliberately as they realize that a study of bond lengths and angles *etc.* cannot possibly provide all the information that they require to ascertain certain properties of systems such as molecular polarity or "atomic charges" within the molecule.

Theoretical Chemists have other reasons to become involved. Although the *ab initio* calculation schemes embodied in the proprietary software packages have evolved to become tractable tools for obtaining an approximate wavefunction, there are inherent limitations in the Hartree-Fock scheme. For large systems the processor time required is substantial, especially when many-Gaussian contractions and polarization functions are utilized in the basis set and such schemes only calculate the wavefunction for an isolated, gas-phase molecule. If our interest is actually in a molecule in a crystalline environment as it might be for example in non-linear optics or piezo-electricity, the only formally correct way to proceed is to perform either a periodic Hartree-Fock calculation or a band theory calculation. These are computationally expensive. For the two examples just mentioned, we may assume that the free molecule wavefunction is sufficiently close to the in-crystal one to allow us to use the gas-phase wavefunction, but for non-localized states such as those found in superconductors or semi-conductors band theory is unavoidable.

A second reason is that while current calculation schemes give good reproducibility of strong, covalent interactions, chemical interest is moving towards weak, inter- and intramolecular interactions such as van der Waals forces, hydrogen bonds and the like which are of fundamental importance in molecular recognition, molecular biology and biochemistry. These forces are not as accurately calculated by current quantum theory without recourse to extremely large scale calculations. Since a crystal is an assemblage of molecules weakly held together, these forces and their manifestations in the charge density may be experimentally accessible *via* the experimentally determined electron density.

The final reason, and to me the most fundamental is that mathematical physics has, as yet, offered no analytical solution to the many body problem. The standard HF-SCF scheme neglects the correlated motion of electrons. Two main avenues are open to approximate inclusion of these effects:

- Möller-Plesset perturbation theory where inclusion of one or more perturbation terms in the Hamiltonian help to describe the inter-electron interaction.

- Configuration Interaction where excited state wavefunctions are allowed to mix in with the ground state. Despite the fact that excited states have higher energies, the mixing in of small amounts of higher states actually reduces the total energy by incorporating the interelectronic distance into the wavefunction.

Both of the above methods can include a substantial amount of the effects of electron correlation but only with a dramatic increase again in computational effort[6]. One other possible computational route to correlated wavefunctions and densities is Density Functional Theory[7,8,9,10]. This area of quantum chemistry is at last coming into vogue after lagging behind HF theory. Its level of development is not as far advanced but a common view is that alternative approaches

must now be sought as post-HF theories have taken us as far as they can and an alternative, computationally less-demanding approach is required. However, even DFT can only approximately include the true consequences of electron correlation via the exchange-correlation potential.

The point to be emphasised is that any experimental density is *by definition* a correlated density and hence what is difficult to calculate may be experimentally investigated.

1.3 What do we hope to gain?

Development of charge-density research, whether theoretical or experimental is ultimately a waste of time unless the results so obtained can be used in chemical, physical or biological applications. The very first charge-density work was done when the most satisfactory theory of valence was that of Gilbert Lewis, so the fundamental character of bonding was being investigated. However, Born, Schrödinger *et al,* elucidated at least the mathematical principles of wave mechanics and the development of this theory has continued to it's current high level. There is no great justification for conducting a charge density study of small organic molecules (including drugs) when the calculation could so more easily be done and probably more information gained. However, the study is justifiable if applied to one of the four areas I have outlined above (big systems, molecules in crystals, weak interactions, electron correlation).

The relevant areas of application of the results include:

- Bonding and electronic configuration of transition metal complexes. These can be difficult to do all-electron calculations on due to their size. Semi-empirical calculations can be done but the parameterization of some of the integrals means that confidence in reliability of the result is degraded. Utilization of effective core potentials[11] is another way of reducing the computational effort required, but again the reliability of the results may be compromised. This is especially true if two different spin states are close in energy. The experimental determination of the electron density can, in suitable cases, determine the spin state. Some transition metal complexes are currently being developed to act as electronic switches by way of spin-state crossover. Application of pressure to a crystal can change the spin state of the system and so experimental electron density determination is an ideal tool for investigating this behaviour.

- Systems where weak interactions are important. Some of the most important financially are drug-receptor and enzyme-substrate binding. Although the resolution required to actually study a drug bound to a real receptor is not attainable at the moment, it is for model systems, so the binding properties of the drug can be ascertained and hopefully extrapolated to more realistically sized systems. Fundamental knowledge in biochemistry can be obtained in this way, but more importantly it is another avenue to be explored in rational drug design. X-ray scattering can actually help from both sides in this context by providing the structure of the receptor site *via* protein crystallography and the properties of the drug *via* charge density research in a two-pronged attack.

- Rational design of solid state devices such as optical materials, electronics, superconductors and piezoelectrics could follow from a detailed knowledge and theoretical analysis of the

electron density. For example, non-linear optical properties are related to the molecular dipole moment.

- Parameter values for empirical molecular mechanics force fields. Such force fields are usually used in circumstances where calculation fail or are too expensive. Parameter values can be obtained from charge densities, either theoretical or experimental. Applications include molecular dynamics simulations, solutions, thin films and polymers.

The research performed in connection with the above criteria and presented in this thesis falls into two broad categories, namely applications and theoretical development. Firstly, the "standard" technique of fitting a structured model which implicitly accounts for the functional form of the charge density, the so-called multipole model, by least-squares techniques to experimentally determined structure factor magnitudes for three different compounds was performed. These three compounds represent a wide spectrum of interesting chemical phenomena. The first compound, a nitrogen ylide, is of chemical importance because it contains three nitrogen atoms, all in different chemical environments, and therefore provides a good test of the model's sensitivity to different bonding situations of the same element. The chemical information gained includes atomic charges which are compared with those predicted by the Lewis structures of the resonance forms. The second compound is a large pendant-arm nickel complex, at this time the largest compound to have its charge density determined experimentally. The results for this compound are particularly novel because the coordination of the metal by the ligand is non-centrosymmetric and of particularly low symmetry, unlike the most commonly encountered and studied octahedral case. The space group for this crystal is also non-centrosymmetric which causes extra difficulties from the crystallographic point of view. The third compound studied by this method was a small organic molecule containing a carbon-carbon triple bond. It is one of a series of derivatives of di-benzyl acetylene where, because of the phenyl-ring substituents, through-space effects distort the linearity of the triple bond. Bader's topological Theory of Atoms in Molecules provides an invaluable method of analysis for such weak interactions in theoretically determined electron densities, but I show that the experimental techniques employed here are sufficiently sensitive to detect such small features in the charge density obtained from X-ray diffraction.

The second category of work undertaken in this research is more fundamental, and involved applying and developing two new techniques for the treatment of diffraction data for the extraction of the charge density. The first of these is the technique of maximum-entropy data analysis, which has its foundations in Information Theory and Bayesian statistics. No structured model is employed here at all, the density being described by a three-dimensional pixel map in real space. This technique was used to treat the diffraction data from crystalline acetylene from the literature, and an improved formalism for data analysis within this regime by treating only the valence density was developed.

The second of the newer techniques reverts to fitting a parameterized model of the charge density, but instead of the empirical multipole expansion model, I have fitted the elements of the first-order density matrix. This work has been undertaken in collaboration with Dr. Sean Howard at the University of Wales, Cardiff, who provided an early version of software for this

task, which I have updated and extended. The consequences of idempotency as a restriction of the fit have been investigated.

Chapter 2

Developments From The Spherical Atom

2.1 Conventional Spherical Atom Approach

To a first approximation, justified by the first Born approximation[12,13], X-rays are scattered elastically by the atomic or molecular electron density $\rho(\mathbf{r})$, resulting in set of structure factors $F(\mathbf{S})$. The relationship between the two is the Fourier transform

$$F(\mathbf{S}) = \int \rho(\mathbf{r}) exp(i\mathbf{S}.\mathbf{r}) d\mathbf{r} \tag{2.1}$$

where

$$\mathbf{S} = 2\pi(\mathbf{s} - \mathbf{s}_0)/\lambda \tag{2.2}$$

$\mathbf{s}$, and $\mathbf{s}_0$ are unit vectors in the direction of the scattered and incident beams respectively, $\mathbf{r}$ is the position vector in real space, and λ is the wavelength of the radiation.

In conventional crystallography, the scattering is decomposed into a sum over the scattering factors f_j of spherical, neutral atoms

$$F(\mathbf{S}) = \sum_j f_j(\mathbf{S}) exp(i\mathbf{S}.\mathbf{r_j}) \tag{2.3}$$

The structure factor itself is a complex quantity, *i.e.* has both magnitude and phase

$$F(\mathbf{S}) = |F(\mathbf{S})| exp(i\phi) \tag{2.4}$$

Returning to the formally rigorous continuous electron density, direct inversion of (2.1) to give the Fourier synthesis

$$\rho(\mathbf{r}) = \sum_{\mathbf{S}} F(\mathbf{S}) exp(-i\mathbf{S}.\mathbf{r}) \tag{2.5}$$

cannot immediately be performed since only the magnitude of $F(\mathbf{S})$ is obtained by experiment but not the phase, and hence no information is available on the value of the exponent of the structure factor. This is the well known crystallographic phase problem. There are currently two methods commonly used to circumvent this difficulty:

1. **Heavy atom techniques.** These involve the calculation of the Patterson function:

$$P(\mathbf{u}) = \frac{1}{V} \sum_{\mathbf{S}} |F(\mathbf{S})|^2 exp(i\mathbf{S}.\mathbf{u}) \tag{2.6}$$

The physical reality of the Patterson function is that it is the "square" of the electron density, or more strictly its self-convolution

$$P(\mathbf{u}) = \rho(\mathbf{r}) * \rho(-\mathbf{r}) = \int_V \rho(\mathbf{r})\rho(\mathbf{r}+\mathbf{u})d\mathbf{r} \tag{2.7}$$

The significance is that if we have one or more "heavy" atoms which dominate the scattering in the unit cell, the largest peaks in the Patterson map correspond to the interatomic vectors between the heavy atoms. This allows us to locate these atoms in the unit cell. If we then calculate the structure factors (amplitudes and phases) which would result from scattering by these atoms, assuming they scatter in the molecule the same way as the spherical free atom, we have not only their magnitudes but also a set of trial phases. If we now assign the trial phases to the measured structure amplitudes and compute the electron density using(2.5), the next level of atoms in terms of scattering power will reveal themselves in the Fourier synthesis. The positions of these new atoms are then included in the next structure factor calculation and the cycle is repeated until all atoms (or all non-hydrogen atoms) are revealed.

2. **Direct Methods.** This technique is based on the statistical probability of certain phases given the structure amplitudes. These two components of a general wave are independent but certain relationships do exist for structure factors ***via*** two properties of the electron density function that they describe.

   Firstly, the electron density function must be everywhere positive. Secondly, the molecule is composed of atoms. Direct methods will produce reliable starting phases in most cases, provided that the quality of data is adequate. It is more suited to crystals where the number of electrons is more uniform throughout the constituent atoms, but will still work for metal complexes.

Both of the above methods furnish an approximate solution of the structure. From here the next step is least squares refinement. This involves parameterizing the structure in terms of three positional coordinates and one temperature parameter in the case of isotropic thermal displacement from the equilibrium position, or six independent parameters by way of a third-rank tensor for anisotropic thermal motion for each atom. The thermal smearing is incorporated into the structure factor formalism so that (2.3) becomes:

$$F(\mathbf{S}) = \sum_j f_j(\mathbf{S})T_j(\mathbf{S})exp(i\mathbf{S}.\mathbf{r}) \tag{2.8}$$

As the refinement naming suggests, the purpose of this step is just to try to get the model which "best" fits the data. Least-squares does this by minimizing the "Chi-Square" function

$$\chi^2 = \sum_{\mathbf{S}} w||F(\mathbf{S})_{obs}| - |F(\mathbf{S})_{calc}||^2 \tag{2.9}$$

i.e. it systematically adjusts the parameter values until the discrepancy between the observed and calculated structure factors is minimized. In this way, true random noise in the data will be filtered but systematic errors will not. Assuming good quality data, the main block to lowering the χ^2 value is the model used to calculate the structure factors. A brief summary of crystallographic least squares is given in Appendix A.

2.2 Nature of f_j - The Atomic Scattering Factor.

The first calculations of atomic scattering factors[14] assumed that the atom contained electrons which scattered according to the classical theory of electrodynamics. It was further assumed that the frequency of the radiation is large compared with the absorption frequencies of the atoms, to the effect that the scattering corresponds to that of free electrons. J.J. Thomson's law concerning this scattering is that if unpolarised radiation of unit amplitude falls on an electron, the scattered intensity at unit distance from the electron is $(e^2/mc^2)^2(1 + cos^2 2\theta)/2$. To get the combined scattering from an assemblage of electrons in an atom, we add the individual contributions, remembering the phase differences which result from the electrons being distributed in a volume of space, the cross-section of which is comparable to the wavelength of the incident radiation. The scattering amplitude now becomes $f(e^2/mc^2)^2$, where f is the atomic scattering factor. The nature of f is such that at very low angles the value of f approaches that of the number of electrons in the atom, but falls off rapidly with increasing scattering angle.

The f so far characterized has neglected thermal motion of the atom. This was included to a first approximation by Debye[15,16] by forming an effective scattering factor for an isotropically vibrating atom with Gaussian probability distribution around the equilibrium position

$$f = f_o.e^{-M} \tag{2.10}$$

where

$$M = 2\bar{u}^2\mathbf{S} \tag{2.11}$$

with $\bar{u}^2$ the mean-square atomic displacement. Therefore the separation of temperature effects in (2.8) is justified with $T_j = e^{-M}$. This form of the temperature factor is still often used although anisotropic effects are included by the extension of Waller in 1926. Born[17] describes temperature effects in poetic fashion:

> "the effect of the thermal motion on an X-ray beam traversing the crystal has been compared with the effect of the agitated surface of the sea on the image of the setting sun."

It is now convenient to concentrate on f_o, the scattering factor resulting from a static atomic electron density distribution. It is easiest related to the radial distribution of the static density $U(\mathbf{r}) = 4\pi\mathbf{r}^2\rho(\mathbf{r})$ by

$$f_o = \int_0^\infty U(\mathbf{r})\frac{sin2\mathbf{S}.\mathbf{r}}{2\mathbf{S}.\mathbf{r}}d\mathbf{r} \tag{2.12}$$

Knowledge of $U(\mathbf{r})$ as a function of $\mathbf{r}$ allows equation (2.12) to be numerically integrated to yield f_o for any particular scattering angle. This was first done by Hartree[18] assuming an orbital model for the atom, and treating the time average of the electron density as a classical scatterer in accord with Thomson's equation.

Waller[19] developed a wave-mechanical theory of diffraction and showed that Thomson's formula produced the *total* scattered intensity, assuming the incident wavelength was large compared to the absorption frequency of the atom but not so large that relativistic effects became significant. This *total* scattering is composed of a component deriving from inelastic (Compton)

scattering where the wavelength of detected radiation differs from that of the incident beam and a second, dominant component deriving from coherent elastic scattering. It is only the latter we wish to consider when calculating f. The importance of Waller's theory is that it allows us to relate the radial distribution $U(\mathbf{r})$ to the electronic wavefunction $\psi(\mathbf{r})$.

The production of the scattering factor therefore rests on the ability to produce a wavefunction and deriving the associated charge density. This can be done analytically for the hydrogen atom and hydrogen-like ions but for many electron systems the Hartree-Fock method of the self-consistent field can be used. This of course, becomes intractable for atoms with high atomic number and hence many electrons, but a charge density can still be obtained by reverting to the electron gas, Thomas Fermi regime[20,21] which is the forerunner to Density Functional Theory. Inspection of the atomic scattering factors in International Tables[22] shows that the lighter atoms and ion scattering factors are derived from Hartree-Fock and Relativistic Hartree-Fock calculations while the heaviest ions bear the legend "Dirac Slater" denoting their extension to the Thomas Fermi theory. The important points to take from the James and Brindley formalism for atomic scattering factors are (as summarized by McWeeney[23])

1. Non-spherical atoms may be dealt with as though spherical, using an electron density which is effectively "smeared out" by averaging over all orientations in space.

2. There is no significant difference between the scattering from an isolated atom and from the same atom engaged in chemical (covalent) bonding or 'metallic' bonding.

This is the level of theory utilized in conventional structure determination and least-squares refinement procedures. In the past this was probably justified by the quality of data which could be collected and the data reduction schemes used. However, current diffractometer technology is such that much more information can be recovered from the experimental structure factors.

2.3 Inadequacy of Spherical Scattering Factors

In a letter to the editor of the Physical Review[24], James and Johnson brought to attention their conclusion that discrepancies between the observed and calculated structure factors using the spherical atom model were not due to errors in the data but the nature of the charge distribution

> "We have thus been brought to the conclusion that the valence electrons in the crystal, despite their small numbers, are responsible for the observed anomalies".

From the beginning, the allotropes of carbon have have played a prominent part in the question of the suitability of spherical scattering factors. Bragg[5] noted the probable aspherical nature of atoms during his studies of carbon and silicon. This revolves around the measurement of the so-called "forbidden" reflections. If the scattering from a diamond crystal is calculated using spherical scattering factors for the carbon atoms, certain reflections, notably the (222), have zero intensity. However, the experimental data shows that the (222) reflection has small but definitely non-zero intensity. The discrepancy is caused by the non-centrosymmetric component of the density. A similar effect was noticed by Franklin[25] in the case of powder diffraction from

graphite for the (10) band from single carbon layers and she recognizes atomic asphericity as the cause, proposing that the three sp^2 electrons are concentrated mainly at the centres of the bonds. Bacon[26] points out that while a large bonding concentration would indeed remove the discrepancy for the (10) band, it would cause large discrepancies elsewhere in the data. He narrows the cause down to a *slight* concentration in the bonding directions relative to a spherical atom and shows that use of McWeeny's[23] scattering factors for the sp^2 hybridized carbon reconciles experiment with theory.

2.4 Aspherical Scattering Formalisms

McWeeney[23] has given the scattering factor for an atom in terms of scattering factors for the individual orbital products in an orthogonal basis. Since any orbital product where one orbital is a non s function is not spherically symmetrical, the scattering factor is no longer orientationally independent for a given scattering angle. McWeeny decomposes the scattering factor into components parallel and perpendicular to some symmetry axis, leading to a complex scattering factor. He also shows how to arrive at the scattering factor for hybrid valence states (sp, sp^2, sp^3) by taking linear combinations of the basis functions.

This appears to be a vast improvement theoretically, judging by the comparison McWeeny gives between the parallel and perpendicular components of the anisotropic scattering factor for carbon $2p$ electrons compared to the spherically averaged scattering from the same electrons. He also points out that equal occupancy of the 4 valence orbitals, irrespective of hybridisation state will still lead to a spherical charge distribution and thus a single isotropic scattering factor. The scattering from each individual orbital may be anisotropic but the *total* scattering is still isotropic. This is quite an important point and one which is open to misinterpretation. Given a total wavefunction expressed in the form of a Slater Determinant, addition of the corresponding elements in any two columns of the determinant leave its value unchanged. The effect of this is that we may produce new orbitals by formation of linear combinations of the original orbitals without altering either the total wavefunction or the resulting density. This is the basis of forming orbitals by localizing them spatially[27,28] or energetically[29]. It amounts to performing a unitary transformation on the basis function expansion coefficient matrix. The ability to do this underlines the arbitrary nature of talking about certain orbitals within a molecule.

The next step in McWeeny's development[30] is to include the effect of bonding into the scattering factors. His method of assigning charge in the molecule is the same as that of Mulliken[31] and in fact pre-dates some of Mulliken's work in this area. While the one-centre components are unambiguously assigned, the two-centre ones are only so in the case of bonding between two identical atoms. As far as calculating the scattering from a whole molecule is concerned this is fine, but to decompose the scattering into a sum of one-centre components by assigning half of the scattering to each atom is arbitrary if all atoms are not the same. McWeeny also assumes static atomic positions. Problems with this analysis could easily occur if atoms with overlap populations between them have differing temperature factors in the crystal. The development is applied to a static H_2 molecule so none of these considerations apply. This allows the effect of

the bonding charge or overlap population to be treated as a "correction" to the spherical atomic scattering factor

$$f_j(\mathbf{S}) = \bar{f}_j(\mathbf{S}) + \Delta f_j(\mathbf{S}) \tag{2.13}$$

The correction term derives from the one centre and two centre scattering functions. Since $f_j(\mathbf{S})$ is in general neither spherically symmetrical nor centrosymmetric, the correction term will introduce a phase shift and so is complex

$$f_j(\mathbf{S}) = \bar{f}_j(\mathbf{S}) + i\Delta f_j(\mathbf{S}) \tag{2.14}$$

Although formally similar to inclusion of "anomalous" scattering into the scattering factor, the two effects are entirely separate in origin and not to be confused.

The main implementational problem with this approach is the analytical form of the basis functions. The radial dependency is described by a Slater function, but computing products and integrals over these function is difficult. McWeeny[32] proposes using the Gaussian approximation where the underlying Slater function is "fitted" by a contraction of Gaussians due to their easier mathematical manageability. This is now the norm in *ab initio* MO calculations. The other contention raised earlier about temperature effects is said to be insignificant:

> "The small correction to f_j, based on the diffuse valence-electron distribution are almost certainly relatively insensitive to vibration."

McWeeny's work culminates[33] in the calculation of scattering factors for carbon in both diamond sp^3 and graphite sp^2. Due to the strong bonding in both of these situations causing extreme levels of deviation from atomic asphericity (as also in the case of H_2 in reference 30), the discrepancy from spherical scattering factors is the largest one might expect to occur in real situations. The deviations found to occur are, however, substantial although they derive almost wholly from the "atomic" asphericity part of the correction Δf_j *i.e.* the component derived from orbital products on the same centre. The "bonding" contribution arising from orbital products on neighbouring centres is very small. Justification is therefore provided for using the atomic scattering factors for atoms in the prepared valence state derived in reference 23. The validity of the prepared valence states used (sp^2, sp^3, *etc.*) is perhaps suspect since it has since been shown that the actual proportions of the various contributions of the orbitals to the true hybridisation state deviates from those presupposed[34]:

> "The discrepancy from the "ideal" ratio is very substantial; however, it is not surprising, since it has become more and more apparent in the last decade that the "ideal" ratios are more of linguistic than of physical value."

McWeeny also suggests that a more rigorous approach to temperature effects is desirable, especially for high scattering angles. He has developed a generalized theory for scattering from the electron density in atoms and molecules but states that attention should now be turned to a better description of thermal motion.

Dawson[35] has built upon McWeeny's work and tabulations for the scattering factor of N, P, O, S, F, Cl in ground states and prepared valence states are given. The important point

developed is the decomposition of the aspherical scattering factor from a valence orbital ϕ_v into centrosymmetric and antisymmetric components

$$f(\phi_v) = f_c(\phi_v) + if_a(\phi_v) \tag{2.15}$$

The antisymmetric component of (2.15) is $\pi/2$ out of phase with the centrosymmetric part and hence the total scattering factor is complex. We have now reached an explanation of "forbidden" reflections. When the structure factors are calculated using the spherical atom model and harmonic temperature factors, there are only centrosymmetric contributions to the scattering. By symmetry, some reflections will only have components from the centric part of the scattering. These will have calculated intensities close to the experimental values. Some reflections will have components from both centrosymmetric and antisymmetric parts of the scattering and hence there will be discrepancies between calculated and observed values. Finally, some reflections, the "forbidden" reflections, have component only from the antisymmetric part. Since this is ignored in the structure factor calculation, they have zero calculated intensity but non-zero, although rather small, observed intensity. This is borne out for diamond[36]. Planes whose indices are odd have contributions from both the centrosymmetric and antisymmetric scattering and disagree with the calculated intensities. Planes whose indices are even agree well with the calculated intensities since they arise from only the centrosymmetric part of the scattering and the "forbidden" reflections disagree since their intensity derives exclusively from the antisymmetric part of the scattering.

The aspherical scattering factor can be decomposed further into parallel and perpendicular components related by the angle θ to a symmetry axis of the scattering function:

$$f = f_c + if_a \tag{2.16}$$

with

$$f_c = f_c^{\parallel} cos^2\theta + f_c^{\perp} sin^2\theta, \tag{2.17}$$

$$f_a = f_a^{\parallel} cos\theta \tag{2.18}$$

For a general reflection

$$F(\mathbf{S}) = 2(f_c(\mathbf{S})cos\varphi - f_a(\mathbf{S})sin\varphi) * T(\mathbf{S}) \tag{2.19}$$

where $\varphi = \mathbf{S}.\mathbf{r}$. The spherical atom approach gives

$$\bar{F} = 2\bar{f}_c(\mathbf{S})cos\varphi * T(\mathbf{S}) \tag{2.20}$$

since $\bar{f}_c = \frac{1}{3}(f_c^{\parallel} + 2f_c^{\perp})$ and $\bar{f}_a = 0$.

In order to examine the physical consequences of using the standard spherical atom scattering formalism in the refinement of a true structure, Dawson constructed a hypothetical crystal structure composed of two sp^3 hybridized nitrogen atoms per unit cell[37]. This facilitated the calculation of the true structure factors and also those structure factors resulting from the spherical atom model with the atoms placed at the true positions. This allows one to produce a difference

Fourier map with coefficients $F(\mathbf{S}) - \bar{F}(\mathbf{S})$ which display the inadequacy of the spherical atom model. The result is a plot of $\Delta\rho(\mathbf{r}) = \Delta\rho_c(\mathbf{r}) + \rho_a(\mathbf{r})$. The features of this have remarkable similarity to spherical harmonic functions, an observation that was not lost on Dawson.

As an investigation of the effect of spherical atom refinements on structural parameters, sets of reflection intensities were calculated by Dawson assuming isotropic temperature factors at three different levels, $\bar{B} = 1, 2$ and 3Åand to two different $(sin\theta/\lambda)_{max}$ levels of 0.65Å^{-1} and 0.50Å^{-1}. The net effect of using the $\bar{f}$ model is to produce spurious shifts of the atomic centres of ≈ 0.017Åfor the high angle data and ≈ 0.027Åfor the low angle data. Substantial anisotropy was also found in the temperature factors so the overall effect of using the $\bar{f}$ approach in a least squares refinement is to introduce spurious shifts in both the positional and temperature parameters. Because these shifts actually improve the fit of the model to the data, the standard deviations obtained from the variance-covariance matrix are substantially under-estimated.

The multipolar nature of the deviation from sphericity is noted by Dawson[37]

> "For all except the rare cases of central atoms in linear molecules possessing centrosymmetry, the environment of neighbours about any bonded atom must inevitably generate what is effectively a set of bonding multipoles about each atomic nucleus."

This statement is important since it shaped the development of charge density techniques to the present day.

McWeeny[33] called for a better description of thermal effects and Dawson develops this in terms of centrosymmetric and antisymmetric components, in an analogous way to the charge density formalism

$$t_j(\mathbf{r}) = t_{c,j}(\mathbf{r}) + t_{a,j}(\mathbf{r}) \tag{2.21}$$

giving in reciprocal space

$$T_j(\mathbf{S}) = T_{c,j}(\mathbf{S}) + T_{a,j}(\mathbf{S}) \tag{2.22}$$

Using

$$F(\mathbf{S}) = \sum_j f_j(\mathbf{S}) T_j(\mathbf{S}) exp(i\mathbf{S}.\mathbf{r_j}) \tag{2.23}$$

substituting in with the generalized expressions for $f_j(\mathbf{S})$ and $T_j(\mathbf{S})$ and expressing the structure factor in the form

$$F(\mathbf{S}) = A(\mathbf{S}) + iB(\mathbf{S}) \tag{2.24}$$

gives

$$A(\mathbf{S}) = \sum_j [(f_c T_c - f_a T_a)_j cos\mathbf{S}.\mathbf{r_j} - (f_c T_a + f_a T_c)_j sin\mathbf{S}.\mathbf{r}_j] \tag{2.25}$$

$$B(\mathbf{S}) = \sum_j [(f_c T_c - f_a T_a)_j sin\mathbf{S}.\mathbf{r_j} - (f_c T_a + f_a T_c)_j cos\mathbf{S}.\mathbf{r}_j] \tag{2.26}$$

Neglect of antisymmetric components easily reduces the above to the more orthodox form with spherical scattering factors and harmonic temperature factors. As was shown above, the f_a component in the scattering factor leads to forbidden reflections in the X-ray data. In neutron diffraction, the effective cross-section of the nucleus is many orders of magnitude smaller than the wavelength of the thermal neutrons and hence they act as point scatterers. Thus there

is no antisymmetric component of the nuclear density. However we may conclude that any antisymmetric component of the temperature factors will lead to forbidden reflections in the neutron data in an analogous manner to the X-ray. This is indeed the case and much work has been done in this area by Willis[38] and coworkers[39].

The first application of Dawson's multipole description of the charge density is in an experimental description of the covalent bond in diamond[40]. Due to the "hard" nature of diamond, resulting in its high characteristic temperature, anharmonic motion was thought to be insignificant and only a single harmonic, isotropic temperature factor was employed

$$\bar{B} = 8\pi^2 \bar{u}_S^2 \tag{2.27}$$

The important development in this work is the description of the non-spherical components in terms of combinations of Kubic Harmonics[41] with Gaussian radial functions.

$$\rho(\mathbf{r}) = \bar{\rho}_c(\mathbf{r}) + \delta\rho_c(\mathbf{r}) + \rho_a(\mathbf{r}) \tag{2.28}$$

The antisymmetric component is expanded in terms of the third and seventh order Kubic Harmonic and the centric but aspherical component is expanded in the fourth and sixth order Kubic Harmonic:

$$\rho_a(\mathbf{r}) = \rho_{a,3}(\mathbf{r}) + \rho_{a,7}(\mathbf{r}) + \ldots \tag{2.29}$$

$$\delta\rho_c(\mathbf{r}) = \delta\rho_{c,4}(\mathbf{r}) + \delta\rho_{c,6}(\mathbf{r}) + \ldots \tag{2.30}$$

The spherical part $\bar{\rho}(\mathbf{r})$ is taken to be the spherically averaged Hartree-Fock density of the free atom.

For simplification, the expansion is truncated at the 4th Kubic Harmonic level.

The actual form of the functions used are:

$$\rho_{a,3}(\mathbf{r}) = F_3(\mathbf{r})(xyz)/r^3 \tag{2.31}$$

$$\delta\rho_{c,4}(\mathbf{r}) = G_4(\mathbf{r})((x^4 + y^4 + z^4)/r^4) - \frac{3}{5} \tag{2.32}$$

where the radial functions are of Gaussian form:

$$F_3(\mathbf{r}) = 7.5r^2 exp(-2.2r^2) \tag{2.33}$$

$$G_4(\mathbf{r}) = 2.2r^2 exp(-2.2r^2) \tag{2.34}$$

The values used in these radial functions are admitted to be arbitrary, but they do allow a good agreement between experimental and calculated structure factors.

These density functions are easily Fourier transformed to give the scattering factors; the Kubic harmonics remain invariant under the inversion as do the Gaussian radial functions. This basic recipe for modeling the aspherical nature of the atomic charge distribution has been developed into various "multipole models", the structure of which will be elaborated in the next chapter.

However, Dawson's decomposition of the temperature factor into centric and acentric components is not used. More usually a tensor representing anisotropic but still centrosymmetric temperature displacement is used instead. It has the form

$$T(\mathbf{S}) = exp(-2\pi^2\sigma(\mathbf{S})) \tag{2.35}$$

with σ representing the symmetrical three by three array of temperature factors which describe the harmonic gaussian displacement of the atom from its equilibrium average position.

2.5 Deviations from Elastic Scattering

The above development of scattering processes has relied upon the First Born Approximation to neglect any non-elastic scattering. The regime of the Second Born Approximation includes some effects which are relatively important in this context, and should be accounted for. While elastic scattering is by far the most probable outcome of the incidence of a photon on a crystal, other events may occur. These are best described with the aid of Feynman diagrams. Figure 2.1 is the Feynman diagram for elastic scattering. The wavefunction of the crystal is denoted by the straight arrows with their labels giving the current quantum state that the crystal occupies. The situation of the photon is given by the oscillating line with the label again denoting the state vector. The bold dot indicates that point in time when the event such as absorption, scattering or momentum transfer from photon to crystal occurs. As Figure 2.1 indicates, the crystal remains in the ground state Ψ_o after the scattering event and hence no momentum transfer occurs.

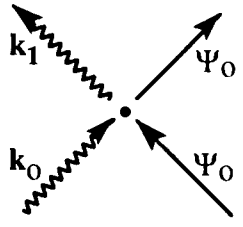

Figure 2.1 - Feynman diagram representing elastic scattering.

However, an incoming photon may interact with the crystal in such a way that momentum transfer occurs from the photon to the crystal, promoting the crystal to an excited electronic state Ψ_n as shown in Figure 2.2. The photon leaving the crystal has a lower energy and hence longer wavelength than the incident photon, the change in wavelength being proportional to the energy transferred

$$\Delta E = hc/\Delta\lambda \tag{2.36}$$

where h is Planck's constant and c is the speed of light in vacuum. This type of inelastic scattering is usually named Compton Scattering after the pioneer in the field, Arthur Holly Compton. If very high energy radiation such as γ-rays are used, the effect is appreciable and is an effective experimental probe of the electronic momentum density, but much softer radiation such as that produced by Copper or Molybdenum sources used in standard diffraction experiments means that the effect is negligible to the extent that it is usually ignored.

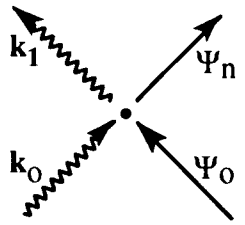

Figure 2.2 - Feynman diagram representing inelastic scattering.

A third type of scattering which may occur involves the absorption of an X-ray photon with similar energy to the core electron excitation energy for an atom. The energy absorbed excites the atom into some other, higher energy state, Ψ_n, by promotion of a core electron into a valence state. The excited state may subsequently decay back into the ground state, emitting a photon of exactly the same wavelength as that absorbed. This photon has undergone a phase change relative to the elastically scattered photons since the excitation/relaxation process takes a small but finite time. In crystallography, this effect is termed "anomalous" scattering, and the corresponding Feynman diagram is shown in Figure 2.3. Again the probability of this effect occuring is wavelength dependent, and most likely where the X-ray energy is close to the atomic $1s$ core energy. For Molybdenum radiation the effect is small, but for Copper radiation it is sufficiently large to be utilized in absolute structure determination. The effect is easily accounted for in charge density analysis by altering the core scattering factors by incorporation of a corrective term in the complex plane and all scattering factors now commonly in use incorporate such a correction.

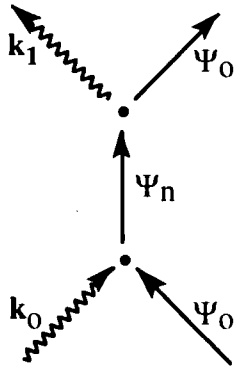

Figure 2.3 - Feynman diagram representing anomalous scattering.

The final type of scattering to be considered is multiple scattering, where the photon undergoes two or more scattering phenomena, and is the underlying explanation for primary extinction. Basically, two elastic scattering events take place within the crystal. Due to the geometry of the crystal while the Laue conditions are satisfied, the final scattered photon has direction the same as that for the incident beam, but has undergone a phase-shift of π, so that destructive interference and hence reduction in magnitude of the observed structure factors occurs. Figure 2.4 shows this diagrammatically. This effect only occurs when a very perfect crystal with few defects is under study. Since the probability of a second elastic scattering event is proportional to the distance travelled within the crystal, the effect is minimized by use of a small crystal.

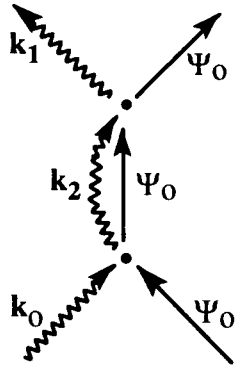

Figure 2.4 - Feynman diagram representing multiple scattering.

2.6 Diffraction - Scattering by a Crystal

Up until this point, X-ray scattering from a general chemical entity has been developed. We now turn our attention to the scattering from a single crystal. A crystal is a perfectly ordered array for which we can define a subvolume from which the whole crystal can be generated by repeated translations in specific directions. This specific volume is called the unit cell, and its three bounding edges are the unit cell vectors **a**,**b** and **c**. The electron density of the crystal is therefore a three-dimensional periodic function

$$\rho(\mathbf{r}) = \rho(\mathbf{r} + j\mathbf{a} + m\mathbf{b} + n\mathbf{c}) \tag{2.37}$$

where j, m, n are integers. This can be restated as a convolution

$$\rho(\mathbf{r}) = \sum_{j,m,n} \rho_{cell}(\mathbf{r}) * \delta(\mathbf{r} + j\mathbf{a} + m\mathbf{b} + n\mathbf{c}) \tag{2.38}$$

where δ is Dirac's delta function and $\rho_{cell}(\mathbf{r})$ is the electron density of the unit cell. According to the Fourier convolution theorem[42]

$$\Im[\rho(\mathbf{r})] = \frac{1}{V}\Im[\rho_{cell}(\mathbf{r})] \sum_{j,m,n} \Im[\delta(\mathbf{r} + j\mathbf{a} + m\mathbf{b} + n\mathbf{c})] \tag{2.39}$$

and hence

$$\Im[\rho(\mathbf{r})] = \frac{1}{V}F(\mathbf{S}) \sum_{h,k,l} \delta(\mathbf{S} + h\mathbf{a}^* + k\mathbf{b}^* + l\mathbf{c}^*) \tag{2.40}$$

with $\Im$ symbolising the Fourier operation. The above equation signifies that, in contrast to the general case where scattering can take place with any scattering vector **S**, for the crystal scattering occurs only in those directions $\mathbf{S} = \mathbf{H}(h, k, l)$ where the Laue conditions are satsified

$$\mathbf{S} = h\mathbf{a}^* + k\mathbf{b}^* + l\mathbf{c}^* \tag{2.41}$$

The vector **H** is called the reciprocal lattice vector and is defined by its three Miller Indices h, k, l.

The structure factor observed from scattering by a crystal is obtained by performing the Fourier transform only over the unit cell

$$F(\mathbf{H}) = \int_V \rho_{cell}(\mathbf{r}) exp(i\mathbf{H}.\mathbf{r}) d\mathbf{r} \tag{2.42}$$

and the relationship of $\rho_{cell}(\mathbf{r})$, the charge density in the unit cell to the structure factor is then the inverse Fourier transform

$$\rho_{cell}(\mathbf{r}) = \frac{1}{V}\sum_{\mathbf{H}} F(\mathbf{H})exp(-i\mathbf{H}.\mathbf{r}). \tag{2.43}$$

Chapter 3

The Multipole Models

There exists a multiplicity of programs available for aspherical atom refinements, all based on multipole models. These fall into two distinct groups:

- Models based on Spherical Harmonic Functions.
- Models based on Cosine Functions.

There are also adherents to "Valence" orbital models. It is the purpose of this chapter to summarize these formalisms.

3.1 Spherical Harmonic Models

Stewart[43] follows the work of McWeeny outlined in the previous chapter by developing "generalized scattering factors" based on density functions obtained by forming orbital products. Orbital products fall into two categories; one-centred and two centred. By consideration of only the one-centred orbital products, Stewart unites the theoretically based functions of McWeeny which are one-centred orbital products, with the arbitrary multipole functions of Dawson, showing them to be equivalent. Stewart also states that a more justifiable set of multipoles is the spherical harmonic functions rather than Dawson's use of the Kubic Harmonics. This is because any product of two spherical harmonics (such as one-centred orbital products) will themselves be spherical harmonic functions.

For all cases, it is assumed that the core remains unaffected by the chemical bonding, which is perhaps, in itself, not strictly true, but any deviation from sphericity will be so slight that it is unlikely to be detectable in the X-ray experiment. The density functions to use are orbital products

$$\rho(\mathbf{r}) = \chi(\mathbf{r})\chi^*(\mathbf{r}) \tag{3.1}$$

for example the core density is described by

$$\rho_{core}(\mathbf{r}) = \chi_{1s}(\mathbf{r})\chi^*_{1s}(\mathbf{r}) \tag{3.2}$$

The $\chi(\mathbf{r})$ functions are the atomic orbital basis and it is conventional to use the spherical harmonics times some radial function as the orbital basis set

$$\chi(\mathbf{r}) = Y_{l,m}(\theta,\phi)r^{n-1}e^{-\zeta\mathbf{r}} \tag{3.3}$$

where $Y_{l,m}(\theta,\phi)$ is the spherical harmonic of order l oriented with respect to m. In these applications we assume the real spherical harmonics which result from taking linear combinations of the complex functions. The relevance of $Y_{l,m}(\theta,\phi)$ is that they are analytical solutions to the eigenfunction problem of the hydrogen atom. The radial function $r^{n-1}e^{-\zeta r}$ is referred to as a Slater Type Orbital or STO. The values of ζ are taken from an analytical fit to Clementi's atomic Hartree Fock calculations[44].

For first row atoms, we use a "frozen" core,

$$\rho_{core}(\mathbf{r}) = \chi_{1s}(\mathbf{r})\chi^*_{1s}(\mathbf{r}) \tag{3.4}$$

and assign it a population of 2 electrons. The radial part of this density function will be

$$(r^{n-1}e^{-\zeta r})^2 \tag{3.5}$$

which is

$$(r^{n-1})^2 e^{-2\zeta r} \tag{3.6}$$

Quite often 2ζ is renamed α. For the valence density, we again use orbital products, but we must form all possible orbital products within a given basis and assign populations to the resultant density functions

$$\rho_{val}(\mathbf{r}) = \sum_{ij} P_{i,j}\chi_i(\mathbf{r})\chi^*_j(\mathbf{r}) \tag{3.7}$$

If we first consider products between functions on the same centre, the case of a first row atom gives:

$2s2s$

$2s2p_x : 2s2p_y : 2s2p_z$

$2p_x2p_x : 2p_x2p_y : 2p_x2p_z$

$2p_y2p_y : 2p_y2p_z$

$2p_z2p_z$

These orbital products combine to give two monopoles, three dipoles and five quadrupoles. In all applications of this formalism, since it is concluded that scattering from the monopoles will be very similar, one monopole replaces the two from above, taking the character of the spherically averaged Hartree-Fock isolated atom valence density. The relation to Dawson's work can now be seen

$$\rho_j(\mathbf{r}) = \bar{\rho}(\mathbf{r}) + \Delta\rho_c(\mathbf{r}) + \rho_a(\mathbf{r}) \tag{3.8}$$

The monopole term will provide $\bar{\rho}(\mathbf{r})$, while the three dipoles will describe the $\rho_a(\mathbf{r})$ term with the five quadrupoles describing the $\Delta\rho_c(\mathbf{r})$ term. For second row atoms, we can lock the $2s$

and $2p$ contributions into the core and the formalism is easily extended to include participation from the third quantum level which includes d-orbitals[45]. The $3s$ and $3p$ functions will provide the monopoles, dipoles and quadrupoles as before, and the $3s3d$ orbital products provide five quadrupoles, the $3p3d$ three monopoles and seven octapoles and the $3d3d$ one monopole, five quadrupoles and nine hexadecapoles. The level of expansion usually chosen is that of truncation at octapoles for first row atoms. At first this seems reasonable, with the expansion to quadrupole level accounting for density deriving from the s and p orbital products and the octapole functions providing for further polarization effects. The development so far mirrors McWeeny's first paper dealing with orbital products on the same centre. For a real molecule there will also be a contribution, albeit small, from the orbital products on neighbouring centres. These are not included *per se* in the multipole model although they should be approximately described by the octapole functions. However they blur our choice of radial exponent for the expansion, since they cannot be based on atomic values. This will be particularly so in molecules with "long" bonds. Inclusion of specific overlap functions at bond mid-points would alleviate this problem.

3.2 Practical Implementation

There are three programs which use this formalism: POP[46,47] by Craven and Weber, Stewart's own program VALRAY[48], and MOLLY[49] by Hansen and Coppens which has latterly evolved into XD[50]. Since they are all very similar, I will outline only XD since it is the only one used during the research reported in this thesis.

The model used develops in two stages

3.2.1 Stage 1. Allow charge transfer between atoms

Atoms in the molecule will have partial charges due to their differing electronegativities. Allowing the population of the valence shell to vary will describe this effect. However, it is an empirical observation[51] that the size of the atom increases with increasing negative charge. The first stage in the XD model allows for this by including a κ' parameter which scales the exponent of the radial function and is varied in the refinement

$$\rho_j(\mathbf{r}) = \rho_{core}(\mathbf{r}) + P_{val}\rho_{val}(\kappa', \mathbf{r}) \tag{3.9}$$

with the specific form of the radial function being

$$R_l(\mathbf{r}) = \kappa'^3 r^{n-1} e^{-\kappa'\zeta r} \tag{3.10}$$

The initial κ'^3 retains the normalization to one of the spherical valence monopole. For first row atoms in organic structures this model itself is surprisingly successful in improving the agreement with the experimental intensities relative to the spherical atom model[51].

3.2.2 Stage 2. Allow atoms to deform from sphericity

$$\rho_j(\mathbf{r}) = \rho_{core}(\mathbf{r}) + P_{val}\rho_{val}(\kappa'\mathbf{r}) + \delta\rho(\mathbf{r}) \tag{3.11}$$

$$\delta\rho(\mathbf{r}) = \sum_{l=0}^{l_{max}} \sum_{m=-l}^{m=l} P_{l,m} Y_{l,m}(\phi,\theta) R_l(\kappa''\mathbf{r}) \tag{3.12}$$

The κ'' parameter again rescales the exponent of the radial function to allow expansion or contraction of the aspherical deformation functions.

The scattering from this model is easily calculated by performing a Fourier transform. The spherical harmonics remain invariant under the process while the Slater radial functions become spherical Bessel's functions under the transform. Restating the complete static charge density model:

$$\rho_j(\mathbf{r}) = P_c\rho_c(\mathbf{r}) + \kappa'^3 P_v\rho_v(\kappa'^3\mathbf{r}) + \sum_{l=0}^{l_{max}} \sum_{m=-l}^{m=+l} \kappa''^3 P_{lm} R_l(\kappa''\mathbf{r}) d_{lmp}(\theta,\phi) \tag{3.13}$$

The normalization of the monopole terms is to one. Since the higher order deformation functions integrate to zero, the normalization chosen is that an occupancy parameter of one indicates a transfer of one electron from the negative lobe(s) into the positive lobe(s).

It is usual practice to omit the second monopole (the $l = 0$ deformation function) for almost all atoms, since it is exactly the same as the spherical valence function, and simultaneous refinement of two identical parameters will give an unstable refinement due to their total correlation. However, it is possible to give these two dipoles differing radial extents to allow simultaneous refinement and improve the model flexibility.

The level of expansion generally used is to octapole level for first row atoms and hexadecapole level for second row atoms. Hydrogen atoms are usually modelled by either the set of three dipole functions, or a single, bond-directed dipole. While hexadecapoles on first row atoms may "improve" the fit of the data in the sense of agreement factors, these functions may not be well determined in the sense of extremely high estimated standard deviations as obtained from the least-squares procedure. The radial flexibility of the deformation functions is usually restricted such that all deformation functions share a common κ'' parameter, but for second row atoms, specifically in the case of Sulphur[52], separate κ'' parameters for each value of l can improve the model. It is generally observed that the most sensitive and therefore least well defined parameter in the model is κ'', and great care need be exercised that a fully converged refinement results.

For an atom in a general crystallographic position in the unit cell, all functions up to the maximum value of l for the particular level of expansion chosen may be refined. In the case of an atom on a crystallographic symmetry element, restrictions on the values of some multipole parameters are required to ensure that the charge density retains the full crystallographic symmetry. For example, a dipolar deformation function perpendicular to a mirror plane must have an occupancy of exactly zero so as not to break the symmetry. Since the spherical harmonic expansion for the charge density is rotationally invariant, the local axis system for each atom is chosen to be related in a convenient way to the crystallographic symmetry elements involved at a particular site to facilitate the easy application of the restrictions. The full set of restrictions for all possible combinations of symmetry elements have been elucidated and are tabulated for reference[53].

The static charge density model for each atom "rides" on the usual crystallographic structural model fractional atomic coordinates and anisotropic temperature factors for non-hydrogen atoms and isotropic temperature factors for the hydrogen atoms.

Since hydrogen atoms formally contain only a single electron, and this is within the covalent bond to the heavy atom, little reliable information of the hydrogen positional or thermal parameters is available from the x-ray experiment. A separate neutron diffraction experiment to obtain these values is a possible way to proceed but is not without difficulties[54]. Utilizing only the X-ray data, a spherical atom refinement may be performed, using the contracted scattering factors of Stewart, Davidson and Simpson[55] for the hydrogen atoms. This is supposed to give more reliable isotropic temperature factors. The hydrogen positions may then be obtained by "normalizing" the bond vector to the average length of a similar bond type obtained in neutron diffraction experiments[56]. An alternative way of defining the hydrogen temperature factor is simply setting it equal to some factor between 1.2 and 1.5 times the isotropic equivalent of the atoms to which it is bonded. The hydrogen structural parameters are kept fixed in the refinement, but all other parameters are refined. An electroneutrality constraint is applied to keep the unit cell neutrally charged.

Within XD, the coordinate system is explicitly defined for each atom. The idea is that chemically similar but non-crystallographically identical atoms can be set up to have the same local axis system allowing multipole parameters to be tied together. This may help the attainment of convergence and reduces the number of independent parameters and hence improves the observations to parameters ratio for a given set of experimental data.

3.3 Cosine Function Models

The only current program utilising cosine functions is Hirshfeld's LSEXP code[57,58]. The model consists of the following basis functions

$$f_{m,n,k} = cos^m\theta_k R(\mathbf{r}, n) \tag{3.14}$$

For $\mathbf{m = 0}$ the functions are spherically symmetric, but they take on three different radial exponents so there are three spherically symmetric functions.

For $\mathbf{m = 1}$ the shape of the functions are $cos\theta_k$. There are three such functions with directions defined by $k = 1, 2, 3$.

For $\mathbf{m = 2}$ the functions are $cos^2\theta_k$. In this case there are six functions with directions defined by $k = 1 - 6$.

For $\mathbf{m = 3}$, there are ten functions with shape part $cos^3\theta_k$. The functions $cos\theta$ and $cos^2\theta$ are antisymmetric while $cos^2\theta$ is centrosymmetric. Therefore this model is fully compatible with Dawson's idea of expansion with centrosymmetric and antisymmetric functions. The functions are not automatically orthogonal via their angular part, however and this may introduce interparameter correlations in the model. The same treatment of temperature effects as in XD is applied. Since there are more functions per level (*e.g.* six for second order functions as opposed to five in the spherical harmonic case) it is claimed to be more flexible. However, the tenuous links that Stewart's model has with theory are absent so the choice of functions is purely arbitrary. It is

the common view that very similar results are produced with the cosine function model as with the spherical harmonic model.

3.4 Valence Models

There are two main schools developing and using valence orbital models

- B.N. Figgis and P.A. Reynolds at the University of Western Australia.
- Kiyoaki Tanaka at the Tokyo University of Technology.

The model of Figgis and Reynolds is

$$\rho(\mathbf{r}) = \sum_i \sum_{k,k'} \sum_{nlm,n'l'm'} C^{ik}_{nlm} C^{ik'}_{n'l'm'} \chi^{nlm}_k(\mathbf{r}) \chi^{n'l'm'}_{k'}(\mathbf{r}) \tag{3.15}$$

where $\chi^{nlm}_k(\mathbf{r})$ is an atomic orbital of quantum numbers n, l, m on centre k. The C^{ik}_{nlm} are expansion coefficients for the χ such that MO i is described. The summation over i thus means the summation over all MOs described as expansions of the atomic orbitals, $\chi(\mathbf{r})$.

This is a purely general description of the density. It is made tractable to least squares refinement by discarding any terms with $k \neq k$, *i.e.* overlap functions are ignored. In this sense the model is pretty similar to the multipole model. In fact, given an infinite expansion the two are identical. The difference is that for a finite expansion the cut-off comes at what is chemically and physically reasonable as opposed to just some level of multipole[59]

> "The use of a restricted set of atomic functions is equivalent to a restricted multipole expansion in which the terms neglected are not cut off at an arbitrary order of multipole but chosen on the basis of chemical intuition."

The sensibility of this assertion is questionable though, since a valence orbital expansion using for example a set of four sp^3 hybrid orbitals on a carbon atom is no different to a multipole expansion up to quadrupole level, however the number of parameters to be refined is less.

In application, the functions used are usually chemically reasonable hybrid orbitals for first row atoms corresponding to a minimal basis set. If higher functions are used, the two centre density will be projected into these functions, but restriction to a minimal basis is thought to exclude this density from the model[59,60]. The advantage of this is that the populations of the functions are physically meaningful and can be analysed literally, especially the refined value of the radial parameter, ζ, since this is not distorted in trying to describe the overlap density. The overlap density excluded from the model should show in the difference synthesis and this is usually the case. One disadvantage is then that an electroneutrality constraint cannot be applied since all charge is not accounted for in the model. Greater requirement for accurate scale factor determination results. The most successful application of this model is to transition metal complexes since the $3d$ and $4p$ populations can be refined directly[61]. In this application, mid-bond functions between the transition metal and ligating atoms are included to account for the overlap density in these "long" bonds. Also, since the model is based on atomic hybrids, experimental data other than from X-ray diffraction can be described by the same model and

direct comparison is possible. For example, in transition metal complexes with unpaired electrons, bonding information can sometimes be seen more easily in a map of the spin density as opposed to the charge density. Polarised neutron diffraction provides this information and can be refined using exactly the same model as the charge density data[62].

The valence orbital method is not unique in providing individual *d*-orbital occupancies. The multipole model can also provide approximate *d*-orbital populations[63,64] since the one-centre *d-d* orbital products contribute only to the even order multipole functions in specific ratios. Matrix transformations bring the *d*-orbital populations from the multipoles but since this is a more indirect method, other density contributions such as $4s$, $4p$ and metal-ligand overlap density can contaminate the result.

Tanaka's[65,66] model is formally similar to the Figgis model[59] but overlap terms are included. He also provides a formalism for estimating the temperature factors for these functions from the temperature factors of the contributing nuclei. Further, by allowing different radial exponents for each of the d-orbitals, an approximate set of experimental, orthogonal, metal centred MO's are derived which have the correct symmetry properties for the particular point group involved.

3.5 Difficulties

The main problems with all of the models are much the same as in orthodox spherical atom refinements. Reliable nuclear positions and temperature factors are difficult to obtain from the X-ray data alone because cross correlation between temperature factors, atomic positions and multipole populations is inevitable. Specifically, the dipole functions correlate with the atomic positions while the quadrupole functions correlate with the temperature factors. We might expect that use of the best description possible for the temperature effects and the charge density will reduce correlation. Work by Mallinson *et al.*[67] indicates that a spherical atom model coupled to anharmonic temperature factors using the Gram-Charlier expansion is as effective at describing the thermally averaged charge density contained within the experimental structure factors as a full multipole expansion with harmonic temperature factors. If the temperature factors can describe the density, it is not unreasonable to expect the multipole parameters to describe the thermal effects. In current implementations, usually only harmonic temperature factors are employed which, of course, have no antisymmetric component. The only way such a component can be expressed is by population of the antisymmetric multipole functions. Anharmonic temperature factors would be expected to improve the situation. The XD package includes the option of anharmonic temperature factors but the large number of parameters these introduce almost definitely precludes their use due to the reduction in the observations to parameters ratio, and large correlation would still be expected.

Hirshfeld[68] proposes that with enough high-angle data the two effects of thermal motion and non-spherical atomic charge density should be separable. The reason for this is that core electrons which are compact in real space, are diffuse in reciprocal space and therefore dominate the scattering at higher angles. Positional and thermal parameters derived from this data should be relatively insensitive to the bonding density since this dominates the low angle scattering because

the valence density is diffuse in real space. The adiabatic approximation[69] is always assumed to be valid in any applications of thermal deconvolution from the dynamic scattering model. This states that the electrons follow the nuclei rigidly as the nuclei execute their vibrational motion. The more familiar Born-Oppenheimer approximation[70] is a special case of the adiabatic approximation. While this approximation is not strictly true and there are many cases known where it breaks down altogether [71], a more appropriate approximation has not been developed. To reduce as far as possible the cross-correlation of thermal and valence parameters, Hirshfeld proposes the use of data to resolution $(sin\theta/\lambda)_{max} = 1\text{Å}^{-1}$ which is much further than for a regular crystal structure analysis. At room temperature, data at high angles are very weak and usually unmeasurable above $sin\theta/\lambda = 0.7\text{Å}^{-1}$ for an average organic crystal[72]. The only way of getting data above this angle is to lower the temperature. Thermal smearing makes the dynamic atomic charge density more diffuse in real space and hence more compact in reciprocal space, meaning a more rapid fall-off of intensity with scattering angle. Lowering the temperature makes the atomic dynamic density more diffuse in reciprocal space and hence measurable to higher resolution. The bonus of low temperature work is that the thermal parameters themselves are smaller so errors in their determination will have a less severe effect. Liquid nitrogen Cryostream coolers[73] will allow a stable working temperature of about $100K$ allowing measurement up to $sin\theta/\lambda = 1.0\text{Å}^{-1}$. Liquid helium devices at $10K$ will give data up to $sin\theta/\lambda = 1.3\text{Å}^{-1}$. The greater number of data means that a least squares fit of thermal parameters will have a more appropriate observations to parameters ratio. This is important for anharmonic effects since more parameters are required per atom. High angle data do not resolve the problem of hydrogen atom parameters since these atoms have no core electrons.

A useful indicator of unreliable temperature parameters for heavy atoms is the rigid bond test[57,74]. Anisotropic temperature factors are known to compensate for inadequacies in the model and systematic errors in the data such as absorption. It is reasoned that the relative vibrational component of a pair of bonded atoms at least as heavy as carbon has an effectively vanishing component along the bond vector. If we denote $z^2_{A,B}$ as the mean-square displacement amplitude of atom A in the direction of the A,B bond then

$$\Delta_{A,B} = z^2_{A,B} - z^2_{B,A} = 0 \tag{3.16}$$

For atoms at least as heavy as carbon, $\Delta_{A,B}$ should be less than 0.001Å^2. If this is confirmed then confidence in the validity of the static charge density deconvolved from the dynamic density should be heightened because the temperature factors are at least not physically unreasonable. A systematic error in the temperature factors such as an isotropic effect will not cause a model to fail the rigid bond test though, since both temperature factors under consideration for a given bond will be incorrect by a similar amount and hence the mean-square difference will be unaffected. At the introduction of this model into the literature for organic structures, no mention was made of likely values for bonds containing atoms of dissimilar masses such as a transition metal to ligand bond. It is reasonable to assume that these bonds will fail the rigid bond test since the heavier atom will probably have much smaller thermal excursions than the lighter atom.

The visualization of the density is sometimes by means of a deformation density. This is the

"true" density as defined by the model minus that of free spherical atoms placed at the nuclear positions. Any mis-estimation of the nuclear positions will mean an inappropriate reference density being subtracted and false conclusions drawn. In fact, deformation densities are still arbitrary due to choice of reference state and should be discouraged because better techniques for analysis of the total density now exist.

In the early 1980's the IUCr initiated a project[75] to investigate the reproducibility of charge density experiments by asking several laboratories to perform multipole refinements on samples of oxalic acid dihydrate. This compound was chosen since it contains a conjugated π system, hydrogen bonds to water molecules and crystallizes well, although it does have a tendency to form twinned crystals. On the whole, the results of the deformation densities produced agreed qualitatively with each other and with theoretical calculations, but relative to the calculations, the lone pair peaks from the experiment were quantitatively smaller. The charge density on the oxygen atoms is acentric and so therefore is the potential experienced by the nucleus. Since only harmonic temperature factors were used, it is reasonable to assume that any anharmonic effects are absorbed by a slight shift of the experimentally determined nuclear position towards the lone pairs, so when a spherical atom is subtracted it lowers the effective lone pair height. This situation emphasizes the need for better temperature parameters and the poor behaviour of deformation densities.

A more serious problem may occur with refinement of the charge density parameters when the crystal is non-centrosymmetric. It has recently been shown[76] that to an approximation, a change in the population of an odd order multipole will change only the phase of the calculated structure factors and not the magnitudes. For a centrosymmetric crystal, the phases may only take the values 0 and π but for non-centrosymmetric cases the reflection phases may take any value. Since it is only the structure factor magnitudes which we measure, in theory the odd order multipoles may take any value and still fit the data equally well. However, this problem is only severe for small and highly symmetric molecules. It is obviously preferential to perform charge density analyses on centrosymmetric crystal structures for this reason.

In summary, given the highest quality data, the multipole models are sufficiently reliable to gain qualitative representations of the electron density and are useful for extracting approximate values, of for example, atomic, group and molecular multipole moments and other one-electron properties. The model cannot provide more fundamental properties such as two-electron properties or first order density matrices.

Chapter 4

Data Collection and Reduction

4.1 Experimental Considerations

At the end of the second chapter, the effect of periodicity of the crystal on the scattering was introduced, and it was shown that scattering only takes place at specific points called the reciprocal lattice points. The real lattice is defined by the unit cell vectors **a**,**b** and **c** while the reciprocal lattice is in terms of $\mathbf{a}^*, b^*, c^*$. The unit cell volume is the vector triple product of the unit cell vectors

$$V = \mathbf{a} \cdot \mathbf{b} \times \mathbf{c} \tag{4.1}$$

while the reciprocal lattice vectors are defined relative to the real-space lattice by

$$\mathbf{a}^* = \frac{\mathbf{b} \times \mathbf{c}}{V}, \mathbf{b}^* = \frac{\mathbf{c} \times \mathbf{a}}{V}, \mathbf{c}^* = \frac{\mathbf{a} \times \mathbf{b}}{V} \tag{4.2}$$

A lattice point where diffraction is observed is any point where the expression

$$\mathbf{H} = h\mathbf{a}^* + k\mathbf{b}^* + l\mathbf{c}^* \tag{4.3}$$

is satisfied. One may expect the most general case to be where each reciprocal lattice point is unique, and a complete set of reflections would require measurement of the structure factor amplitude at each lattice point.

Within the first Born approximation, this is not the case. The internal symmetry of the reciprocal lattice is related to the crystal system. The lowest symmetry crystal system, triclinic, has **a**,**b**, **c** all different magnitudes and all non-orthogonal. The symmetry of the reciprocal lattice is centrosymmetric and hence each reciprocal lattice point has one other reciprocal lattice point, called its Friedel Pair, with the same intensity. The relationship in reciprocal space for the triclinic case is centrosymmetric, that is any reflection $F(hkl)$ has equal intensity to $F(\overline{hkl})$, where the overline means "the negative value of". To collect a complete set of unique data only half of the total reciprocal lattice vectors require to be sampled. For higher symmetry crystal systems such as monoclinic, where all unit cell lengths differ but only one of the internal angles is not 90^o, the multiplicity of the data is four-fold with only a quarter necessary for a complete unique data set. The multiplicity of the data increases with increasing symmetry of the unit cell, to a maximum multiplicity of 48 for some cubic space groups (all unit cell vectors orthogonal and of the same magnitude).

The situation becomes a little more complicated by anomalous scattering. In addition to the elastic scattering which follows the above rules, the anomalous scattering acts to lower the overall symmetry of the reciprocal lattice because the Friedel Pairs become inequivalent in cases where the crystal space group is non-centrosymmetric. For a centrosymmetric space group, the full multiplicity of the data is retained, even with the inclusion of anomalous scattering.

In least squares analysis of the measured data only the unique set of data is utilized. There are two possible strategies for improving the reliability of this unique set. The first is to measure only one of the symmetry equivalent reflections slowly and carefully, or to measure several of them more quickly and merge the result. The latter is the better option because statistical considerations[77] indicate that the latter will provide a more accurate intensity, and if one of the equivalent measurements is poorly measured or subject to either a random or systematic error, comparison with the related measurements should allow the outlier to be detected.

The preferred strategy for charge density data collection is to collect four equivalents. Measurement of only two makes it impossible to detect which of the pair is the outlier in the case of poor internal agreement, while measurement of greater than four would be excessively time consuming and would not provide a significant increase in accuracy.

Almost all contemporary charge density data sets are collected on automated diffractometers which are provided with suitable data collection software as standard. All data sets used in the work reported in this thesis were measured either on an Enraf-Nonius CAD4 or Siemens P4 diffractometer. The X-ray source for both machines is a hot X-ray tube with Molybdenum target. The production of X-rays by such a device is achieved by bombarding the target with a high intensity electron beam. A single core electron is ejected from the atomic core followed by relaxation of a valence electron into the "hole" left by the ejected electron. A photon of energy equivalent to the difference of the two atomic states is emitted. With a Molybdenum tube, two main radiation wavelengths are produced. Since the de-excitation producing the radiation is into the core, or K shell, the two radiations are known as Mo-K_α and Mo-K_β. The ratio of K_α to K_β is approximately 2 to 1. A wide background of radiation of progressively longer wavelengths is also produced by the tube and this needs to be removed to give what is known as a monochromatic source, although in fact, there are the two slightly different wavelengths of radiation left in the beam. The raw source beam monochromatization is achieved by Bragg diffraction on a single crystal of graphite.

In the nomenclature of standard four-circle diffractometer geometry, the recommended[78] data collection mode is $\theta - 2\theta$, often referred to as bisecting mode. The alternative data collection mode of parallel geometry is not recommended for charge density studies. At higher scattering angles, the spread of a single reflection in real space becomes very large in bisecting mode.

The relationship between the crystal axes and the set of axes of the diffractometer is called the crystal orientation, and is contained in the orientation matrix. This is obtained in the first instance by simply driving the diffractometer around with the crystal under X-ray flux until the detector comes across a point in reciprocal space with high X-ray intensity. This process is continued until a sufficient set of such points have been accumulated and standard routines determine both the cell constants and the orientation matrix. Given the orientation

matrix, calculation of the angles where all the remaining reciprocal lattice points are is fairly straightforward and the diffractometer is instructed to drive to all such points and collect the intensity data for all the required reflections. The reflection profile is scanned across with step-scans of ninety-six steps being measured. The treatment of these raw scan profiles to extract the peak intensity and correct for geometrical effects in the diffraction process is called data reduction and is a critical step on the way to production of accurate diffraction intensities.

4.2 Data Reduction

4.2.1 Raw Reflection Intensities

The DREAM package of programs used for data reduction are freely available FORTRAN code written specifically for charge density data sets by Bob Blessing at the Hauptmann-Woodward Institute, Buffalo, USA. The programs are the subject of a review article[79] and use standard theory. The first step in data reduction is the determination of the peak centroids. This gives the exact positions of the reciprocal lattice points and hence an accurate unit cell. The orientation of the crystallographic unit cell relative to the machine is contained within the orientation matrix. Within DREAM, a new orientation matrix is determined and used for data reduction. It is derived from the centroids of a well distributed range of reflections with well defined profiles and intensities passing signal to noise ratio tests.

This same subset of reflection profiles is then used to determine peak width parameters. Accurate peak widths are essential in the determination of background counts which must be subtracted. Peak widths can be calculated for all reflections after the relevant parameters are obtained from the well defined reflection profiles.

The next step is to correct for two geometrical factors of diffraction called Lorenztian and Polarization. They are often made together and referred to singly as LP corrections. The correction is applied to every one of the 96 steps on the scan individually. The Lorentzian correction is connected to the manner in which the reciprocal lattice point appears as the crystal is rotated into the diffracting position and has the form

$$L = \frac{1}{sin2\theta} \tag{4.4}$$

while the second accounts for polarization of the beam on diffraction

$$P = \frac{1}{2} + \frac{1}{2}(cos2\theta)^2. \tag{4.5}$$

The corrected intensity is now given by

$$I = \frac{I_{measured}}{LP} \tag{4.6}$$

The above equations are the correct for diffraction once of an unpolarized incident beam. However, by the time the beam impinges on the crystal, diffraction has already occurred on the graphite monochromation crystal at a Bragg angle θ_m of 6.0817^o, so the beam incident on the sample is already partially polarized. The combined effect of both Lorenztian and Polarization from both diffractions are made together giving a total LP factor of[80] (assuming a perfect

monochromator crystal)

$$LP = \frac{cos^2 2\theta |cos^2 2\theta_m| + 1}{sin 2\theta (1 + |cos^2 2\theta_m|)} \tag{4.7}$$

The unsubscripted θ angle is the diffraction angle of the sample. Once each step has been LP corrected, the background of the peak is determined and subtracted from that part of the scan deemed to represent the true peak. The remaining counts for each step within the peak are summed to give the net intensity. If the background has been slightly over-estimated for very weak reflections, for example if the estimated peak width is smaller than the true peak width, the net intensity appears to be negative. Even if the peak widths are correctly determined, truly random statistical fluctuations across the scan range may still combine to give a net negative intensity.

4.2.2 Decay Correction

The crystalline sample under study experiences a substantial X-ray flux for much of the total experimental duration, brief relief being provided when the diffractometer drives between reciprocal lattice points with the X-ray shutter closed. Decay of the crystal under such harsh conditions is inevitable. Because all charge density experiments are conducted in the temperature range 10-150K the damage is somewhat less than would be experienced at ambient temperature, however the decay is still appreciable enough to require correction. Generally speaking, as the crystal deteriorates, the intensities of reflections reduce in a linear manner. By remeasuring a small sample of reference reflections, called the "standards", throughout the data collection an approximate measure of the decay is obtained. Five or six reflections at lattice points well separated in reciprocal space are usually remeasured every two hours (CAD4) or after every 96 normal reflections (Siemens P4) to give a plot of intensity *versus* time for these reflections. A moderate amount of decay is to be expected but substantial reduction in intensity signifies that the crystal has deteriorated to an unacceptable level for high quality studies. The intensity *versus* time profile is fitted by least-squares to a polynomial function of variable order, either linear, quadratic or cubic. Purely random fluctuations in the intensities unconnected with decay will not be fitted by only these low order functions. The standard deviations of this least squares fit provide a useful indication of the instrument instability, and can be further used in assigning the estimated standard deviation to each reflection intensity.

4.2.3 Absorption

Absorption is the name given to the general attenuation of the beam intensity as it passes through the crystal. The crystal absorbs energy most effectively when certain atomic electronic transitions are close to the energy of the X-ray photons. For heavier elements, lead being the classic example, this absorption is severe. The most usual Molybdenum X-ray source produces X-ray wavelengths far from the atomic core promotion energies of first and second row atoms and therefore this type of absorption is small. More generally, the degree of absorption per unit length of sample traversed is proportional to the linear absorption coefficient.

For monochromatic radiation passing straight through a block of material, the transmission

factor A is

$$A = \frac{I}{I_o} = exp(-\mu t) \tag{4.8}$$

where I_o is the intensity of the incident beam, I the intensity of the attenuated beam, t is the path length of the X-ray beam through the sample and μ is the linear absorption coefficient. μ is calculated from knowledge of the unit cell contents according to

$$\mu = \rho \sum_{i=1}^{n} f_i (\frac{\mu}{\rho})_i \tag{4.9}$$

with ρ the crystal density, f_i the mass fraction of the ith element in the unit cell and $(\frac{\mu}{\rho})_i$ is the mass absorption coefficient of the ith element, standard values of which are available from the International Tables.

The analytical absorption correction program ABSORB[81,82] was used for all absorption correction. Having evaluated μ as above, the path length t of the beam through the crystal is required for each reflection. For diffraction at any point in a crystal, the total path length t is the sum of the incident t_I and diffracted t_D path lengths. The transmission factor is then[83]

$$A = \frac{1}{V} \int exp[-\mu(t_I + t_D)] dV \tag{4.10}$$

which requires the evaluation of t_I and t_D for every point in the crystal for every diffraction angle. The approximation invoked is to overlay the crystal with a 3-dimensional grid and t_I and t_D are evaluated for the centre points of each grid cell and are taken to be representative of those for any point within the cell. Most crystals are irregular in shape and consequently the peripheral cells are not fully occupied by the crystal. These outer cells are assigned a weighting in the absorption correction proportional to their occupied fraction, and a weighted average value for t_I and t_D are obtained from a knowledge of the crystal boundaries. These boundaries can be measured optically and are described by their Miller indices and their perpendicular distances from the geometric centre of the crystal. The number of cells used varies but a grid of 8 × 8 × 8 is considered satisfactory.

4.2.4 Data Merging

The data produced up to this point have not been merged, that is symmetrically equivalent reflections have not been combined to produce a value of $F(\mathbf{S})$ and $\sigma F(\mathbf{S})$. Least squares analysis uses only the unique data and hence the symmetry equivalent reflection intensities need to be sorted and averaged. This is performed automatically in DREAM but care needs to be applied to check the consistency of equivalent reflections. Given the ideal number of four equivalents, the internal agreement provides an adequate indicator for the rejection of discordant data. Various tests for truly discordant data (perhaps a reflection was measured for a detector position where the diffracted beam is fouled by the beam-stop) are performed, and statistical tests determine true outliers. The poorer the internal agreement of the equivalent reflections, the larger the standard deviation assigned to the merged, unique datum. One test of the quality of a data set is the overall merging agreement factor defined by

$$R_{merge} = \Sigma |I(\mathbf{S}) - \overline{I}(\mathbf{S})| / \Sigma I(\mathbf{S}) \tag{4.11}$$

however this tends to be dominated by the more intense data. Evaluation of R_{merge} for batches of data in ranges of resolution or intensity gives a better indication of the data quality.

The relationship between structure factor $F(\mathbf{S})$ and observed intensity $I(\mathbf{S})$ is

$$F(\mathbf{S}) \propto \sqrt{I}(\mathbf{S}) \tag{4.12}$$

It is obviously not possible to obtain values for the magnitude of $F(\mathbf{S})$ in cases where $I(\mathbf{S})$ remains negative after merging . There are several possible ways of dealing with this problem. The first is to deal with $F(\mathbf{S})^2$ in the refinement since the calculated structure factor magnitudes may easily be squared, or alternatively to simply remove from the refinement all data with $I(\mathbf{S}) < 0$. The former is probably the better course of action since it will retain all the available experimental information, while the latter will not. It is conceivable although unlikely that the model may take on parameter values which lead to $F_{calc}(\mathbf{S})$ large for data points which have been removed. For those data points with $I(\mathbf{S})$ negative, it is fair to assume that $F_{obs}(\mathbf{S})$ is in fact small and positive and therefore retaining this information would prevent the model parameters taking values which give large $F_{calc}(\mathbf{S})$ values for these reflections. The treatment of "negatives" in all cases in this thesis is a compromise of working with $F(\mathbf{S})$ values, but setting any negatives to a small positive value and assigning a large standard deviation to them. It is thought that refinements on $F(\mathbf{S})$ and $I(\mathbf{S})$ lead to almost identical final models, at least for the standard crystallographic approximation of spherical atoms[84].

A significant quantity for each datum is the final estimated signal to noise ratio, $I(\mathbf{S})/\sigma(I(\mathbf{S}))$. For data with a low value for this, the error is of similar magnitude to the intensity, and therefore the reliability of these data is less than ideal. For this reason a lower limit cut-off of anything between $I(\mathbf{S}) \geq 2\sigma(I(\mathbf{S}))$ and $I(\mathbf{S}) \geq 3\sigma(I(\mathbf{S}))$ is commonly applied.

4.2.5 Extinction

In general, extinction is only a real experimental problem for large and very highly ordered crystals, and hence is much more of a problem in neutron diffraction experiments which require large samples. For the X-ray case, the crystals are much smaller and extinction does not present major difficulties. In most cases, crystals of sufficient long-range internal order for extinction to be prevalent are unobtainable by the standard crystal growth techniques employed on the bench. The effects of extinction become evident when refining the structural model against the data. While most calculated structure factor magnitudes fit the data well with the occasional outlier present, the very strongest reflections will have systematically smaller observed values than the values calculated from the model. Analysis of the mis-fit statistics of the data batched in terms of structure factor magnitude is easily performed and extinction effects are easily spotted.

Primary Extinction

The standard definition of a crystal is an infinite array of perfectly ordered repeating units (unit cells). While this is an unattainable limit for a real crystal which contains many different types of defect, it is a limit which may be approached quite closely under certain circumstances and is called a "perfect" crystal. The foregiven relationship of the observed structure factor

to the composition of the crystal have excluded the possibility of multiple reflection, where the reflected beam may undergo a second reflection taking it back into the same direction of the incident beam, although the Feynman diagram was given in Figure 2.4. When this effect occurs, the doubly reflected beam is returned to the incident direction of the primary beam, but has undergone a phase-shift of π and hence induces destructive interference to the incident beam. The net effect is a reduction of intensity of the incident beam experienced by the next layers of the crystal, causing a general reduction in the intensity of observed reflections, most noticeably for the very strongest of reflections. The same effect may occur with the diffracted beam while still inside the crystal, again with the effect of reducing the observed structure factor intensities.

Secondary Extinction

A more realistic model of the internal structure of a crystal is the mosaic model of the "ideally imperfect crystal"[85]. In this case, small domains of effectively perfect crystal exists, but are slightly misoriented to one another by a small amount, of the order of seconds. This model is used to justify another similar effect, that of secondary extinction. In this case, for a domain undergoing Bragg reflection, those subsequent domains further on in the crystal which have exactly the same orientation, experience a reduced intensity of incident radiation. The intensity which these further domains diffract is lessened and again a reduction of intensity of the most intense reflections occurs.

A suitable model with refinable parameters to take account od extinction effects has been formulated[86] and is used within the XDLSM program. The parameters refined are the average domain size, and the width of the distribution of domain misorientation angle, which may take either a Gaussian or Lorentzian form.

Chapter 5

Interpretation of Results

5.1 Fourier Based Maps

In essence, given a complete set of noiseless structure factors $F_{obs}(\mathbf{S})$, reconstruction of the electron density in the crystal $\rho(\mathbf{r})$ is a trivial matter, performed by the Fourier relationship

$$\rho(\mathbf{r}) = \frac{1}{V}\sum_{\mathbf{H}} F_{obs}(\mathbf{H})e^{-i\mathbf{H}.\mathbf{r}} \tag{5.1}$$

However, three problems become apparent when actually trying to perform such an operation with experimental data

- The phase problem: while the magnitude of the structure factor $|F_{obs}(\mathbf{H})|$ is known, the phase $e^{i\phi}$ is not.
- The set of structure factor magnitudes measured is far from complete, limited to a certain resolution limit by experimental considerations.
- This subset of magnitudes is contaminated by noise, *i.e.* both random and systematic errors.

Fortunately, nature is kind to the small molecule crystallographer (unlike the protein crystallographer) in that the vast majority of small molecules crystallize in centrosymmetric space groups. The centre of inversion restricts the structure factor to the real line giving only two possibilities for the phase of 0 and π. For refinements performed using the spherical atom approximation, the calculated structure factor phases will be all correct with perhaps the exception of a few structure factors with very small absolute value. These calculated phases can be put to the observed structure factor magnitudes and used in the Fourier synthesis

$$\rho(\mathbf{r}) = \frac{1}{V}\sum_{H}[|F_{obs}(\mathbf{H})|e^{i\phi_{calc}}]e^{-i\mathbf{H}.\mathbf{r}} \tag{5.2}$$

While such an electron density would resemble the true one, series termination effects would be most apparent. These occur because the data is limited in resolution to a certain value, no structure factor magnitudes above this value being incorporated in the Fourier synthesis. This is equivalent to multiplying a complete set of structure factor magnitudes by a step function at the resolution limit. The Fourier inversion of a step function in reciprocal space gives a sine function

in real space with frequency related to the resolution in reciprocal space where the step function applies. This sine function in real space permeates the electron density and manifests itself in the so called "Fourier-ripples", distorting the finer details.

The final problem is that of noise in the structure factor magnitudes. While good experimental technique should minimize these, no filtering can occur in the Fourier inversion and random noise (unstructured features in the real space map of small magnitude) occur.

In the centrosymmetric case, the phase indetermination is not a real problem although it persists for non-centrosymmetric crystals. Not a great deal can be done with noise in the data. However there is a simple and effective way of reducing series termination effects.

5.1.1 Difference Maps

If we have two Fourier series such as two sets of structure factors, both of which are restricted to some given resolution limit, simply subtracting one set of magnitudes from the other and using these difference amplitudes as coefficients of the Fourier series substantially reduces the series termination effects. Both sets of structure factors have a step function at the resolution cut-off value, above which the structure factor amplitudes are unknown. For any reasonable pair of sets of amplitudes pertaining to the same structure, the unknown coefficients will be similar in magnitude and hence their difference close to zero. In the difference Fourier techniques the coefficients are zero above the resolution limit anyway, and hence the series termination effect is reduced markedly.

The general form of a difference Fourier series is

$$\Delta\rho(\mathbf{r}) = \frac{1}{V}\sum_{\mathbf{H}}[|F_A|e^{i\phi_A} - |F_B|e^{i\phi_B}]e^{-i\mathbf{H}.\mathbf{r}} \tag{5.3}$$

5.1.2 Residual Map

The most elementary Fourier map and probably the most important one is the Residual map. The Fourier coefficients are the difference in observed and calculated structure factor magnitudes and therefore indicates the agreement between model and data

$$\Delta\rho^{res}(\mathbf{r}) = \frac{1}{V}\sum_{\mathbf{H}}[(|F_{obs}| - |F_{calc}|)e^{i\phi_{calc}}]e^{-i\mathbf{H}.\mathbf{r}} \tag{5.4}$$

For a good experiment well refined with a suitable model, there will still be small (certainly less than $0.15\text{e}\text{Å}^{-3}$) peaks in the residual map due to noise in the data. Unstructured features in the residual map of large magnitude indicates either poor quality data or insufficient correction for a systematic error. Structured features in the residual map indicate model inadequacies. Since the map is in real space, it is relatively easy to see where the model requires extra flexibility.

5.1.3 Dynamic Deformation Maps

Since the effects of bonding in the charge density are subtle and many orders of magnitude smaller than the absolute value of the density, particularly at the atomic core regions, some method is required to accentuate the bonding and other structural features. A simple way of

thinking about the manifestations of a chemical bond is as the difference between the electron density in a molecule and that which would occur if spherical, neutral atoms were placed at the same atomic positions, called the promolecule density. This idea leads to the concept of the deformation density, the difference between the experimental density and the promolecule density, giving the dynamic deformation density

$$\Delta\rho^{dyn}(\mathbf{r}) = \frac{1}{V}\sum_{\mathbf{H}}[(|F_{obs} - |F_{pro}|)e^{i\phi_{pro}}]e^{-i\mathbf{H}.\mathbf{r}} \tag{5.5}$$

with *pro* indicating structure factors calculated from the promolecule atoms smeared by the experimental thermal parameters. This is not so straightforward however, since the promolecule requires accurate positions and thermal parameters to be known and assigned to the neutral, spherical atom scattering model. The standard spherical atom model when refined against standard data does not provide sufficiently accurate structural parameters for this purpose, as discussed in Chapter 3. The first dynamic deformation maps were produced by Coppens[87] using neutron diffraction to locate the atomic structural parameters unbiased by the non-spherical nature of the atomic charge density. This method went on to become known as the $X - N$ method. Utilizing the high-angle X-ray scattering also provides approximately unbiased atomic structural parameters, and analogous maps were produced, known as $X - X'$ maps. Both sets of structure factors include the effects of thermal vibrations and hence both the $X - N$ and $X - X'$ methods produce a dynamic map in the sense that the deformation density is averaged over the nuclear motion.

5.1.4 Static Deformation Maps

To approximately remove the effects of thermal motion from the maps, a structured model capable of accounting for the static electron density convoluted by thermal motion is required and hence the observed structure factor can no longer be used. The static deformation map uses the difference between the structure factors calculated from the static multipole model and the static promolecule

$$\Delta\rho^{stat}(\mathbf{r}) = \frac{1}{V}\sum_{\mathbf{H}}[|F_{mul}|e^{i\phi_{calc}} - |F_{pro}|e^{i\phi_{pro}}]e^{-i\mathbf{H}.\mathbf{r}} \tag{5.6}$$

This reciprocal space summation is not really required however. The multipole model provides an analytical description of the static charge density in real space, and it is easy to calculate the static promolecule density in reals space, so a direct space sum may be used instead

$$\Delta\rho(\mathbf{r}) = \rho_{mul}(\mathbf{r}) - \rho_{pro}(\mathbf{r}) \tag{5.7}$$

All deformation maps have peaks in bonding regions and also show lone-pairs rather nicely. They can also show occupied and unoccupied *d*-orbitals in transition metal complexes.

While the deformation map concept has undoubtedly been useful, there are two flaws in the idea. The first is that subtracting a promolecule of neutral, spherical atoms is a little arbitrary. An alternative procedure of subtracting oriented, non-spherical atoms in place of the promolecule has been proposed[88,89] and called the chemical deformation density.

The second flaw is that small effects in the deformation density in the lone-pair region are dependent upon the local coordination, since this determines the promolecule density subtracted. A neighbouring atom's remaining negative deformation density cause more promolecule density to be subtracted from the current atom than the true promolecule density from just the current atom. This effect has been studied by Olovsson and coworkers[90,91].

The overall arbitrary nature of deformation densities means that they are unsuitable for accurate, quantitative studies. Fortunately, a relatively new and far more rigorous way of looking at electron densities has been developed.

5.2 Atoms in Molecules

A complete quantum mechanical theory has been built around the one-particle electron density in real space, $\rho(\mathbf{r})$ by Bader[92]. It is not the purpose of this chapter to recover his work, but merely to give an outline of the components of his Theory of Atoms in Molecules (AIM) of most relevance in the analysis of experimental charge densities. AIM is primarily a topological theory, dealing with the 3-dimensional shape of the charge density to provide chemical and physical information.

5.2.1 Critical points in $\rho(\mathbf{r})$

Critical points in any 3-dimensional scalar function occur when the gradient of that function is equal to zero.

$$\nabla\rho(\mathbf{r}) = \mathbf{i}\frac{\partial\rho(\mathbf{r})}{\partial x} + \mathbf{j}\frac{\partial\rho(\mathbf{r})}{\partial y} + \mathbf{k}\frac{\partial\rho(\mathbf{r})}{\partial x} = 0 \tag{5.8}$$

with **i**,**j** and **k** representing unit vectors. Classification of critical points (CPs) is given by curvatures, that is the second derivatives of $\rho(\mathbf{r})$. For an arbitrary axis system, these are expressed by the three by three square array of partial derivatives called the Hessian of $\rho(\mathbf{r})$

$$\begin{pmatrix} \partial^2\rho(\mathbf{r})/\partial x^2 & \partial^2\rho(\mathbf{r})/\partial x\partial y & \partial^2\rho(\mathbf{r})/\partial x\partial z \\ \partial^2\rho(\mathbf{r})/\partial x\partial y & \partial^2\rho(\mathbf{r})/\partial y^2 & \partial^2\rho(\mathbf{r})/\partial y\partial z \\ \partial^2\rho(\mathbf{r})/\partial x\partial z & \partial^2\rho(\mathbf{r})/\partial y\partial z & \partial^2\rho(\mathbf{r})/\partial^2 z \end{pmatrix} \tag{5.9}$$

Being a real, square, symmetric matrix, it can be diagonalized to yield the three principle axes of curvature with respect to which the magnitudes of the three second derivatives have extremal values. This is equivalent to a rotation of axes to a new coordinate system $(x, y, z) \rightarrow (x', y', z')$

$$\begin{pmatrix} \partial^2\rho(\mathbf{r})/\partial x'^2 & 0 & 0 \\ 0 & \partial^2\rho(\mathbf{r})/\partial y'^2 & 0 \\ 0 & 0 & \partial^2\rho(\mathbf{r})\partial z'^2 \end{pmatrix} \tag{5.10}$$

We may rename the diagonal elements in this new coordinate system as parameters λ_1, λ_2, λ_3 to give:

$$\begin{pmatrix} \lambda_1 & 0 & 0 \\ 0 & \lambda_2 & 0 \\ 0 & 0 & \lambda_3 \end{pmatrix} \tag{5.11}$$

where the values of λ are the the curvatures, or eigenvalues, corresponding tp three principle axes. The numerical value of the Laplacian at any point in space is the trace of the Hessian

$$\nabla^2\rho(\mathbf{r}) = \nabla.\nabla\rho(\mathbf{r}) = \frac{\partial^2\rho(\mathbf{r})}{\partial x'^2} + \frac{\partial^2\rho(\mathbf{r})}{\partial y'^2} + \frac{\partial^2\rho(\mathbf{r})}{\partial z'^2} \tag{5.12}$$

Critical Points are classified by their rank, ω, the number of non- zero eigenvalues and their signature, σ, the algebraic sum of the signs of these eigenvalues. The symbolism is (ω, σ). All stable critical points have rank three, giving four possible (ω, σ) combinations.

- (3,-3) all curvatures are negative and hence $\rho(\mathbf{r})$ is a local maximum at $\mathbf{r}_c$. Nuclear position behave as if (3,-3) CPs.
- (3,-1) two curvatures are negative and $\rho(\mathbf{r})$ is a maximum at $\mathbf{r}_c$ in the plane defined by their eigenvectors. $\rho(\mathbf{r})$ is a minimum at $\mathbf{r}_c$ along the third axis. This feature is called a saddle point and is characteristic of a bond CP.
- (3,+1) two curvatures are positive and $\rho(\mathbf{r})$ is a minimum at $\mathbf{r}_c$ in the plane defined by their eigenvectors. $\rho(\mathbf{r})$ is a maximum at $\mathbf{r}_c$ along the third axis.
- (3,+3) all curvatures are positive and $\rho(\mathbf{r})$ is a local minimum at $\mathbf{r}_c$. This characterises the CP at the centre of a cage.

For any pair of atoms sharing a common interatomic surface, a bond path is present. This is a line of maximal charge density linking the two nuclei. The charge density along a bond path reaches a minimum at the (3,-1) critical point and thus λ_3 is positive. The other two perpendicular eigenvalues λ_1 and λ_2 are both negative. For cylindrically symmetrical bonds $\lambda_1 = \lambda_2$. However, for a bond with π-character in one plane, $\nabla\rho(\mathbf{r})$ is less in one direction than the other and the corresponding curvature λ_2 is less than that of the perpendicular eigenvalue λ_1. We define the ellipticity of a bond in terms of the two negative curvatures:

$$\varepsilon = \frac{\lambda_1}{\lambda_2} - 1 \tag{5.13}$$

For example, a saturated carbon-carbon bond has $\varepsilon = 0$; an aromatic C-C bond has $\varepsilon = 0.23$; a full isolated C-C double bond has $\varepsilon = 0.45$. The bond ellipticity is useful in quantifying multiple bonding, conjugation and delocalization effects.

5.2.2 The Laplacian, $\nabla^2\rho(\mathbf{r})$

The Laplacian of a scalar field is a very important property, for it determines where the field is locally concentrated and depleted.

A function is maximally concentrated where the curvature *i.e.* the second derivative has its largest value even though the function itself need not have a maximum at this point. Extrema in the Laplacian are classified in a similar manner to $\rho(\mathbf{r})$ *i.e.* where $\nabla.\nabla^2\rho(\mathbf{r}) = 0$. The eigenvalues of the Hessian of $\nabla^2\rho(\mathbf{r})$ are the curvatures of the Laplacian.

A local concentration of electronic charge occurs at a (3,-3) critical point in $-\nabla^2\rho(\mathbf{r})$. Although this does not exactly represent a localized pair of electrons, the occurance of (3,-3) critical points strongly echo the Lewis electron-pair model of valence. (3,-3) CPs in $-\nabla^2\rho(\mathbf{r})$ occur in the valence shell charge concentration of an atoms in the same number and same direction as

the corresponding arrangement of both bonding and non-bonding electron pairs in the Lewis theory. It is by looking not at the total density, $\rho(\mathbf{r})$, but at the Laplacian $\nabla^2\rho(\mathbf{r})$ we find a physical quantification of the Lewis model. This extends not only to bonding phenomena, but also non-bonding concentrations in $\nabla^2\rho(\mathbf{r})$ corresponding to the classical "lone-pair".

Because the Laplacian is a direct function of the density, unlike the various types of deformation densities, there is no arbitrariness associated with it.

In this thesis, all analysis of the charge density is done using AIM, with both the density and Laplacian being the fundamental functions of study.

There is a second, more fundamental property of the Laplacian however The Laplacian occurs in the local form of the virial theorem

$$(\hbar^2/4m)\nabla^2\rho(\mathbf{r}) = 2G(\mathbf{r}) + V(\mathbf{r}) \tag{5.14}$$

where $G(\mathbf{r})$ and $V(\mathbf{r})$ are the electronic kinetic and electronic potential energy densities respectively. While the integral of the Laplacian over a whole molecule is zero

$$(\hbar^2/4m)\int \nabla^2\rho(\mathbf{r})d\tau = 0 \tag{5.15}$$

such that

$$\int 2G(\mathbf{r})d\tau = -\int V(\mathbf{r})d\tau \tag{5.16}$$

in accord with the virial theorem, such a situation need not occur locally, and hence the value of the Laplacian is determined by the local dominance of one or other of the energy densities relative to their virial ratio.

The topological features of the Laplacian such as local concentrations and depletions are directly related to the mechanics of the system at that point *via* the local virial expression.

5.3 Experimental *d*-orbital populations

As stated in Chapter 3, the charge density of a set of *d*-orbitals can be equally described by the expansion of even-order multipoles to hexadecapole level. The relations were first given in the context of working backwards from the experimentally determined multipole populations to gain the *d*-orbital occupancies[64]. The approximation inherent in this analysis is that all the metal valence density derives from the set of 5 *d* orbitals,

$$\rho_d(\mathbf{r}) = \sum_{l=1}^{5} P_l d_l^2 + \sum_{i=1}^{5}\sum_{j<i}^{5} P_{ij} d_i d_j \tag{5.17}$$

Zero overlap with the ligand atom density is assumed and it is therefore a crystal-field approximation. For the general case, the population parameters may be obtained from the multipole populations by

$$P_i = M^{-1} P_{lm\pm} \tag{5.18}$$

where P_i is the 15-element vector of *d*-orbital coefficients, $P_{lm\pm}$ is the matrix of multipole populations of functions generated by the *d*-*d* orbital products, and M is the 15×15 matrix relating the two.

Chapter 6

Experimental Charge Density of a Nitrogen Ylide

6.1 Introduction

Ylides of first row elements in general contain a quaternary ammonium group bonded to an electronegative atom [R_3N^+-X^-]. Other than in the case of X=oxygen, the electronegative atom usually requires further stabilization, achieved by substitution with electron withdrawing groups to delocalise the formal negative charge. Multiple bonding is not possible due to the full coordination sphere of the quaternary nitrogen atom and the non-availability of nitrogen *d* orbitals for participation in $p\pi - d\pi$ bonding, as in the case of the more familiar phosphorus ylide. This unusual N^+-X^- bond is of fundamental interest, having both covalent and ionic contributions according to its Lewis formula. Theoretical investigations of such bonds are always limited by computational capabilities, however some excellent studies into the simple model compound H_3N-CH_2 have been conducted; a study using the generalized valence bond approach[93] gives pictorial evidence for the lack of $p\pi - d\pi$ bonding in this molecule while a correlated study[94] at the MP2 level using the DZ+d basis set gave a calculated bond length of 1.561Å, considerably longer than the 1.473Å calculated for a single bond in CH_3-NH_2, signifying a weaker bond than expected. In addition, the natural bond order was calculated by the method of Weinhold[95,96], yielding a bond order of only 0.773. Atomic partial charges obtained by the same method give q_N=–0.795 and q_C=–0.741 signifying that far from the electrostatic contribution across the bond being favourable, it is actually repulsive. It is not too surprising that the formally positive nitrogen atom in fact bears a negative charge; a positive pole is highly electronegative and therefore pulls electron density strongly from its substituents into its own valence shell.

A particular subclass of first-row ylides are the aminimides[97]. In these molecules, the first row atom is also nitrogen giving the general form R_3N^+-N^--Y. The stabilizing Y group is often one which contains a carbonyl group such as Y=CHO, CO.Ph, CO.Me, CO_2Me, thus allowing the non-bonded density on N^- to be delocalized into the π system as with conventional amides. Such molecules have found utility as carriers for zinc salts through membranes[98]. The weakness of the N^+-N^- bond proves industrially useful; thermolytic cleavage of this bond to yield tertiary amines makes aminimides useful polymerisation initiators[99]. A further derivative is the case where R and X are part of the same group. Such cyclical aminimides have been investigated by

nitrogen nmr[100] and X-ray photoelectron spectroscopy[101,102] where the authors have interpreted their results to be consistent with a displacement of the bonding charge in the N^+-N^- bond towards the N^+ atom.

The electron withdrawing group may take on a different form, and in this work we have investigated the electronic properties of trimethylamine nitroimide[97,103],**1**, where X=NO_2. In this case there are three nitrogen atoms all with different bonding environments, and a strong electron withdrawing group to stabilize the negative charge by delocalization as shown by the resonance forms (Figure 1). In order to ascertain the characteristics of the N^+-N^- bond and the extent of the delocalization of N^- non-bonding charge in **1**, we have performed an experimental charge density determination by fitting X-ray diffraction data to a model which explicitly accounts for the complicated functional form of the electron density.

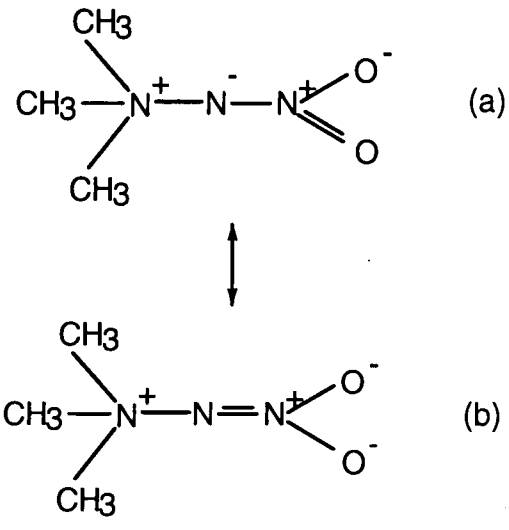

1

Figure 6.1 - The two major resonance forms of trimethylamine nitroimide.

6.2 Experimental

High resolution, single-crystal X-ray diffraction data were measured at 123K on an Enraf Nonius CAD4 automated diffractometer by Paul Mallinson and Chris Frampton at the University of Glasgow as previously described[104]. Although present at the time of data collection, I was not directly involved in this aspect of the work and therefore claim no credit for it. Reflection profiles became available to me and I performed all subsequent data analysis. Data reduction was performed with the DREAM[79] program suite. The intensities of 5 standard reflections had been measured every two hours and were fitted to cubic polynomials to scale the data for decay correction, and the instrument instability factor, P, was obtained from the errors in the fit of the polynomials and fluctuations in the standards. An analytical absorption correction was applied on a 16 x 16 x 16 grid using ABSORB[81,82]. Experimental data are summarized in Table 1.

Formula	$C_3N_3O_2H_9$
M	119.13
Crystal system	Orthorhombic
Space group	Pnma
T/K	123(1)
a/ Å	12.064(2)
b/ Å	6.622(2)
c/ Å	7.051(1)
V/ Å^{-3}	563.4(2)
Z	4
D_c/g cm^{-3}	1.405
Crystal dimensions/ mm	0.12 x 0.16 x 0.26
μ/cm^{-1}	1.09
Range of corrections for absorption	0.980 - 0.987
Radiation(λ/Å)	Mo-K_α(0.7107)
Scan type	θ - 2θ
(sin $\theta/\lambda)_{max}$/Å^{-1}	1.08
Standard reflections	2 3 $\bar{4}$, 6 0 $\bar{4}$, $\bar{2}$ 3 4, 0 2 0, and 0 10 0
No. reflections measured	13958
Range hkl	-12 to 25; -14 to 14; -15 to 15
No. symmetry-independent reflections	3105
No. $I > 2.5\sigma(I)$ reflections	1732
Agreement factor $R = \Sigma\|I - \bar{I}\|/\Sigma I$	0.0277
Refined on	F
R	0.0305
R_w	0.0288
S	0.9190
No. variables	133
Weighting scheme, w	$w = \frac{1}{\sigma^2(F)} = \frac{4F^2}{\sigma^2(F^2)}$ $\sigma^2(F^2) = \sigma^2_{counting}(F^2) + P^2F^4$
P	0.018

Table 6.1 - Experimental data for Trimethylamine nitroimide.

6.2.1 Multipole refinement

The crystal structure had been determined by earlier work[97]. The backbone of the molecule occupies a mirror plane at y=1/4, with two symmetry related CH_3 groups completing the molecule. The multipole refinements were performed using the least-squares part of the XD package[50]. The function $\sum w(|F_o(\mathbf{S})| - k|F_c(\mathbf{S})|)^2$ was minimised where $F_o(\mathbf{S})$ and $F_c(\mathbf{S})$ are the observed and calculated structure factors respectively and k is the scale factor which minimizes the sum. Only those reflections with $I > 2.5\sigma(I)$ were included in the refinement.

An electroneutrality constraint was applied in the refinements. In addition, the crystallographic mirror plane places restrictions[53] on the allowed populations of the spherical harmonics and certain functions were fixed at zero accordingly. A further chemical constraint of identical valence parameters for the two oxygen atoms was introduced.

The level of expansion was truncated at the octapole level (l_{max}=3) for C, N and O while the asphericity of all H atoms was modeled by a single bond-directed dipole. Both symmetry-independent carbon atoms are expected to have similar environments so they shared the same κ' and κ'' values. However, given the disparity in bonding environment of the three nitrogen atoms, they were assigned individual expansion-contraction coefficients. For each atom, the κ'' was the same for each l value. Each non-hydrogen atom had an anisotropic temperature

factor refined while the isotropic temperature factors for the hydrogen atoms were those obtained during conventional, spherical atom refinements using the contracted scattering factor of Stewart, Davidson and Simpson[55]. The C-H bond lengths were subsequently normalized to 1.06Å, an average value obtained from neutron diffraction experiments[56]. Hydrogen κ' and κ'' were fixed at 1.16 which is equivalent to using the contracted scattering factors.

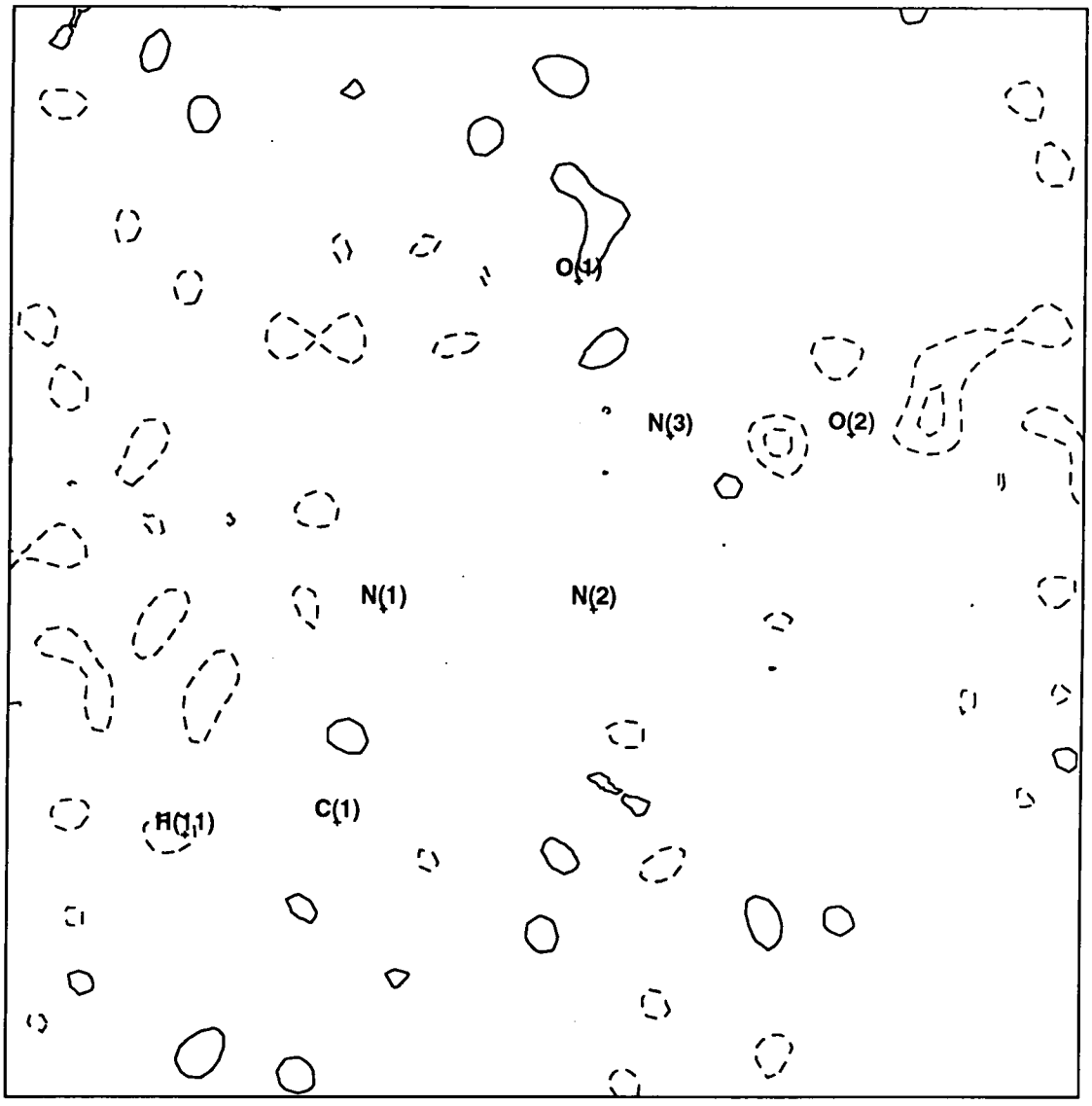

Figure 6.2 - Residual map in the molecular plane. Contours at $0.1e\text{Å}^{-1}$.

The refinement resulted in reasonable values for all parameters, however the maximum shift/esd was 0.5 signifying an unconverged refinement. Careful checking of the mis-fit statistics showed two reflections (5 12 4 and 23 0 2) with $F_o(\mathbf{S})$ an order of magnitude greater than $F_c(\mathbf{S})$. Removal of these reflections from the refinement allowed convergence to be obtained, improved the agreement statistics and slightly reduced the maximum discrepancies in the residual map. The reason for these rogue reflections could not be ascertained. The in-plane residual map (Figure 6.2) shows the disagreement between the data and the model. Only in the region around O(2) is there evidence of discrepancy; various attempts were made to alleviate it, for example

by removing the imposed non-crystallographic symmetry between the two oxygen atoms, none of which was successful. There is no structured residual density anywhere else in the molecule.

A second factor which increases faith in the fitted model is the result of Hirshfeld's rigid bond test[57,74]. All bonded pairs of atoms satisfy the necessary criterion.

6.3 Results and Discussion

Final agreement factors for the refinement are given in Table 1. A thermal ellipsoid plot is shown in Figure 6.3 which also details the numbering scheme used.

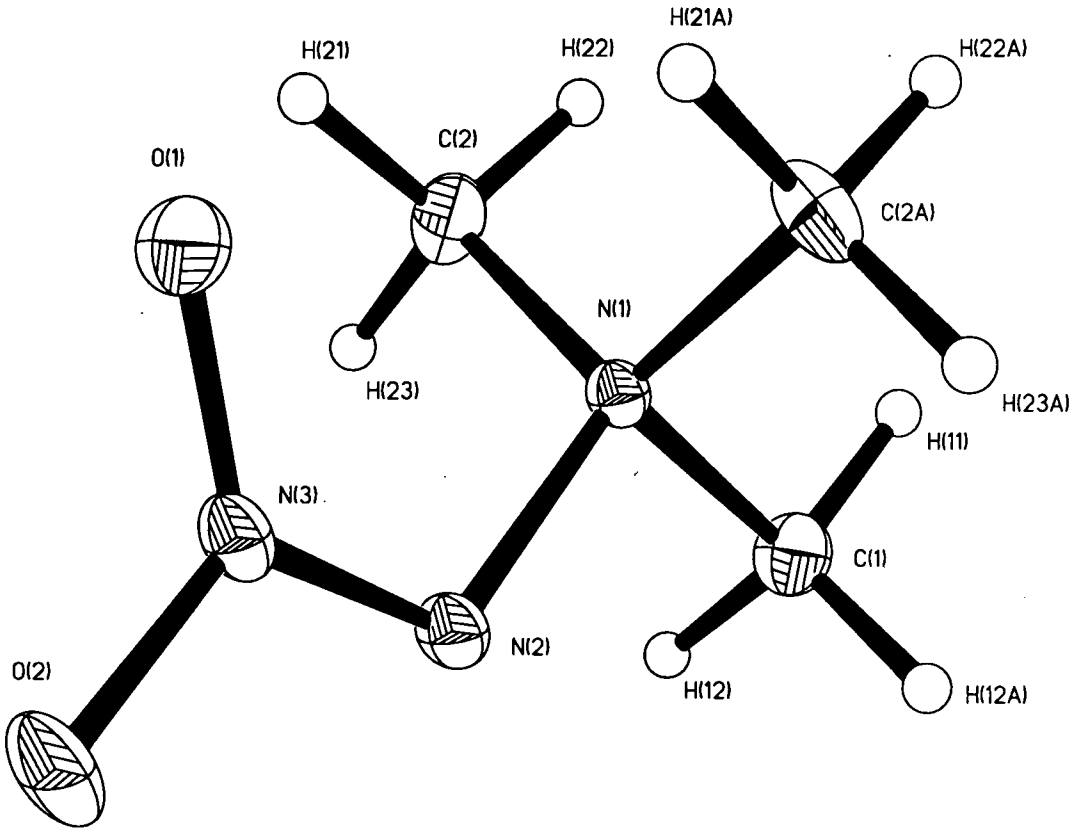

Figure 6.3 - Thermal ellipsoid plot at the 50% probability level.

The initial structure determination[97] for this molecule was performed at room temperature and refinements used the independent atom approach. In the current work with high-resolution data and an aspherical atom model, we have observed some small differences in the geometrical parameters. Table 6.2 contains the bond lengths and angles for non-hydrogen atoms determined here and in the previous study. Of most interest are the lengths of the nitrogen-nitrogen bonds. The N(1)-N(2) bond has length 1.472(1)Å which is comparable to a single covalent bond. The N(2)-N(3) bond however is much shorter at 1.315(2)Å indicating that the resonance form (b) is a more accurate depiction of the electronic structure.

Bond	Length(this work, Å)	Length(ref 97, Å)
C(1)-N(1)	1.498(1)	1.490(9)
C(2)-N(1)	1.500(1)	1.507(7)
N(1)-N(2)	1.472(1)	1.470(8)
N(2)-N(3)	1.315(2)	1.323(8)
N(3)-O(1)	1.247(1)	1.265(8)
N(3)-O(2)	1.267(1)	1.252(8)
O(1)···H(21)	2.228(1)	2.26(5)
Atoms	Angle(this work, °)	Angle(ref 97, °)
C(1)-N(1)-N(2)	101.9(1)	102.8(5)
C(2)-N(1)-N(2)	113.2(1)	112.4(3)
C(1)-N(1)-C(2)	107.8(1)	107.6(4)
C(2)-N(1)-C(2A)	112.2(1)	113.2(4)
N(1)-N(2)-N(3)	113.6(1)	115.0(5)
N(2)-N(3)-O(1)	125.0(1)	123.0(6)
N(2)-N(3)-O(2)	114.2(1)	115.5(6)
O(1)-N(3)-O(2)	120.9(1)	121.5(6)

Table 6.2 - Bond Lengths and Angles.

The electronic charge in a molecule is a single continuous distribution and there exist many schemes for the assignment of "atomic charges", all of various degrees of rigour. The set of monopole populations of the pseudoatoms from the multipole refinement is one such decomposition and it is reasonable to assume that they provide an approximate guide to the distribution of charge throughout the molecule. The monopole populations for non-hydrogen atoms are shown in Table 6.3. According to this scheme, the formally positive N(1) has a valence monopole population of 5.58(6) electrons, its substituent carbon atoms are also slightly negatively charged, while all hydrogen atoms are positively charged. This is a manifestation of the alkyl inductive effect. The net valence population of the $(CH_3)_3N^+$ fragment is 25.3(3) electrons compared with the neutral value of 26, indicating that while the nitrogen atom itself does not carry the positive charge as the Lewis structure suggests, this group of the molecule does bear the best part of a full positive charge.

Atom	Monopole Charge (electrons)	κ'	κ''
C(1)	4.74(8)	0.984(8)	0.77(2)
C(2)	4.53(8)	0.984(8)	0.77(2)
N(1)	5.58(6)	0.964(9)	0.78(4)
N(2)	5.14(8)	0.995(7)	1.08(6)
N(3)	5.2(1)	0.99(1)	0.75(3)
O(1)	6.21(7)	0.998(6)	0.85(6)
O(2)	6.21(7)	0.998(6)	0.85(6)

Table 6.3 - Monopole populations and κ parameter values.

Independent evidence that the charge resides on the hydrogen atoms is provided by proton nmr studies[97,101] on this and similar compounds where the methyl protons have a chemical shift of 3.40ppm, indicating significant depletion of electron density about their nuclei. The formally fully negatively charged N(2) has a charge of only -0.2(1) while for the NO_2 group this is -0.6(3) showing the extent of electron withdrawal and hence stabilization of the ylide.

A more informative analysis of the experimental charge density is based upon the topological properties of $\rho(\mathbf{r})$. We have performed such an analysis, in the first instance by searching for

the (3,-1) bond critical points (CPs). Such critical points were located between every atom pair bonded by conventional criteria. In addition, a bond critical point was also located between O(1) and H(21). The values of functions of the density at the bond CPs are listed in Table 6.4, and a map of the Laplacian of the density, $-\nabla^2\rho(\mathbf{r})$ is shown for the molecular plane in Figure 6.4.

Bond	Length(Å)	$\rho(\mathbf{r}_b)$(eÅ^{-3})	$\nabla^2\rho(\mathbf{r}_b)$(eÅ^{-5})	ε
C(1)-N(1)	1.498(1)	1.64(4)	-9.2(2)	0.45
C(2)-N(1)	1.500(1)	1.68(7)	-13.6(2)	0.32
N(1)-N(2)	1.472(1)	1.90(3)	-2.52(8)	0.01
N(2)-N(3)	1.315(2)	3.34(5)	-30.6(2)	0.53
N(3)-O(1)	1.249(1)	3.82(7)	-25.7(2)	0.32
N(3)-O(2)	1.268(1)	3.46(6)	-21.0(2)	0.33
O(1)···H(21)	2.228(1)	0.12(1)	1.65(1)	0.54

Table 6.4 - Electronic Properties at $\mathbf{r}_b$.

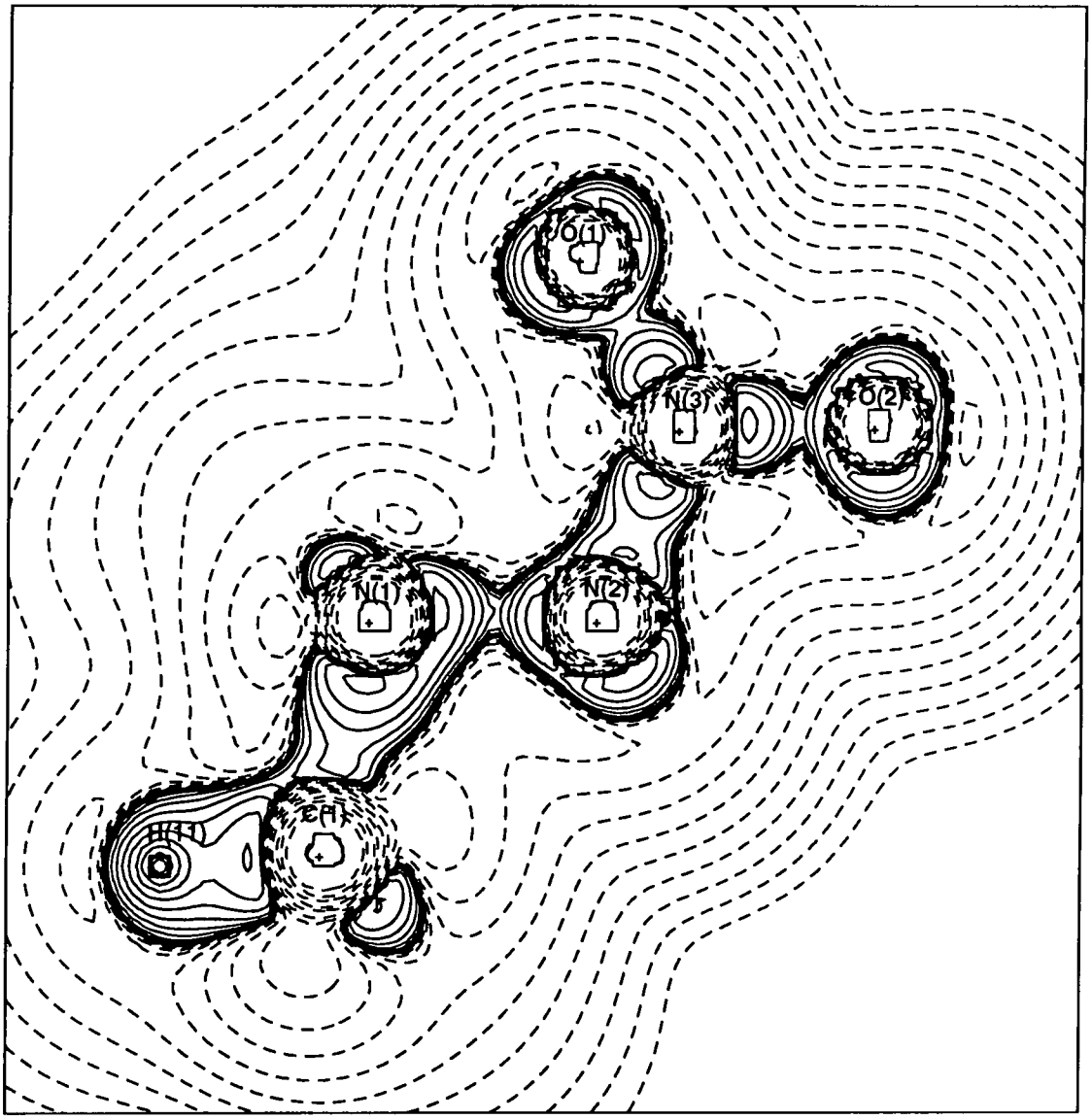

Figure 6.4 - $\nabla^2\rho(\mathbf{r})$ in the mirror plane.

The values of the density in the C(1)-N(1) and C(2)-N(1) bonds at 1.64(4) and 1.68(7) eÅ^{-3} are quite similar and in the range expected, while both bonds show negative Laplacian indicating a local concentration of charge in the bond and hence covalence. Of note are the unexpectedly

high ellipticities of these bonds which may be due to the high degree of polarization of N(1) which is quite pronounced in the Laplacian map.

The N(1)-N(2) bond appears rather pinched here and has $\nabla^2\rho(\mathbf{r}_b)$ of a mere -2.52(8)eÅ^{-5}, although the density itself is reasonably high at 1.90(3)eÅ^{-3}, higher than for the C-N bonds. The ellipticity is not significantly different from zero, indicating no π contribution to the bond. This forces the conclusion that this is a relatively weak bond in agreement with the thermolytic cleavage properties of similar compounds mentioned in the introduction and also the calculated bond order of only 0.773 in the H_3N^+-C^-H_2 molecule. In contrast, the N(2)-N(3) bond has a far greater electron density of 3.34(5) eÅ^{-3} and a more negative Laplacian value of -30.6(2) eÅ^{-5} indicating a substantially stronger interaction than a mere single bond. Additionally the ellipticity of 0.56 is consistent with a high degree of double bonding character.

Of the two resonance forms (a) and (b), one major structural difference in orbital terms is the hybridization of N(2); for form (a), N(2) has sp^3 hybridization with two σ-bonding and two non-bonding or lone-pair orbitals while for form (b), the hybridization is sp^2 with two σ-bonds, one π-bond and a single sp^2 lone pair. While lone pairs do not show themselves in the total electron density, they do appear as local concentrations of charge in the Laplacian.

The Laplacian through N(2) and perpendicular to the molecular plane such that it bisects the expected lone-pair region is shown in Figure 6.5. Only one, albeit diffuse, lone-pair is observed giving further evidence for resonance form (b) being more representative of the true structure.

In the original structural report of this compound[97], the *cis* conformation was attributed to the $N(1)^+\cdots O(1)^{\delta-}$ electrostatic interaction. However, according to the monopole charges, N(1) bears a substantial negative charge and this must bring such a conclusion into question. Also noted in the original work was the existence of a pair of weak hydrogen bonds between O(1) and H(21) and O(1) and H(21A) at 2.26(5)Å. Given that we have shown the positive charge of the amino end of the molecule to reside wholly on the hydrogen atoms, this seems reasonable. All bonds, even weak ones such as these should possess a bond path and (3,-1) CP. This is found to be the case: $\rho(\mathbf{r}_b)$ is very low at 0.17(1) eÅ^{-3} while the $\nabla^2\rho(\mathbf{r}_b)$ value is positive at 1.65(1) eÅ^{-5}, indicating a closed-shell interaction entirely consistent with a weak hydrogen bond. The Laplacian map in the plane defined by C(2), H(21) and O(1) is shown in Figure 6. The lone pair of O(1) is approximately aligned with the hydrogen atom.

6.4 Conclusions

We have investigated the bonding in **1** by analysing the experimentally determined charge distribution, obtained by refining a multipole model against high resolution X-ray diffraction data. We find that the distribution of charge is more subtle than the Lewis formula suggests with the formally positive nitrogen atom bearing a negative charge. The N^+-N^- bond is weaker than a normal single covalent bond while the nitro group delocalizes much of the non-bonding charge on N(2), leaving it with only one lone-pair. The N(2)-N(3) bond has high double bond character. The original assertion that there exists a hydrogen bond between O(1) and H(21) has been proved correct, and this is probably the reason for the *cis* conformation.

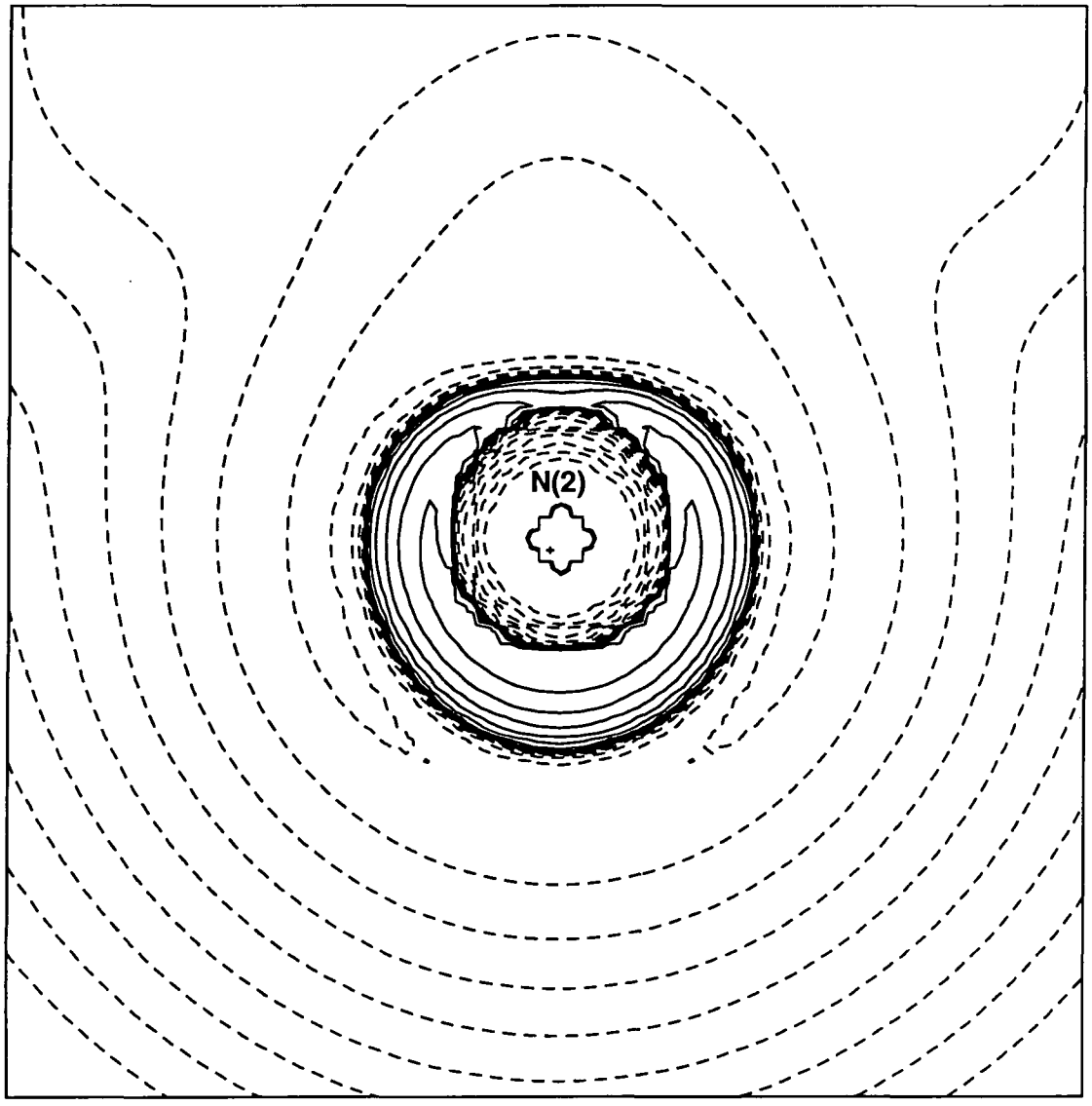

Figure 6.5 - $\nabla^2\rho(\mathbf{r})$ perpendicular to the molecular plane and bisecting the N(1)-N(2)-N(3) angle.

Multipole populations and local coordinate systems *etc.* are tabulated in Appendix B.

6.5 Acknowledgements

Thank are due to Dr. D.G. Morris for a sample of the ylide (1), and Drs. C.S. Frampton and P.R. Mallinson for making their experimental data available.

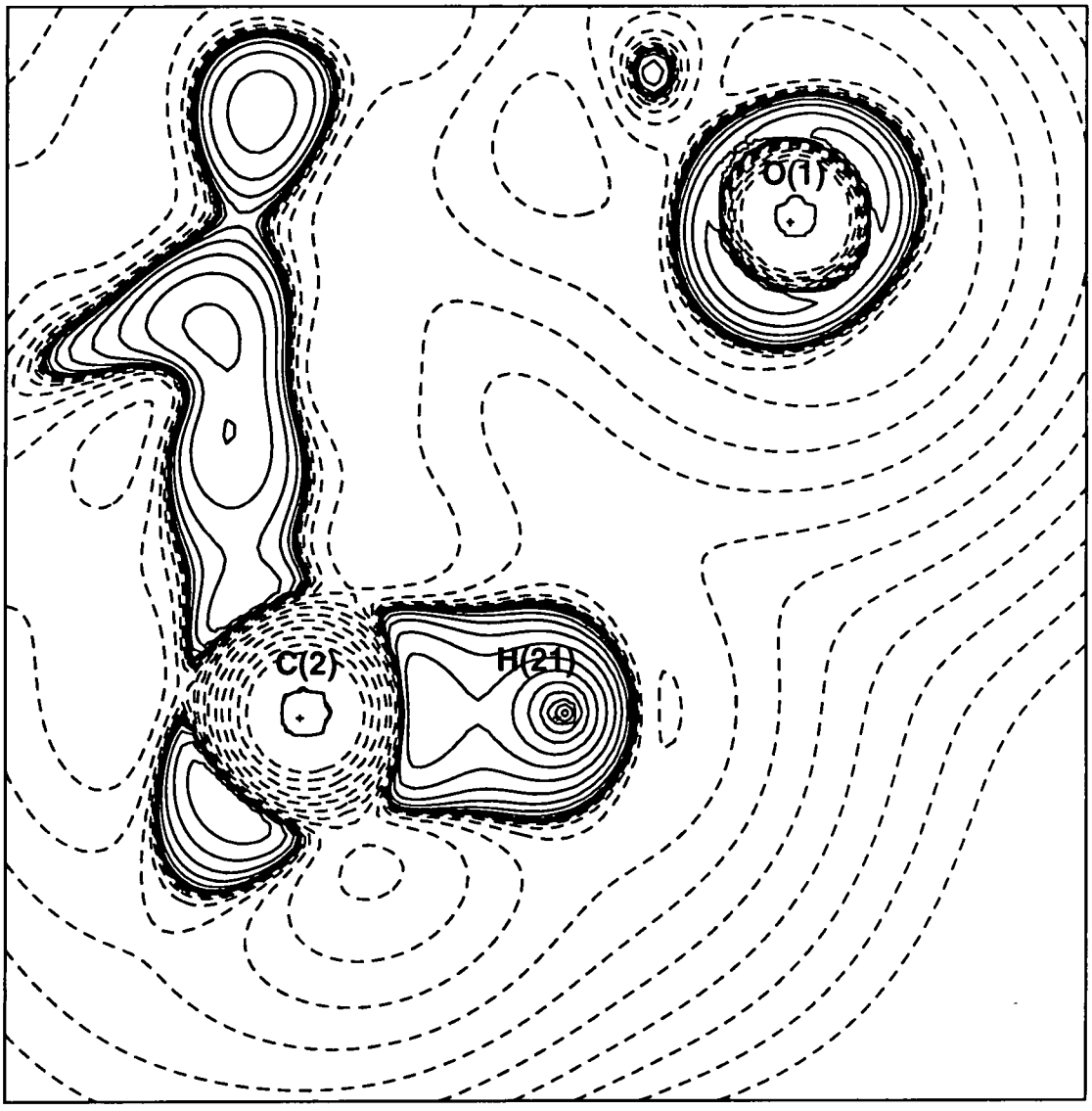

Figure 6.6 - $\nabla^2\rho(\mathbf{r})$ in the plane of C(2), O(1) and H(21).

Chapter 7

Experimental Charge Density of a Nickel Complex

7.1 Introduction

While the standard quantum chemical techniques, either *ab initio* or density functional, undoubtedly provide huge insight into chemical bonding phenomena, their limitations with respect to molecular size has already been stated. It is for those molecules of sufficient size to make calculations excessively expensive or unreliable that the experimental technique of X-ray diffraction for the determination of the charge density becomes particularly competitive. An obvious class of molecules large enough for this to be the case are transition metal complexes, particularly those of low symmetry. In fact, in his timeless text on transition metal complexes[105], Orgel mused on the insight which would be provided by such a technique *before* the technical difficulties inherent in the method had been overcome. An immediate advantage of the experimental approach is that the charge density obtained is *by definition* correlated, being a representation of the true density. While the one-electron approximation is reasonable for organic molecules, its validity is more questionable in transition metal complexes where correlation effects are greater.

This chapter of the thesis reports research on a large N-substituted triaza macrocycle investigating the fundamental nature of metal-ligand bonding. This molecule is sufficiently large and of low enough symmetry to lie on the upper limits of what can be tackled by theoretical techniques, and provides important independent results with which to compare any such theoretical calculations. We also believe this to be the most difficult experimental determination of the topological properties of the charge density attempted so far due to the size of the complex and the non-centrosymmetric space group of the crystal.

The particular macrocyclic complex chosen for study in this work is [Ni(H_3L)], [H_3L=N,N′,N″-tris(2-hydroxy-3-methylbutyl)-1,4,7- triazacyclononane], (**1**). It is of interest because the metal atom is ligated by trimethyl-ammonium nitrogen atoms and alcoholic oxygen atoms. The former is conventionally thought of as a very strong σ-donor while the latter is considered as much weaker in this respect, although potentially capable of π-bonding.

The large difference of the ligating properties of these two atoms should be reflected by the properties of the charge distribution. Additionally, the complex has the low symmetry point group C_3 in the crystal which is much less studied than the octahedral case.

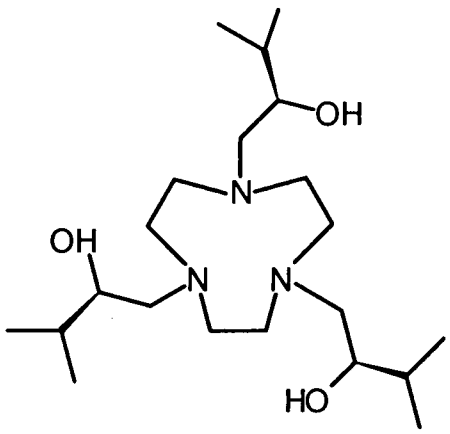

H3L

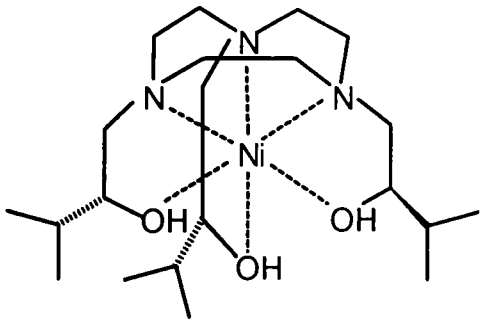

$Ni^{II}H_3L$

The crystal structure and absolute configuration are as determined previously[106]. Figure 7.1 shows a thermal ellipsoid plot of the complex cation at the 90 percent probability level. The nickel ion lies on a crystallographic three-fold axis and is complexed by three nitrogen atoms above and three oxygen atoms below the basal plane, with an 18^0 twist away from pseudo-octahedral coordination. The Ni-N and Ni-O bond lengths at 2.064(1)Å and 2.094(1)Å respectively do not indicate *a priori* any substantial difference in bond characteristics. The NO_3^- and PF_6^- counterions also lie on the three-fold axis above and below the main complex respectively. A preliminary account, using a less flexible model of the charge density has already been published[107].

7.2 Experimental

A dark blue octahedral crystal of $[Ni^{II}(H_3L)\ (PF_6^-)\ (NO_3^-)]$ was chosen for analysis. High resolution, single-crystal X-ray diffraction data were measured at 123(1)K on an Enraf-Nonius CAD4 automated diffractometer as previously described[104]. As with the data from the nitrogen ylide in the previous chapter, the data was collected by Drs. P.R. Mallinson and C.S. Frampton at the University of Glasgow. Data reduction was performed with the DREAM[79] program suite, including an analytical absorption correction by Gaussian quadrature using ABSORB[81,82]. The intensities of 5 standard reflections were measured every two hours and fitted to cubic polynomials to scale the data for decay correction, and the instrument instability factor, P, was obtained from the errors in the fit of the polynomials and fluctuations in the standards. Experimental data are summarized in Table 7.1.

7.2.1 Multipole refinements

Only those reflections with $I > 2\sigma(I)$ were included in the refinement. Due to the crystallographic C_3 site symmetry of the Ni, and counterion P and N atoms, only certain deformation functions may take non-zero populations for these sites[53]. Each non-hydrogen atom had anisotropic temperature factors refined while the isotropic temperature factors for the hydrogen atoms were those obtained during conventional, spherical atom refinements using the contracted scattering

factor of Stewart Davidson and Simpson[55], with the bond length to C normalized to 1.06Å, an average value obtained from neutron diffraction experiments[56]. Hydrogen κ' and κ'' were fixed at 1.16 during the multipole refinements which is equivalent to using the contracted scattering factors.

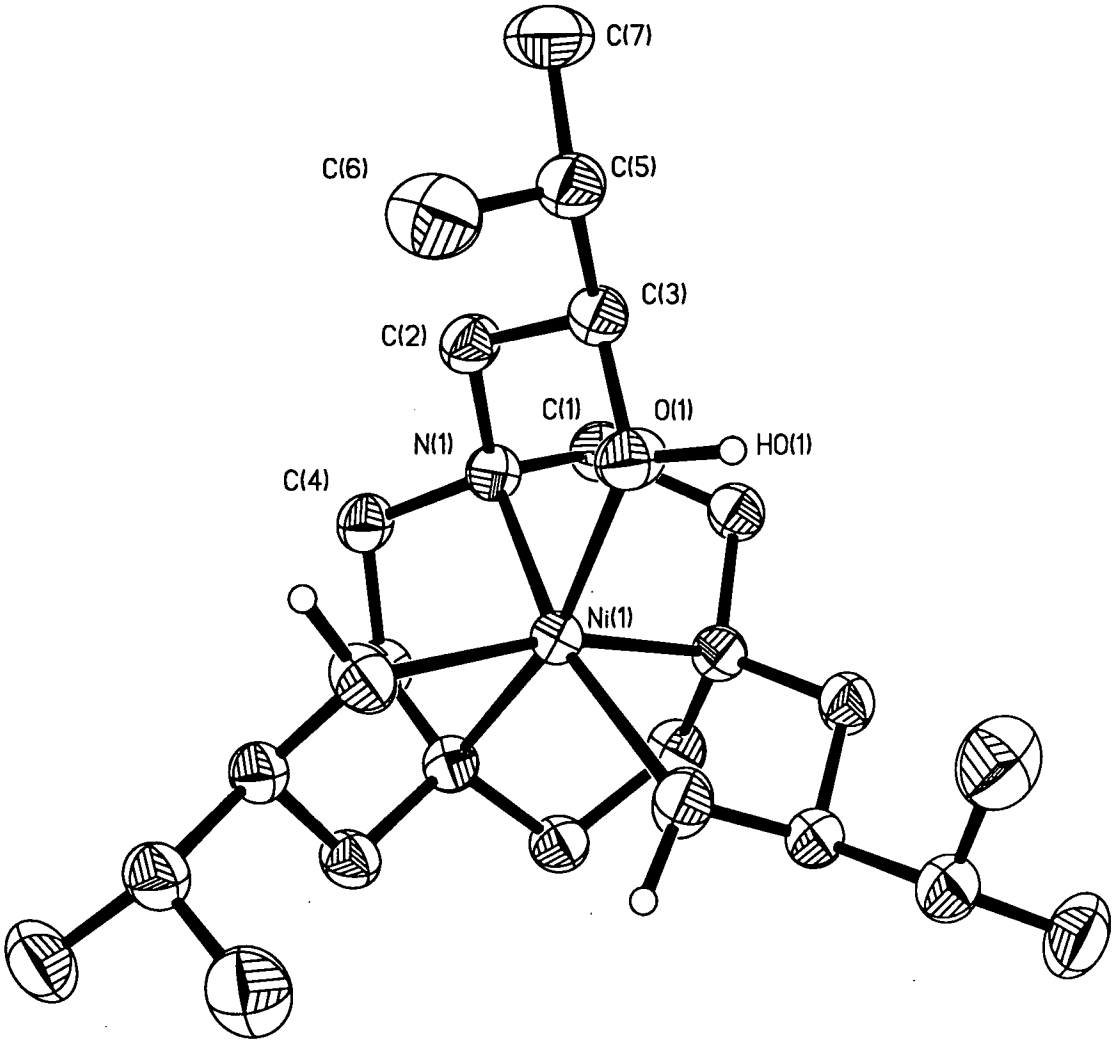

Figure 7.1 - Thermal ellipsoid plot of **1** at the 90% probability level.

In all refinements in this study, the charge of each of the counterions was constrained to be -1 and the metal-ligand complex total charge was held at +2. For the counterions, the κ'' parameters were not refined. The non-centrosymmetric space group $P2_13$, introduces additional complications to multipole refinement resulting from the ambiguity in phase assignment of the reflections. In such cases, extreme care must be taken to ensure that the final model is physically sensible and this is best done by examining physical attributes such as the temperature factors using Hirshfeld's rigid bond test[55,74], topological properties etc. A second complication arises because the multipole model, being a one-centred expansion, is not designed for the efficient projection of diffuse, two centred (or overlap) terms of the experimental density into the model[60].

Here, we specifically mean those parts of the density in the N-Ni and O-Ni bonds, which are far from either nucleus. For example, the 4*s* and 4*p* orbitals on the metal which have maximal overlap with the ligand lone-pairs are so diffuse that they will contribute only to the very lowest angle data and these data are those most affected by extinction effects. It should be pointed out that these difficulties arise from the specific scattering formulation of the multipole model; by the Fourier transform relation, *all* of the density determines *all* of the structure factors, but by modeling the density as discrete single centred pseudo-atoms, the diffuse density in such a model is determined only by the low angle data.

Formula	$C_{21}H_{45}N_3O_3Ni^{2+}$ (NO_3^-) (PF_6^-)
M	653.28
Crystal system	Cubic
Space group	$P2_13$
T/K	123(1)
a/Å	14.008(2)
V/Å^3	2748.7(7)
Z	4
D_c/g cm^{-3}	1.578
Crystal dimensions/mm	0.4 x 0.4 x 0.6
μ/cm^{-1}	8.47
Range of corrections for absorption	0.774 - 0.804
Isotropic extinction	Gaussian mosaic spread 11s domain size 3.8 x 10^{-5} cm
Radiation(λ/Å)	Mo-K_α(0.7107)
Scan type	θ - 2θ
(sin $\theta/\lambda)_{max}$/Å^{-1}	1.08
Standard reflections	8 8 $\bar{8}$, 0 4 9, 0 4 $\bar{9}$, 0 26 0, 4 0 4
No. reflections measured	20445
Range *hkl*	1 to 30; 0 to 30; -17 to 10
No. Symmetry-independent reflections	6017
No. $I > 2\sigma(I)$ reflections	5094
Agreement factor $R = \Sigma\|I - \bar{I}\|/\Sigma I$	0.017
Refined on	F
R	0.0220
R_w	0.0155
S	1.07
No. variables	400
Weighting scheme, w	$w = 1/\sigma^2(F) = 4F^2/\sigma^2(F^2)$ $\sigma^2(F^2) = \sigma^2_{counting}(F^2) + P^2F^4$
P	0.018

Table 7.1 - Experimental data for [Ni^{II} (H_3L)] (NO_3) (PF_6).

For organic molecules containing only first row atoms, many fine multipole studies have been published using the standard multipole model including some excellent recent works[108,109,110]. In our particular case, the standard scattering formalism including expansion to hexadecapolar functions on P and Ni produced a good fit to the data in terms of agreement indices and a reasonable residual map, but resulted in an unconverged κ'' refinement for the ligating N and O atoms which became extremely diffuse. One imagines this was due to the functions on these atoms "reaching out" towards the metal to incorporate the density in the metal-ligand bond which is not explicitly accounted for by the model. It has been shown previously[63,64] that the electron density distribution of the 3*d*-orbitals of a transition metal can be described fully

by the set of multipolar functions of orders 0,2 and 4. We therefore tried using only these functions in the scattering expression for the nickel atom. While the refinement was stable and converged, the ligating atoms again had unrealistic κ'' values and the C-N, C-O and metal to ligand bonds failed the rigid bond test indicating deficiencies in the charge density model for the ligating atoms. Additionally, no metal to ligand bond paths could be traced in the charge density. It became apparent that it was essential to include the odd order multipoles on the metal atom which account for valence density other than $3d$ such as $4s$, $4p$ and metal-ligand overlap density. This also meant than any analysis based only on metal d-orbital occupancies would be of limited value in describing the metal ligand bonding. Since the odd order terms would be describing density which was more diffuse than the $3d$ density, we reasoned that a more elaborate radial treatment of the metal would be appropriate. Thus $3d$ HF radial functions were assigned to the first monopole and to the order 2 and 4 multipoles. A Slater type radial function was assigned to the 0,1 and 3 order multipoles. We refined individual kappa parameters for these three sets and an acceptable, stable refinement resulted. The C-N and C-O bonds became acceptable in terms of the rigid bond test indicating physically sensible temperature factors for the ligating atoms and bond paths with (3,-1) critical points were located between the metal and ligating atoms. However, the N-Ni and O-Ni bonds still failed the rigid bond test, having values of 0.0015 and 0.0018Å^2 respectively compared to the Hirshfeld criterion of $\leq$ 0.001Å^2. This could indicate that the metal temperature factors are deficient in some way, or may just be a reflection of the substantial difference in mass between these bonded atoms. The κ value for the HF monopole took the value of 1.04(1) while the order 2 and 4 kappa was 1.15(4). Both of these are slightly contracted compared with the free metal ion. The κ value of the 0, 1 and 3 order multipoles with the Slater-type radial function (which were included to describe the diffuse density) refined to 0.44(1) which indicates a far greater diffuseness than the $3d$ radial density function used as the starting value. The κ'' values for the ligating N and O atoms were 0.70(2) and 0.78(2) respectively, again indicating a move towards greater diffuseness. As required for non-centrosymmetric structures, special care was taken to check the absolute values, shifts and e.s.d.'s of the odd order multipoles to ensure that they are well defined in the refinement. In all cases they appeared to have reasonable values and the supposed difficulties specific to non-centrosymmetric systems[76] were not immediately obvious. The typical e.s.d. for the multipole parameters, at 0.03 is a little higher than the average value of 0.02 usually encountered for small organic charge density studies, but given that this is a large transition metal complex this is not unreasonable. They are certainly not high enough to draw suggest inherent difficulties with the refinement. An isotropic extinction parameter (type 1, Gaussian distribution[86]) was also included in the refinement. This "best" refinement has a residual peak of 0.41eÅ^{-3} at the nickel position and other small, unstructured residual features in the nickel coordination sphere as can be seen in Figure 7.2. Irrespective of the treatment of the metal (including using the neutral scattering factors in place of those corresponding to the doubly charged ion) these residual features could not be further diminished. Additionally, the least-squares correlation coefficients were checked. There were many large ($C_{ij} \geq 0.80$) correlations between multipole parameters describing the density in the PF_6^- and NO_3^- counterions which are most likely attributable to slight disorder of

the counterions.. The only substantial correlations of note in the complex cation were between the off-diagonal temperature factors for the nickel, which are constrained by symmetry to be equal, and the single symmetry allowed quadrupole along the 3-fold axis. The correlation coefficient is 0.94 indicating almost complete correlation. One possible explanation for the high correlation is the inadequacy of the Clementi Hartree-Fock scattering factors, which incorporate neither correlation nor relativistic effects. These are probably significant for an element of such a high atomic number[111].

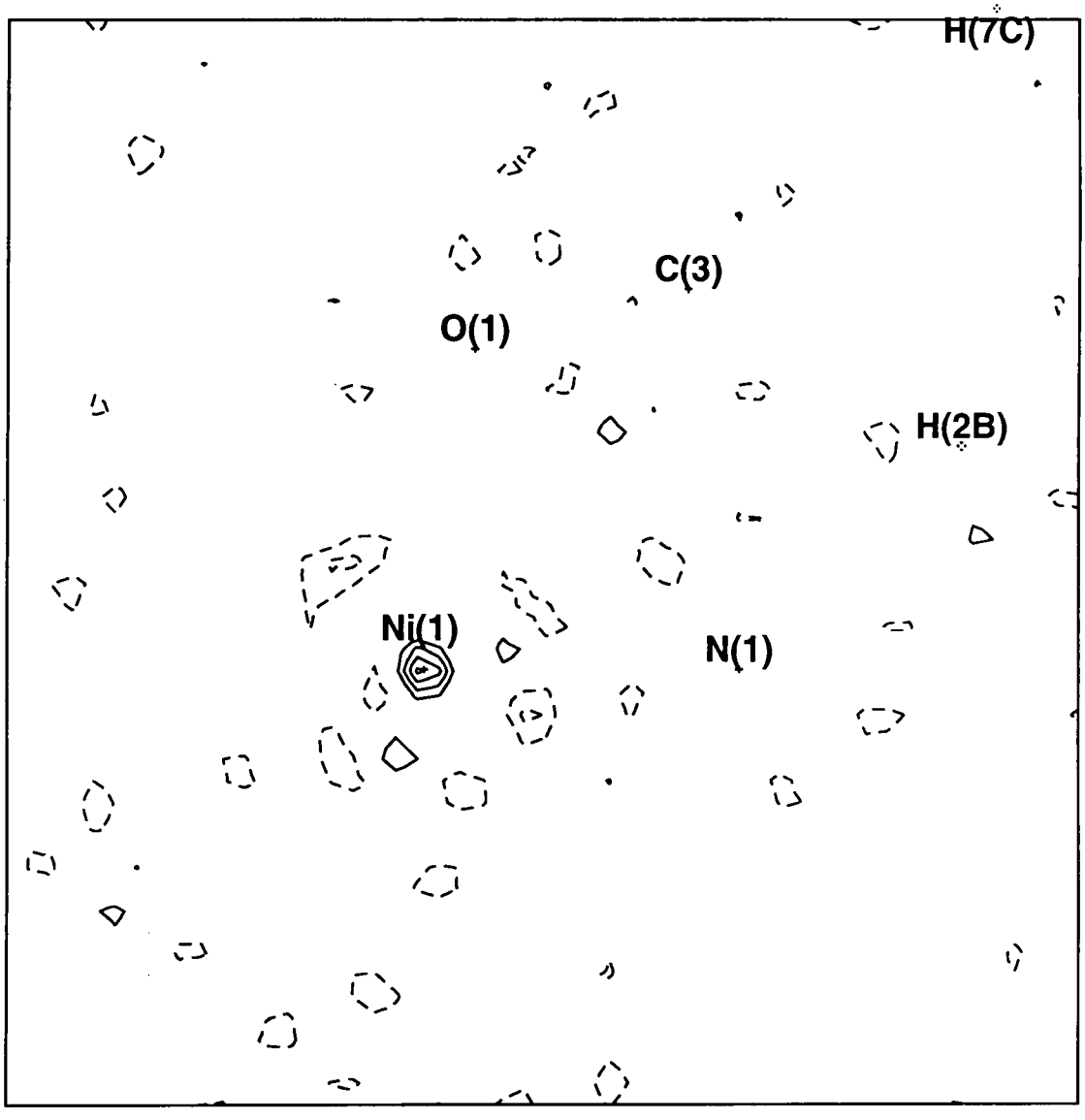

Figure 7.2 - Residual map in the plane of the Ni(1), O(1) and N(1) atoms.

Given the above mentioned limitations, slight caution must be applied in the quantitative analysis of the results. However we assume that the model is qualitatively accurate. The conclusions we draw from these refinements is that the residual maps and R-factors do not allow one to discriminate between all the models which fit the data reasonably well. It is the physical properties such as the result of the rigid bond test, the appearance of bond paths in the refined model where expected and the stability and convergence of the refinement which indicate an

appropriate model. From our final refinement, it appears necessary to account for the diffuse metal density implicitly and also the metal-ligand overlap density in the model. This we have done by accepting κ'' parameters with more diffuse values than usual on ligating atoms, and a model for the metal atom with greater radial flexibility than normal. Final R-factors etc. are incorporated in Table 7.1, and Figure 7.2 shows the residual map in the N(1), Ni(1), O(1) plane.

7.3 Results

7.3.1 The H_3L Ligand

The results of topological analysis of $\rho(\mathbf{r})$ with respect to the bonding in the ligand is reported in Table 7.2. As expected for covalent bonds, (3,-1) bond critical points with negative $\nabla^2\rho(\mathbf{r})$ values are observed in all of the intra-ligand bonds. All C-C bonds have small ellipticities indicating pure sigma bonding, with the values of the electron density at the critical points, $\rho(\mathbf{r}_b$, in the range 1.80(5) to 1.99(4) eÅ^{-3}.

bond	length/Å	$\rho(\mathbf{r}_b)$/eÅ^{-3}	$\nabla^2\rho(\mathbf{r}_b)$/eÅ^{-5}	ϵ
C(1)-C(4)	1.533(1)	1.91(7)	-16.8(1)	0.08
C(2)-C(3)	1.522(1)	1.99(4)	-29.9(1)	0.08
C(3)-C(5)	1.537(1)	1.93(5)	-17.9(1)	0.07
C(5)-C(6)	1.527(2)	1.81(5)	-16.8(1)	0.08
C(5)-C(7)	1.531(2)	1.80(5)	-13.9(1)	0.03
C(1)-N(1)	1.493(1)	2.08(7)	-22.2(2)	0.16
C(2)-N(1)	1.482(1)	2.09(6)	-21.9(2)	0.20
C(4)-N(1)	1.486(1)	2.06(6)	-21.8(1)	0.11
C(3)-O(1)	1.447(1)	1.78(6)	-11.8(3)	0.14

Table 7.2 - Critical Point Properties for H_3L.

The C-N bonds show excellent internal agreement and a higher value of $\rho(\mathbf{r}_b)$ ranging from 2.06(6) to 2.09(6) eÅ^{-3} when compared to the C-C bonds, which correlates well with the observation of the C-N bonds being approximately 0.05Å shorter. The C-N bonds show slightly higher ellipticities which are likely to be due to polarization at the nitrogen atom end of the bond, rather than any π-contributions to the bonding. Finally, the C-O bond again has bond critical point properties consistent with a polar covalent bond.

One major conclusion of this study is the disposition of the chemical "lone-pairs" on the ligating N and O atoms since a conventional picture of the bonding in transition metal complexes predicts a dative bond from the lone-pairs to the metal. Unfortunately lone-pairs do not reveal themselves in the total density $\rho(\mathbf{r})$. However, it has been observed in a range of molecules that the negative of the Laplacian function of the electronic distribution, $-\nabla^2\rho(\mathbf{r})$, posesses local maxima, or (3,-3) critical points (CPs) in their distributions in every instance where the Lewis electron pair theory requires a lone-pair to be present[92]. Additionally there are also (3,-3) CPs in the VSCC in the direction of covalent bonds. Thus an oxygen atom in water exhibits four such features in an approximately tetrahedral arrangement; two which correspond to covalent bonds and two to the lone-pairs[92]. In our study, we located four (3,-3) CPs in the VSCC of N(1), three associated with the bonds to carbon and one to the lone-pair. The angles between the CPs are approximately tetrahedral as expected. Table 7.3 contains the properties of these

CPs, with the nomenclature chosen to indicate the atom towards which the CP is directed. An important observation is that the lone-pair which points towards the nickel ion has higher density due to it being a little closer to the nitrogen nucleus. An interesting feature is that the CPs are not directed exactly along the bond vectors. Table 7.4 shows that the angular deviation of the N(1)-CP vector from the N(1)-X bond is smallest for the bonds to carbon indicating that these covalent bonds are holding the orientation of the nitrogen atom such that the apex of its tetrahedron, where the lone pair is located, does not point directly at the metal (Fig 7.3).

CP	r/Å	$\rho(\mathbf{r}_c/e\text{Å}^{-3}$	$\nabla^2\rho(\mathbf{r})_c/e\text{Å}^{-5}$
CP(1)→C(1)	0.410	3.6(1)	-72.7(7)
CP(2)→C(2)	0.411	3.6(1)	-66.3(6)
CP(3)→C(4)	0.413	3.6(1)	-65.8(7)
CP(4)→Ni(1)	0.402	4.3(1)	-79.2(6)

Table 7.3 - Properties at the (3,-3) CPs in $-\nabla^2\rho(\mathbf{r})$ in the VSCC of N(1).

C(1)-N(1)-CP(1)	6.8
C(2)-N(1)-CP(2)	12.3
C(4)-N(1)-CP(3)	10.7
Ni(1)-N(1)-CP(4)	20.8

Table 7.4 - Angles between bond vectors and corresponding N(1)-CP vectors in degrees.

The situation for O(1) is a little more complex. If O(1) is sp^3 hybridized as in water or a simple alcohol, we should expect four (3,-3) CPs in a tetrahedral arrangement, corresponding to two bonds and two lone pairs. On complexation with the metal, we may expect one lone pair to act as a σ donor. However if O(1) is sp^2 hybridized, we should see only three (3,-3) CPs arranged in trigonal-planar fashion, two associated with the bonds to C(3) and H(O1) and one acting as a σ-donating lone pair. The remaining unhybridized p-orbital will act as a π-donor to the metal. Our studies show O(1) to possess only three (3,-3) CPs, two for direct, covalent bonds, and one lone-pair directed at the metal. A mean plane fit of the CPs with O(1) shows them to be almost exactly planar with a maximum deviation of 0.02Å. The trigonal nature of $-\nabla^2\rho(\mathbf{r})$ about the oxygen atom is shown in Figure 7.4. This evidence forces the conclusion that O(1) is indeed sp^2 hybridized. However, the three centres to which it is bonded are far from coplanar; the angle between the Ni(1)-O(1) vector and the C(3)-O(1)-H(O1) plane is 35.9^0. Table 7.6 shows the orientation chosen by the trigonal planar arrangement of CPs. Since the CP(7)-O(1)-Ni(1) angle is only 5.9^0, this proves that in contrast to the case of the nitrogen atom, the oxygen atom is oriented in the direction which makes the lone-pair almost colinear with the bond vector to the metal, rather than maximize the colinearity of the CPs to its directly bonded substituents. The additional consequence of this arrangement is that any π-interaction to the metal from O(1), which must be perpendicular to the plane defined by the three CPs, is maximized.

CP	r/Å	$\rho(\mathbf{r}_c)/e\text{Å}^{-3}$	$\nabla^2\rho(\mathbf{r}_c)/e\text{Å}^{-5}$
CP(5)→C(3)	0.347	6.2(2)	-146(1)
CP(6)→H(O1)	0.344	6.5(2)	-160(1)
CP(7)→Ni(1)	0.345	6.3(1)	-161(1)

Table 7.5 - Properties at the (3,-3) CPs in $-\nabla^2\rho(\mathbf{r})$ in the VSCC of O(1).

C(3)-O(1)-CP(5)	21.8
H(O1)-O(1)-CP(6)	23.3
Ni(1)-O(1)-CP(7)	5.9
CP(5)-O(1)-CP(6)	114.6
CP(5)-O(1)-CP(7)	117.9
CP(6)-O(1)-CP(7)	126.0

Table 7.6 - Angular disposition of (3,-3) CPs in $-\nabla^2\rho(\mathbf{r})$ in the VSCC of O(1) in degrees.

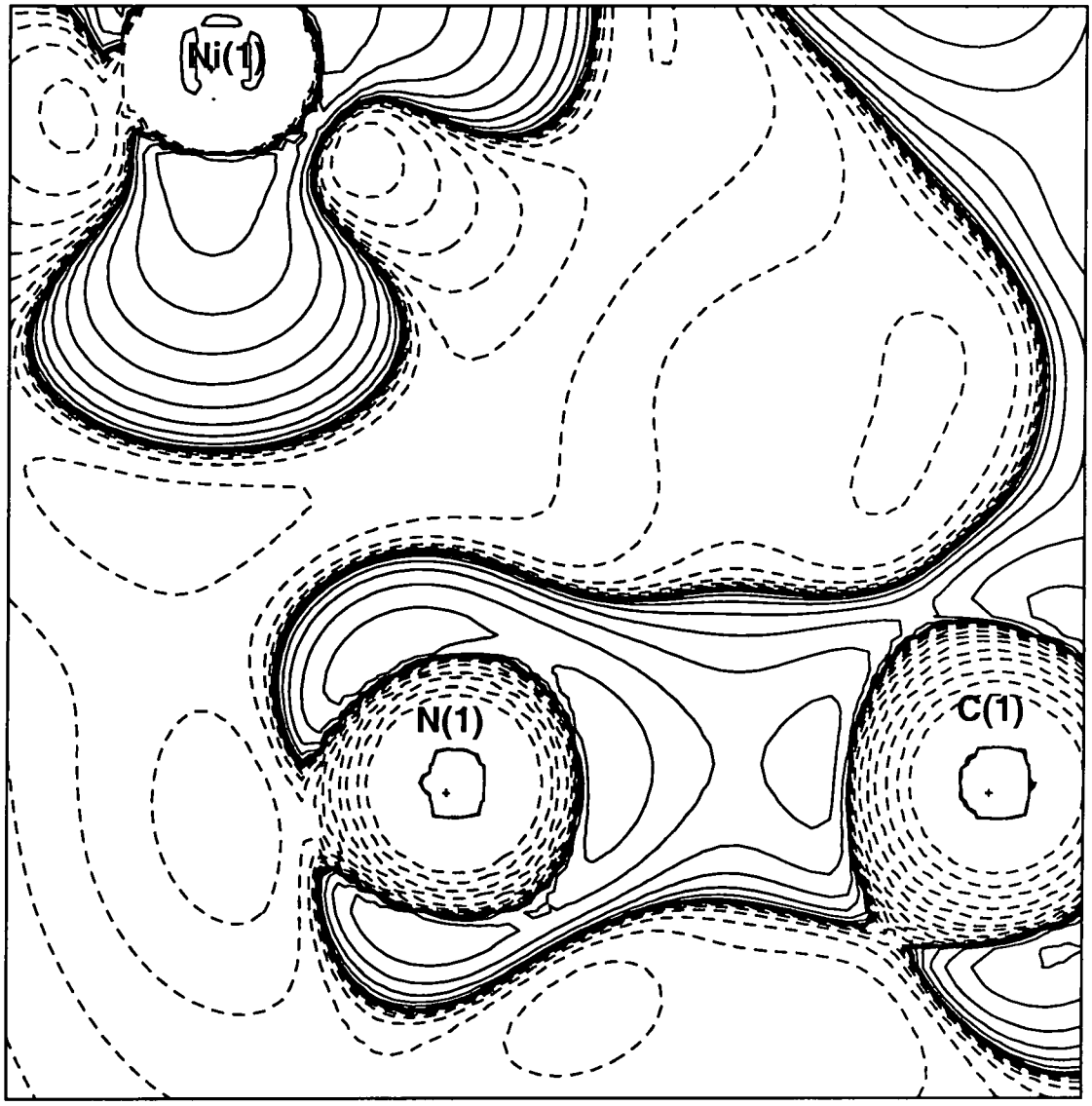

Figure 7.3 - $\nabla^2\rho(\mathbf{r})$ in the plane of the C(1), N(1) and Ni(1) atoms.

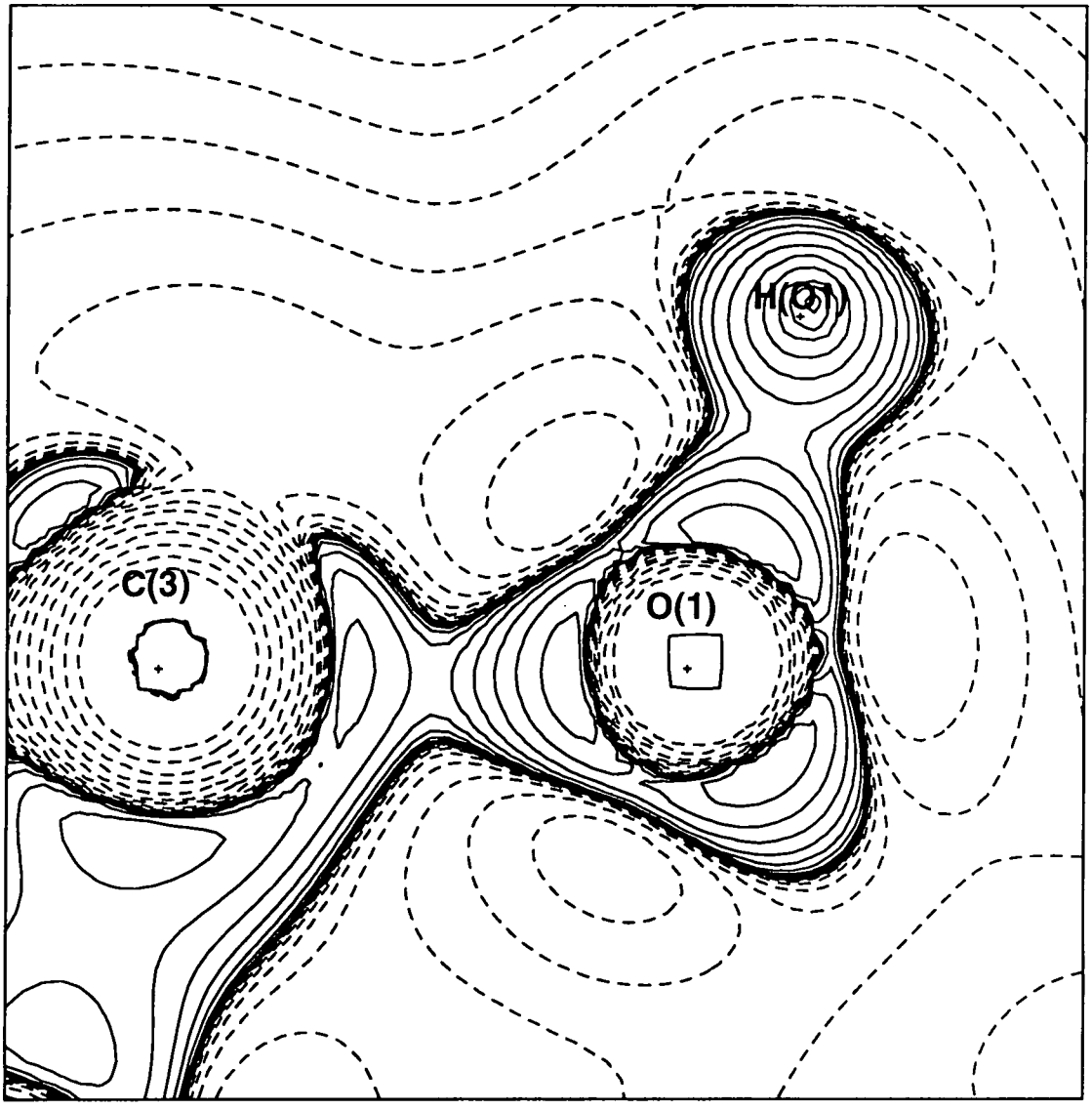

Figure 7.4 - $\nabla^2\rho(\mathbf{r})$ in the plane of the Ni(1), O(1) and C(3) atoms.

7.3.2 The nickel ion

As with all members of the first period of the transition elements, the charge density distribution of the nickel ion in the bonded environment may be thought of as deriving from $3d$ density and more diffuse density predominantly of $4s/4p$ character. The symmetry of the $3d$ density is *gerade* and hence can contribute only to the even-order multipoles. Due to the asymmetric coordination geometry of the ligating atoms about the metal atom, the more diffuse metal density associated with metal-ligand overlap will project mainly into a monopolar function and the odd-order multipoles. We included two monopolar functions in the refinement. The first was assigned a $3d$ radial function while the second monopole shared the κ parameter of 0.44(1) with the odd-order multipoles. Refining the populations of these two monopoles simultaneously is possible in this case due to the large difference in radial extents. The populations obtained of $3d$=7.8(1) and diffuse=1.3(2) give a net charge of +0.9 for the metal which concurs with chemical expectation, *i.e.* the formally double charged ion has its charge reduced by donation from the ligands. The

values of the populations we have obtained here are remarkably similar to those of Figgis *et.al.*[59] who report $3d$=7.7(1), diffuse=1.61(2) and hence a net charge of +0.8, with a rather different type of refinement.

The total d-orbital charge may be further decomposed[63,64] into symmetry adapted d-orbital populations. For a crystallographically imposed trigonal field, the d-orbital set consists of an a_1 orbital and an e pair, which are a symmetry adapted derivation from the t_{2g} set in O_h, and a remaining e pair, symmetry adapted from the O_h e_g set. The orbital energy level diagram obtained by relaxing from O_h to C_3 symmetry is shown in Figure 7.5. The a_1 orbital has the same form as a d_{z^2} orbital oriented along the 3-fold axis, while the $e(t_{2g})$ pair lie perpendicular to this axis in the basal plane. The remaining orbitals are an $e(e_g)$ pair and lie out of the basal plane, with lobes pointing directly at the ligands.

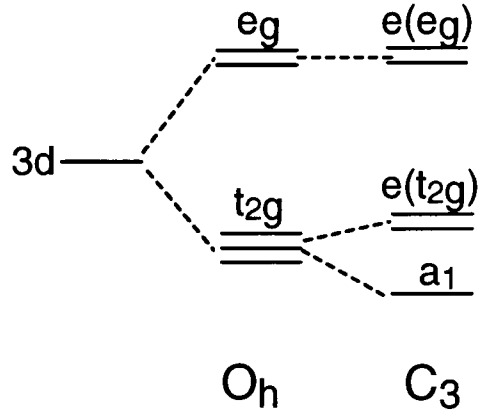

Figure 7.5 - d-orbital splitting diagram in O_h and C_3 fields.

The results of the orbital occupancy determination carried out in this study are displayed in Table 7.7. They are in the order expected for splitting under a crystal field. However the stabilized a_1 and $e(t_{2g})$ orbitals have lower populations than expected while the destabilized $e(e_g)$ set has a higher population. These facts are consistent with an appreciable ligand field effect.

Orbital	Population	Crystal Field
a_1	1.60(6)	2.00
$e(t_{2g})$	3.53(7)	4.00
$e(e_g)$	2.62(6)	2.00

Table 7.7 - Symmetry adapted d-orbital populations.

The 3 dimensional disposition of the diffuse density in the nickel coordination sphere has lobes pointing towards the three ligating nitrogen atoms and a fourth lobe pointing along the 3-fold axis on the oxygen side of the metal and is very diffuse. In form it bears a close similarity to that expected for a set of sp^3 hybrid orbitals composed from a $4s$ and $4p$ basis.

7.3.3 Topological Properties of the Metal-Ligand Bonds

Bond paths in $\rho(\mathbf{r})$ for both nitrogen-nickel and oxygen-nickel have been found with the (3,-1) CP properties shown in Table 7.8. The Ni(1)-N(1) bond CP has a far greater value of the electron density than that for the Ni(1)-O(1) bond. This is due to the observed orientation of the diffuse charge on the metal which orients its lobes directly towards the ligating nitrogen atoms. A second effect of this is the nature of the bond path, which has a total length of 2.10Å and is therefore almost linear: the direct distance between these atoms is 2.063(1)Å. The bond CP is situated 0.67Å from the nitrogen terminus. The Ni(1)-O(1) bond path at 2.45Å is substantially longer than the direct internuclear distance of 2.094(1)Å. Starting at the nickel nucleus, the bond path to oxygen leaves the metal along the diffuse lobe directed along the C_3 axis and then curves around towards the oxygen lone pair, with the bond CP lying 0.91Å from the oxygen nucleus. For both bonds, the critical point lies much closer to the ligator than to the metal atom reflecting their differing sizes.

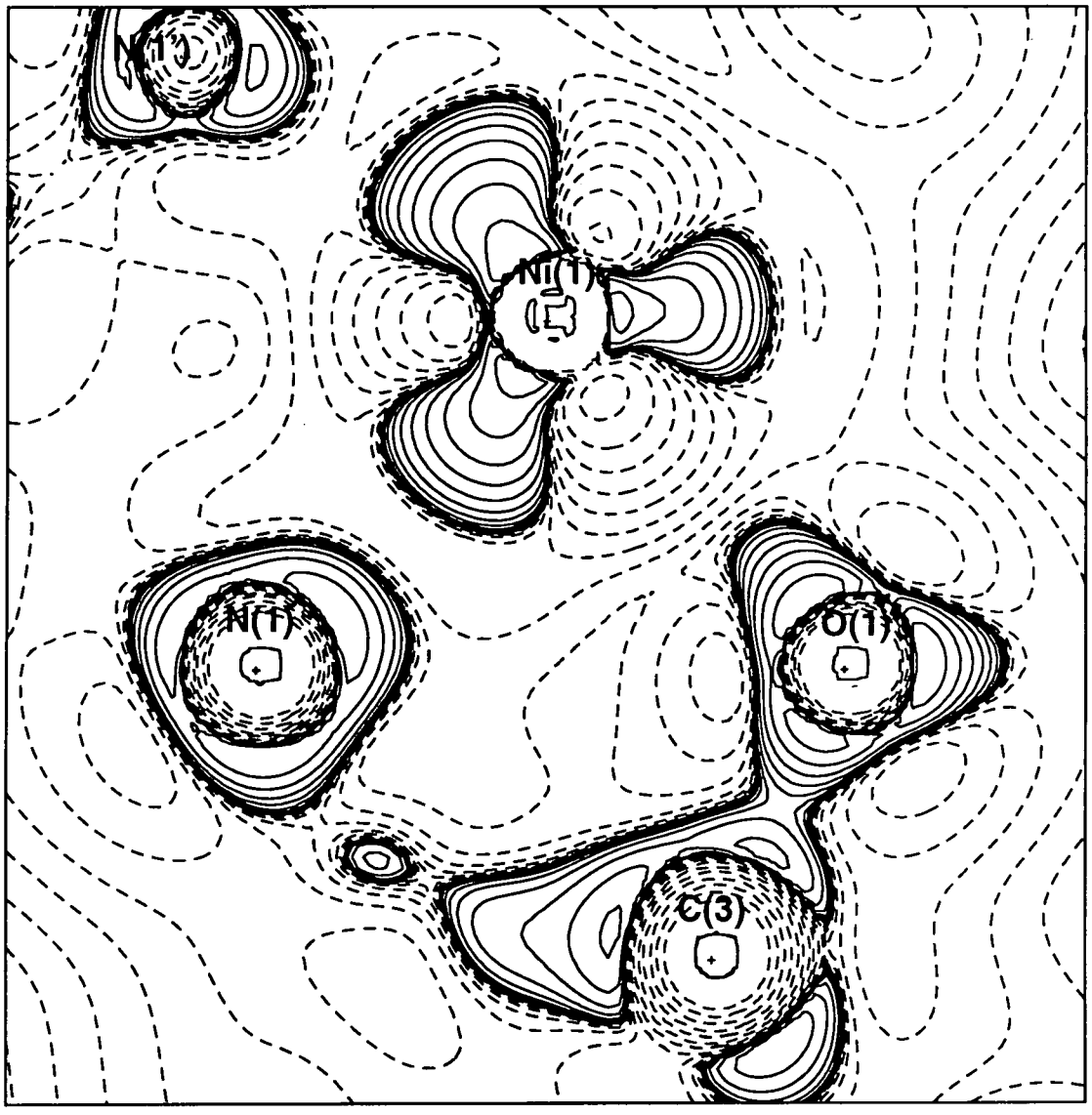

Figure 7.6 - $\nabla^2\rho(\mathbf{r})$ in the plane of the Ni(1), O(1) and N(1) atoms.

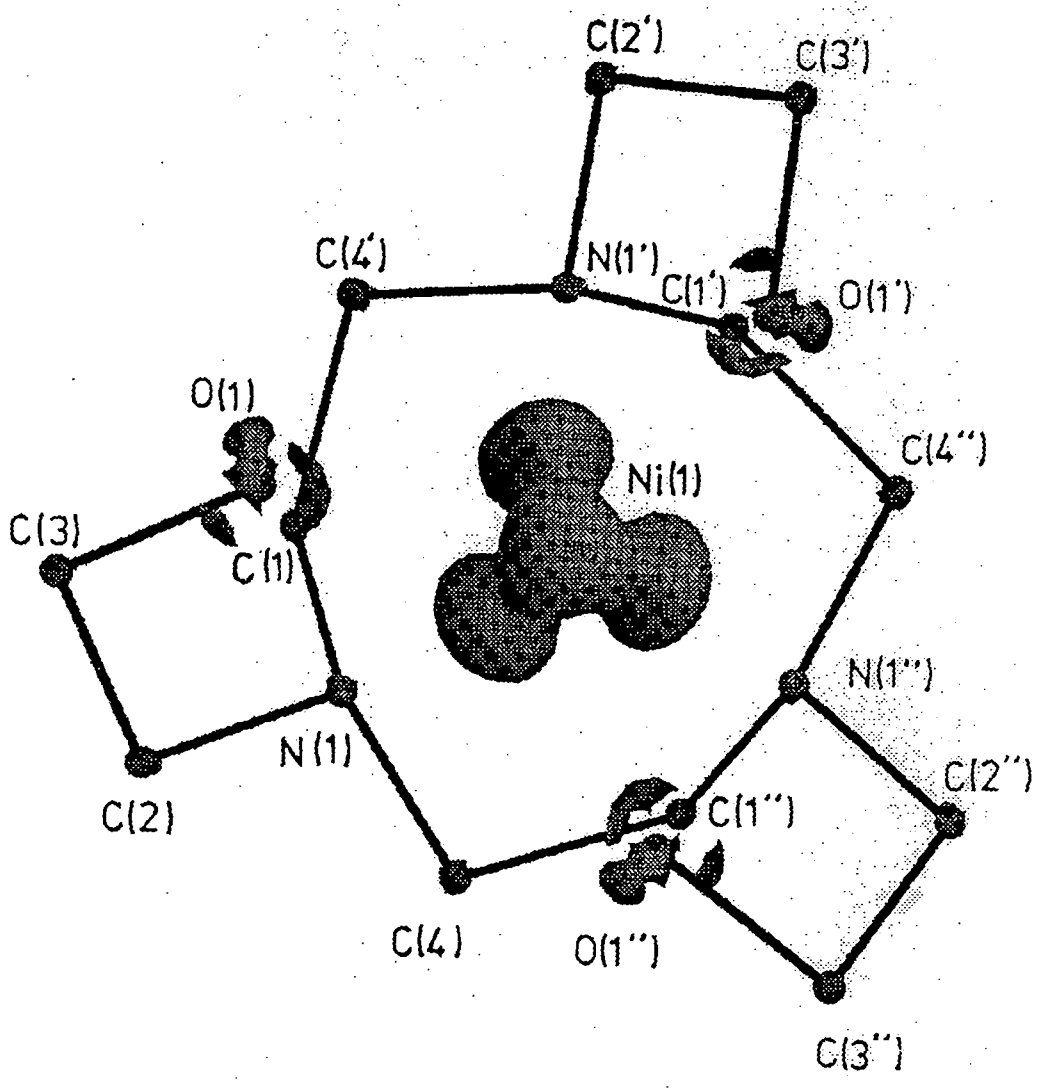

Figure 7.7 - Isosurface of - $\nabla^2\rho(\mathbf{r})$ at the -100eÅ^{-5} level.

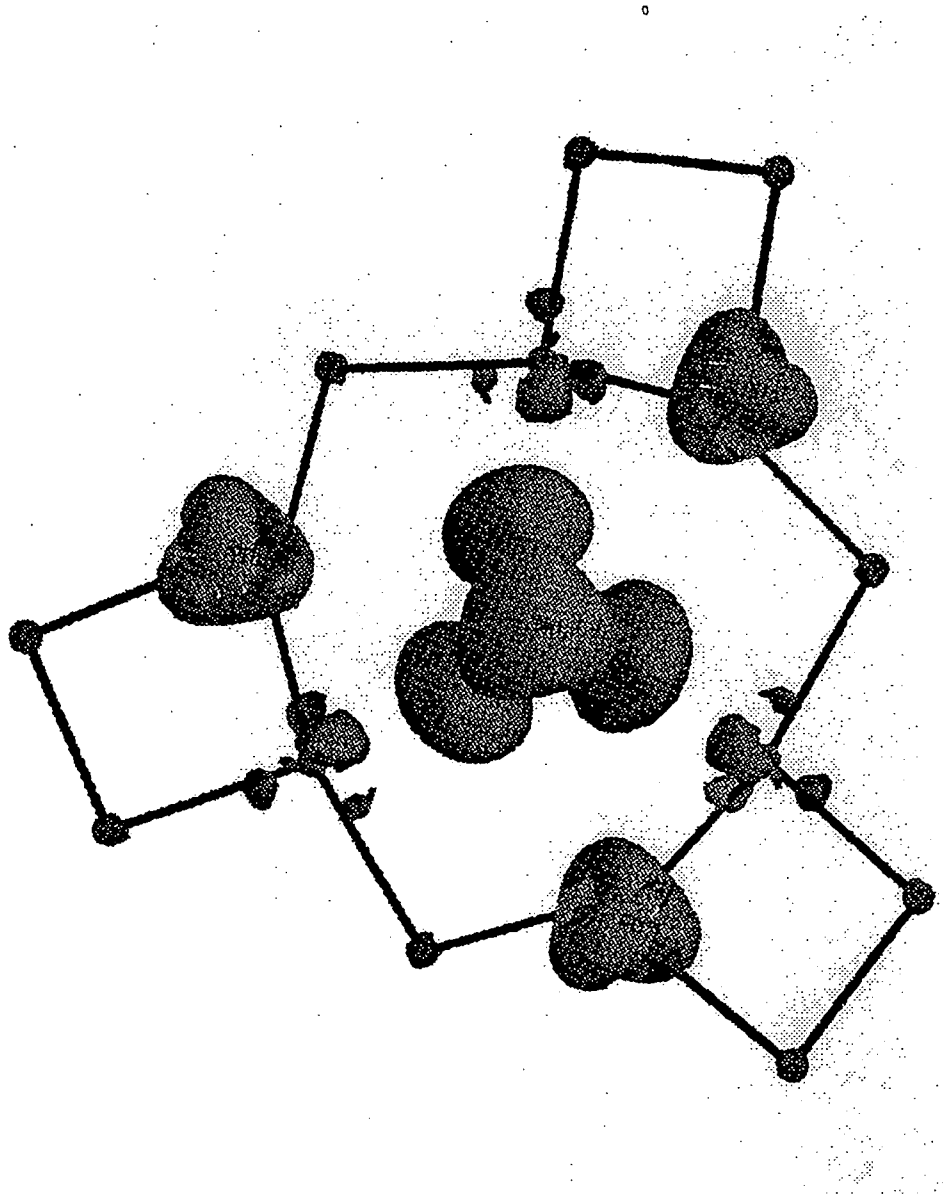

Figure 7.8 - Isosurface of - $\nabla^2\rho(\mathbf{r})$ at the -50eÅ^{-5} level.

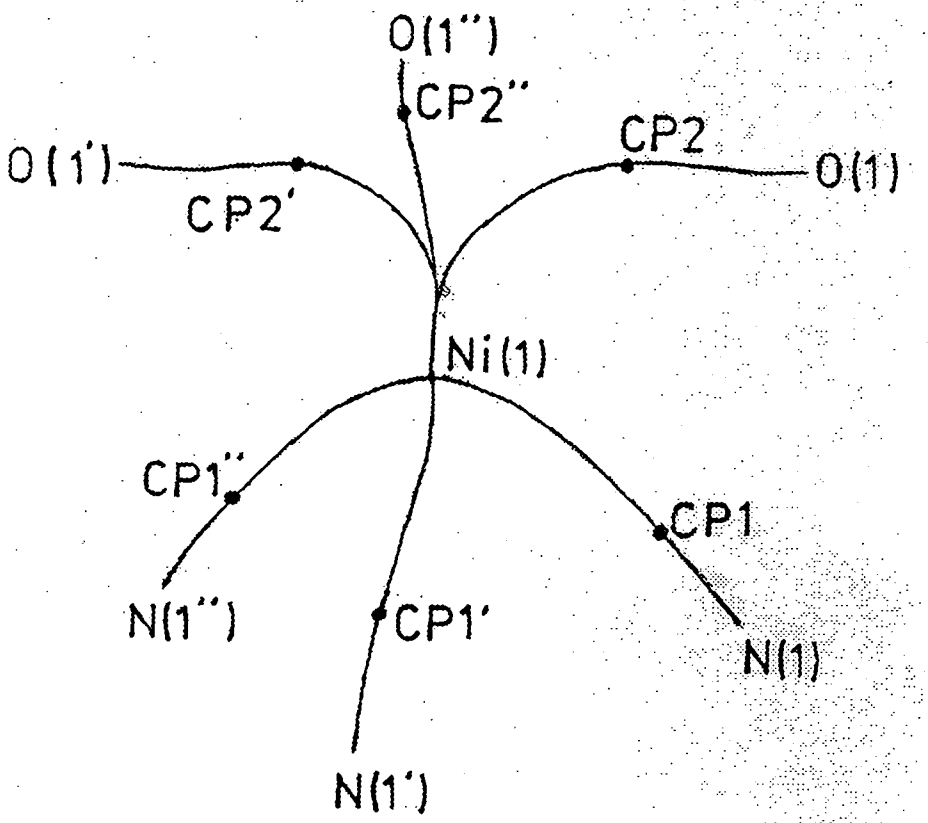

Figure 7.8 - Metal to ligand bond paths.

bond	r_i/Å	r_j/Å	$\rho(\mathbf{r}_b)$/eÅ^{-3}	$\nabla^2\rho(\mathbf{r}_b)$/eÅ^{-5}	ϵ
Ni(1)-N(1)	1.405	0.674	3.10(9)	+1.4(3)	0.15
Ni(1)-O(1)	1.367	0.908	0.93(4)	+9.77(7)	1.29

Table 7.8 - Critical Point Properties for the metal-ligand bonds.

Interestingly, both critical points show positive Laplacian, which is *usually* indicative of a closed shell, non-covalent interaction. Given the rather curved nature of the Ni-O bond, the ellipticity is not a particularly reliable indicator of π-bonding and therefore its high value should not be over-interpreted in this context. The ellipticity of the metal-nitrogen bond however is more valuable, since the bond is reasonably linear, and its small value indicates a lack of π-bonding as expected. A plot of $-\nabla^2\rho(\mathbf{r})$ in the plane of N(1), O(1) and Ni(1) is shown in Figure 7.6. 3-dimensional isosurfaces of $-\nabla^2\rho(\mathbf{r})$ at the -100 and -50 eÅ^{-5} levels are shown in Figure 7.7. These values give the clearest view of the topological properties of $-\nabla^2\rho(\mathbf{r})$ for the oxygen and nitrogen atoms respectively. It can be clearly seen in three dimensions that the nitrogen lone-pair ligates towards a lobe of negative $\nabla^2\rho(\mathbf{r})$ while the single oxygen lone-pair ligates between these lobes. Figure 7.8 shows traces of the bond paths between metal and ligands. Despite there being a total of six ligating atoms, only four bond paths leave the metal. Three conventional,

approximately linear bond paths from the metal to the nitrogen atoms are in evidence, while the fourth bond path trifurcates into branches, each leading to an oxygen atom.

7.4 Discussion

The overall picture of metal-ligand bonding consists of donation of approximately 1.1 electrons to the metal from the ligands as determined by the monopole populations. This donation does not increase the occupancy of the *d*-orbitals, but does produce an arrangement of diffuse density of approximate tetrahedral symmetry consistent with sp^3 hybridization of the $4s$ and $4p$ orbitals. These hybrids point towards the three ligating nitrogen atoms and also along the three-fold axis between the oxygen atoms. This results in much higher electron density in the Ni-N bonds than the Ni-O bonds. Bond paths in $\rho(\mathbf{r})$ with (3,-1) bond critical points are traceable from metal to ligand. The value of $\rho(\mathbf{r}_b)$ in the Ni-N bond is 3.10(9) $e\text{Å}^{-3}$ which is very high and the bond path is almost linear. This contrasts with the Ni-O bond path which follows the diffuse density away from the nickel but then curves towards the oxygen atom (Figure 7.8). Since the diffuse density on the metal does not point directly at the oxygen atoms, the Ni-O bond has a much lower $\rho(\mathbf{r}_b)$ value of 0.93(4) $e\text{Å}^{-3}$. The covalency indicated by the topology of the charge density appears to derive from the diffuse density about the metal rather than preferential occupancy of the individual *d*-orbitals. The nature of the ligating nitrogen atom is as expected, with a single lone-pair pointing at the nickel. The oxygen is sp^2 hybridized with a single lone-pair oriented towards the metal atom and an unhybridized *p*-orbital available for π-bonding.

Both types of metal-ligand bond critical point exhibit positive Laplacian values. In more usual covalent bonds such as C-C, C-N etc, the Laplacian value is negative indicating a *local* concentration of charge in the bond. In ionic bonds such as Na^+-Cl^- the Laplacian is positive indicating a *local* depletion and therefore a closed shell and ionic bond. A literal application of these observations to the less well studied Ni-N and Ni-O bonds would conclude that these bonds are ionic. However, this is at odds with both accepted chemical notions and the other evidence presented here. It has been observed previously that the behaviour of the Laplacian becomes less easily interpreted as the diffuseness of the charge density increases. For example, its ability to show shell structure in atoms[112] as local concentrations and depletions of charge no longer holds for $Z \geq 40$. Also, in covalent bonds between electronegative atoms such as in Cl-Cl, $\nabla^2\rho(\mathbf{r}_b)$ has only a small negative value, due to the large magnitude of the single positive curvature of the density. In F-F, this curvature is sufficiently large to make $\nabla^2\rho(\mathbf{r}_b)$ positive, even though the bond is obviously covalent[113]. All other published computational studies[114,115,116,117,118,119] which incorporate Laplacian values in metal ligand bonds also show positive Laplacian and therefore our experimental results provide an important, independent confirmation of this behaviour. It would appear that the topological properties of covalent metal-ligand bonding does not have the same characteristics as covalent bonding between first row atoms.

7.5 Conclusion

We have determined the experimental charge density of a large pendant arm macrocyclic complex by fitting a multipole model to high resolution X-ray diffraction data. We find covalent bonding of the ligating nitrogen and oxygen atoms with the central nickel ion which considerably reduces the charge on the metal. While the metal *d*-orbital populations are in accord with ligand-field modification of the populations predicted by crystal-field theory, the characteristics of the charge density on the metal are dominated by four diffuse lobes which point at the ligating nitrogen atoms but between the ligating oxygen atoms. The disposition of the lobes is consistent with sp^3 hybrids from the $4s$ and $4p$ metal orbitals. The properties of the Ni-N and Ni-O bond critical points differ considerably reflecting the chosen orientation of the diffuse hybrids which is presumably determined by the differing ligating properties of the two atom types. Additionally, the (3,-3) critical points in $-\nabla^2\rho(\mathbf{r})$ within the VSCC of the ligating oxygen atom provide evidence for metal-oxygen π-bonding. We have shown this technique to be tractable for large molecules with many electrons, even when they crystallize in non-centrosymmetric space groups.

Multipole populations and local coordinate systems *etc.* are available in Appendix C.

7.6 Acknowledgements

Thanks are due to Drs. P.R. Mallinson and C.S. Frampton for making their experimental data available and Drs. R.D. Peacock and L.J. Farrugia of the University of Glasgow for providing a crystalline sample.

Chapter 8

Experimental Charge Density of Weak Interactions

As outlined in the introduction, one class of molecules well worth investigating by experimental charge density determination are those containing weak interatomic interactions. Those weak interactions most commonly investigated include hydrogen bonds, electrostatic and van der Waals interactions. In this chapter, the definition of a weak interaction is one where an attractor interaction line[92] links two nuclei not thought to be bonded by conventional criteria. While not a rigorous definition, it is a useful one in this context. The particular class of molecules under study are those where an oxygen atom makes a close approach to a carbon atom of a carbon-carbon triple bond, inducing a distortion from linearity of the triple bond. As will be seen, this C$\cdots$O interaction cannot possibly be covalent, however the equilibrium geometries of a series of molecules would seem to indicate an attractive interaction here as opposed to a steric one.

Alkyne groups are known to undergo both nucleophilic and electrophilic addition reactions depending upon the nature of their substituents. Electron withdrawing groups enhance the susceptibility to nucleophilic attack, whereas electron donating groups encourage electrophilic attack on the acetylene. For example, but-3-yne adds one equivalent of bromine[120], whereas the electron-deficient alkynes methyl propiolate and dimethyl but-2-yne-1,4-dioate add aziridine[121]. Tolane (ethynylenedibenzene) occupies an intermediate position, reacting with both electrophiles and nucleophiles. Thus it will add chlorine[122] or bromine[123] as well as adding thiols[124,125,126], tributylphosphine (to give a betaine)[127] and n-butyl lithium[128].

Short of full chemical reaction, acetylene groups in molecules also participate in non-covalent interactions; hydrogen bonds to acetylenic π-systems have been accepted in the literature as a real occurrence due to their investigation by crystallography, infra-red spectroscopy and theoretical techniques. More novel interactions are those involving the approach of nucleophilic atoms such as O, N, H^-. In many cases, the equilibrium structure of molecules or dimers containing non-covalent interactions to acetylenic moieties have the interesting property of a distorted geometry about the triple bond. The ability of a molecule to distort geometrically under the the approach of, but non-reaction with the functional group of another molecule may well be an efficient method of transmitting through its own molecular structure the specific recognition of the approaching molecule. The consequences of such action within the context of signaling mechanisms such as those which occur in the non-covalent binding of a drug to a receptor protein or in molecular

switch devices, may be important.

Steiner *et.al.*[129] have performed a study aimed at validating the description of relatively weak C-H···C≡C interactions as true hydrogen bonds. To this end a database analysis, crystal structure determinations, vibrational spectroscopy and correlated *ab-initio* calculations all indicate that their criteria for such a description are met by these systems, and Hobza *et.al.*[130] have performed high-level *ab-initio* calculations on the acetylene dimer at the frozen monomer geometries, yielding a binding energy of 5.9 kJmol^{-1}. Reports of H-bonds to acetylenes which mention distortion to the linearity of the triple bond are somewhat rarer; Pilkington *et.al.*[131] have determined the crystal structure of the diboronic acid **1** by X-ray diffraction, reporting a C≡C-C bond angle of 178.15(8)^o and Block *et.al.*[132] have reported a very small distortion of 0.75^o for the T-shaped complex of acetylene with HCN from *ab-initio* calculations performed in reference to infra-red spectroscopic measurements, with the acetylenic H atoms moving away from the impending HCN molecule.

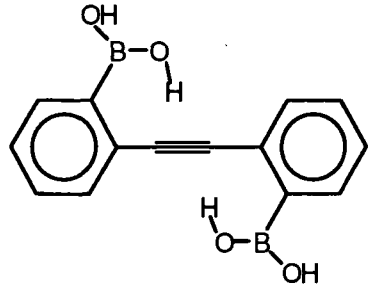

1

The largest distortions discovered so far are for the set of $CH_{n-4}Cl_n$ T-shaped dimers[133] with the rather exotic C_2Na_2 molecule. The maximum deviation from linearity of the triple bond is 22.0^o for the $CH_2Cl_2 \cdots C_2Na_2$ calculation at the MP2 level where the Na atoms move toward the H bond donor. This is also true for $CHCl_3 \cdots C_2Na_2$ where the distortion is 18.6^o. Conversely, the $CH_3Cl \cdots C_2Na_2$ dimer is characterized by a bending of the Na atoms away from the H-bond donor by only 4^o. All of the above systems are representative of accepted chemical intuition of attractive, bonding, albeit weak interactions.

The analogous approach of electron-rich groupings to acetylenic carbon atoms enjoy less of a precedent. Such situations are an important model for the early stages of nucleophilic attack on the acetylene. A molecular orbital study of the nucleophilic attack of the hydride anion[134] on acetylene found the optimum geometry to have a $H^- \cdots C{\equiv}C$ angle of 126^o, which remains similar through the transition state to the final vinyl anion product.The approach of H^- is accompanied by a *trans* bending of the H atoms, which increases progressively along the reaction coordinate. A subsequent study[135] has identified the transition state of the same reaction to have a nucleophile approach angle of 127^o accompanied by a distortion of the H-C≡C angle of 24^o at the attacked carbon and 32^o at the secondary carbon. This *trans* bending is attributed to the large energy drop of the π^* LUMO on such distortion.

Similar early stages of nucleophilic attack by other electron-rich atoms such as oxygen should

be recognizable by an O···C distance within the sum of the respective van der Waals' radii, an approach angle of approximately 126° and a *trans* bending of the acetylene. It is the aim of the first part of this chapter to highlight structural evidence for the existence of such interactions which occur intramolecularly in organic crystal structures.

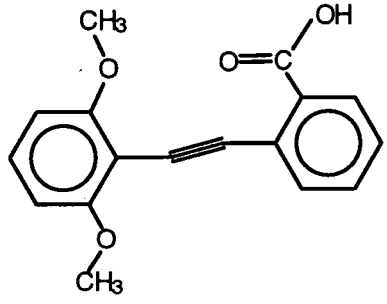

2

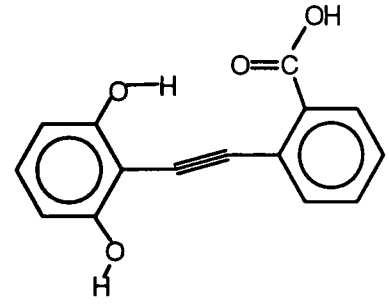

3

Of the molecules analyzed in this study, two main groupings exist; those in which the oxygen atom of a carbonyl group in either an ester or carboxylic acid approaches the acetylene and those where the "attacking" atom is the oxygen of a nitro group. Methyl 2-[(2,6-dimethoxyphenyl)ethynyl]benzoate[136], **2**, is a member of the former. The O···C distance is 2.827(2)Å(well within the van der Waals' sum of 3.18Å) and the angle of attack is 109.2(1)°. Confirmation of this interaction falling into our characterization of being a model of nucleophilic attack is given by the non-linearity of the triple bond. A bend of 9.5(1)° at the primary carbon accompanied by a very small 0.7(1)° bend in *trans* mode at the secondary carbon atom occurs. The lack of a bend of similar magnitude at the secondary carbon may be due to the proximal positioning of the two ether oxygens on the second aromatic ring.

The geometric parameters pertaining to the O···C interactions for **2** along with those for 2-[(2,6-dihydroxyphenyl)ethynyl]benzoic acid[137], (**3**), 2-[(2,6-dimethoxyphenylethynyl]-3-methoxybenzoic acid[138] (**4**) and 2,2-ethynylenedibenzoic acid[139] (**5**) are displayed in Table 8.1.

	O···C(Å)	O···C≡C(°)	1^{ry} distortion(°)	2^{ry} distortion(°)
2	2.827(2)	109.2(1)	9.5(1)	0.7(1)
3	2.767(2)	104.2(2)	5.9(2)	7.7(2)
4	2.785(2)	107.8(2)	9.0(1)	3.6(1)
5	2.775(2)	104.9(2)	5.9(2)	5.9(2)

Table 8.1 - Observed geometrical parameters for **2** to **5**.

Points worth noting are the small ranges of the O···C distance (0.059Å) and attack angle (5.01°). These are both constrained by molecular geometry, preventing the attack angle moving closer to the optimum 126° found for the $H^- \cdots C_2H_2$ system. Of special interest is structure **5**. It is shown to possess a *cis* bent alkyne. This is not inconsistent with the previous structures because **5** undergoes simultaneous *cis* attack at both carbon atoms. An explanation consistent with this observation is that the more important distortion occurs at the primary carbon, with the secondary *trans* distortion occurring if possible. In the case of **5**, both atoms are in fact primary carbon atoms and the more important primary distortion overrides the secondary distortion.

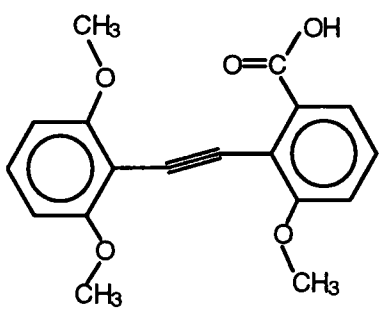

4

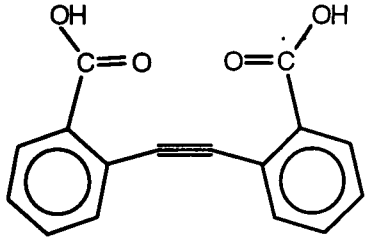

5

Somewhat more perplexing is the fact that this molecule would chose to be in the *cis* conformation at all. The distance between the two carbonyl oxygen atoms is 3.120(2)Å, slightly outside the sum of the van der Waals' radii, but this is achieved by twisting the aromatic rings from planarity by 19.7(1)^o and the acid groups by 15.4(1)^o from their respective aromatic rings, disturbing the π-conjugation. Even at this distance apart, the oxygens are presumably repelling one another electrostatically if not sterically. A hypothesis for the favourability of the *cis* isomer over the *trans* given by Pilkington *et.al.*[139] is that the approach of a nucleophile will induce an incipient lone-pair on the secondary carbon in the *trans* position. The approach of a second nucleophile *trans* to this first one would cause steric and electrostatic repulsion between itself and this incipient lone-pair, and hence the favoured geometry of simultaneous approach of two nucleophiles is *cis*.

The second series of molecules showing similar interactions include ethyl 3-(2-nitrophenyl)-propynoate[140] **6**, 2-amino-2'-nitro-ethynylenedibenzene[141] **7**, and the unpublished, room temperature structure 2,2'-dinitro-ethynylenedibenzene[142] **8**.

For these molecules, the oxygen of a nitro group makes a close approach to the triple bond. The relevant geometric parameters are summarized in Table 8.2. The O$\cdots$C distances are slightly shorter here compared to those in Table 8.1, while the angles of approach lie within the previous range, again due to geometric constraints. **8** is of interest since it is chemically similar to **5**, having two identical attacking nucleophilic groups. In this case the approach is *trans* questioning the validity of the argument given for the greater stability of *cis* approach of both groups.

	O$\cdots$C(Å)	O$\cdots$C$\equiv$C(^{o})	$1^{r\prime}$ distortion(^{o})	distortion(^{o})
6	2.642(2)	106.4(2)	6.8(2)	6.9(2)
7	2.672(4)	108.3(2)	8.1(3)	6.6(3)
8	2.647(4)	108.3(3)	8.2(2)	8.2(2)

Table 8.2 - Observed geometrical parameters for **6** to **8**.

While the above structural data from X-ray crystallographic measurements suggest the presence of some sort of C$\cdots$O interaction, the molecular geometries themselves do not provide much further information. Within the context of Bader's Theory of Atoms in Molecules, if the hypothesised interactions do occur, they must manifest themselves by the presence of a (3,-1) bond critical point between the nuclei accompanied by an attractor interaction line. Theoretical ev-

idence for the existence of weak interactions, either attractive or sterically repulsive, using the topological theory is relatively rare.

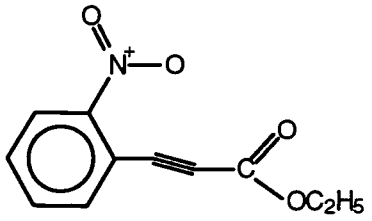

6

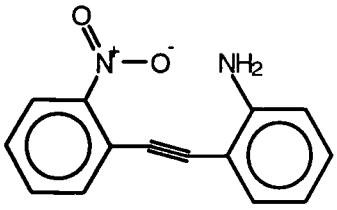

7

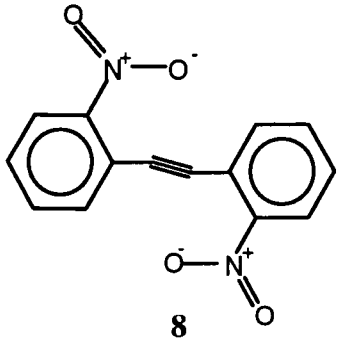

8

Charge transfer ion-pairs[143] have been found to exhibit bond paths as do steric interactions in ortho-substituted biphenyls[144]. The presence of bond paths has been confirmed between sterically crowded H atoms in benzenoid hydrocarbons[145] and also between halogen atoms in perfluoronated hydrocarbons[146]. Steric F···O bond paths in fluoro-acetone[147] and N···N bond paths[148] have also been observed.

The values of $\rho(\mathbf{r})$ at the bond critical point in all of the above cases are very low, and hence a charge density determination of such features is likely to be on the limits of currently attainable accuracy.

McCormack *et. al.*[149] have located S···S trans-annular interaction within a C_2S_4 ring in *ab-initio* calculations on 3,3,6,6-tetramethyl-S-tetrathiane, but have been unable to locate the same features in the experimentally determined charge density. They did locate S···S intermolecular interactions between neighbouring molecules in the experimental study. The value of $\rho(\mathbf{r})$ at the bond critical point was low, while $\nabla^2\rho(\mathbf{r}_b)$ was small and positive, indicating a weak, closed-shell interaction. Tsirelson *et. al.*[113] have conducted studies of the theoretical and experimental charge densities of solid Cl_2 and again located intermolecular bond paths with similar properties. The original intention of this part of the work was to perform charge density determinations on as many molecules in the series **2** to **8** as part of a collaboration with Dr. J.D. Wallis at the University of Kent, Canterbury. Preliminary crystallographic investigations of **7** indicated a phase transition during cooling which resulted in the crystal turning to powder. Several attempts

to cool a crystal very slowly while retaining its integrity proved futile. Samples of **8** were unstable under X-ray flux and the prolonged exposure inherent in charge density experiments meant that this experiment also had to be discarded. Fortunately, one single crystal of **5** proved ideal for a charge density determination. This molecule is perhaps the most interesting of the whole series of substituted acetylenes. In addition to the C···O intramolecular interaction of primary interest, the crystal structure also shows strong intermolecular hydrogen bonding *via* head to head pairing of carboxylic acid groups.

8.1 Experimental

A well formed, transparent crystal of $[C_7H_4CO_2H]_2$ was selected and mounted on a glass fibre. Preliminary rotation photographs showed strong diffraction to high Bragg angles, a prerequisite for suitable crystals for charge density analysis. The crystal was cooled slowly to 123(1)K using an liquid nitrogen cryostream device[73] after being mounted on the diffractometer, a Siemens P4, and rotation photographs taken confirmed that no degradation or phase change had occurred due to temperature change. The crystallographic unit cell was determined from the setting angles of 56 reflections in the 2θ range 12.28-50.18°. Pairs of equivalent reflections were measured in shells of 10° in 2θ starting from low angle to a maximum resolution of 1.04Å^{-1} (95.3° in 2θ). The crystal did not appear to suffer from any appreciable decay, so the remaining pair of symmetry equivalent reflections were measured commencing from high angle. Six standard reflections were measured periodically to correct the data for decay. The total X-ray exposure time of the crystal was 704.65 hours.

Data reduction was performed with the DREAM package[79]. It became apparent on careful examination of reflection profiles that there was a problem with the very highest angle data. The peak limits calculated for data reduction lay outside the measured scan range, indicating peak truncation due to insufficient scan widths at high angle. A discussion of this problem is given by Destro and Marsh[150]. Remeasurement of the highest angle data with increased scan widths was the preferred option, however the diffractometer was no longer available. The next best option was to evaluate the resolution limit where the calculated peak widths lay far enough within the scan for reliable background estimation. After inspection of a substantial sample of profiles, only those reflections with $\sin\theta/\lambda \leq 0.935$Å^{-1} were deemed usable. Absorption corrections applied using the ABSORB[81,82] program slightly worsened the internal agreement of symmetry equivalent reflections and degraded the residual maps by a small degree, so uncorrected data was used in the final refinements. The small absorption coefficient coupled to the small crystal size suggests that absorption effects would be neglegible.

8.1.1 Multipole refinement

The crystal structure was as determined[139] previously. Figure 8.1 is a thermal ellipsoid plot of the molecule from this study. Only half of the molecule is unique by symmetry with a twofold rotation relating the two halves. There is a dihedral angle of 21.0(1)° between the two aromatic rings, while the carboxylic acid groups have a torsion angle of 15.5(1)° with their respective

phenyl rings. Separate molecules come together *via* their carboxylic acid groups to form head to head dimers where the monomers are related by a centre of inversion, a common motif in crystal packing. For the molecule under study, the hydrogen atoms involved in these hydrogen bonds are well ordered in single sites, presumably due to the different different nature of the two different oxygen atoms. This is not always the case[108].

Thermal vibrations were modeled in the refinements by assigning anisotropic thermal parameters to all non-hydrogen atoms, while the hydrogen atoms were given an isotropic temperature factor of 1.2 times the isotropic equivalent of the heavy atom to which they are bonded.

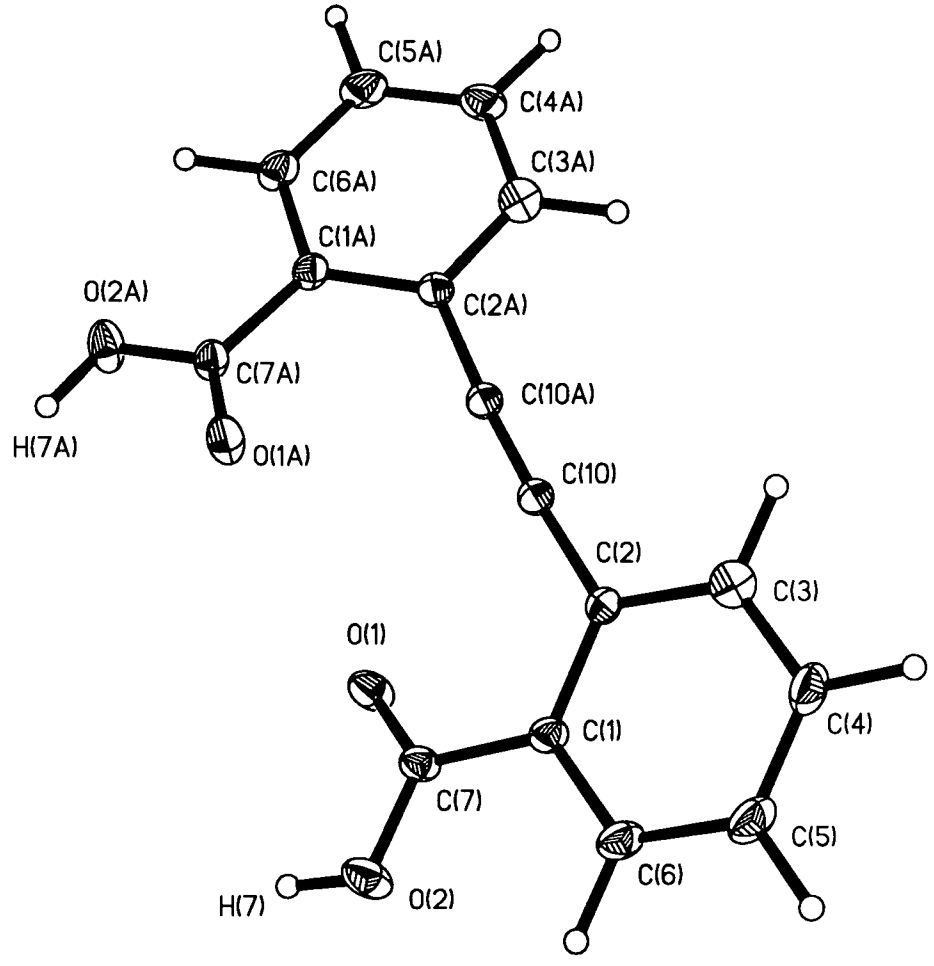

Figure 8.1 - thermal ellipsoid plot of **5** at the 50% probability level.

An electroneutrality constraint was applied in all refinements. The level of expansion was truncated at the octapole level (l_{max}=3) for C, and O while the asphericity of H(3) to H(6) was modeled by a single bond-directed dipole. H(7) was given the greater flexibility of three dipole functions to allow for proper description of the hydrogen bond. The two oxygen atoms shared a common kappa set, as did all the carbon atoms.

Hydrogen atom κ' and κ'' were fixed at 1.16 which is equivalent to using the contracted scattering factors of Stewart, Davidson and Simpson[55]. After multipole refinement, the C-H bond

lengths in the aromatic ring were subsequently normalized to 1.084Å, the value in benzene[151], while H(7) was moved out along its bond vector to the value of 0.95Å as in methanoic acid[151].

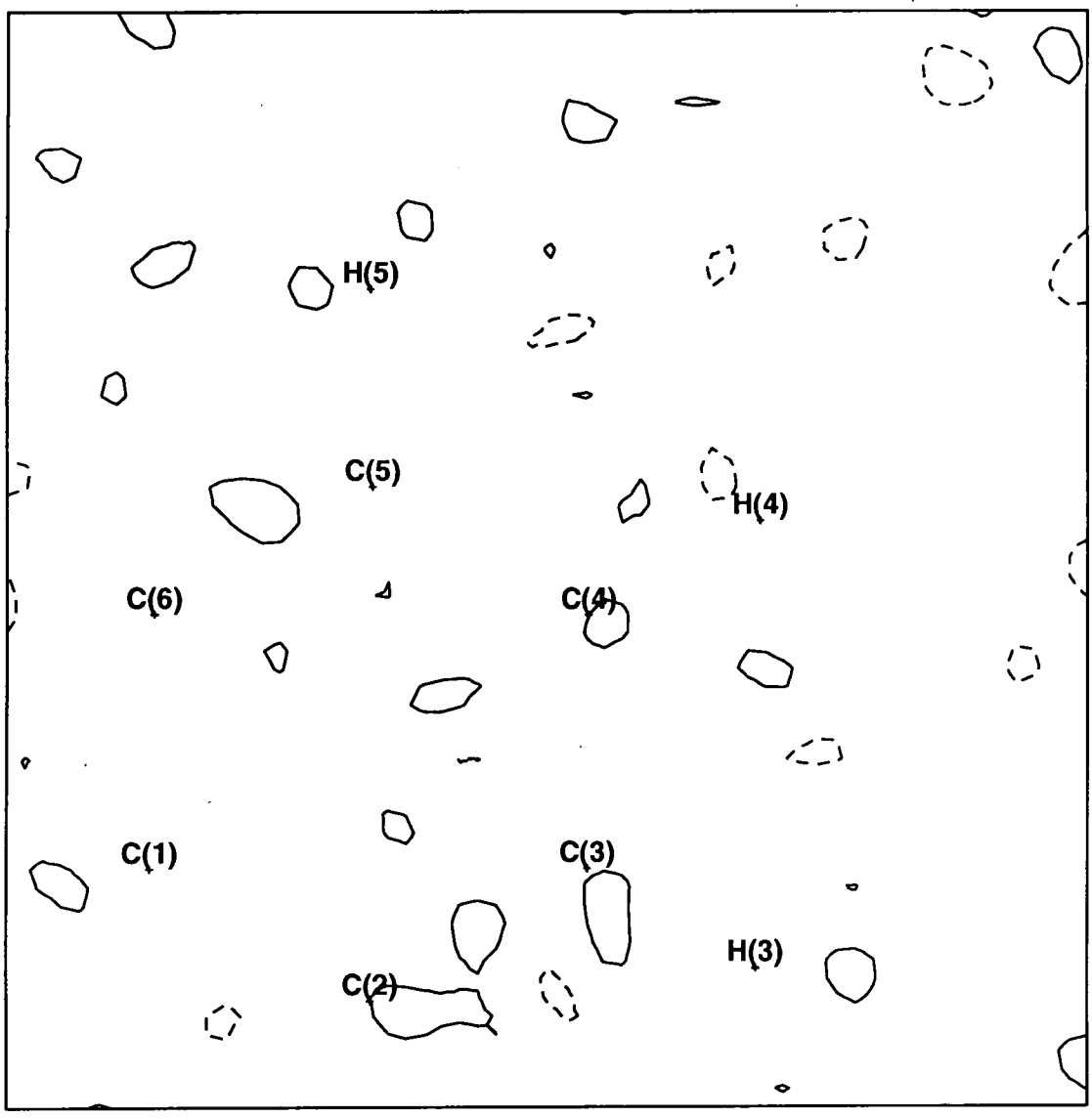

Figure 8.2 - Residual map in the plane of the benzene ring. Contours at 0.1 eÅ^{-3}.

The refinement converged smoothly with stable values for all parameters and no large least-squares correlation coefficients. Various residual maps were plotted and no structured features indicating either model or data inadequacy were noted. Additionally, all bonded pairs of atoms easily satisfy the rigid bond test criterion. Figure 8.2 shows the residual electron density in the plane of the aromatic ring. Table 8.3 summarizes experimental data and refinement details.

Formula	$C_{16}H_{10}O_4$
Crystal System	Monoclinic
Space group	$C2/c$
T/K	123(1)
a/ Å	11.801(1)
b/ Å	13.233(1)
c/ Å	7.874(1)
β/ ^{o}	90.326(1)
V/ Å^3	1229.6(1)
Z	4
Crystal dimensions/mm	0.18 x 0.12 x 0.10
Radiation(λ/Å)	Mo-K_α(0.7107)
Scan type	θ - 2θ
sin θ/λ_{max}/Å^{-1}	0.935
Standard reflections	2 0 0, 0 $\bar{2}$ 0, 0 0 2, 1 7 2, 3 $\bar{7}$ 0, 6 4 $\bar{1}$
No. reflections measured	20689
Range (hkl)	-22 to 22; -24 to 24; -14 to 14
No. symmetry-independent reflections	4214
No. $I > 2\sigma(I)$ reflections	2738
Agreement factor $R = \Sigma\|I - \overline{I}\|/\Sigma I$	0.0154
Refined on	F
R	0.0348
R_w	0.0266
S	1.0211
variables	267
Weighting scheme, w	$w = \frac{1}{\sigma^2(F)} = \frac{4F^2}{\sigma^2_{counting}(F^2)}$

Table 8.3 - Experimental data for **5**.

8.2 Results

Figure 8.3 shows the Laplacian distribution, $-\nabla^2\rho(\mathbf{r})$ in the plane of the phenyl ring. Figure 8.4 $-\nabla^2\rho(\mathbf{r})$ in the plane of the acetylenic carbon atoms C(10) and C(10A), and O(1) while Figure 8.5 shows

shows the molecular graph (the network of bond paths) in the mean-plane of the molecule. Finally, Figure 8.6 shows $-\nabla^2\rho(\mathbf{r})$ in the plane of the intermolecular carboxylic acid hydrogen bond dimer. Table 8.4 shows the bond lengths, $\rho(\mathbf{r})$, $-\nabla^2\rho(\mathbf{r})$ and ellipticity (ϵ) at the bond critical points for all covalent bonds, while Table 8.5 contains these properties for the hydrogen bond and the intramolecular interactions of interest.

Bond	Length(Å)	$\rho(\mathbf{r}_b)$(eÅ^{-3})	$\nabla^2\rho(\mathbf{r}_b)$(eÅ^{-5})	ε
C(1)-C(2)	1.414(2)	2.52(5)	-29.5(1)	0.25
C(2)-C(3)	1.404(2)	2.51(5)	-29.2(1)	0.28
C(3)-C(4)	1.390(2)	2.51(5)	-27.8(1)	0.29
C(4)-C(5)	1.393(2)	2.55(6)	-29.0(1)	0.24
C(5)-C(6)	1.391(2)	2.57(5)	-31.2(1)	0.21
C(6)-C(1)	1.398(2)	2.51(5)	-29.0(1)	0.26
C(2)-C(10)	1.427(2)	2.21(4)	-21.4(1)	0.14
C(10)-C(10A)	1.214(2)	3.19(6)	-34.8(2)	0.01
C(1)-C(7)	1.484(2)	2.29(5)	-25.3(1)	0.22
C(7)-O(1)	1.227(2)	3.15(8)	-35.4(5)	0.24
C(7)-O(2)	1.319(2)	2.46(7)	-26.1(4)	0.23
O(2)-H(7)	0.95(-)	2.29(6)	-37.7(4)	0.04

Table 8.4 - Electronic Properties at $\rho(\mathbf{r}_b)$ for Covalent Bonds.

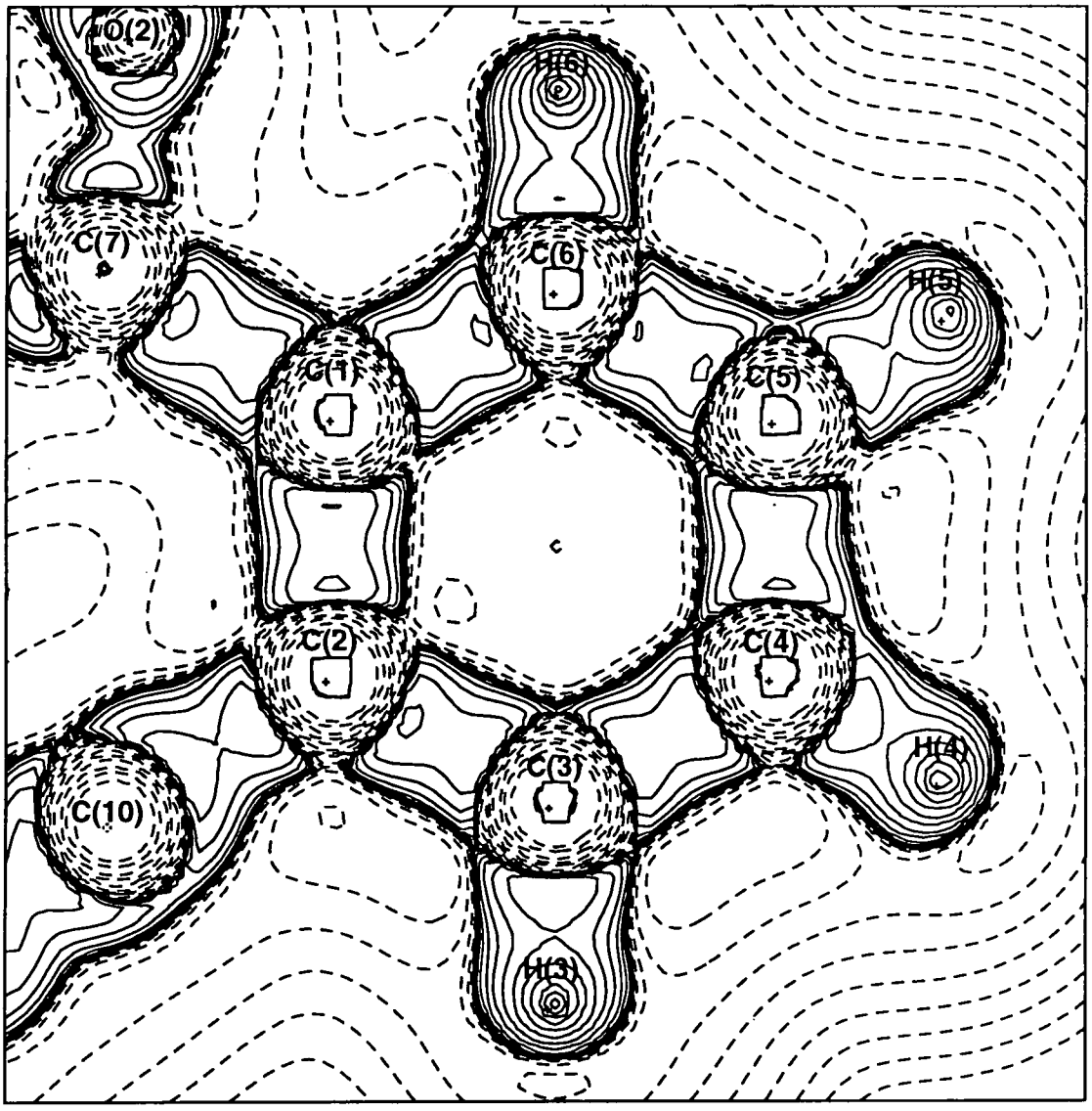

Figure 8.3 - $\nabla^2\rho(\mathbf{r})$ in the plane of the benzene ring.

8.3 Discussion

The internal agreement of the carbon-carbon bonds within the phenyl ring by inspection of Figure 8.3 and Table 8.4 is excellent, especially given that no constraints on the multipole parameters were applied for these atoms. A relatively high value for $\rho(\mathbf{r}_b)$ coupled with negative $-\nabla^2\rho(\mathbf{r}_b)$ values at the bond critical points indicates strong covalent bonds as expected. The ellipticity, defined as one minus the ratio of the two negative Hessian eigenvalues of the density at the critical point gives a good indication of π-bonding in systems such as these, given the proviso that the π-density is accumulated only in one plane. The range in the aromatic bonds, ϵ=0.21-0.29 is entirely consistent with the theoretically calculated value of 0.23 quoted for benzene[92].

Basic electron delocalization considerations suggest that the formally single C(2)-C(10) bond would have a bond order greater than 1, and the ellipticity of 0.14 concurs with this expectation. Interestingly, the C(1)-C(7) bond has ϵ=0.22 which is comparable to the fully aromatic bonds and suggests higher delocalization of the π-system than expected. The triple bond C(10)-C(10A)

has effectively zero ellipticity within experimental error indicating equal π-bonding in the two perpendicular planes parallel to and containing the bond. This bond has the largest value for the density at the critical point, along with greater diffuseness of the charge density in the bond as shown by Figure 8.4.

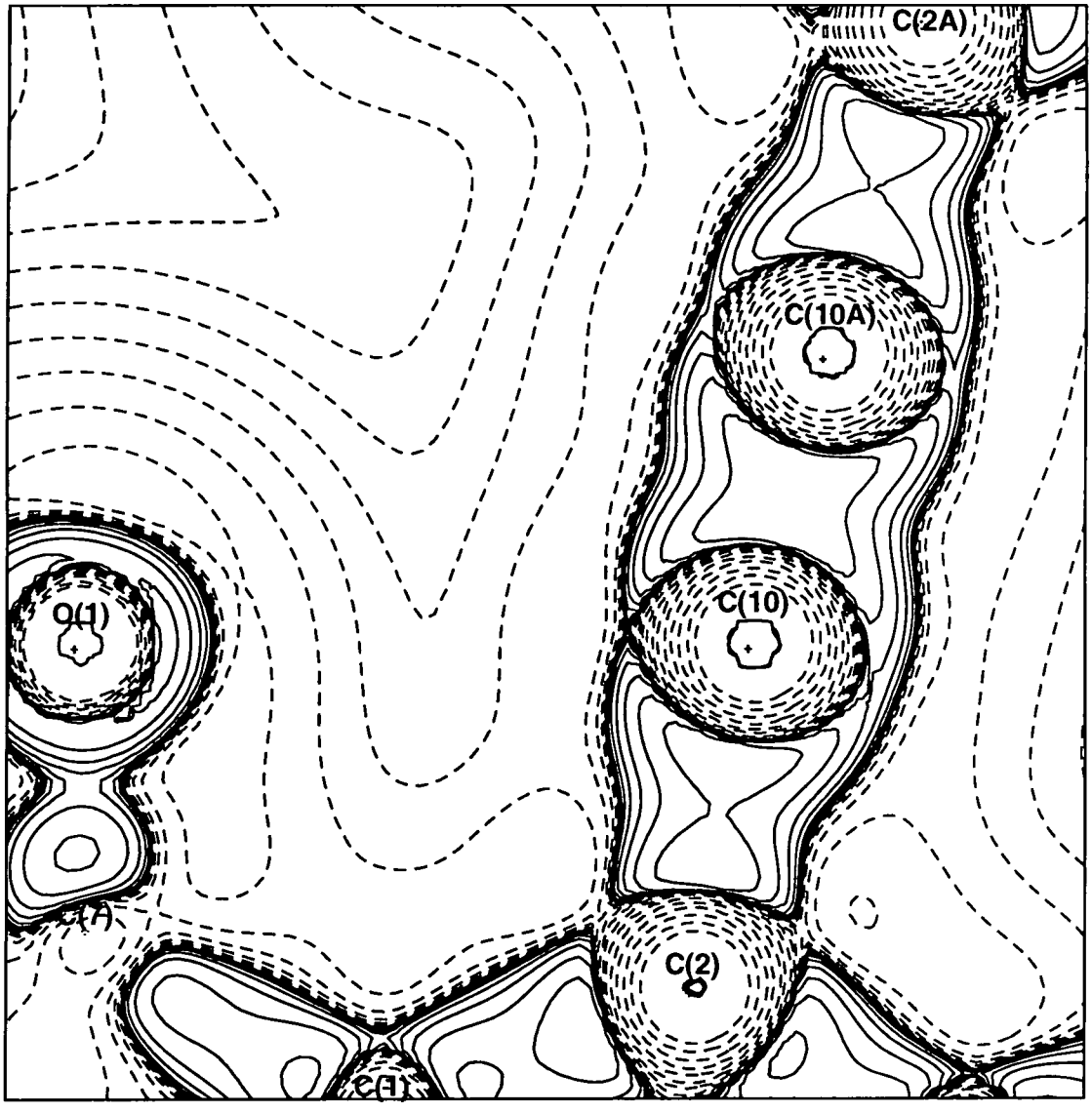

Figure 8.4 - $\nabla^2\rho(\mathbf{r})$ in the plane of the weak interaction.

The above observations, being in accord with chemical expectation, heighten our confidence in the results, however it is the much weaker O(1)-C(10) interaction which is the prime interest of this study. A conventional assignment of bonds in this molecule would not place a bond between these two atoms, however the evidence for the existence of some sort of interaction is twofold; the O(1)-C(10) distance is short at 2.774(2)Å, and the triple bond is non-linear by $5.9(1)^0$. According to AIM, if these two atoms are directly interacting, a bond path and associated bond critical point should exist, linking the two nuclei. The experimentally determined charge density does indeed posses a bond path between the two nuclei, and the bond critical point has the expected characteristics of a weak, closed-shell interaction: the value of $\rho(\mathbf{r}_b)$ is a mere $0.06(1)\text{eÅ}^{-3}$, while

$\nabla^2\rho(\mathbf{r}_b)$ is small and positive. The Laplacian field in the plane of O(1), C(10) and C(10A) is shown in Figure 8.4, while the molecular graph of bond paths for the molecule is shown in Figure 8.5.

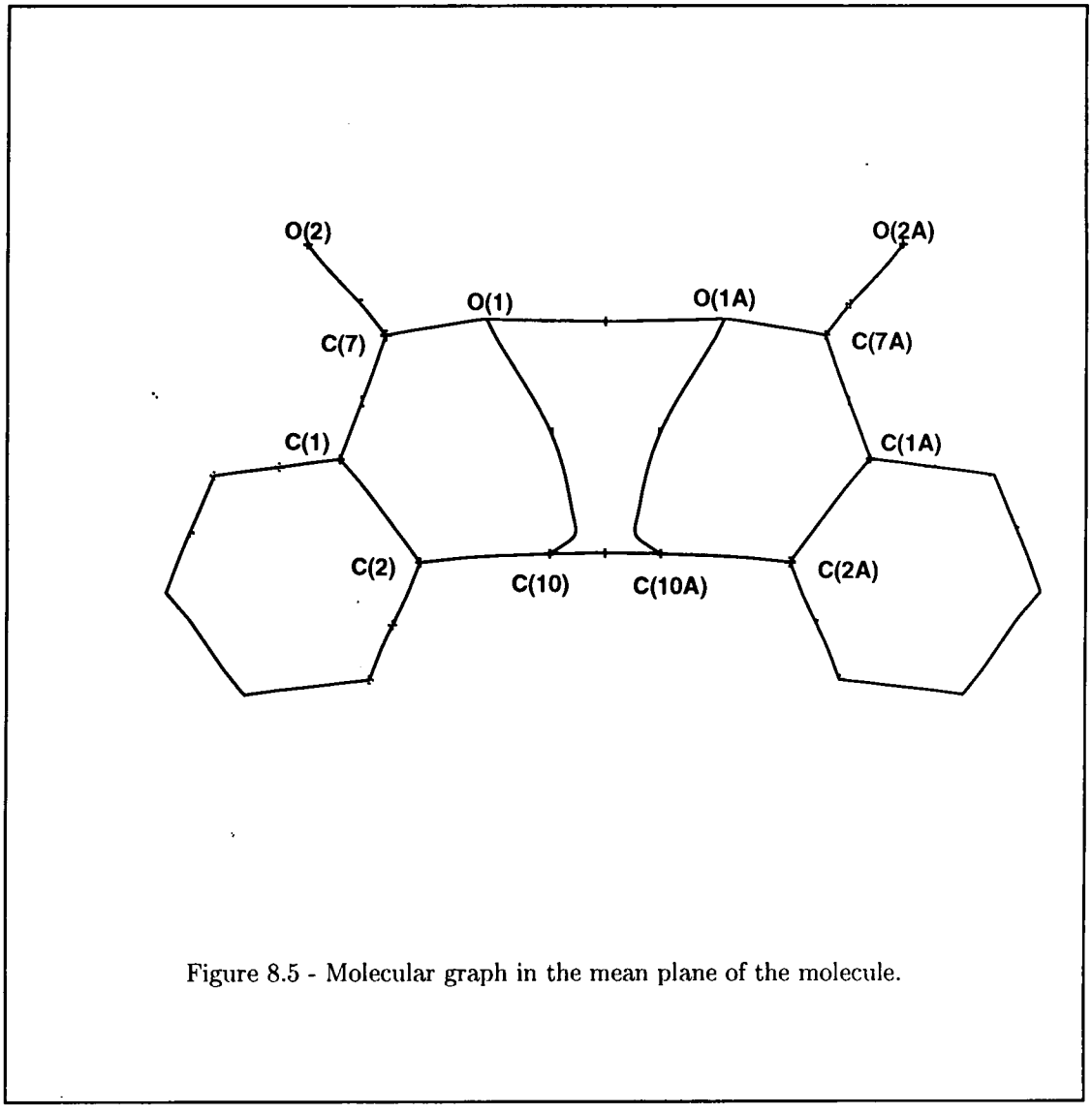

Figure 8.5 - Molecular graph in the mean plane of the molecule.

Bond	Length(Å)	$\rho(\mathbf{r}_b)$(eÅ^{-3})	$\nabla^2\rho(\mathbf{r}_b)$(eÅ^{-5})	ε
H(7)-O(1′)	1.671(-)	0.39(3)	4.50(3)	0.04
O(1)-C(10)	2.774(2)	0.06(1)	1.06(1)	0.11
O(1)-O(1A)	3.125(2)	0.03(1)	0.46(1)	0.05

Table 8.5 - Electronic Properties at $\mathbf{r}_b$ for Weak Interactions.

A local concentration of charge on O(1) associated with a lone-pair is observed to point almost exactly at a small hole, and hence positive Laplacian, in the Valence Shell Charge Concentration (VSCC) of C(10). This arrangement of a (3,-3) CP in $\nabla^2\rho(\mathbf{r})$ of O(1) with a (3,+1) CP in $\nabla^2\rho(\mathbf{r})$ of C(10) mirrors the situation found by Tsireslon *et al*[113] for the intermolecular

interactions of chlorine molecules in the solid. In fact, this alignment of negative Laplacian and hence local concentration of charge on the nucleophilic atom and positive Laplacian hence local depletion of charge on the electrophile is generally found along the reaction coordinate for Lewis acid/base reactions. Under certain circumstances, **5** undergoes intramolecular cyclisation to give the corresponding lactone presumably by nucleophilic attack of O(1) on C(10).

With regard to the fundamental reason why the close approach of O to C in these molecules is attractive, we turn to the Laplacian, $\nabla^2\rho(\mathbf{r})$ to examine the inherent chemical reactivity of these molecules. Such an analysis is founded in the occurrence of the Laplacian function in the expression for the local virial;

$$(\frac{\hbar^2}{4m})\nabla^2\rho(\mathbf{r}) = 2G(\mathbf{r}) + V(\mathbf{r}) \tag{8.1}$$

where $G(r)$ and $V(r)$ are the electronic kinetic and electronic potential energies respectively. While the integral of the Laplacian over a whole molecule is zero

$$(\frac{\hbar^2}{4m})\int \nabla^2\rho(\mathbf{r})d\tau = 0 \tag{8.2}$$

such that

$$\int 2G(\mathbf{r})d\tau = -\int V(\mathbf{r})d\tau \tag{8.3}$$

in accord with the virial theorem, such a situation need not occur locally, and hence the value of the Laplacian is determined by the local dominance of one or other of the energy densities relative to their virial ratio. Where potential energy locally dominates, there exists a volume in space of local concentration of charge and hence negative Laplacian. Such volumes are known to behave in a nucleophilic manner. Similarly, positive Laplacian is indicative of electrophilic behaviour. The Laplacian map in the region of the O···C interaction for the *trans* form of **5** shown in Figure 8.5 shows that the attacking oxygen atom, O(1) lines up a lone-pair region with the local depletion of charge on the attacked carbon atom C(10). It is proposed that the consequence is that since the expression for the Laplacian contains the full quantum potential and not merely the classical electrostatic part, we may have a net attractive interaction between these two regions of charge, *i.e.* the region of positive Laplacian on C(10) applies an attractive force on the charge density possessing negative Laplacian in the general vicinity, and particularly the charge density of the lone-pair on O(1).

On checking the molecular geometry, it was noticed that O(1) and O(1A) are in relatively close contact, with internuclear separation of 3.125(2)Å. Once again, despite the very low level of electron density in this region, the experimental technique has detected a bond path and bond CP here with the properties given in Table 8.5. The geometric distortions from planarity of this molecule are consistent with repulsion between the two oxygen atoms, and we assume the bond path to be representative of either a steric or electrostatically unfavourable interaction.

As mentioned in the introduction, an interesting observation regarding this molecule is that the crystal structure displays a *cis* arrangement of carboxylic acid groups about the triple bond despite the steric repulsion between the two oxygen atoms which could be relieved on going to the *trans* conformation. It has been proposed[139] that the *cis* conformation is more stable than

the *trans* because strong repulsion occurs between an incipient *trans* lone-pair on the second acetylenic carbon atom and the second approaching oxygen atom. This is proposed to be of sufficient magnitude to force the molecule into the *cis* conformation despite the fact that this geometry places O(1) and O(1A) close together, sufficiently close for a bond path between the atoms to appear in what appears to be a repulsive interaction. An alternative explanation for the *cis* arrangement about the triple bond is that this geometry allows strong hydrogen bonding *via* head to head pairing of the carboxylic acid groups. It is possible that the additional energy stabilization of these hydrogen bonds is sufficient to override the less favourable conformation.

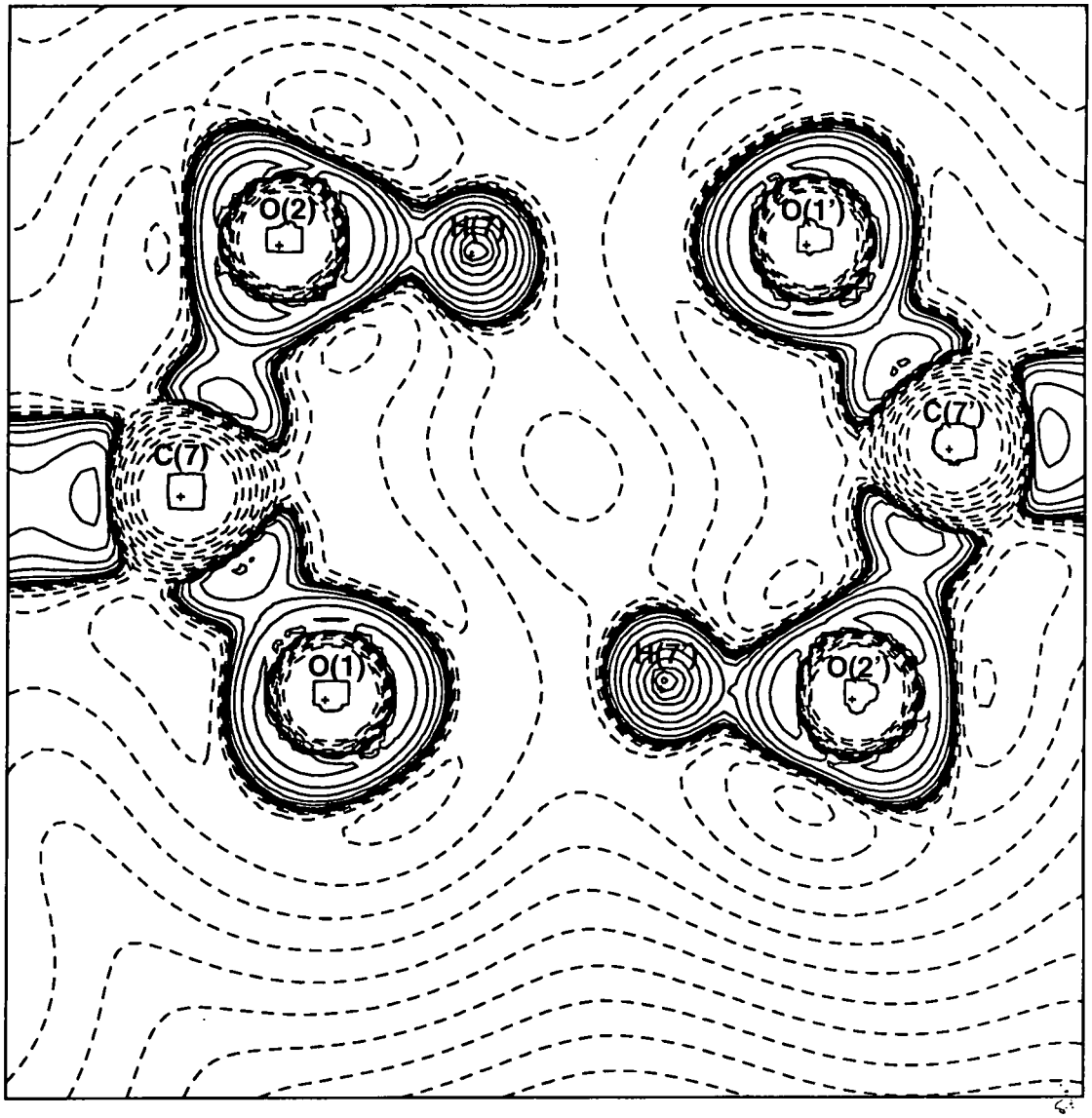

Figure 8.6 - $\nabla^2\rho(\mathbf{r})$ in the plane of the carboxylic acid dimer.

Although we cannot determine the energy of the hydrogen bonds from the experimental charge density, we can obtain a relative idea of how favourable such interactions are by ascertaining from the Laplacian distribution how well the various atoms are aligned, with particular emphasis on the lone-pair properties of the oxygen atoms. Figure 8.6. shows this distribution in the plane of the carboxylic acid dimer.

It is immediately obvious that the lone-pairs in the O(1) and O(1A) atoms are almost exactly aligned with the hydrogen atoms. Indeed, a more favourable arrangement of electron density would be difficult to conceive. Table 8.5 shows that, as expected, the O(2)-H(7) bond is covalent since $\nabla^2\rho(\mathbf{r}_b)$ is negative, while H(7)-O(1′) is ionic with positive Laplacian. This is the usual situation encountered in topological studies of conventional hydrogen bonds[152]. In the solid state, every molecule has a half share in two of these head to head interactions and it is therefore likely that these interactions lower the overall energy to overcome the intramolecular steric repulsion of the O(1) and O(1A) atoms.

8.4 Conclusion

In this work we have attempted to locate and classify weak interactions by the method of topological analysis. This analysis has been performed on a charge density determined from high-resolution X-ray diffraction data. We find topological bond paths which indicate weak interactions between a carbonyl oxygen atom and an acetylenic carbon atom in a manner analogous to that found in the previous study of the theoretically derived charge density. We have also located a weak interaction between two sterically crowded carbonyl oxygen atoms. We believe this to be the first experimental observation of topological bond-paths for weak intramolecular interactions.

This work demonstrates that the technique of high-resolution X-ray diffraction can be sensitive enough to locate and classify interactions which are much weaker even than hydrogen bonds. Additionally, the technique has provided information on the molecule in the crystalline environment, especially with respect to hydrogen bonding to neighbouring molecules. This information is not directly obtainable from *ab-initio* quantum chemical calculations performed on isolated, gas-phase molecules.

Multipole populations and local coordinate systems *etc.* are available in Appendix D.

8.5 Acknowledgements

I thank Dr. J.D. Wallis of the University of Kent at Canterbury for providing both the crystalline sample used in this analysis and the unpublished structural parameters for molecule **8**. The help of Dr. C.W. Lehmann during data collection is appreciated.

Chapter 9

The Maximum Entropy Method

9.1 Introduction

The preceding analyses have all implicitly assumed that performing a least-squares fit to a structural model is the best way to extract experimental information from the data. There is an alternative which goes under the intriguing name of maximum entropy. Although maximum entropy theory[153] has been around for a *long* time, practical application to important physical problems is only now becoming apparent in the literature. The areas of application are still few, but the generality of the method is indicated by the very diversity of these areas which includes signal processing in optical and radioastronomy, seismic exploration, magnetic resonance imaging, plasma physics and, of course, crystallography. The common point is that the data is noisy and incomplete and usually in one space while the desired result is in another space and while an analytical expression usually exists to perform the transformation, it is only truly valid for noiseless and complete data. In the case of crystallography, the data are in reciprocal space and the mathematical device of Fourier transformation allows visualization of the electron density in direct space. The data are certainly incomplete since they will only have been measured up to a certain resolution in $sin\theta/\lambda$ and they will also be contaminated by experimental noise. Assuming completely known phases, performing a Fourier synthesis on such a data set will provide a density which is noisy and suffers from series termination errors which manifest themselves as the so-called Fourier ripples due to the incomplete nature of the data.

This is probably not the context that most crystallographers have heard of "maximum entropy" within crystallography. So far the major impact of the method within this area of science has been in structure solution *i.e.* as an extension to direct methods[154] for gaining phase information on structure factors from their magnitudes. It should be emphasised that this type of implementation, pioneered by Gerard Bricogne, has been as an extension to direct methods for the express purpose of structure solution. However, for electron density studies structure solution at the level of atomic resolution is generally treated as a preliminary task. What we require is some way to get more from the data again. Fourier synthesis and model fitting are the two commonly used but the maximum entropy method is another possibility. The current implementation of this method in charge density research is *via* the Single Pixel Approximation[155]. In some ways it is rather crude and should be treated as the starting point in using this powerful technique in charge density research rather than the finished article. This is a new and promising

area and attention should be turned to improving the method. Hopefully it will have as big an impact in accurate charge density analysis at some point in the future as it has in other areas of science.

9.2 General Data Processing Philosophy

Any experiment defines data points in data space, in our case structure factor magnitudes $|F_{obs}(\mathbf{H})|$. The reality of the situation is described in direct or $\mathbf{r}$ space as the electron density, $\rho(\mathbf{r})$. It us usually possible, at least for centrosymmetric structures, to determine almost all of the structure factor phases, and hence when coupled to their observed magnitudes we have the complete structure factor, $F_{obs}(\mathbf{H})$. We may think of data processing as determining N numbers describing $\rho(\mathbf{r})$from K observations. K is obviously finite whereas N may be finite or infinite, depending upon our point of view. In our situation, K is the number of structure factors and N is a description of the electron density of the crystal in real space. N therefore is certainly large and possibly tends to infinity since since an infinite number of functional parameters are required to completely describe the density perfectly. We have a situation where $N > K$ and hence insufficient data is available to fully describe the situation. The problem is underdetermined. There are several methods commonly employed to try to overcome the problem:

9.2.1 Model Fitting

The complicated functional form of the smeared electron density may be described by a model. This may be a spherical atom model supplemented by isotropic temperature factors or it may be a complicated multipole expansion supplemented by anisotropic temperature factors. If we believe that the model exactly and concisely describes the true situation then the problem is now one of parameter fitting and N was less than K from the start. If we are not sure whether the model is sufficient or not then the model produced by fitting is just one of a multitude of conclusion which fits the data. We don't know whether this model is typical or not or whether an analysis will highlight those factors resulting from the data or from the model. While we may think that the multipole model is reasonably sound, it is not a fully sufficient description of all possible features in the charge density.

9.2.2 Invent More Data

The linear transformation of Fourier synthesis comes into this category because while the Fourier coefficients are known up to the cut-off level, the method of Fourier Inversion formulates the electron density by making all the higher coefficients zero. The direct method of going from reciprocal space to real space is only valid for a full set of noiseless Fourier coefficients which we never have. The error introduced is due to the assignment of zero to the higher coefficients. The assignment of zero for the higher resolution fourier coefficients effectively moves the problem from a $N > K$ situation to a $N = K$ one, however the addition of the zero coefficients obviously does nothing to improve the result. While most people are aware of this effect, they still ignore it to an extent by computing deformation densities. These are Fourier series where the coefficients

are those from the experiment minus those which would result from spherical atoms placed at the atomic positions. The error now is that the difference of the higher coefficients is now supposed zero. It presents itself as halos about the nuclear positions in the valence region, exactly the volume of greatest interest in charge density studies.

9.2.3 Non-linear Transformation

The third method, and the one that this chapter deals with is to perform a non-linear transformation from reciprocal to real space. The restoration of the charge density from noisy and incomplete structure factors is only one member of the general class of problems of restoring an image in real space from incomplete and noisy data points in some other space[156]. The description of the structure factor set as often as a "band-limited" function, meaning that knowledge of them is only available within a certain band of resolution. Any non-linear transformation is one which will produce a map in real space which gives non-zero calculated Fourier components for scattering vectors (**H**) outwith the limited band used as the initial source of data and hence an element of "superresolution" occurs. This obviously involves more information being applied to the problem since we may not expect to improve our result without the application of more data. For the case of the electron density, one obvious piece of information is that the density must be everywhere positive. This is not a result guaranteed by Fourier Inversion. We have stated that we are dealing with a problem with $N > K$, and while the additional information provided by positivity will help reduce this deficit, it will not do so to the extent of providing a unique solution and the problem will remain ill-conditioned. There will be a large set of positive electron density maps which fit the data, and choosing between them and deciding which is the "best" one requires yet further discriminatory powers.

9.3 Regularizing Functions

The approach taken in producing a map which fits the data, and is also unique by some other criterion is that we introduce a function of the data in reciprocal space which measures agreement of the map to the data, then from all maps which agree with the data by this measure, introduce a regularizing function in real space to discriminate between the maps. This is therefore a minimization with constraints procedure. If we call the two functions A and B, one obvious choice for A is the chi-square function of least-squares analysis

$$A = \chi^2 = \sum_{\mathbf{H}} \frac{1}{\sigma_{\mathbf{H}}^2} ||F_o(\mathbf{H})| - |F_c(\mathbf{H})||^2 \tag{9.1}$$

B is some regularizing or smoothing function of the density in real space. Nityananda and Narayan[157] have taken a pragmatic view on the choice of B. Their candidates for the smoothing function include $\rho(\mathbf{r})^{3/2}$, $\rho(\mathbf{r})^{1/2}$, $ln\rho(\mathbf{r})$, $-\rho(\mathbf{r})ln\rho(\mathbf{r})$.

The constrained minimization is performed using the Lagrange Multiplier technique, minimizing $A + \lambda B$.

In the absence of B we just revert to the ill-conditioned least-squares case with $N > K$. What makes the method tractable is that B encodes more information. B is in real space and the

only criteria which rigorously restrict the charge density in real space are the N-representability criteria. These state that any quantum mechanically acceptable one-particle charge density must integrate to the correct number of electrons

$$\int \rho(\mathbf{r})d\mathbf{r} = N \tag{9.2}$$

where N is the number of electrons and that it must be everywhere positive

$$\rho(\mathbf{r}) \geq 0 \tag{9.3}$$

All of the candidates proposed above as regularizing functionals meet the everywhere positive criteria and an additional Lagrange multiplier may easily be incorporated to ensure correct normalization. Hence, this approach is potentially superior to the multipole projection method since it ensures an N-representable density.

9.3.1 Choice of B

Two particular choices of the regularizing functional are most common. The former is the "Burg" entropy

$$\int ln\rho(\mathbf{r})d\mathbf{r} \tag{9.4}$$

This form of entropy is suited to astronomical reconstructions because of its tendency to produce a flat background and sharp, Lorentzian peaks, which are representative of point sources such as stars. The second form is the Shannon entropy[153]

$$-\int \rho(\mathbf{r})ln\rho(\mathbf{r})d\mathbf{r} \tag{9.5}$$

which has a greater tendency towards producing gaussian peaks. The form of both entropy functions lead to a flat background[158], and indeed both have local extremum for a flat, continuous distribution. In the absence of any useful data, the method will default to the most uninformative map.

9.3.2 Preliminary Applications

One of the first applications of the maximum entropy method was by Gull and Daniell to radio-astronomical data[159]. Using normalized data, they maximized the function

$$Q(\lambda) = \sum_j m_j lnm_j - \frac{\lambda}{2}\sum |M_k - E_k|^2/\sigma^2 \tag{9.6}$$

where M_k and E_k are observed and calculated data points respectively. The map is defined by digitizing it on a j by j grid, with m_j representing the occupancy of the jth pixel. The assumed that the errors on the data were Gaussian, and hence used the Lagrange multipler to constrain χ^2 equal to the number of data, while maximizing the entropy. The results for these radio-astronomical reconstructions were promising. The incorporation of the data by means of the χ^2 function leads to this general method being called "least-squares MEM".

The next stage in development of the method in this context was given by Bryan and Skilling[160]. Using a similar formulation, with each data point being the intensity of a pixel of a

digitized photograph, they consider the distribution of the residuals obtained by the method. A serious difficulty becomes apparent at this point. The largest residuals (observed minus calculated pixel intensities) are for those pixels at the positions of peaks in the photograph. This is not unexpected, although it is certainly undesirable. The entropy expression is trying to give the flattest map possible, and penalizes large peaks in the map. Setting the desired chi-square value equal to the number of data points gives a common pool of mis-fit to be distributed about the data points, but does not constrain the distribution of this mis-fit. Close fit to data with high values is heavily penalized by the entropy functions since it would incorporate a large degree of structure into the map and consequently these data are are heavily mis-fitted. Most of the chi-square value is used by a small number of data and hence the majority of points which have small intensity are over-fitted.

The authors go on and suggest an improved formulation where the data are incorporated in a way which ensures a Gaussian distribution of residuals. If the residuals n_i from an initial step are ordered

$$n_1 < n_2 < \cdots < n_N \tag{9.7}$$

the ith sorted residual v_i should have the value

$$v_i = \Phi^{-1}(\frac{i-1/2}{N}) \tag{9.8}$$

where Φ is the cumulative normal probability

$$\Phi(x) = (2\pi)^{-1/2} \int_{-\inf}^{x} exp(-1/2u^2)du \tag{9.9}$$

The distance measure E between the observed and expected residuals is introduced

$$E = (\sum_{i=1}^{N}(n_i - v_i)^2)^{1/2} \tag{9.10}$$

The expected vale of this function is shown to be $< E > \sim (\ln N)^{1/2}$. This new function in place of χ^2 obviously gives a Gaussian distribution of residuals and greatly reduces but does not eliminate the positive residuals at the peaks, which are believed to be inherent in any formulation of the method. The same authors subsequently publish algorithms for efficiently performing the optimization procedures[161].

9.3.3 Crystallographic Applications

Several authors introduce maximum entropy ideas into the crystallographic problem in the mid 1980's. The most well-known is the work of Bricogne[154] for phasing structure amplitudes from first principles. Livesey and Skilling[162] provide the relevant equations but no real applications. It falls to Steven Wilkins in a series of papers entitled "Statistical Geometry" to work through the theory of least-squares MEM to applications. The general theory as outlined above is developed in the first paper[153], while a numerical procedure for evaluation of the maximum entropy electron density is subsequently provided[163], called the singel pixel equation, so named because of the digitization of the unit cell, and the definition of the entropy in terms of the values of the individual pixels. At this point in the development in the theory, reference is made to the work

of Jaynes[164] on the entropy expression. Without recourse to either Bayesian or Information Theoretic arguments at this stage, Jaynes states that while the entropy on a discreet probability distribution is

$$S = \sum_i p_i ln p_i \tag{9.11}$$

the seemingly obvious generalization to a continuous distribution of

$$S = \int \rho(\mathbf{r}) ln \rho(\mathbf{r}) d\mathbf{r} \tag{9.12}$$

is not in fact correct. The correct entropy expression according to Jaynes is

$$S = \int \rho(\mathbf{r}) ln \frac{\rho(\mathbf{r})}{\tau(\mathbf{r})} d\mathbf{r} \tag{9.13}$$

where $\tau(\mathbf{r})$ is some other electron density function and S is a relative entropy of $\rho(\mathbf{r})$ with respect to $\tau(\mathbf{r})$. The application of the single pixel equation is to partially phased structure factors measured from the small protein α-lactalbumin[165,166], and the results are described as "encouraging". No mention is made of the distribution of residuals.

An alternative way of tackling the distribution of residuals problem comes about by following direct method structure solution philosophy. The more common way of working in this side of crystallography has been to use the structure amplitudes directly to infer phase information and the emphasis is on reciprocal space. No model fitting occurs at this stage and as a consequence little attention is paid to the errors in the structure factor amplitudes. As a result the values of the amplitudes are used directly as "hard" constraints with no mis-fit allowed and hence no difficulties with poor distribution of residuals which are all zero. Navaza[167] formulates maximum entropy in this way, using a constraint equation and hence Lagrange multiplier for every data point. All phased data are incorporated using

$$C_{\mathbf{H}} = \frac{1}{V} \int \rho(\mathbf{r}) exp(i\mathbf{Hr}) d\mathbf{r} - F_{obs}(\mathbf{H}) \tag{9.14}$$

and the unphased data are incorporated using

$$C_{\mathbf{H}} = |\frac{1}{V} \int \rho(\mathbf{r}) exp(i\mathbf{Hr}) d\mathbf{r}| - |F_{obs}(\mathbf{H})| \tag{9.15}$$

while noise in the data is incorporated to a certain degree, a higher degree of Fourier extrapolation appears to occur. This is expected since peak heights in the final map will be higher than for least-squares MEM, and it is the higher frequency fourier components which are related to the peaks. While the N-representability criteria are the only fundamental characteristics of the density which must be displayed, the concept of atomicity is one which should prove to be powerful. Any realistic electron density in a crystallographic unit cell is expected to display peaks which integrate to the number of electrons in that atom. Navaza suggests introducing atomicity by using non-local functions of the density[168].

9.3.4 Charge Density Applications

The first applications of the maximum entropy method to accurate charge density determinations[169] were performed by the Nagoya group using their MEED program[170]. The first data set so analysed was the very accurate Pendellösung data for Silicon measured by Saka and Kato[171]. This

data must be considered a special case since it is not obtained by standard X-ray diffraction, but by a different technique which yields structure amplitudes with much smaller e.s.d.'s than usual. The algorithm used is the same one used in the novel research reported in the latter part of this thesis and it is hence worth elaborating on more fully. The basic formalism is the same as Wilkin's single pixel approximation described earlier.

The entropy is defined by the charge density relative to some previous density

$$S = -\int \rho'(\mathbf{r}) ln \frac{\rho'(\mathbf{r})}{\tau'(\mathbf{r})} d\mathbf{r} \tag{9.16}$$

The densities in the above equation are normalized to one by

$$\rho'(\mathbf{r}) = \rho(\mathbf{r}) / \int_{\mathbf{r}} \rho(\mathbf{r}) \tag{9.17}$$

$$\tau'(\mathbf{r}) = \tau(\mathbf{r}) / \int_{\mathbf{r}} \tau(\mathbf{r}) \tag{9.18}$$

For computational expediency, the integral is replaced by a sum over pixel values digitized on a regular grid

$$S = -\sum_i p_i ln \frac{p_i}{t_i} \tag{9.19}$$

and the χ^2 function is used as a constraint to incorporate the data

$$C_1 = \frac{1}{N} \sum_{\mathbf{H}} \frac{1}{\sigma^2_{\mathbf{H}}} ||F_{cal}(\mathbf{H})| - |F_{obs}(\mathbf{H})||^2 \tag{9.20}$$

Since N is the number of data, setting this constraint equal to one is equivalent to setting $\chi^2 = N$ and doing this while maximizing the entropy gives

$$Q(\lambda_1) = -\sum_i p_i ln \frac{p_i}{t_i} - (\lambda_1/2) C_1 \tag{9.21}$$

An extremum of Q is then required

$$\partial Q(\lambda_1)/\partial p_i = 0 \tag{9.22}$$

The solution is performed by an iterative method and the distribution taken as $\tau'(\mathbf{r})$ is the value of $\rho'(\mathbf{r})$ from the previous iteration.

The phases of the structure factors are easily evaluated since Silicon in the solid state has the same structure as diamond. The maximum entropy map of the charge density produced by this procedure for the Silicon data is of much higher quality than the Fourier synthesis. For Silicon there are only thirty measured structure factor amplitudes and the consequences of this for a Fourier synthesis in terms of series termination effects must be expected to be severe. While the maximum entropy map appears very good, there are peaks in the centre of the bonds, which are not expected. The distribution of residuals appears to be good, but this is due to the very low standard deviations on the experimental data. There is only a very small pool of mis-fit available to the method and therefore its is difficult for a few strong reflections to mis-fit badly. Further applications to Rutile[172], Ice[173] and Beryllium metal[174] have subsequently appeared.

Despite no mention of it being made by the Nagoya group, other workers had noticed the problem of severely non-random residual distribution. Using the MEED program to analyse γ-ray

diffraction data[175] from both MnF_2 and NiF_2, it was observed that a few very strong reflection used up the majority of the total residual allowed. It was later suggested that the intrinsically high dynamic range of the charge density function was the cause of the non-random residuals and that an exact fitting procedure for the data rather than the least-squares MEM would be more appropriate[176].

De Vries and coworkers have adopted an alternative procedure[177] which retains the chi-square function but uses a modified weighting scheme for the data. Upweighting the low angle reflections to improve their fit is appropriate and empirical tests on a hypothetical water crystal settled on the optimum weighting scheme of

$$w_{\mathbf{H}} = 1/|\mathbf{H}|^4 \tag{9.23}$$

to be used with

$$C_1 = \sum_{\mathbf{H}} w_{\mathbf{H}}(|F_{obs}(\mathbf{H})| - |F_{calc}(\mathbf{H})|^2/\sigma^2_{\mathbf{H}})) = N \tag{9.24}$$

This produces a closer residual distribution to that required, although it is still not perfect. Application of the modified weighting scheme to the Pendellösung data for Silicon makes little difference since the $\sigma_{\mathbf{H}}$ values are so small to begin with that very little mis-fit is allowed.

9.3.5 Non-uniform measures

More recent developments by De Vries[178] have involved using different measures in the relative entropy expression. The unexpected result of non-nuclear maxima at the mid-bond positions in crystalline Silicon are not substantiated by density functional calculations[179] and therefore their real occurrence must be questioned. Indeed, when structure factors were calculated from the theoretical density and processed with the standard MEM, non-nuclear maxima appeared, even though they were not in the known initial density. In place of a flat, normalized measure as $\tau(\mathbf{r})$ in the relative entropy expression, a structured measure would be a way of incorporating some a *priori* knowledge into the reconstruction, giving the method additional power. A good candidate is the theoretically determined charge density. When this is used with the standard weighting scheme, the non-random residual distribution remains, but the non-nuclear maxima in the bonds disappear and are therefore shown to be an artefact of the method and not physically real. The same procedure of using a calculated density as the measure in the relative entropy expression for Beryllium also removes the non-nuclear maxima.

Non-uniform measures have also been applied in the analysis of magnetic structure factors. Magnetic structure factors are obtained by diffraction of polarized neutrons from crystals containing unpaired electrons. The fourier synthesis of these magnetic structure factors yields the electron spin-density in an analogous manner to X-ray structure factors yielding the electron density. An alternative entropy expression has been proposed in the MEM analysis of magnetic data from a crystal containing the tetracyanoethylenide anion radical[180]

$$S = \int \rho(\mathbf{r}) - \tau(\mathbf{r}) - \rho(\mathbf{r}) ln \frac{\rho(\mathbf{r})}{\tau(\mathbf{r})} d\mathbf{r} \tag{9.25}$$

This new entropy expression acts to reduce the discprepancy between the current density and the measure. Excellent looking maps are produced by using the experimental data and a local spin density calculated measure.

9.3.6 Deformation densities

Since the maximum entropy method suppresses peaks, it automatically discriminates against functions with high dynamic range. Unfortunately the electron density is such a function with very high peaks, while the valence features of most interest are at a much lower value. If an alternative function of the density can be used with lower dynamic range, a more realistic reconstruction should ensue. Use of the deformation density in the MEM has recently been attempted[181]. An immediate problem with this approach is that the deformation is not everywhere positive, and in fact should have equal integrated positive and negative volumes. The standard entropy expression is undefined for a deformation density so an alternative, "two-channel" approach was developed. The deformation density in real space is defined as

$$\Delta\rho(\mathbf{r}) = \rho(\mathbf{r}) - \rho_{sph}(\mathbf{r}) = \rho^{+}(\mathbf{r}) - \rho^{-}(\mathbf{r}) \tag{9.26}$$

With $\rho^{+}(\mathbf{r})$ and $\rho^{-}(\mathbf{r})$ being the positive and negative deformation densities respectively.

Assuming known atomic positions and temperature factors, the structure factors from neutral, spherical atoms with these parameters can be calculated and subtracted from the experimental structure amplitudes to give "deformation structure factors"

$$\Delta F(\mathbf{H}) = F_{obs}(\mathbf{H}) - F_{sph}(\mathbf{H}) \tag{9.27}$$

to be used with

$$S(\Delta\rho(\mathbf{r})) = \int \rho^{+}(\mathbf{r}) ln\frac{\rho^{+}(\mathbf{r})}{\tau^{+}(\mathbf{r})} + \rho^{-}(\mathbf{r}) ln\frac{\rho^{-}(\mathbf{r})}{\tau^{-}(\mathbf{r})} \tag{9.28}$$

which quantifies the entropy of the deformation density. Both flat and structured measures were used in this work. While the results are undoubtedly better than those produced by the single channel reproduction of the total density, it is stated that the best maps produced are not really competitive with those from the least-squares fit of the multipole model.

9.3.7 Impressions from existing applications

The overall conclusion is that maximum entropy maps produced from small data sets of very limited resolution are better than the corresponding Fourier synthesis, primarily because of the ripple suppression which occurs by Fourier extrapolation by the non-linearity of the method. Such small data sets could not be used in least-squares fit to the multipole model and hence the MEM probably represents the best that may be obtained. Unfortunately some of the finer details in the maps such as the non-nuclear maxima found for Silicon and Beryllium are merely artefacts of the method. The extension to non-uniform measures in the relative entropy expression certainly improves the results, as does reconstructing the deformation density with its reduced dynamic range. For powder diffraction data sets, or polarized neutron data sets, the method is well worth applying but for high quality, high resolution diffraction data it is difficult to conceive of a case where the MEM provides better results than the multipole model. In addition it merely gives a representation of the dynamically smeared charge density, with no means of thermal deconvolution to give the static charge density available.

9.4 Information Theory and Bayesian Inference

The preceding exposition of the application of maximum entropy techniques to the problem of image reconstruction from incomplete data has taken the pragmatic approach of static the entropy function merely as some smoothing function. There is a more fundamental reason for using maximum entropy, which is as an information measure within a Bayesian framework for statistical inference. An informative account of justifications of maximum entropy within this context is available[182].

Bayes' Theorem requires that we choose a prior probability assignment, chosen by using a probabilistic argument known as the maximum entropy criterion. It is a theorem of probability and is therefore only applicable to situations where a probability distribution is required. Fortunately the Born interpretation of the wavefunction states that the square of the wavefunction subsequently integrated over all particle coordinates bar one is the probability of finding an electron in some volume of space $d\tau$ and hence maximum entropy can be applied.

9.5 Bayes' Theorem

Bayes' Theorem may be stated as

P(conclusion|new data) $\propto$ P(conclusions|old data) $\times$ P(new data|conclusions)
where P(A|B) means the probability that A is true given that B is true. In our specific case

P(map|new data) $\propto$ P(map|old data) $\times$ P(new data|map)

Bayes' Theorem can therefore be re-stated as "the probability that the density map is true is proportional to the probability of the map given the old data times the probability that the new data is produced given the true map."

This takes a bit of thinking about but does intuitively make sense. The P(map|old data) part is called the *prior*. In cases where the data is strong and plentiful, its actual properties are pretty insignificant because the second term on the RHS of Bayes' equation swamps it and any reasonable prior can be used. It can usually be assigned on a combination of theoretical grounds. In our case, we want a density map which is everywhere positive and whose integral over the space which it describes is equal to some value, usually the integral over the unit cell being equal to the number of electrons in that unit cell.

The P(new data|map) part is the probability that the new data is produced given the true map. It is called the *likelihood*. We don't need to know the true map to calculate this, just a knowledge of the characteristics of the apparatus. For example, we might know that for any map, the data produced will have a Gaussian distribution of errors. For good data with small σ values this term of the Bayes' equation overrides the prior and so choice of prior is insignificant.

The problem occurs when the data is not so good and the prior now has a significant effect on the P(map|new data). If we wish to invoke Bayes' Theorem we need some way to define the prior.

9.5.1 Entropy Maximization

There are many arguments invoked when justifying maximum entropy philosophy. One of the easiest to grasp is the monkey argument[183]. Imagine that we can divide up our function in real space into cells of width Δx. This is the process of digitization. Although it is an approximation, if the size of the cells is much smaller than the experimental resolution, there isn't really any approximation introduced in terms of the effect it will have on the result. Now let the intensity in the cells be quantized such that cell i has intensity $f_i = n_i\delta$. Again let the quanta δ be so small that no effective approximation is invoked. The image of the electron density can be represented such that $f(x) = n_1, n_2, \ldots n_{pix}$ where n_{pix} is the number of pixels. If the monkeys now throw balls into the boxes, such that there is a box representing each pixel, the random nature of the assignment of balls to boxes means that the probability of gaining some picture $f(x)$ *via* $n_1, n_2, \ldots, n_{pix}$ is

$$2^{-M}\frac{M!}{n_1!n_2!\ldots} \tag{9.29}$$

where M is the number of balla given to the monkeys at the start. Since both M and the n_i are large Stirling's approximation can be invoked to give

$$P(f_1, f_2, \ldots) \propto exp(\alpha S) \tag{9.30}$$

where

$$S = -\sum_i f_i ln\frac{f_i}{b} \tag{9.31}$$

If we forget about α and b for the moment and just say that they are constants, we can define S as the entropy of the function $f(x)$. This functional form for the entropy was first introduced into information theory by Shannon[153] during his investigations into sending signals down a telephone wire. In the above justification, maximizing the entropy will produce the map $f(x)$ which is most probable since the monkey process is random and the map with maximized entropy can come about in the greatest number of ways since the order of the balls entering the boxes does not change the final outcome. There are also other, probably more convincing arguments for choosing the maximum entropy distribution for the prior. Shannon initially used the entropy as a measure of how much information was incorporated in a probability distribution. The maximum entropy distribution is the one with the least information; it is the flattest map from those possible. This reasoning is intuitively more appealing. The prior should be derived from the data we have. Since it is derived before any measured data are admitted, it makes sense to choose the prior which embodies the least information.

We have thus defined our prior in Bayes formula. It remains to define the probability that the data will be observed given the map. If we assume for simplicity that the experiment is linear and introduces Gaussian errors on the data points,

$$P(data|map) = R\rho + \sigma n \tag{9.32}$$

in other words the distribution of data points is the response of the system R times the map producing that data plus a random number coming from the normal distribution n times the

standard deviation of the data point. The probability for any value of n is

$$P(n) = \frac{1}{\sqrt{2\pi}} exp(-n^2/2) \tag{9.33}$$

If we have N data points

$$P(data|map) = \prod \frac{1}{\sqrt{2\pi\sigma^2}} exp(-1/2\chi^2) \tag{9.34}$$

By Bayes' Theorem

$$P(map|newdata) \propto exp(\alpha S - 1/2\chi^2) \tag{9.35}$$

where χ^2 is the usual mis-fit statistic

$$\chi^2 = \sum_{\mathbf{S}} \frac{1}{\sigma^2} (|F(\mathbf{S})_c| - |F(\mathbf{S})_o|)^2 \tag{9.36}$$

We want to choose one map from the space of all maps with the highest probability of coming from the data. To do this we maximize P(map|new data). This is the same as maximizing $\alpha S - 1/2\chi^2$. So the way to proceed is to maximize

$$\alpha \sum_i f_i ln \frac{f_i}{b} - 1/2\chi^2(f_1, f_2, \ldots) = Q \tag{9.37}$$

The effect of the two terms is this:

The prior, which is the entropy term tries to make the distribution as flat as possible, that is to say makes the map contain as little information as it can.

The second, χ^2 term incorporates the data and introduces structure into the map.

The α acts in a way to moderate the two opposing effects. It balances uniformity against structure. Since the map must agree with the data, only structure that is justified by the data will appear in the map.

The entropy of the map is maximized subject to being in agreement with the data. The effect is that from all maps which satisfy the data, we choose the one with the greatest entropy. The data act as a constraint *via* the χ^2 functions and that is why this kind of procedure is sometimes called constrained entropy maximization. The effect is that the map produced will contain only information implicit in the data and should filter out noise. It should be least-biased toward missing information such as the higher order structure amplitudes above the $sin\theta/\lambda$ cut off level. Jaynes puts it

> "The probability assignment shall be the one with maximum entropy consistent with the available knowledge so as to remain maximally non-committal with regard to missing information."

The Shannon entropy for a *discrete* distribution is that given in (9.11). However, the obvious generalization to a continuous distribution

$$H' = -\int p(x) ln p(x) dx \tag{9.38}$$

does not hold since (9.11) is not an invariant measure of information. For a continuous distribution (*e.g.* an electron density) an absolute measure of informational entropy does not exist, only a *relative* entropy[164] can be defined

$$H_{cont.} = -\int p(x) ln \frac{p(x)}{m(x)} dx \tag{9.39}$$

The exact role of $m(x)$ is not clearly defined generally but it has similar properties to $p(x)$. It does provide a way to encode prior information into the method however.

While the Bayesian argument is intuitively appealing, it is worth stating that it only provides an additional interpretation to the maximum entropy method, not a justification.

Chapter 10

MEM results for acetylene

10.1 Introduction

Much of the currently published work using the maximum entropy method has used the extremely accurate Silicon pendellösung data, with its limited extent and low noise level. These data probably represent the best possible scenario for maximum entropy and therefore a more realistic X-ray diffraction data set was sought to provide a fairer evaluation of the method.

A multipole refinement of single crystal data for acetylene in the cubic phase at 141K has been published[184]. Diffraction is limited in resolution to $\sin\theta/\lambda = 0.8\text{Å}^{-1}$ due to the relatively high temperature. The high symmetry of the space group (cubic, $Pa3$) leads to only 164 reflections up to this resolution limit. The unit cell is small with a reported value of $a = 6.091(3)$ with four molecules per unit cell. Lower temperature data for the cubic modification is not attainable due to a phase change to orthorhombic occurring at 131K. The paucity of higher angle data for deconvolution of thermal effects led to high correlations between the static deformation parameters and the thermal parameters.

It is in those cases where the data are limited in resolution that we may expect the Fourier extrapolative properties of the MEM to be beneficial and therefore the acetylene data appeared to be an ideal candidate for such analysis. The crystal system is cubic so there is no difficulty in digitizing the unit cell uniformly and the number of reflections is small making all calculations relatively swift.

All maximum entropy calculations performed used the publicly available MEED program[170]. The input to this program requires the reflections to be phased and on an absolute scale, so a preliminary multipole refinement to obtain reflection phases and an overall scale factor for the data was performed. The interparameter correlations found previously[184] were again in evidence and therefore no attempt was made to analyse the multipole results further than the acquisition of calculated structure factor phases and the scale factor. It should be noted that the scale factor parameter is affected by correlations so it's value may only be taken as an estimate. The scale factor is seldom totally free from correlation with the temperature factors and monopole populations so in any practical application of the MEM, mis-estimation of the scale factor is always a possibility. For a centrosymmetric structure such as the one under consideration, it is reasonable to assume that the phases may be accurately determined from an aspherical atom refinement. Of the 164 measured reflection, only 138 had intensity greater than zero. A further

six of the calculated structure factors had zero magnitude and hence undefined phase. The observed reflections corresponding to these were omitted from the analysis since ambiguity exists on the calculated phase to be assigned to the observed magnitudes. The density in the unit cell was approximated on a grid of 64 × 64 × 64 pixels of uniform size.

10.2 Standard MEM analysis

In the first instance, the standard analysis was tried using all of the experimental data and the method converged successfully to the required χ^2 value. One acetylene molecule lies along the body diagonal of the unit cell, and the most informative plane for viewing the density is along this body diagonal which also allows the ends of two neighbouring molecules to be viewed. The density in this plane is shown in Figure 10.1. The contour level is arbitrarily chosen such that the features are shown most clearly.

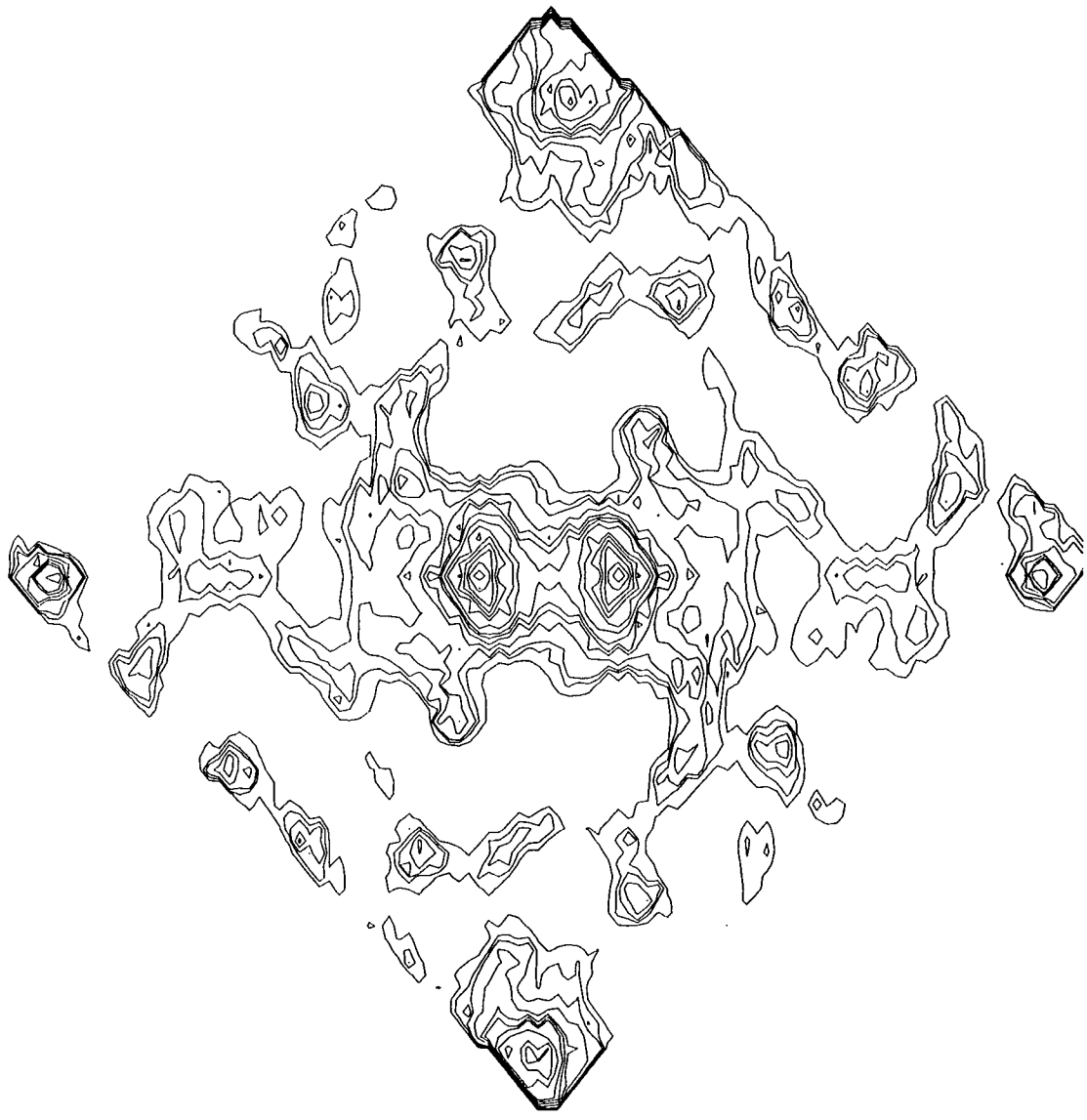

Figure 10.1 - Charge Density by the Standard MEM.

The acetylene molecule can be seen lying horizontally in the figure. Two distinct peaks can be seen for the carbon atoms but no discernible peaks for the hydrogen atoms are present. While the overall shape of the acetylene molecule can be made out, there are many extraneous features imbedded in the background with no obvious cause. The overall impression is that the reconstruction is poor. This is not surprising when one considers the distribution of residuals as shown in Table 10.1. As the studies detailed in the previous chapter revealed, the mis-fit allowed by the χ^2 function is taken up mostly by the strongest few reflections, with almost all of the remaining reflections fitted too tightly. The exceptions from the representative sample of reflections shown are the 552 and 725 reflections which have large deviations, suggesting them to be outliers.

h	k	l	F_o	F_c	$F_o - F_c$	$\sigma(F_o)$	h	k	l	F_o	F_c	$F_o - F_c$	$\sigma(F_o)$
1	1	1	27.110	16.478	10.631	1.004	5	3	4	0.327	0.217	0.110	0.079
2	0	0	21.917	15.428	6.489	0.614	5	4	1	-3.470	-3.470	0.001	0.010
2	1	0	-7.990	-7.212	0.777	0.088	9	1	3	-0.372	-0.265	0.108	0.103
2	1	1	-6.062	-5.719	0.343	0.048	5	4	2	-0.499	-0.533	0.035	0.051
2	2	0	12.206	11.210	0.997	0.102	7	2	1	-1.060	-1.052	0.008	0.025
2	2	1	-2.679	-2.659	0.020	0.025	5	4	3	-1.405	-1.411	0.007	0.012
2	2	2	7.216	6.991	0.225	0.087	7	2	2	-0.728	-0.733	0.005	0.036
3	0	2	-7.841	-7.936	0.095	0.047	5	4	4	-0.409	-0.365	0.044	0.065
3	1	1	7.022	6.677	0.346	0.049	7	2	3	-0.434	-0.514	0.080	0.041
3	1	2	-0.673	-0.732	0.058	0.042	7	2	4	-0.744	-0.793	0.049	0.037
3	2	1	-6.708	-6.617	0.091	0.045	9	3	1	-0.288	-0.535	0.247	0.133
3	2	2	-4.264	-4.249	0.015	0.019	5	5	2	0.137	1.306	1.169	0.190
3	3	1	0.303	0.368	0.065	0.021	7	2	5	0.223	1.161	0.939	0.167
3	3	2	-2.104	-2.096	0.008	0.014	9	3	2	0.315	0.330	0.015	0.153

Table 10.1 - Statistics for sample of reflections using standard MEM.

10.2.1 Hard constraints

Since a few reflections mis-fit drastically, one way to try to improve the fit is to tighten up the overall fit. This was attempted by setting all of the σ values to a very very small value, making the desired value of χ^2 very small indeed, effectively using the data as hard constraints. Convergence could not be obtained by this method. Slackening the fit slightly by setting the σ value for every reflection to 0.01 did give convergence. Table 10.2 lists the statistics for the same sample of reflections as before. The experimental standard deviations are listed, but were not used.

h	k	l	F_o	F_c	$F_o - F_c$	$\sigma(F_o)$	h	k	l	F_o	F_c	$F_o - F_c$	$\sigma(F_o)$
1	1	1	27.110	26.061	1.048	1.004	5	3	4	0.327	0.291	0.036	0.079
2	0	0	21.917	22.143	0.226	0.614	5	4	1	-3.470	-3.365	0.105	0.010
2	1	0	-7.990	-7.661	0.328	0.088	9	1	3	-0.372	-0.353	0.019	0.103
2	1	1	-6.062	-5.757	0.306	0.048	5	4	2	-0.499	-0.326	0.173	0.051
2	2	0	12.206	12.313	0.107	0.102	7	2	1	-1.060	-0.996	0.064	0.025
2	2	1	-2.679	-2.930	0.251	0.025	5	4	3	-1.405	-1.861	0.456	0.012
2	2	2	7.216	7.126	0.091	0.087	7	2	2	-0.728	-0.978	0.250	0.036
3	0	2	-7.841	-7.900	0.059	0.047	5	4	4	-0.409	-0.433	0.026	0.065
3	1	1	7.022	7.109	0.087	0.049	7	2	3	-0.434	-0.720	0.286	0.041
3	1	2	-0.673	-0.839	0.166	0.042	7	2	4	-0.744	-0.793	0.049	0.037
3	2	1	-6.708	-6.974	0.266	0.045	9	3	1	-0.288	-0.288	0.000	0.133
3	2	2	-4.264	-4.006	0.258	0.019	5	5	2	0.137	0.279	0.142	0.190
3	3	1	0.303	1.008	0.705	0.021	7	2	5	0.223	0.267	0.044	0.167
3	3	2	-2.104	-2.063	0.041	0.014	9	3	2	0.315	0.273	0.042	0.153

Table 10.2 - Reflection statistics with data as hard constraints.

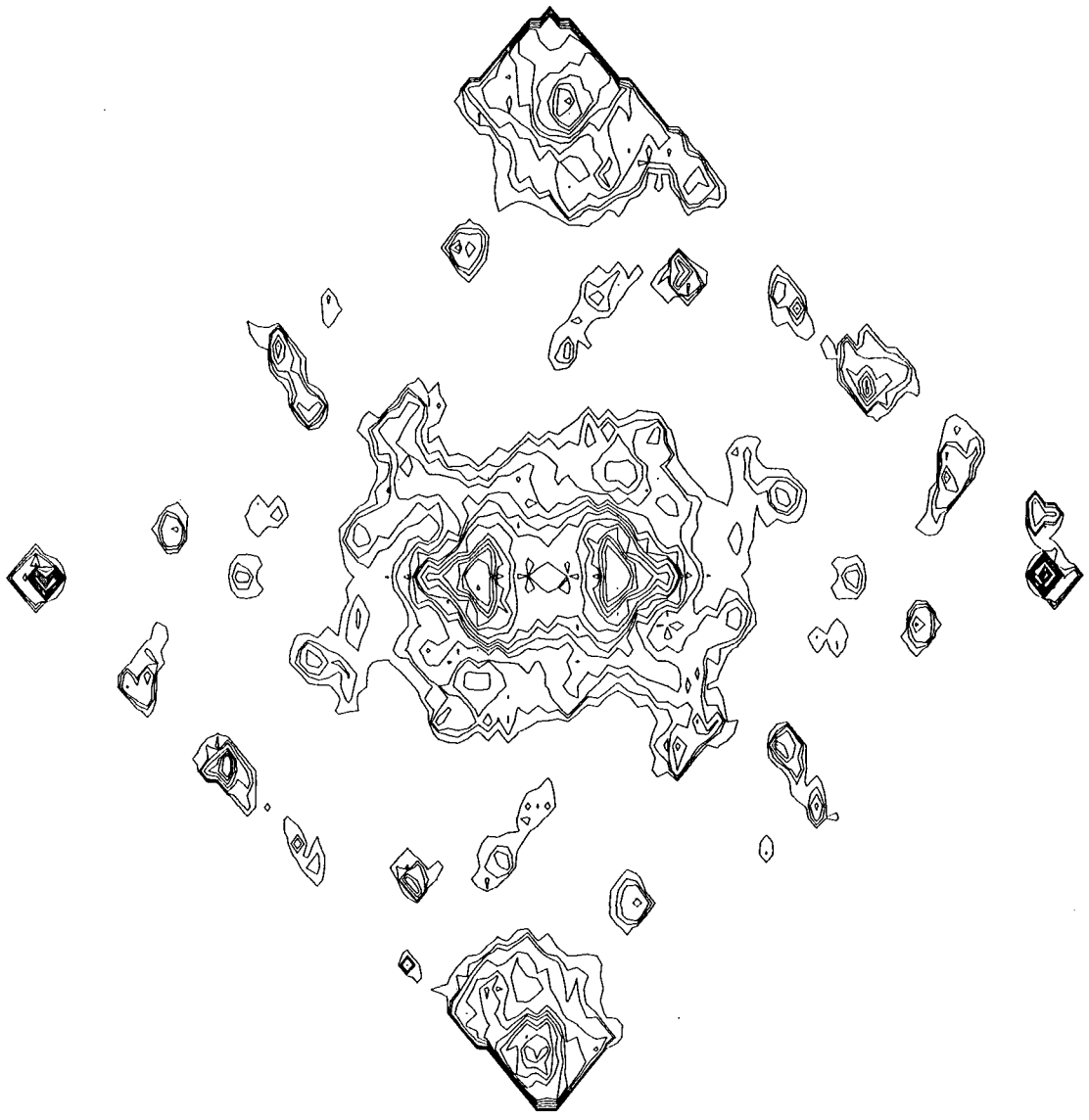

Figure 10.2 - Charge Density with hard constraints.

For this variant of the method, the residuals are much more evenly distributed, with the strongest reflections fitting much more closely. Despite the fact that there is much less mis-fit allowed, the low intensity, high angle data is not fitted more tightly than in the previous case, with some better fitted, and some more poorly fitted. The 552 reflection which was hypothesised to be an outlier from the standard MEM now fits rather well, and no worse on average than any other reflection. The contour level for Figure 10.2 is the same as 10.1, so direct comparison is possible. The spurious background peaks (aliases) appear more localized, but are higher in intensity. Although the fit to the data is much better, it is not possible to conclude that the map shows a great improvement. No distinct peaks are visible at the hydrogen positions.

10.2.2 Low-angle data

Another way to reduce the total mis-fit allowed is to retain the experimental σ values and truncate the data set. This should force tighter fitting of the strong reflections, while removing the problem

of over-fitting the weak ones since they are no longer in the data set. An additional rationale for this is that at the experimental temperature, only the carbon core density is likely to scatter to higher angle and therefore removing this data should not impair the reconstruction of valence density. To test this hypothesis, the data were truncated to $\sin\theta/\lambda = 0.410\text{Å}^{-1}$, leaving only 21 reflections.

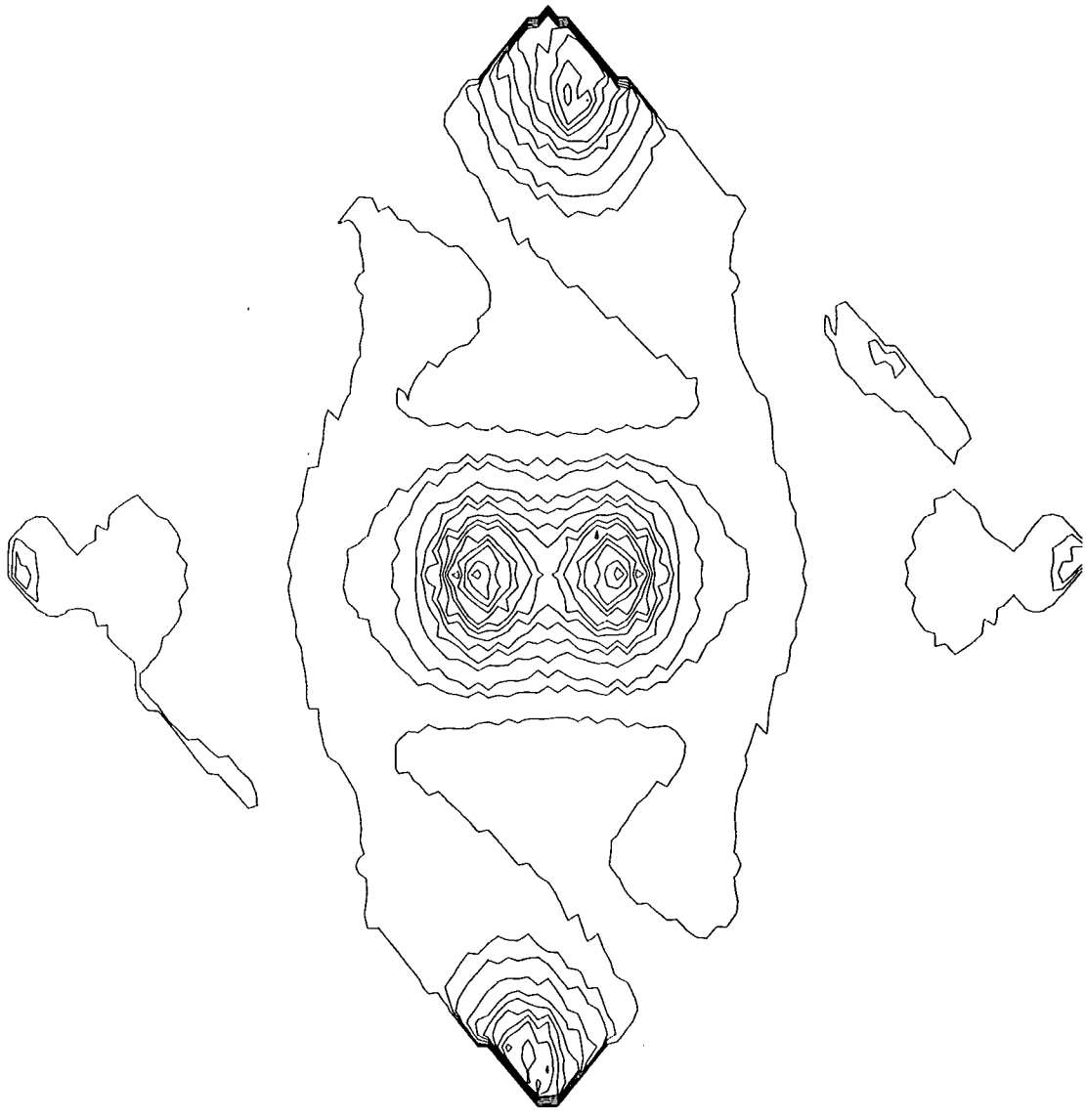

Figure 10.3 - Charge Density with only low-angle data.

The most immediate effect on the map has been to suppress the aliasing. The contours of the carbon atoms are also considerably smoother, but the absolute value of the peaks have been reduced. There are still no indications of the hydrogen atoms. Overall, this map probably contains slightly less detailed information than the previous two, but it "looks" better due to the smoother contours and suppression of the spurious background features. Table 10.3 shows that the old problem of non-random residuals still occurs, but the absolute value of mis-fit of the strongest data is less than in the standard MEM. Overfitting of the weaker data seems to be more of a problem though, with most of the reflections fitted almost exactly.

h	k	l	F_o	F_c	$F_o - F_c$	$\sigma(F_o)$
1	1	1	27.110	22.670	4.440	1.004
2	0	0	21.917	21.231	0.686	0.614
2	1	0	-7.990	-7.989	0.001	0.088
2	1	1	-6.062	-6.066	0.004	0.048
2	2	0	12.206	12.247	0.041	0.102
2	2	1	-2.679	-2.682	0.002	0.025
2	2	2	7.216	7.211	0.005	0.087
3	0	2	-7.841	-7.843	0.002	0.047
3	1	1	7.022	7.030	0.008	0.049
3	1	2	-0.673	-0.675	0.002	0.042
3	2	1	-6.708	-6.710	0.002	0.045
3	2	2	-4.264	-4.263	0.001	0.019
3	3	1	0.303	0.303	0.000	0.021
3	3	2	-2.104	-2.104	0.000	0.014
4	0	0	1.767	1.768	0.001	0.047
4	0	2	1.596	1.595	0.001	0.049
4	1	0	-3.386	-3.386	0.000	0.042
4	1	1	-3.010	-3.010	0.000	0.045
4	1	2	-2.158	-2.157	0.001	0.019
4	2	0	1.608	1.608	0.000	0.021
4	2	2	0.807	0.803	0.004	0.014

Table 10.3 - Reflection statistics using only low angle data.

10.2.3 Low angle data as hard constraints

Removing the higher angle data suppresses the background noise in the map, and using the data as hard constraints considerable improves the fit of the strong reflections while not increasing the overfit of the weaker ones. An obvious next step is to try both techniques together.

h	k	l	F_o	F_c	$F_o - F_c$	$\sigma(F_o)$
1	1	1	27.110	27.010	0.009	1.004
2	0	0	21.917	21.917	0.000	0.614
2	1	0	-7.990	-7.982	0.008	0.088
2	1	1	-6.062	-6.059	0.003	0.048
2	2	0	12.206	12.218	0.012	0.102
2	2	1	-2.679	-2.687	0.008	0.025
2	2	2	7.216	7.210	0.006	0.087
3	0	2	-7.841	-7.841	0.000	0.047
3	1	1	7.022	7.011	0.011	0.049
3	1	2	-0.673	-0.687	0.014	0.042
3	2	1	-6.708	-6.711	0.003	0.045
3	2	2	-4.264	-4.254	0.010	0.019
3	3	1	0.303	0.330	0.027	0.021
3	3	2	-2.104	-2.105	0.001	0.014
4	0	0	1.767	1.767	0.000	0.047
4	0	2	1.596	1.597	0.001	0.049
4	1	0	-3.386	-3.390	0.004	0.042
4	1	1	-3.010	-3.016	0.006	0.045
4	1	2	-2.158	-2.151	0.007	0.019
4	2	0	1.608	1.609	0.001	0.021
4	2	2	0.807	0.787	0.020	0.014

Table 10.4 - Reflection statistics using low angle data as hard constraints.

As expected, the strong reflections now fit much better. Again, despite the total mis-fit allowed being reduced, the weaker data now have slightly larger deviations and do not appear to be over-fitted quite so drastically. The appearance of the map (Figure 10.4) does not seem to have improved much over the one produced using experimental σ values and the truncated data set, even though the residual distribution is much better. Once again, no evidence for the hydrogen atoms is present.

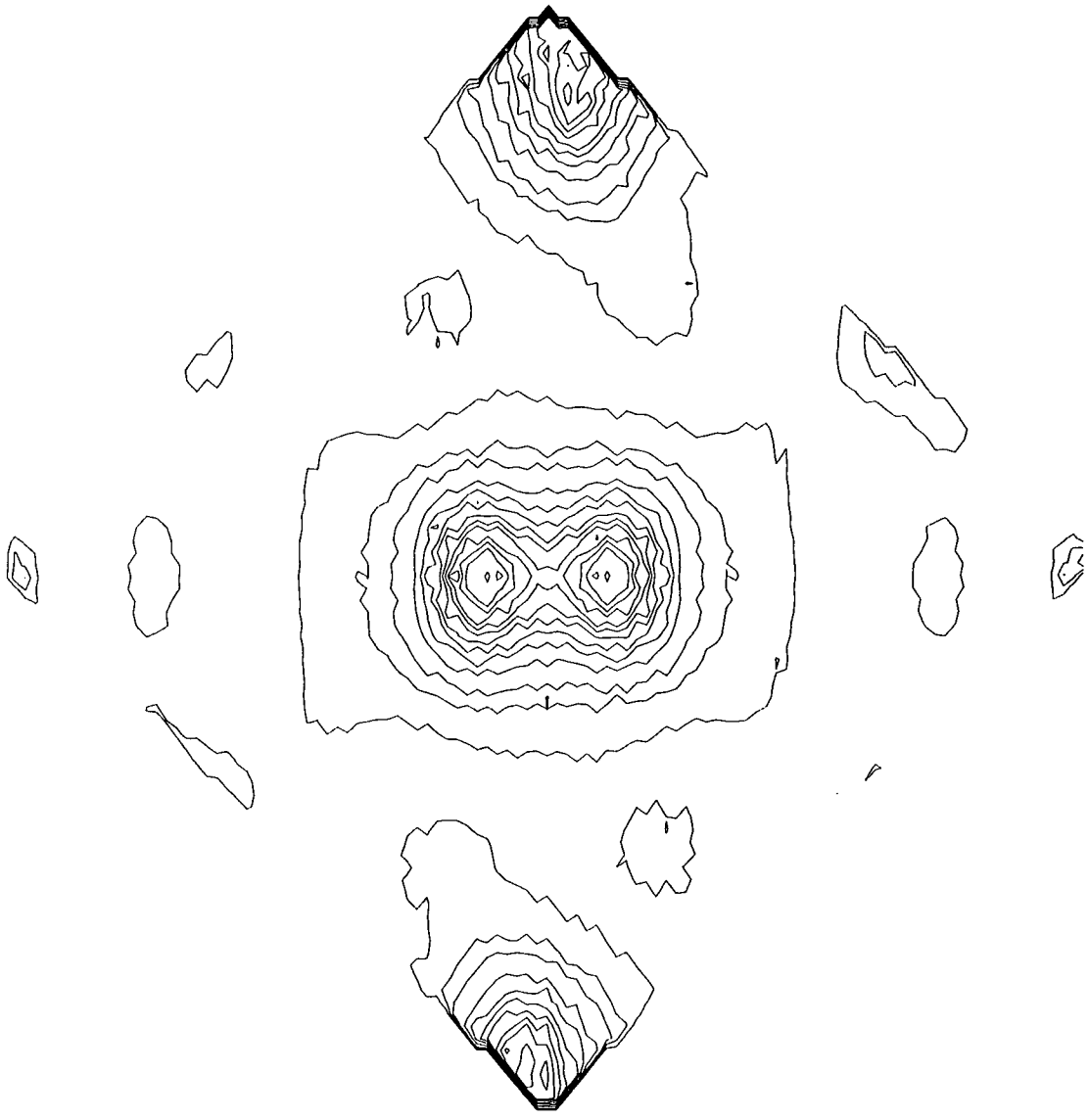

Figure 10.4 - Charge Density using low-angle data as hard constraints.

10.3 L-shell projection MEM

It was stated in the preceding chapter that one major limiting factor on the applicability of maximum entropy reconstruction methods to the charge density was the intrinsically high dynamic range of the function. Coppens[181] has tackled this problem by reconstructing the deformation density, however the soundness of the two-channel maximum entropy approach may be questioned. Because the vast spikes which occur in the charge density at nuclear positions are primarily caused by the asymptotic behaviour of the core electron density, reconstruction of the valence density is a suitable alternative. The valence density is everywhere positive and can still be interpreted as a probability distribution defining the probability of finding a valence electron at any particular point in space, and hence such a method is closer to the information theoretical ideas which are phrased in probabilistic terms. In the early stages of development of the multipole formalism, Stewart[185] obtained experimental valence densities by fitting aspherical

form factors to "valence structure factors". These are defined as $F_{obs}(\mathbf{H}) - F_{core}(\mathbf{H})$ with the calculation of $F_{core}(\mathbf{H})$ from two $1s$ electrons placed at the fractional coordinates of first row atoms and attenuated by the temperature factor refined for that atom from a spherical atom model. Because the K-shell scattering had been removed within a reasonable approximation, Stewart called this method "L-shell projection". The next section oft his chapter deals with "L-shell projection MEM" where we have subtracted the core scattering from the carbon atoms to leave valence structure factors.

The first application uses the standard MEM method with all data assigned their experimental σ values. This is not strictly correct since the standard deviations assigned to the valence structure factors should certainly be less than those on the full data, however without any direct knowledge of the correct values for the valence standard deviations it was decided to retain those from the full data. In any case, we know from our previous studies that tightening the fit by making all of the standard deviations small will probably improve the fit considerably, even if we knew the correct valence σ values.

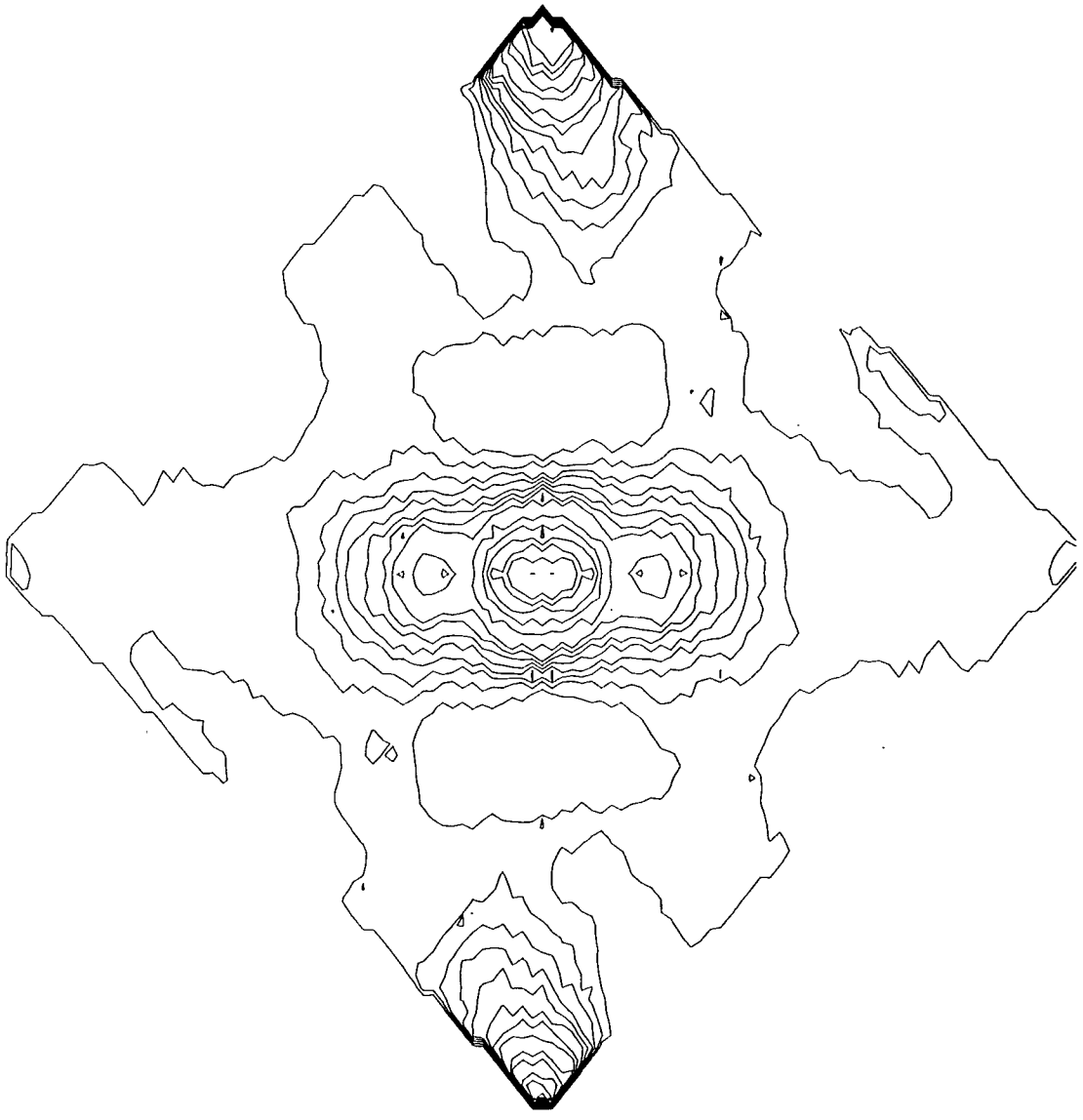

Figure 10.5 - Valence density by standard MEM.

Inspection of Figure 10.5 shows that by reducing the dynamic range of the problem we have allowed additional detail to become immediately apparent. Peaks have appeared for the hydrogen atoms for the first time, along with an obvious concentration of charge density in the central bond. Unwanted noise in the background is also heavily subdued, with an almost flat background between the molecules. This is undoubtedly the most informative map so far. The problem of mis-fit of residuals remains (Table 10.5) with the strongest reflection underfitted.

h	k	l	F_o	F_c	$F_o - F_c$	$\sigma(F_o)$	h	k	l	F_o	F_c	$F_o - F_c$	$\sigma(F_o)$
1	1	1	15.775	7.295	8.479	1.004	5	3	4	0.014	0.044	0.010	0.079
2	0	0	9.855	5.555	4.300	0.614	5	4	1	0.050	0.051	0.001	0.010
2	1	0	-5.177	-5.131	0.046	0.088	9	1	3	-0.031	-0.006	0.025	0.103
2	1	1	-3.476	-3.465	0.011	0.048	5	4	2	-0.059	-0.066	0.007	0.051
2	2	0	5.646	5.605	0.041	0.102	7	2	1	0.036	0.038	0.002	0.025
2	2	1	-0.692	-0.692	0.000	0.025	5	4	3	-0.024	-0.023	0.001	0.012
2	2	2	3.062	3.117	0.055	0.087	7	2	2	0.036	0.040	0.004	0.036
3	0	2	-2.311	-2.330	0.019	0.047	5	4	4	-0.099	-0.084	0.015	0.065
3	1	1	2.677	2.687	0.010	0.049	7	2	3	-0.081	-0.080	0.001	0.041
3	1	2	0.543	0.550	0.007	0.042	7	2	4	-0.064	-0.069	0.049	0.037
3	2	1	-1.637	-1.658	0.021	0.045	9	3	1	0.053	0.049	0.004	0.133
3	2	2	-0.398	-0.398	0.000	0.019	5	5	2	-0.124	-0.169	0.025	0.190
3	3	1	1.455	1.459	0.065	0.021	7	2	5	-0.004	-0.103	0.099	0.167
3	3	2	0.213	0.211	0.002	0.014	9	3	2	-0.091	-0.028	0.063	0.153

Table 10.5 - Reflection statistics using valence data.

10.3.1 *L*-shell MEM with low angle data

It is questionable what effect the higher resolution data have upon the refinement. Almost all of their intensity derives from the core scattering, and since this is removed, the higher angle valence structure factors all have very small magnitudes of similar size to their σ values. It is reasonable to assume that removing these data from the refinement will not degrade the result, with the added benefit that the pool of mis-fit is reduced so that strong data are fitted more tightly. Table 10.6 shows that the strong data do indeed come into much closer agreement but the rest of the data are far too tightly fitted, with many data points having a perfect fit.

h	k	l	F_o	F_c	$F_o - F_c$	$\sigma(F_o)$
1	1	1	15.775	11.205	4.570	1.004
2	0	0	9.855	9.577	0.278	0.614
2	1	0	-5.177	-5.180	0.003	0.088
2	1	1	-3.476	-3.480	0.004	0.048
2	2	0	5.646	5.668	0.022	0.102
2	2	1	-0.692	-0.693	0.001	0.025
2	2	2	3.062	3.065	0.003	0.087
3	0	2	-2.311	-2.313	0.002	0.047
3	1	1	2.677	2.685	0.008	0.049
3	1	2	0.543	0.542	0.001	0.042
3	2	1	-1.637	-1.639	0.002	0.045
3	2	2	-0.398	-0.398	0.000	0.019
3	3	1	1.455	1.455	0.000	0.021
3	3	2	0.213	0.213	0.000	0.014
4	0	0	0.458	0.458	0.000	0.047
4	0	2	1.021	1.021	0.000	0.049
4	1	0	-0.421	-0.421	0.000	0.042
4	1	1	-0.294	-0.294	0.000	0.045
4	1	2	-0.099	-0.099	0.000	0.019
4	2	0	1.033	1.033	0.000	0.021
4	2	2	0.646	0.645	0.001	0.014

Table 10.6 - Reflection statistics using low angle valence data.

Despite having very small magnitudes, removal of the higher angle data has a negative effect on the map (Figure 10.6). The hydrogen atoms have disappeared and there is much less information

in the carbon valence region.

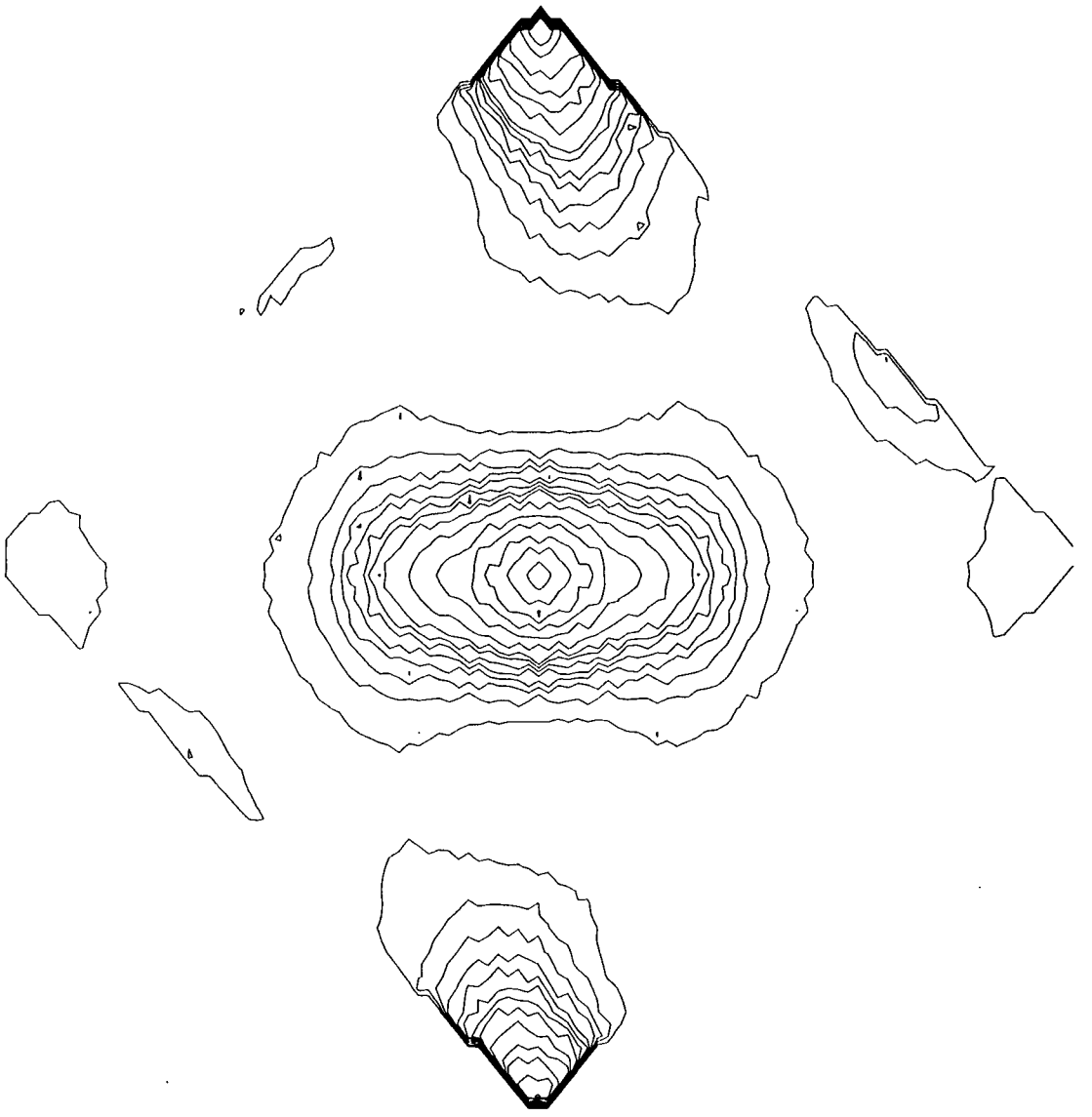

Figure 10.6 - Valence density using low angle data.

10.3.2 *L*-shell MEM with low angle data as hard constraints

From the subset of low angle reflections, only the two strongest have appreciable mis-fit and it would therefore seem unlikely that these two reflections contain the missing valence information that was present in the previous map, therefore tightening the fit of these reflections by using the data as hard constraints is unlikely to improve matter greatly. However, it is possible that the valence information has been lost by fitting the remaining reflections too tightly. We saw from the first part of the chapter that tightening the fit for all data actually caused the higher angle data to mis-fit more where necessary so an obvious next step is to use the data as hard constraints to see if the weaker data are not so overfitted and reintroduce valence structure back into the map.

h	k	l	F_o	F_c	$F_o - F_c$	$\sigma(F_o)$
1	1	1	15.775	15.759	0.016	1.004
2	0	0	9.855	9.867	0.012	0.614
2	1	0	-5.177	-5.180	0.003	0.088
2	1	1	-3.476	-3.471	0.005	0.048
2	2	0	5.646	5.665	0.019	0.102
2	2	1	-0.692	-0.693	0.001	0.025
2	2	2	3.062	3.071	0.009	0.087
3	0	2	-2.311	-2.313	0.002	0.047
3	1	1	2.677	2.646	0.031	0.049
3	1	2	0.543	0.543	0.000	0.042
3	2	1	-1.637	-1.635	0.002	0.045
3	2	2	-0.398	-0.398	0.000	0.019
3	3	1	1.455	1.443	0.012	0.021
3	3	2	0.213	0.212	0.001	0.014
4	0	0	0.458	0.462	0.004	0.047
4	0	2	1.021	1.027	0.006	0.049
4	1	0	-0.421	-0.421	0.000	0.042
4	1	1	-0.294	-0.294	0.000	0.045
4	1	2	-0.099	-0.099	0.000	0.019
4	2	0	1.033	1.038	0.005	0.021
4	2	2	0.646	0.651	0.005	0.014

Table 10.7 - Reflection statistics using low angle valence data as hard constraints.

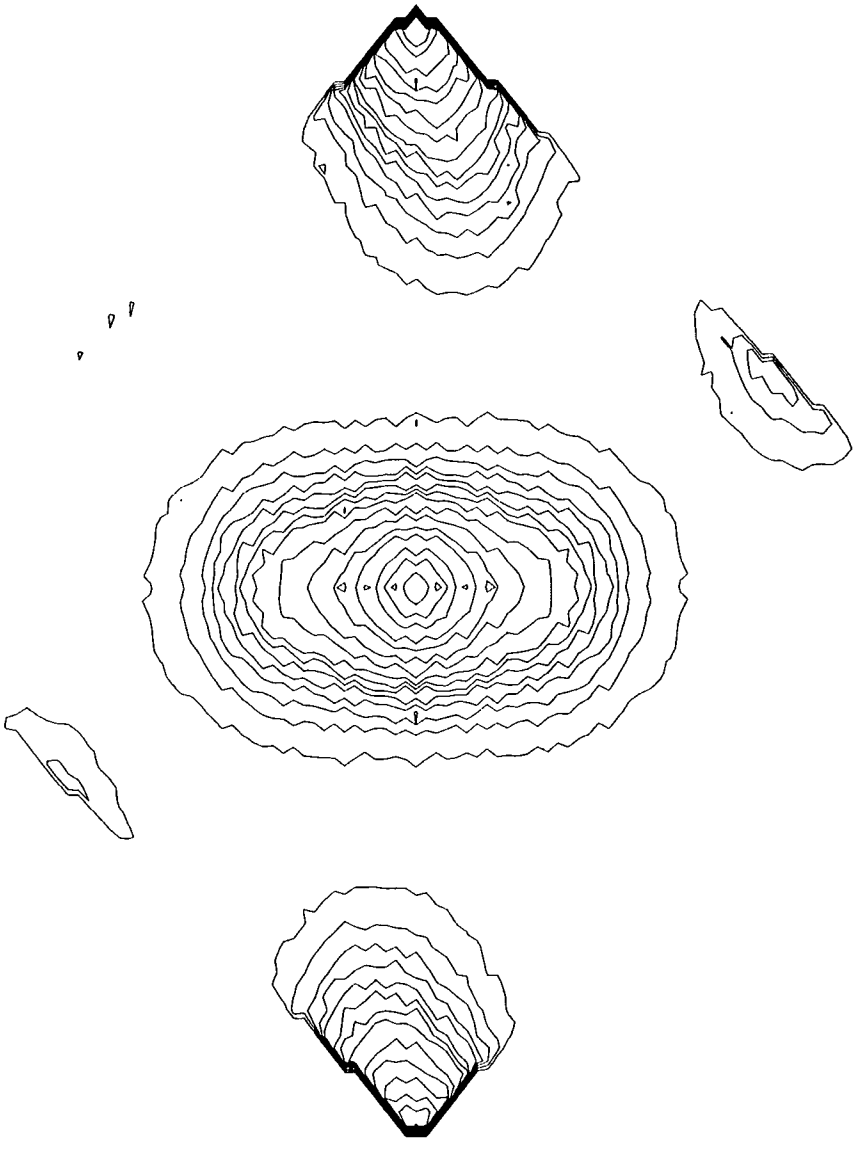

Figure 10.7 - Valence density using low angle data as hard constraints.

Tightening the overall fit slightly increases the deviation for the weaker reflections but does nothing to improve the map, further degrading the reproduction of the valence density in the central bond region.

It would appear from the last two refinements that inclusion of the higher angle data is essential to reproduce the valence density, although it is not obvious why this should be the case.

10.3.3 L-shell MEM with hard constraints

We now turn to the last remaining derivative of the L-shell projection variation of maximum entropy. The higher angle data is retained while the data are used as hard constraints to reduce the residual on the strongest reflections.

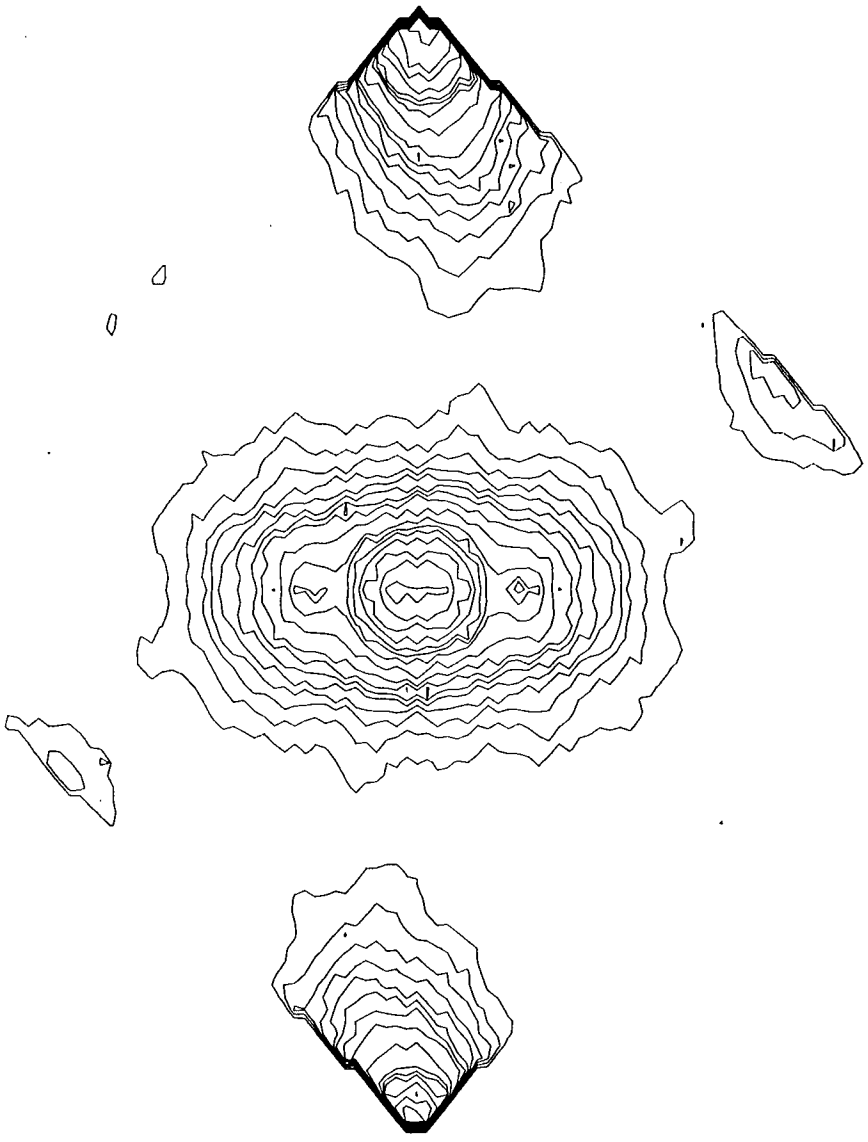

Figure 10.8 - Valence density using data as hard constraints.

h	k	l	F_o	F_c	$F_o - F_c$	$\sigma(F_o)$	h	k	l	F_o	F_c	$F_o - F_c$	$\sigma(F_o)$
1	1	1	15.775	15.740	0.035	1.004	5	3	4	0.014	0.024	0.010	0.079
2	0	0	9.855	9.877	0.022	0.614	5	4	1	0.050	0.041	0.009	0.010
2	1	0	-5.177	-5.175	0.002	0.088	9	1	3	-0.031	-0.035	0.004	0.103
2	1	1	-3.476	-3.469	0.007	0.048	5	4	2	-0.059	-0.051	0.008	0.051
2	2	0	5.646	5.671	0.025	0.102	7	2	1	0.036	0.037	0.001	0.025
2	2	1	-0.692	-0.689	0.003	0.025	5	4	3	-0.024	-0.014	0.010	0.012
2	2	2	3.062	3.074	0.012	0.087	7	2	2	0.036	0.038	0.002	0.036
3	0	2	-2.311	-2.307	0.004	0.047	5	4	4	-0.099	-0.109	0.010	0.065
3	1	1	2.677	2.637	0.040	0.049	7	2	3	-0.081	-0.078	0.003	0.041
3	1	2	0.543	0.543	0.000	0.042	7	2	4	-0.064	-0.062	0.002	0.037
3	2	1	-1.637	-1.654	0.017	0.045	9	3	1	0.053	0.049	0.004	0.133
3	2	2	-0.398	-0.391	0.007	0.019	5	5	2	-0.124	-0.102	0.022	0.190
3	3	1	1.455	1.444	0.011	0.021	7	2	5	-0.004	-0.002	0.002	0.167
3	3	2	0.213	0.213	0.000	0.014	9	3	2	-0.091	-0.088	0.003	0.153

Table 10.8 - Reflection statistics using valence data as hard constraints.

The appearance of the map is similar to Figure 10.5 which used the experimental standard deviations on the data. If anything it is marginally better with more pronounced peaks at the hydrogen positions and slightly cleaner background. There is also a little more detail in the central bonding region, although the contour lines are less smooth than before. Overall this is probably the best map. Fitting the data tightly reduced the large deviations (Table 10.8) from the strong reflections without increasing the overfit of the weaker ones.

10.4 Summary

This work was undertaken with the aim of learning the relative characteristics of different maximum entropy reconstructions, ultimately to produce better quality results. Of particular importance was the use of a real data set, representative of the type usually obtained in charge density experiments using standard equipment. This has been achieved by three different approaches of using the data as hard constraints by reducing the size of the pool of mis-fit, truncating the data set to reduce the size of the pool of mis-fit, and removing approximately the core scattering to produce valence only maps. From the various possible combinations of the above variations of the method the following conclusions can be drawn.

- The standard MEM gives poor quality maps. For the particular data set used, no peaks for the hydrogen atoms of the acetylene molecules could be located in the density map. Spurious features in the background of substantial magnitude are common. The few strongest reflections are substantially underfitted while the remainder are overfitted.

- Tightening the fit by assigning each reflection a small experimental σ value in the refinement improves the agreement of the strong reflections as expected. Contrary to expectation however, such an approach also causes the weaker data to be slightly less tightly fitted. The effect on the maps is to sharpen features while suppressing the general background, although spurious background peaks also appear sharpened.

- Retaining the experimental σ values while truncating the data set reduces the deviation of the strong reflections by reducing the total amount of mis-fit, but overfitting of the weaker data is increased. The maps are markedly less informative than the corresponding all-data results

- Removing the core scattering from the data to give L-shell projection MEM gives the biggest improvement. Substantially reducing the dynamic range of the function being reconstructed allows far greater detail in the lower regions to be observed, in this particular case, it allows the hydrogen atoms to become apparent.

10.5 Conclusions

From this particular study, the maximum entropy method does not seem to be competitive with the multipole model for charge density analysis. The L-shell projection technique does improve matters, allowing additional detail to be obtained, but not to a sufficient degree to make it a worthy alternative.

Further advances such as using non-uniform measures in the relative entropy expression or even entirely different entropy expressions are worth considering, particularly if valence structure factors are used, but the inability to deconvolute thermal motion to give the static density limits the ultimate utility of the method.

Chapter 11

Density Matrix Refinement

11.1 Introduction

Given the inherent limitations of the maximum entropy method, one must conclude that X-ray diffraction data themselves contain insufficient information to adequately describe the system under study, and the return to least-squares refinement of a structured model is necessary. The multipole models already described are slanted more towards the conventions of crystallography than those of quantum chemistry, being somewhat *ad hoc* improvements to the standard static scattering model of spherical atoms. One is entitled to think that more accurate charge densities may be obtained by improving the refinement model. Unfortunately, it is difficult to see where further improvements may be made to the multipole model, save perhaps for improvements in the atomic scattering factors used. Since molecular electron densities are quantum chemical entities, it is reasonable to look to molecular quantum mechanics for an improved model of the charge density.

Such a model exists, and is a description of the charge density in terms of orbital products introduced by Coulson[185] and named by him as the Charge and Bond-Order Matrix. It is the representation in a particular basis set of one of a set of interesting functions, the reduced density matrices.

11.2 Wavefunctions, Densities and Density Matrices

11.2.1 Density functions

Given an N electron waveunction $\Psi(\mathbf{x}_1, \mathbf{x}_2, \ldots, \mathbf{x}_N)$, where $\mathbf{x}$ contains both the spatial ($\mathbf{r}$) and spin (s) variables for that electron, the quantity

$$\Psi(\mathbf{x}_1, \mathbf{x}_2, \ldots, \mathbf{x}_N)\Psi^*(\mathbf{x}_1, \mathbf{x}_2 \ldots, \mathbf{x}_N)d\mathbf{x}_1 d\mathbf{x}_2 \ldots \mathbf{x}_N \tag{11.1}$$

is interpreted as the probability of simultaneously finding electron 1 in $d\mathbf{x}_1$, electron 2 in $d\mathbf{x}_2$ etc. A more useful property is the probability of finding electron 1 in $d\mathbf{x}_1$ and the other electrons anywhere which is

$$d\mathbf{x}_1 \int \Psi(\mathbf{x}_1, \mathbf{x}_2, \ldots, \mathbf{x}_N)\Psi^*(\mathbf{x}_1, \mathbf{x}_2, \ldots, \mathbf{x}_N)d\mathbf{x}_2 \ldots d\mathbf{x}_N \tag{11.2}$$

Since the wavefunction is completely symmetrical in the variables of the N electrons and each one therefore has the same probability of being in a given volume element, the probability of

finding any of the N electrons in $d\mathbf{x}_1$ must be N times this. This is the one electron spin density function

$$\rho(\mathbf{x}) = N \int \Psi(\mathbf{x}_1, \mathbf{x}_2, \ldots, \mathbf{x}_N)\Psi^*(\mathbf{x}_1, \mathbf{x}_2, \ldots, \mathbf{x}_N)d\mathbf{x}_2 \ldots d\mathbf{x}_N \tag{11.3}$$

The more familiar spinless one electron density is obtained by integrating over spin

$$\rho(\mathbf{r}) = \int \rho(\mathbf{x})d\mathbf{s} \tag{11.4}$$

This is just the probability of finding an electron in $d\mathbf{r}_1$ irrespective of its spin. Similar density functions may be defined for more than one electron, for example, the two-electron density which defines the probability of simultaneously finding electron 1 in $d\mathbf{x}_1$ and electron 2 in $d\mathbf{x}_2$ irrespective of the positions of any other electrons is the pair function

$$\pi(\mathbf{x}_1, \mathbf{x}_2) = N(N-1) \int \Psi(\mathbf{x}_1, \mathbf{x}_2 \ldots, \mathbf{x}_N)\Psi^*(\mathbf{x}_1, \mathbf{x}_2, \ldots, \mathbf{x}_N)d\mathbf{x}_3 \ldots \mathbf{x}_N \tag{11.5}$$

This is reduced to spinless form as before by integrating over spin

$$\pi(\mathbf{r}_1, \mathbf{r}_2) = \int \pi(\mathbf{x}_1, \mathbf{x}_2)d\mathbf{s}_1 d\mathbf{s}_2 \tag{11.6}$$

The pair function contains information on the correlated motion of electrons and thus is of considerable interest.

The extraction of an expectation value from a wavefunction is fairly straightforward for any general operator[186]

$$\langle O \rangle = \int \Psi^*(\mathbf{x})\hat{O}\Psi(\mathbf{x})d\mathbf{x} \tag{11.7}$$

If $\hat{O}$ is just a multiplicative operator such as the position operator then

$$\langle O \rangle = \int \hat{O}\Psi(\mathbf{x})\Psi^*(\mathbf{x}) \tag{11.8}$$

and since $\hat{O}$ is a multiplier we can use the commutative law of multiplication so that

$$\int \hat{O}\Psi(\mathbf{x})\Psi^*(\mathbf{x})d\mathbf{x} = \int \hat{O}\rho(\mathbf{x}_1)d\mathbf{x} \tag{11.9}$$

11.2.2 Density matrices

In the case of a differential or integral operator, the commutative law will not apply and the rearrangement cannot be performed. This problem is overcome by introducing a new piece of notation[187]. We say that $\hat{O}$ operates only on $\mathbf{x}$ deriving from ψ. Now change the variables of ψ^* from $\mathbf{x}$ to $\mathbf{x}'$ to make it immune from $\hat{O}$. Rewrite the operator expression as

$$\langle O \rangle = \int_{\mathbf{x}'=\mathbf{x}} \hat{O}\Psi(\mathbf{x})\Psi^*(\mathbf{x}')d\mathbf{x} \tag{11.10}$$

and put $\mathbf{x}' = \mathbf{x}$ after performing the integration. The generalised density function is now written as

$$\rho(\mathbf{x}) = \rho(\mathbf{x};\mathbf{x}') \tag{11.11}$$

so that

$$\langle O \rangle = \int_{\mathbf{x}'=\mathbf{x}} \hat{O}\rho(\mathbf{x};\mathbf{x}')d\mathbf{x} \tag{11.12}$$

Exactly the same procedure holds for extraction of an expectation value from the two electron density matrix.

These generalised density matrices are obtained by squaring the wavefunction and integrating out the extra particles, but retaining the coordinate information separately from $\Psi(\mathbf{x})$ and $\Psi^*(\mathbf{x})$. For example for the spin-traced charge density

$$\rho(\mathbf{r};\mathbf{r}') = N \int \Psi(\mathbf{r}_1, \mathbf{r}_2, \ldots, \mathbf{r}_N)\Psi^*(\mathbf{r}'_1, \mathbf{r}_2, \ldots, \mathbf{r}_N)d\mathbf{r}_2 \ldots d\mathbf{r}_N \tag{11.13}$$

This separate storage of coordinate information from $\mathbf{r}$ and $\mathbf{r}'$ is the essential difference between the density and the corresponding density matrix. Obtaining the density from its matrix is called the collapse of the density matrix

$$\rho(\mathbf{r}) = \int \delta(\mathbf{r} - \mathbf{r}')\rho(\mathbf{r};\mathbf{r}')d\mathbf{r}' \tag{11.14}$$

The density is hence that element of the full density matrix when $\mathbf{r} = \mathbf{r}'$, and is therefore called the diagonal of the density matrix. The density matrix contains more information than the density. In fact, for molecular electronic wavefunction the density matrix contains sufficient information to calculate all energy components, while this cannot be done, at least within operational form, from the density.

11.2.3 Natural Orbitals

The concept of the natural expansion of the density matrix was introduced by Löwdin[188,189]. Any proper one-electron density matrix derived from the corresponding N-electron wavefunction will be Hermitian

$$\rho(\mathbf{r};\mathbf{r}') = \rho^*(\mathbf{r}';\mathbf{r}) \tag{11.15}$$

and can therefore be brought to diagonal form by some unitary transformation. The eigenvectors of the density matrix are called the natural orbitals, and their respective eigenvalues the occupation numbers. The spin-traced density matrix can therefore be restated

$$\rho(\mathbf{r};\mathbf{r}') = \sum_i n_i\phi_i(\mathbf{r})\phi_i^*(\mathbf{r}') \tag{11.16}$$

where n_i is the occupation number of the natural orbital $\phi_i(\mathbf{r})$. The Hermiticity of the matrix leads to real occupation numbers and orthonormal natural orbitals[190].

If we diagonalise the spin-included density matrix we obtain the natural spin-orbitals

$$\rho(\mathbf{x};\mathbf{x}') = \sum_i n_i\phi_i(\mathbf{x})\phi_i^*(\mathbf{x}') \tag{11.17}$$

The natural orbitals have a special place in the context of this work. Not all possible one-electron density matrices can derive from an N-particle wavefunction so a way to discriminate between those which do and are hence quantum mechanically acceptable and those which are not is sought. The proof of this problem, the N-representability problem for the one-electron density matrix has been given by Coleman[191], and is in terms of the matrix eigenvalues. Using the normalisation of $Tr\rho(\mathbf{r};\mathbf{r}') = N$, the N-representability criteria for the spin-traced density matrix are

$$0 \leq n_i \leq 2 \tag{11.18}$$

and that the matrix should be correctly normalised

$$\sum_i n_i = N \tag{11.19}$$

These criteria may be thought of as a restatement that no orbital may contain more than two electrons, and the sum of the occupation numbers must sum to the total number of electrons.

11.2.4 Idempotency

Of the class of N-representable one matrices, a particular subset are those matrices where the natural orbital occupancies are either zero or two exactly, and the density matrix has the characteristics of a projection operator. Such a density matrix is described as idempotent and has the special property that in a sense it equals its own square[192]. Idempotent matrices correspond to "pure" quantum mechanics in the sense that the system is in a single, pure state. For any isolated atom or molecule of N electrons, not interacting with its surroundings, the N-electron density matrix will be idempotent. However, due to the instantaneous interactions of the individual electrons, the one-electron density matrix will not be idempotent, since all of the one-electron states or orbitals are interacting with each other.

In atomic and molecular theory there is a special case, however. Within the Hartree-Fock approximation, no account is taken of electron correlation with the result that within HF theory, the one particle states are pure in the above sense, and hence the one-electron density matrix is idempotent. The natural orbitals of a wavefunction from HF theory have integral occupation numbers. As is known, post-HF treatments of electron correlation produce orbitals with non-integral occupation numbers and hence a non-idempotent matrix.

Although the true one-matrix must be non-idempotent, it has been proven that an idempotent matrix can describe the true density exactly[193,194], and hence an idempotent one-matrix would make an ideal model for the charge density. It has the advantage over the multipole model that it is quantum mechanically acceptable.

11.2.5 Basis Set Representation

The preceeding density matrices have been in their most general form as continuous functions, and would be better named as density kernels. The projection of the one-matrix into a basis set representation is relatively painless. Starting with our natural expansion (11.16) and expanding the natural orbitals into a basis set of m atomic orbitals $\chi_i(\mathbf{r})$ by the linear combination of atomic orbitals principle

$$\phi_i(\mathbf{r}) = \sum_{j=1}^{m} \chi_j(\mathbf{r}) c_{ji} \tag{11.20}$$

In this representation, the density matrix becomes a more conventional matrix P with elements P_{jk}

$$P = P_{jk} = \sum_i c_{ji} n_i c_{ki}^* \tag{11.21}$$

or equivalently

$$P = CNC^T \tag{11.22}$$

with $C = c_{ji}$ and $N = N_{ii} = n_i$, the diagonal matrix of natural orbital occupation number. A simplified statement of the density matrix is in terms of the contributions of the orbital products

$$\rho(\mathbf{r};\mathbf{r}') = \sum_{jk} P_{jk}\chi_j(\mathbf{r})\chi_k^*(\mathbf{r}') \tag{11.23}$$

In general, the atom centred basis function will be non-orthogonal giving an idempotency relation modified by the overlap matrix S

$$PSP = 2P \tag{11.24}$$

where the factor of two comes from working with the spin-traced density matrix and hence doubly occupied orbitals.

11.2.6 X-Ray Scattering

The introduction of density matrices into X-ray scattering is relatively trivial[195,196]. In the non-relativistic limit, the total scattering (sum of elastic and inelastic scattering) is a function of the two-electron density matrix and occurs at all scattering vectors (not just reciprocal lattice points), given as its ratio to the classical scattering of a free electron (I_{cl})

$$I_{tot}(\mathbf{H})/I_{cl} = N + 2\int\int \pi(\mathbf{r}_1,\mathbf{r}_2;\mathbf{r'}_1,\mathbf{r'}_2 exp(i\mathbf{H}(\mathbf{r}_1 - \mathbf{r}_2))d\mathbf{r}_1 d\mathbf{r}_2 \tag{11.25}$$

Our interest lies only in the elastically scattered intensity from a crystal however, and being a one-electron property wholly defined by the charge density it is defined by the diagonal of the one-matrix

$$I_{elastic}(\mathbf{H})/I_{cl} = |\int \rho(\mathbf{r};\mathbf{r}) exp(i\mathbf{H}\mathbf{r})d\mathbf{r}|^2 \tag{11.26}$$

Of more interest is the structure factor in terms of the density matrix and scaled relative to the total elastic scattering from a unit cell, obtainable by simply taking the square root of the above equation

$$F(\mathbf{H}) = \int \rho(\mathbf{r};\mathbf{r}) exp(i\mathbf{H}\mathbf{r})d\mathbf{r} \tag{11.27}$$

This can be recast in terms of the natural expansion of the one-matrix

$$F(\mathbf{H}) = \sum_i n_i \int \phi_i(\mathbf{r})\phi_i^*(\mathbf{r}) exp(i\mathbf{H}\mathbf{r})d\mathbf{r} \tag{11.28}$$

The density matrix formulation of the scattering of X-rays was later applied to investigate the difference in total and elastic scattering from density matrices at the HF and post-HF levels for atomic Beryllium[197]. This work is important because it draws attention to the differences in scattering curves with varying levels of correlation. Inelastic scattering, being a function of the two-electron density matrix is most affected by incorporation of electron correlation but the changes to the elastic scattering curve are not negligible.

11.3 Determination of the One-Matrix

The first attempts to directly determine the one-matrix[198] used the electrostatic and virial theorems as constraints in a fitting procedure of Slater functions for H_2^+, H_2, and He_2. The process

was successful except for the fact that one natural orbital had either a negative occupation number, or an occupation number greater than two. The subsequent approach[199] to this problem which ensured N-representability was the imposition of idempotency on the matrix. McWeeny has given an iterative means of returning to idempotency an almost idempotent matrix[192]

$$P_{n+1} = 3P_n^2 - 2P_n^3 \tag{11.29}$$

Generalising this equation to incorporate other constraints in the form of expectation values of operators on the one matrix

$$TrP\hat{O}_k = \langle O_k \rangle \tag{11.30}$$

using the method of Lagrange multipliers gives

$$P_{n+1} = 3P_n^2 - 2P_n^3 + \sum_k \lambda_k \hat{O}_k \tag{11.31}$$

This methodology was applied with some success to subsequent direct determinations of the one-matrix for small atoms and molecules[200,201,202].

11.4 Application to the Crystallographic Case

The first attempts to fit the one-matrix to structure factors were made by Coppens[203]. No restriction was placed upon the occupation of the density functions and therefore the density was in fact represented in terms of one and two centred orbital products in a minimal basis. No heed was paid to the N-representability of the density matrix. The general conclusion reached from this work was that severe linear dependencies among the orbital product functions existed, leading to very large correlation coefficients in the least squares procedure. The removal of poorly determined density functions such as two centre orbital products on atoms not bonded and also removal of all two centre terms is considered in refinement against several data sets[204,205,206]. The two centre orbital products are observed to be essential for realistic description of the charge density and a general description of the density in terms of one and two centred orbital products is seen to give reasonable charge densities. The individual values of orbital product occupancies however are not physically meaningful due to their severe correlations.

Clinton[207] was the first to produce and idempotent matrix from X-ray diffraction data, albeit simulated data. Structure factors were calculated from Stewart, Davidson and Simpson's bonded hydrogen atom[55] in H_2 and these were fitted in the least squares sense to a model density matrix derived from a $1s$ and a $2s$ basis set. In such a limited basis set, there is only one free parameter available in an idempotent matrix while there are two in the corresponding normalised but non-idempotent matrix. The non-idempotent matrix invariably fails to be N-representable, although it gives a slightly better fit to the structure factors. This is interesting from a practical point of view since the proofs[193,194] given that an idempotent matrix can reproduce a density exactly assumed an unlimited basis set. Given a limited basis set it is not unexpected that a non-idempotent matrix will have greater flexibility to describe a density, but this extra flexibility will come at the expense of N-representability.

The imposition of idempotency restricts the number of independent parameters in the matrix and hence will reduce the correlation problems encountered by Coppens. The number of conditions required to fix an idempotent matrix is[208]

$$K_I(M,N) = N(M-N) \tag{11.32}$$

where M is the number of basis functions used and N is the number of doubly occupied orbitals while for the normalised but non-idempotent matrix the number is

$$K_{NI}(M) = \frac{M(M+1)}{2} - 1 \tag{11.33}$$

The idempotent matrix is linear in the dimension of the basis set while the non-idempotent matrix is quadratic.

Examination of the effect of starting guess in the refinement of an idempotent density matrix has been performed for simulated data from the hydrogen molecule[209] and a recommendation of the HF density matrix is made.

So far, it has been assumed that the molecular states in the crystal are genuinely localised. While this is a fair assumption for organic crystal structures, it is not so for conductors and semiconductors where the states are delocalised over the whole crystal in bands. The appropriate generalisation of the basis functions to Bloch orbitals has been published[210].

The first application of the localised state density matrix to real experimental data has been performed on the Beryllium data set of Larsen and Hansen[211] by Massa and coworkers[212]. The fit to the data is excellent despite the limited basis set and proves that the formalism will work in real situations. Pecora has fitted an idempotent density matrix to positron annihilation data from a Cu-Ge alloy[213].

11.4.1 Thermal Effects

The multipole model of the charge density is a one-centred expansion of pseudoatoms. The treatment of thermal motion within the multipole model is of independently moving pseudoatoms, and the charge density of each pseudoatom is convoluted with the thermal parameters assigned to that nucleus. An obvious treatment of thermal motion for one-centre orbital products in the density matrix expansion is to convolute the charge density of that orbital product with the thermal parameters assigned to the nucleus on which it is centred. An appropriate practical treatment of thermal motion for two-centred orbital products does not suggest itself so easily[214]. A reasonable empirical estimate is to use the average of the temperature factors for the two centres[65,215]. In the case of an orbital product between bonded centres, the component parallel to the bond will be a good approximation since the rigid bond test[57,74] shows that this component seldom differs for the two atoms in question. Averaging the perpendicular components for the two atoms is more of an approximation. This procedure is even less rigorous when the two centres are not bonded and the rigid bond criterion does not apply, although low temperature experiments do reduce the degree of thermal motion considerably.

The greatest part of the thermal motion of molecules in crystals can be interpreted as a rigid body executing translational, librational and screw motions, the so-called TLS approach[216]. This

approximation comes about because the lattice modes are much lower in energy and therefore much more highly populated than the internal molecular modes. Additionally, the lattice modes involve a far greater magnitude of nuclear motion than the internal bond stretching and bending. Treatment of thermal motion of two-centre orbital products within the TLS formalism is much simplified[217].

Practical fits of density matrices for molecular systems incorporating thermal smearing have used the average temperature factor for two centre orbital products, in the fit of a minimal basis set to structure factors from crystalline formamide[215] and to transition metal d-orbitals in a copper complex[66].

11.5 Practical Application in DENMAT

The original work carried out on fitting density matrices to experimental data used the Fortran program DENMAT[218] kindly supplied by Sean Howard at the University of Wales, Cardiff. The density matrix is expressed in terms of products of standard basis set orbitals expressed as gaussian expansions such as STO-6G, 3-21G etc. The basis set is general but restricted to s and p type functions, and the populations of the orbital products are refined. The atomic positions and temperature factors are not refined and are assumed known from an independent source such as a neutron structure determination or a multipole refinement of X-ray data. In its standard form, no account is taken of anomalous scattering by the atomic core electrons. The starting guess is the HF density matrix computed by the GAMESS program.

11.5.1 Algorithm

The fitting algorithm is based on that of Pecora[213]. The usual χ^2 function is minimised

$$\chi^2 = \frac{1}{N_{obs}} \sum_{\mathbf{H}} w_{\mathbf{H}} ||F_{obs}(\mathbf{H}) - k|F_{calc}(\mathbf{H})||^2 \tag{11.34}$$

where k is the scale factor chosen to minimise the sum and the calculated structure factor is

$$F_{calc}(\mathbf{H}) = \sum_{j,k} P_{jk} T_{jk}(\mathbf{r}) exp(i\mathbf{Hr}) \int \chi_j(\mathbf{r}) \chi_k(\mathbf{r})^* exp(i\mathbf{Hr}) d\mathbf{r} \tag{11.35}$$

with T_{jk} the temperature factor assigned to the jk-th orbital product. In the case of more than one molecule per unit cell, the orbital products are transformed to their symmetry equivalent positions and a further summation over all molecules in the unit cell is performed.

The fit is performed by varying the P_{jk} to minimise χ^2. Two methods are available, both iterative. The first is to utilise the gradient vector $\nabla\chi^2$ and perform a steepest descent method. The elements of $\nabla\chi^2$ are computed as[218]

$$\frac{\partial \chi^2}{\partial P_{jk}} = -\sum_{\mathbf{H}} \frac{k w_{\mathbf{H}}}{N_{obs}|F_c(\mathbf{H})|} (|F_o(\mathbf{H})| - k|F_c(\mathbf{H})|).(F_c(\mathbf{H})(\frac{\partial F_c(\mathbf{H})^*}{\partial P_{ij}}) + \frac{\partial F_c(\mathbf{H})}{\partial P_{ij}}) F_c(\mathbf{H})^*) \tag{11.36}$$

For a reasonable sized basis set for a molecule this is a relatively large calculation. Given this vector, the current density matrix is perturbed by a small amount δ giving a new matrix

$$P' = P - \nabla\chi^2.\delta \tag{11.37}$$

The second method is less elegant but much less computationally demanding. Random perturbations to the matrix elements are made and if χ^2 is reduced, the perturbed matrix becomes the current one. If not, a new set of random perturbations are applied to the current matrix until a lower χ^2 value is obtained.

The above methods will produce a general matrix, neither normalised nor idempotent. If we wish to consider non-idempotent matrices, they should at least be normalised. This is easily performed by computing the current normalisation of the density matrix, PS, and then rescaling each element by the ratio of the desired normalisation to the current one. This is performed after each step of perturbation before computing the new χ^2. To produce an idempotent matrix, the McWeeny algorithm is used, suitably modified to take into account the non-orthogonality of the basis functions

$$P_{n+1} = \frac{3}{2}P_nSP_n - \frac{1}{2}P_nSP_nSP_n \tag{11.38}$$

This procedure is iterated until the value of $P_nSP_n - 2P_n$ is below a specified tolerance.

Chapter 12

DM refinements of formamide

12.1 Introduction

In collaboration with Dr. Sean Howard and as an extension to the published work[219], I have implemented some new features into the DENMAT code. The first is the normalisation routine to produce non-idempotent but normalised matrices. Output of a Fourier coefficient file to produce residual maps has also been added and this is particularly useful in evaluating the changes between the initial HF starting guess and the final fitted matrices.

A second more fundamental change has been the use of anomalous dispersion corrected structure factors as input data. Although the anomalous scattering for first row atoms with Molybdenum radiation is small, it is worth accounting for. This has been achieved by correcting the experimentally observed structure factors using the atomic core positions and temperature factors from a multipole refinement, which is performed before density matrix refinement proceeds.

The data set used in this work was collected at the University of Glasgow by Drs. Paul Mallinson and Chris Frampton. The molecule is formamide, space group $P2_1/n$, $Z = 4$ and the data were collected at 123K on a CAD4 automated diffractometer. After data merging there were 1789 reflections with $F > 3\sigma(F)$. A multipole refinement using XD gave $R = 2.540\%$ and was used as the source of atomic positions and temperature factors. The data were rescaled according to the multipole refinement and are therefore approximately on an absolute scale.

12.2 Minimal Basis Set

As a first approximation, a minimal basis set of gaussian contractions was used. The basis set chosen was the standard STO-6G basis[220,221], giving 18 basis function per molecule. The minimum number of data points required to uniquely determine an idempotent matrix of 18 basis functions is 72, while for the non-idempotent matrix it is 170. Both of these values are far less than the 1789 reflections used in the fit.

12.2.1 Hartree Fock Starting Matrix

A Hartree Fock calculation was carried out using the GAMESS code[222] to provide the initial density matrix. This matrix is of course idempotent. Before any refinement takes place, it is instructive to note how well this density compares with the experimental data. While the χ^2

and R factor give a rough guide to the agreement, more information is gained from the residual density which shows where the data and the current Hartree-Fock density are in disagreement in real space.

Figure 12.1 - Residual density for the STO-6G HF matrix. Contours at $0.1 e\text{Å}^{-3}$.

The most striking feature from this residual map is that the minimal basis Hartree Fock calculation has much more density in the oxygen lone-pair regions and too little in the carbonyl bond. Elsewhere, the agreement is not too bad, but there is a general underestimate of bonding density by the calculation. The agreement factors for the initial density matrix are reasonable (Table 12.1) showing that on the whole the HF guess isn't too bad a representation of the crystalline density.

	χ^2	$R(F)$	Scale
P_{HF}	19.806	5.255%	1.033
P_{Idemp}	7.725	3.802%	1.028
P_{Norm}	4.832	2.985%	0.918

Table 12.1 - Fit statistics for the STO-6G basis set.

An interesting feature is that the scale factor for the data is 1.033, appreciable different from the multipole value of 1.00. The reason for this is not obvious.

As mentioned previously, the total density $\rho\mathbf{r})$ does not provide a great deal of information so the Laplacian of the density, $\nabla^2\rho(\mathbf{r})$ will be used to assess the chemical sense of the fitted densities.

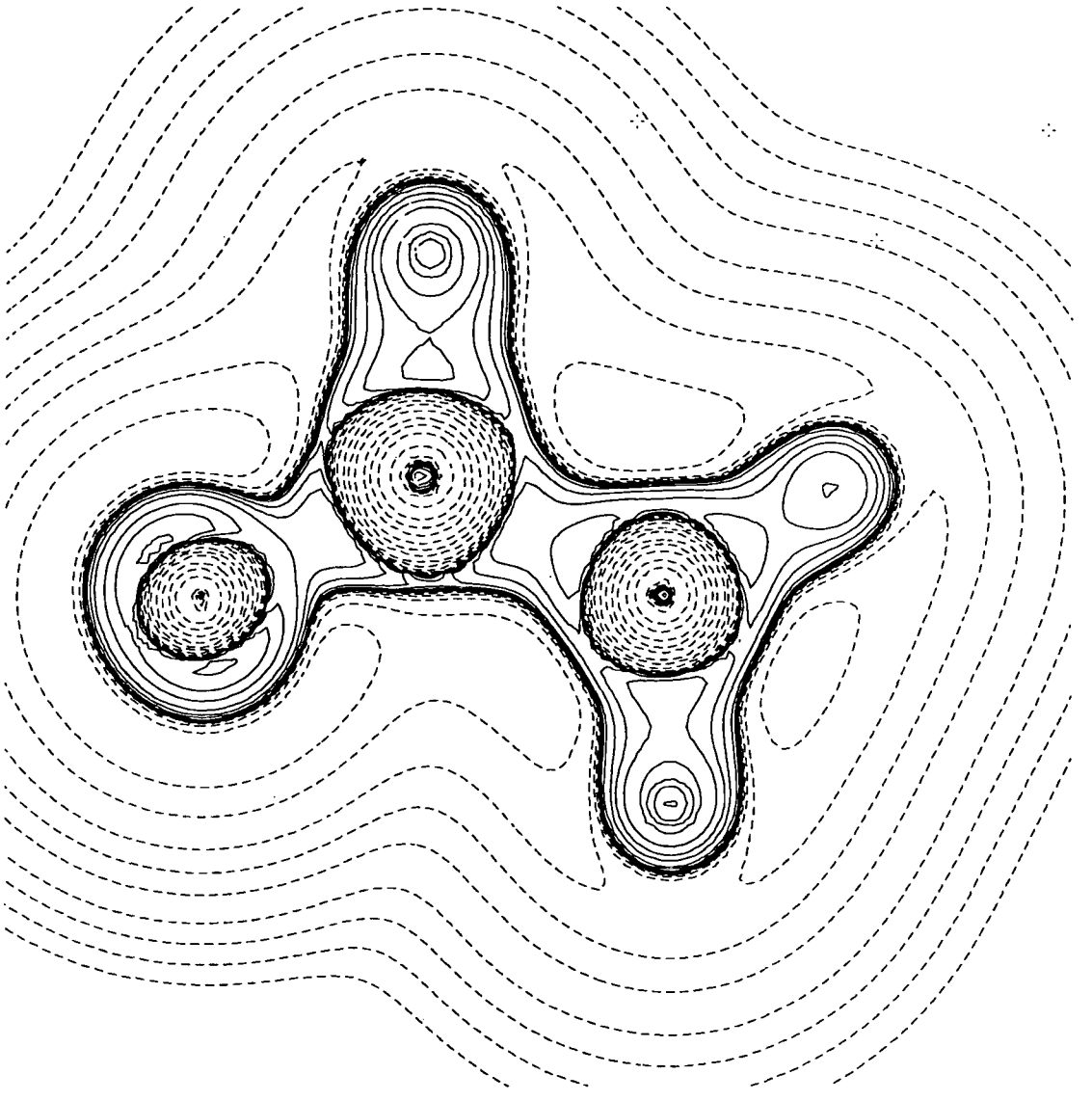

Figure 12.2 - STO-6G HF Laplacian map.

The Hartree Fock Laplacian map (Fig 12.2) is as expected with negative $\nabla^2\rho(\mathbf{r})$ in all covalent bonds. The lone-pairs on the oxygen atom appear a little too equatorial, and we know that this general area is where the experiment and theory are in most disagreement.

12.2.2 Idempotent Fitted Matrix

The next stage of the analysis was to vary the matrix elements while retaining the idempotency constraint. As Table 12.1 indicates, the fitted matrix is in far closer agreement to the data than the HF matrix, with a reduction in χ^2 from 19.806 to 7.725. The R factor is also substantially

improved from 5.255% to 3.802%. The experimental residual map (Figure 12.3) shows that the fitted matrix gives a better reproduction of the experimental density both in the oxygen lone-pair and carbonyl bond regions. There remain substantial deviation of up to 0.2eÅ^{-3} elsewhere in the molecule, but at least the most serious discrepancies have been reduced.

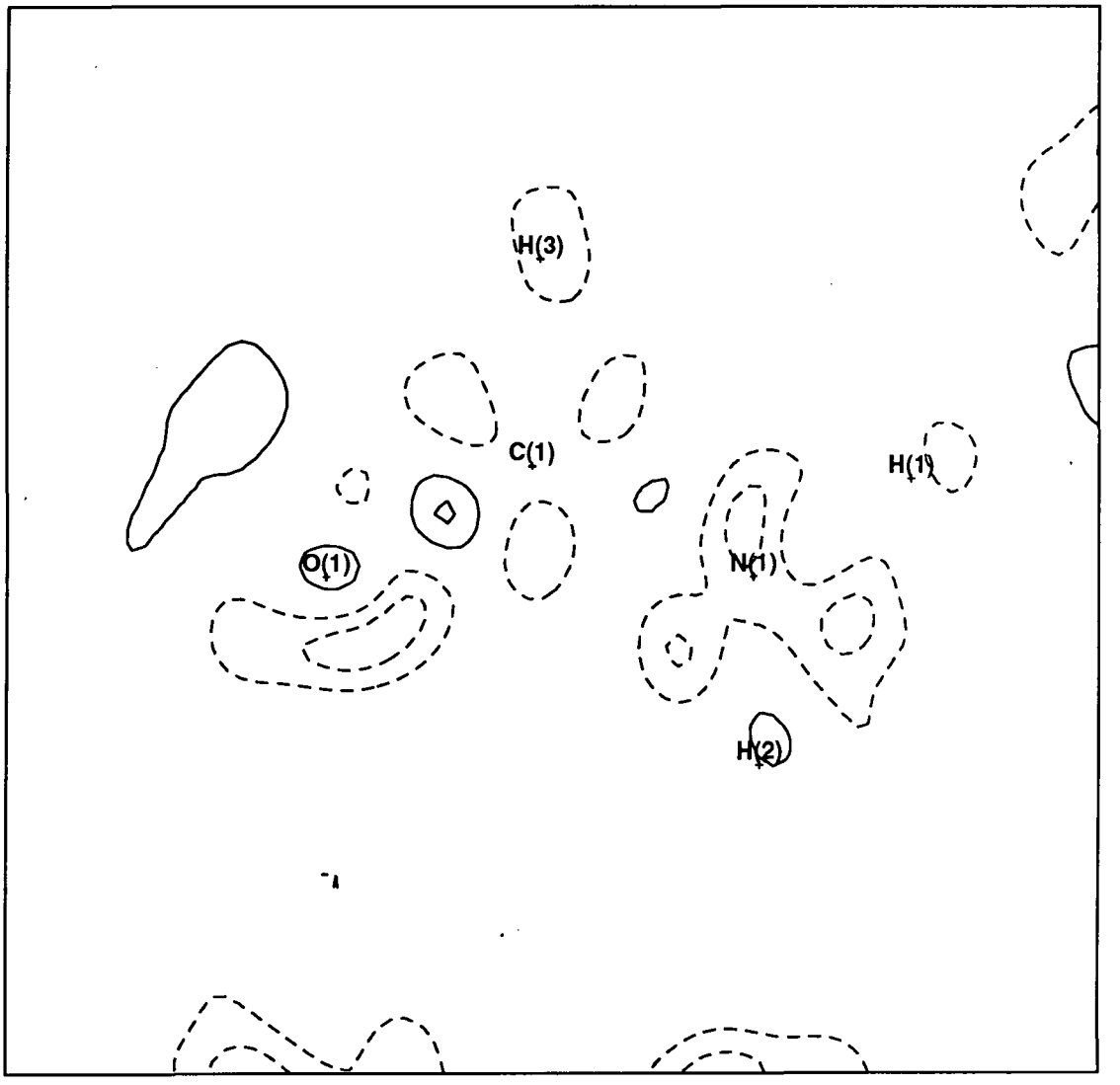

Figure 12.3 - Residual density for the STO-6G idempotent matrix. Contours at 0.1eÅ^{-3}.

This gives hope that the Laplacian distribution (Figure 12.4) from the fitted idempotent matrix will also be better than the HF one. Unfortunately, it is surprisingly poor, with unphysical features such as an effectively ionic carbonyl bond, no local concentrations of the charge corresponding to lone-pairs and an almost ionic C-N bond. It is obvious that the idempotent fitted matrix in this minimal basis set, while being N-representable is chemically unreasonable. The N-representability conditions on the charge density itself are that it be differentiable, normalised and everywhere positive[194]. Numerical analysis of the density shows that it is everywhere positive, and being expanded in a set of gaussian orbitals it will be differentiable. It is also normalised so although the density is N-representable, it is not chemically meaningful.

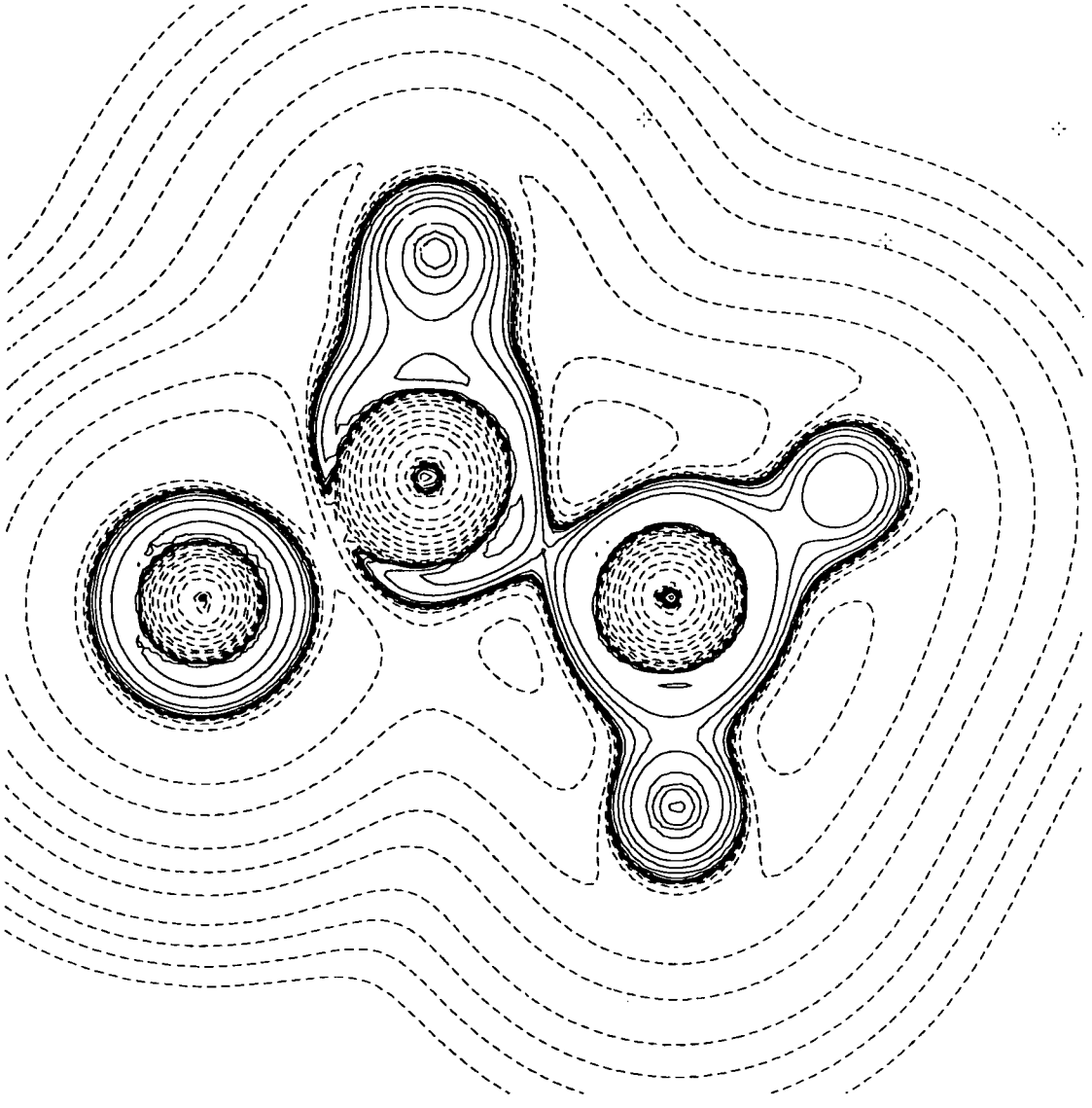

Figure 12.4 - STO-6G idempotent Laplacian map.

12.2.3 Normalised Fitted Matrix

The preceeding section has shown that the idempotent density matrix in the minimal STO-6G cannot simulatneously fit the data and give a chemically sensible Laplacian map. Starting with the idempotent fitted density matrix, the idempotency constraint was lifted to produce the best fitted normalised density matrix. Further improvements in the χ^2 function to a value of 4.832 and $R = 2.985\%$ were achieved. More worrisome is the refined scale factor for the normalised matrix of 0.918 compared the multipole scale factor of 1.00, which should be reasonably accurate.

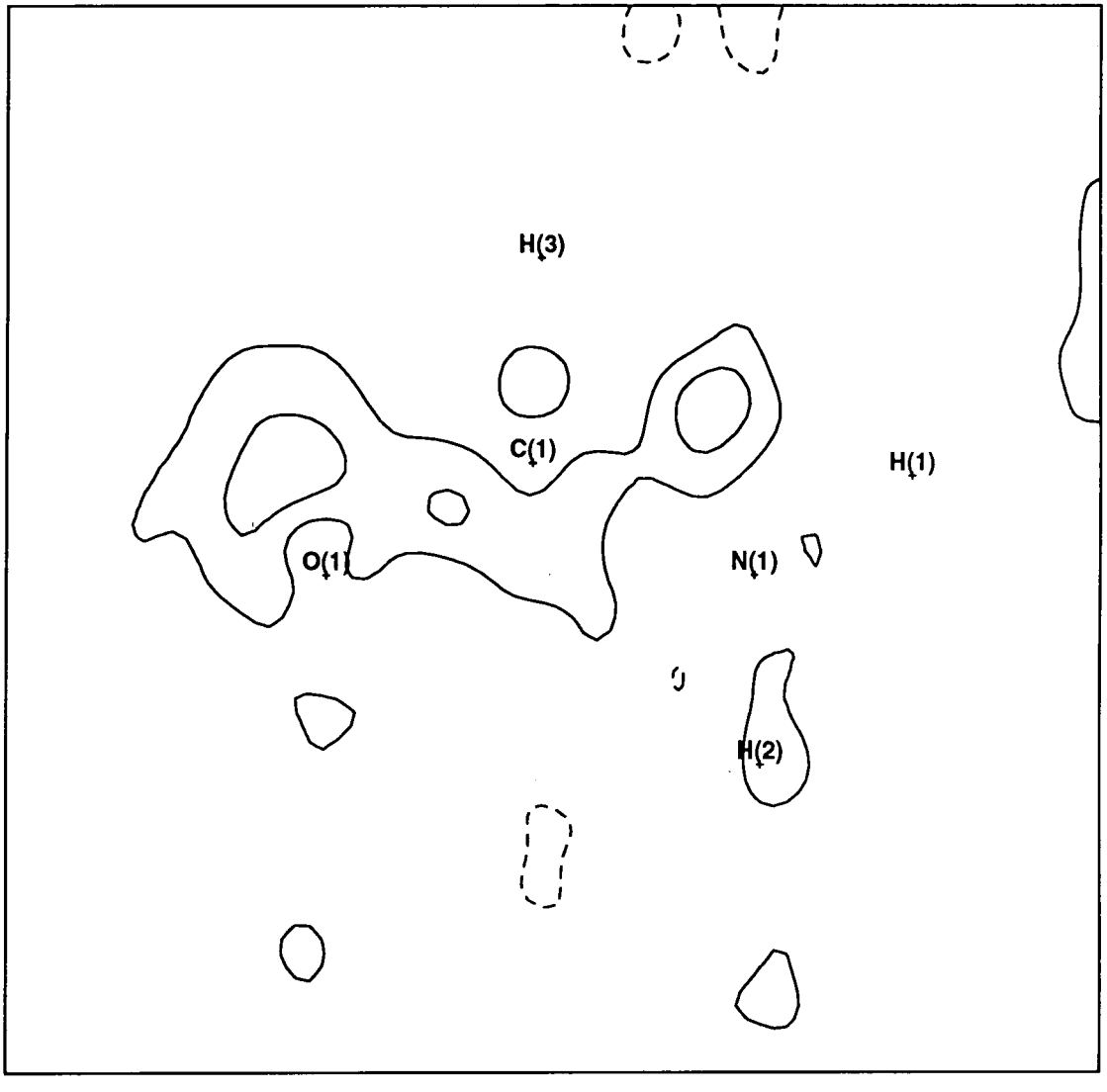

Figure 12.5 - Residual density for the STO-6G normalised matrix. Contours at 0.1eÅ^{-3}

The residual map for the normalised density matrix (Figure 12.5) is comparable to the one resulting from the idempotent fitted matrix. There are no gross features about the oxygen atom or in the carbonyl bond although there is a general lack of density in these areas. This is probably related to the scale factor discrepancy. There is also a relatively large peak outwith the molecule between H(1) and H(3). Despite the better value for χ^2, the residual map does not really indicate a substantially better fit to the data.

By lifting the idempotency constraint, there is no surety of producing either an N-representable density matrix or density. Examining firstly the density, numerical analysis shows that the density does take small negative values at several areas in the molecular plane, and hence is not quantum mechanically acceptable.

Turning to the density matrix, we might hope that by chance the eigenvalues remain between zero and two and an acceptable density matrix results. This is not the case in practice for the normalised matrix. The lowest eigenvalue is -1.424 while the highest is 4.762, both massively outside the required limits. In fact only eight of the eighteen eigenvalues lie between zero and two, with four negative and six greater than two.

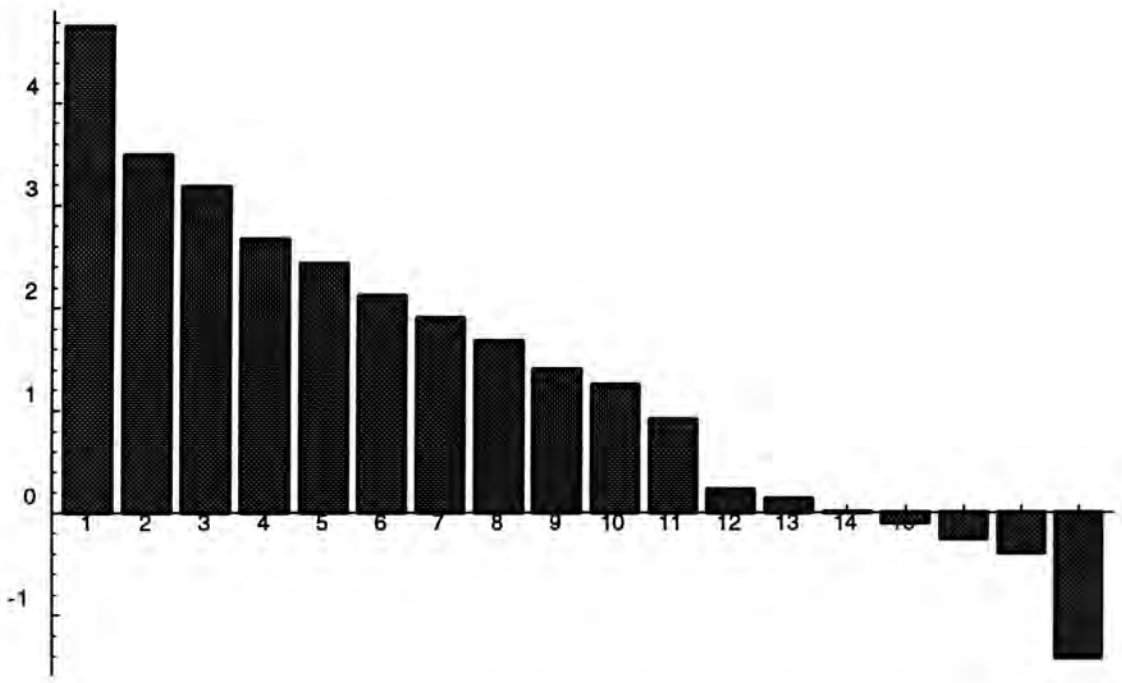

Figure 12.6 - Eigenvalue spectrum for the normalised STO-6G density matrix.

The spread of eigenvalues can be seen in the eigenvalue spectrum in Figure 12.6. The eigenvalues for the idempotent matrix are two for the first twelve natural orbitals and zero for the remaining six. There is no correspondence between the two spectra in this case.

The Laplacian map (Figure 12.7) for this fit is much better than the idempotent matrix. All bond are covalent with a negative $\nabla^2\rho(\mathbf{r})$ at the bond critical points. The lone-pairs are just about visible on the oxygen atom, and at more reasonable positions compared to the HF density.

12.2.4 Conclusions from STO-6G matrices

The first conclusion reached for the STO-6G density matrices is that the Hartree Fock density is in considerable disagreement with the experiment. The two possible causes are that the Hartree Fock density is accurate and the experiment differs due to solid state effects perturbing the free molecule density, or that the minimal basis set calculation is deficient, with the latter the more likely. The idempotent fitted density matrix is a far better reproduction of the experiment but gives a chemically unreasonable density and is therefore of little use. The normalised fitted density matrix gives a good fit to the experiment and a chemically reasonable Laplacian map. It has already been stated that an idempotent matrix may describe any reasonable density[195,196], and therefore there should be no gain in lifting the idempotency condition. However, this situation will only prevail in the case of a sufficiently flexible basis set. A minimal basis set obviously does not meet these criteria and substantial deviation from idempotency is required to make up for the basis set inadequacy.

A similar effect can occur in calculations in a minimal basis set. Inclusion of correlation in a minimal basis set calculation leads to unrealistically high "correlation". This is not true correlation but merely the calculation adapting in a way to make up for the minimal basis set.

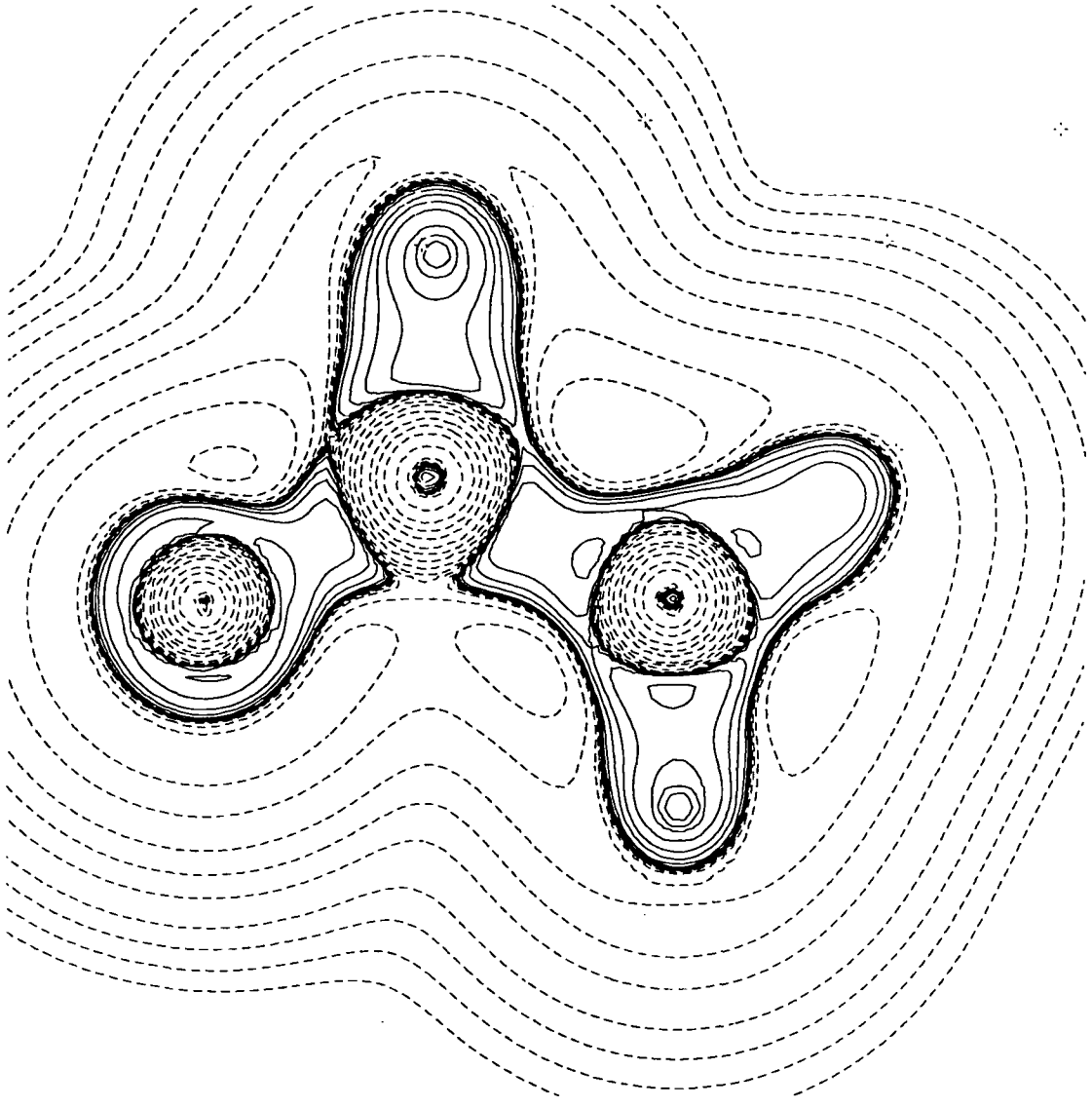

Figure 12.7 - STO-6G normalised Laplacian map.

The density matrix for a true, correlated wavefunction expanded in an infinite basis set will be of infinite order. It is known that the most rapidly convergent series approximation to the true wavefunctions is the natural expansion, and for a given number of terms, the approximation with the greatest overlap with the true wavefunction of a specified order is obtained by truncating the natural expansion at this order and renormalising the result[190]. A related question of more relevance in this case concerns the best approximation to the true one-electron density matrix. Given the true one-electron density matrix $\rho_o(\mathbf{r};\mathbf{r}')$ in an infinite basis set, the "best density" approximation to $\rho_o(\mathbf{r};\mathbf{r}')$ is trivially[223]

$$Tr(\rho(\mathbf{r};\mathbf{r}') - \rho_o(\mathbf{r};\mathbf{r}'))^2 = minimum \tag{12.1}$$

This best density approximation to order n is given as before by truncating the natural orbital expansion at the nth term and renormalising the result. Our main problem with the normalised fitted density matrix is that it is not N-representable. The above discussion suggests an obvious way to obtain the best density approximation to the normalised fitted density matrix which is

idempotent and hence N-representable. For formamide with 24 electrons, truncate the natural orbital expansion at twelve terms, and rescale the eigenvalues of these natural orbitals to two. The Laplacian map produced from this "best density" idempotent matrix is shown in Figure 12.8.

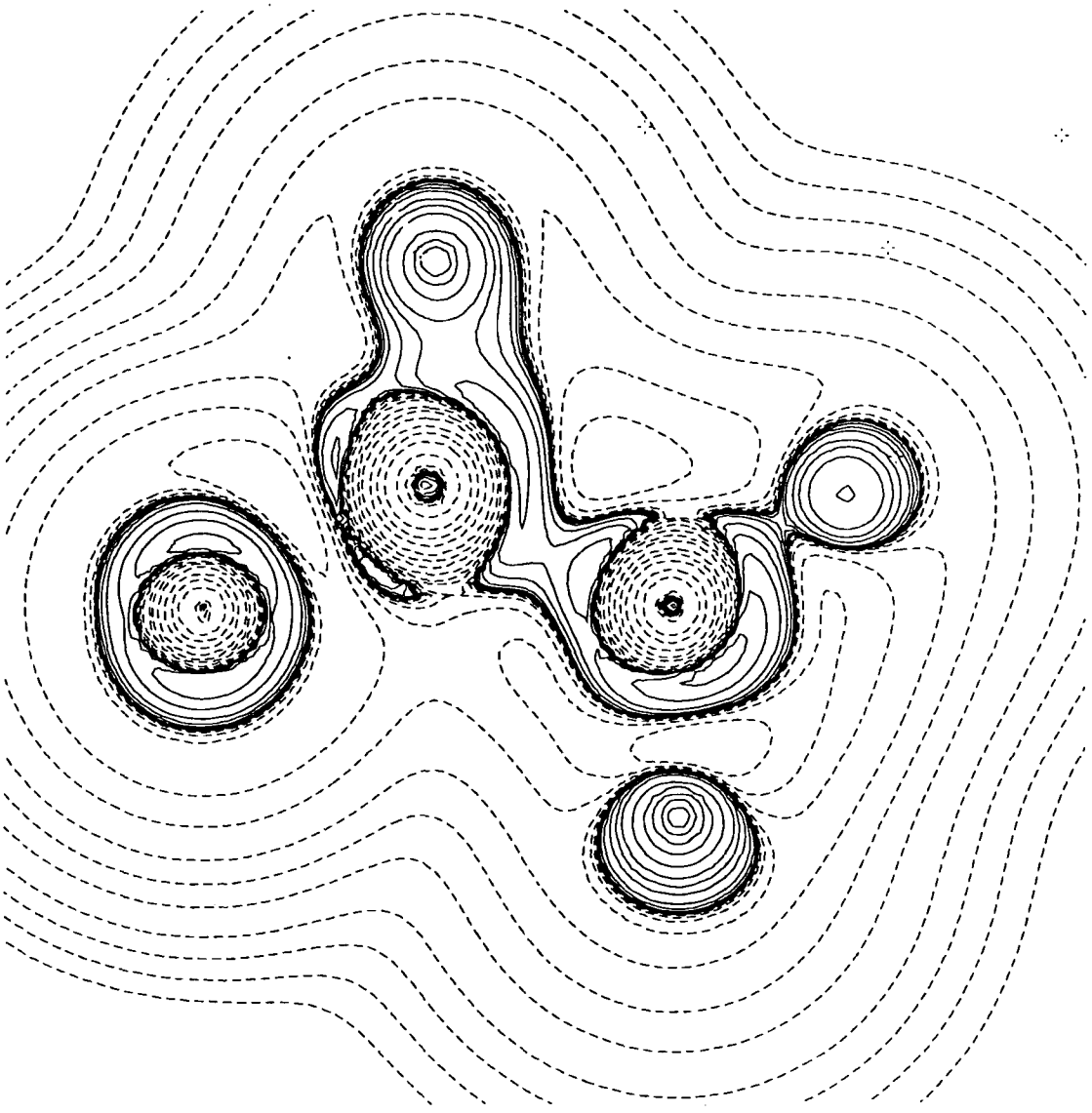

Figure 12.8 - STO-6G "best density" idempotent Laplacian.

It generally appears worse than the idempotent fitted matrix. While truncation of the natural expansion followed by renormalisation of the eigenvalues will provide the best approximation to an N-representable matrix, it may not be the best approximation to a markedly non N-representable one. The poor flexibility of the minimal basis set is almost certainly the cause of the large deviation from N-representability so no conclusions on the "best density" idea should be draw on this result alone.

12.3 Split-Valence Basis Set

The most obvious next stage of development is the use of a better quality basis set. In the next part of the work, the 6-31G split valence basis set[224] was used. For the formamide case this comprises 33 basis functions. The minimum number of data to uniquely fit an idempotent density matrix is 252 giving an approximate data to parameters ratio of ten, while for the non-idempotent matrix it is 560 data reducing the data to parameters ratio to approximately five.

12.3.1 Hartree Fock Starting Matrix

The residual for the Hartree Fock starting density (Figure 12.9) shows that the 6-31G Hartree Fock density is much closer to the experimental density than the corresponding minimal basis set calculation, although some of the features are common. There is still too much density in the calculated lone-pairs compared to the experiment while there is too little density in the carbonyl bond. The agreement in the remainder of the molecule is far better.

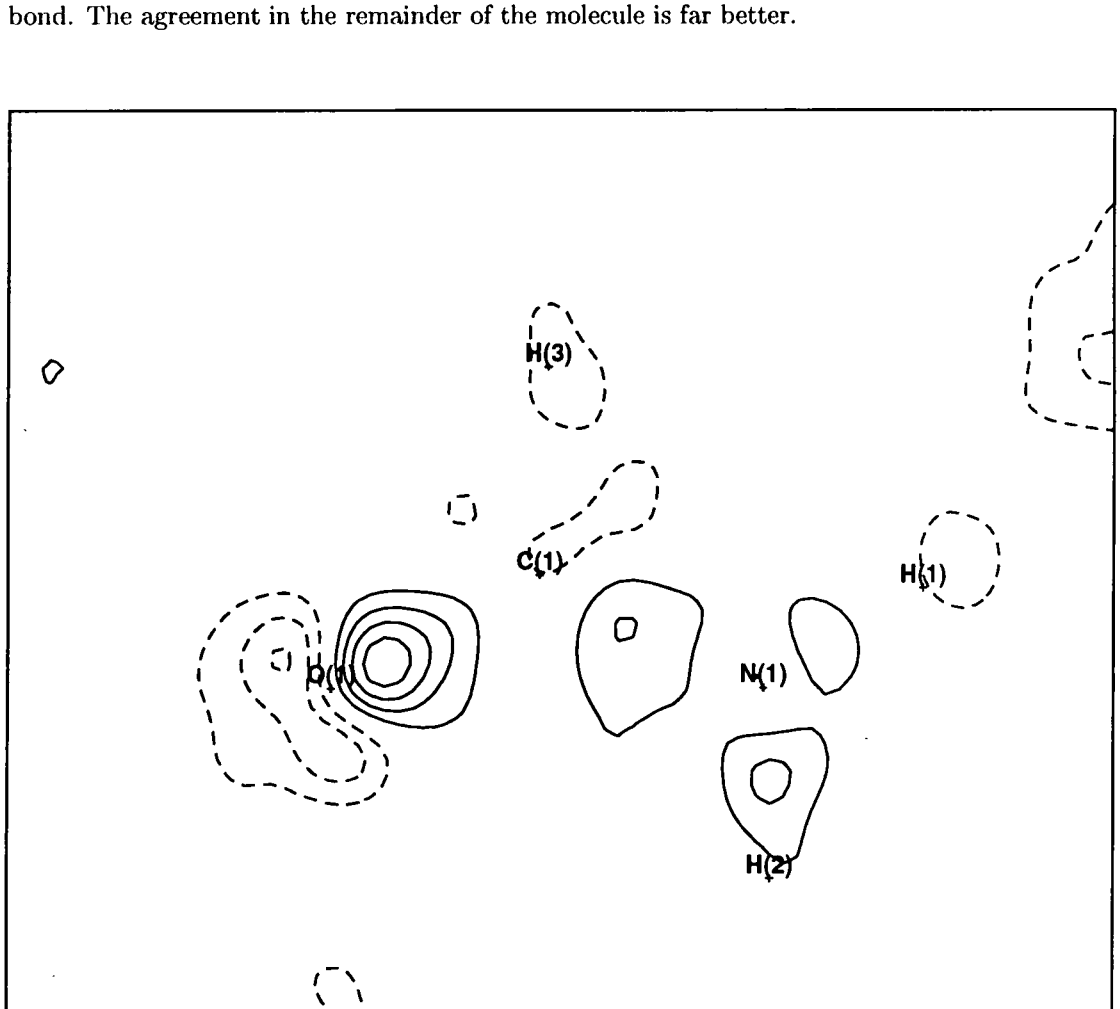

Figure 12.9 - Residual density for the 6-31G idempotent matrix. Contours at $0.1e\text{Å}^{-3}$.

The statistics for the fitted 6-31G density matrices along with the Hartree Fock calculated one are shown in Table 12.2. The calculated density matrix fits the data much better than the STO-6G calculated one with χ^2 reduced from 19.806 to 10.430, and R factor reduced from 5.255% to 3.531%. The scale factor is 1.026, a little closer to the multipole refined value.

	χ^2	$R(F)$	Scale
P_{HF}	10.430	3.531%	1.026
P_{Idemp}	9.969	3.494%	1.026
P_{Norm}	3.635	2.508%	1.004

Table 12.2 - Fit statistics for the 6-31G basis set.

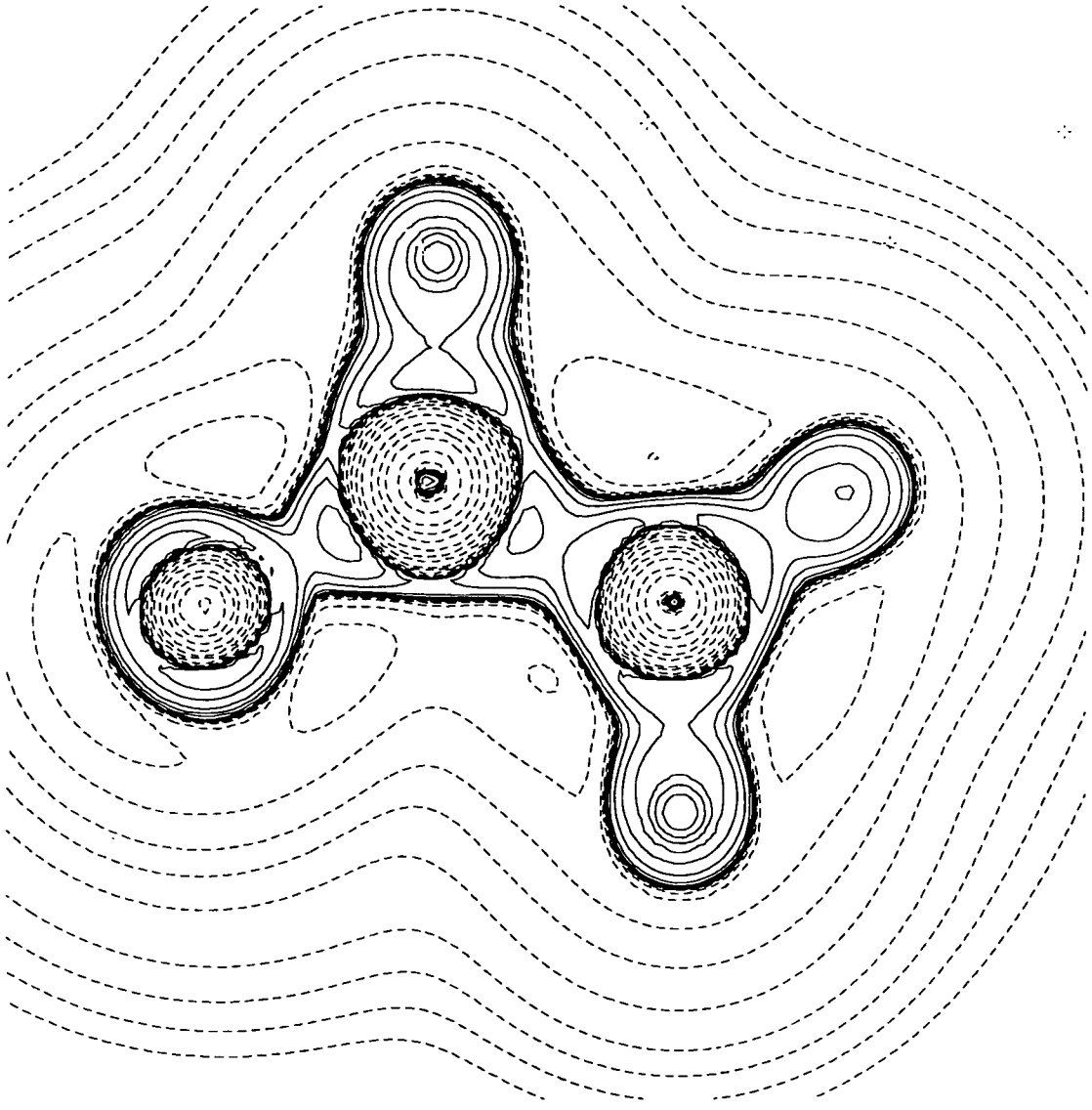

Figure 12.10 - Laplacian distribution for the 6-31G HF matrix.

The calculated Laplacian map in this basis is obviously reasonable. Compared to the STO-6G Laplacian, the oxygen atom lone-pairs are at less equatorial positions, closer to the positions given by the fitted normalised STO-6G matrix. This suggest that the deficiencies in the calculated density at the minimal basis set level are more likely to be the cause of the poor fit of that density

to the experiment in the oxygen lone-pair region, rather than solid state effects, although some discrepancy between the 6-31G density and the experiment still occurs here.

12.3.2 Idempotent Fitted Matrix

Refining the density matrix elements while retaining the idempotency requirement was the next step. The improvement in agreement factors is quite small, giving a higher χ^2 value than the even the idempotent fitted STO-6G matrix.

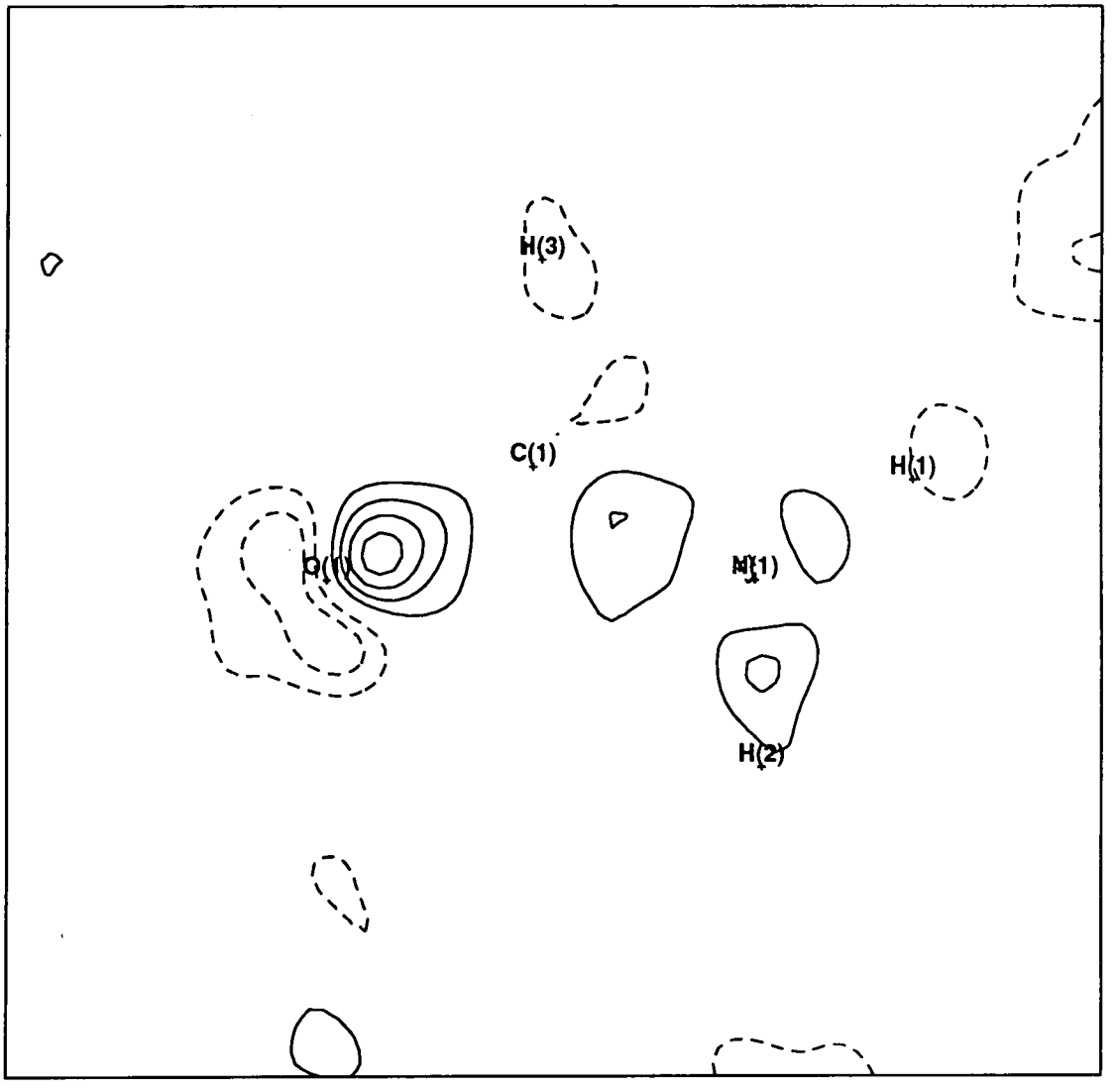

Figure 12.11 - Residual distribution for the 6-31G idempotent fitted matrix.

The residual map indicates that the main discrepancies around the oxygen between the calculated matrix and the data remain. Since both of the STO-6G fitted matrices managed to remove this feature, it is possible that the minimisation procedure used is stuck in a false minimum and that the final matrix obtained may be dependent upon the starting point. Given the number of basis functions, the topology of the χ^2 surface is probably far more complicated than the STO-6G one, making a global minimum much easier to locate in the latter case. The small differences

in agreement indices between the Hartree Fock and idempotent fitted matrices suggest that the idempotent matrix has changed only a little from the starting point, further evidence that a false minimum has been reached and the Laplacian distribution does not differ in markedly from the Hartree Fock one.

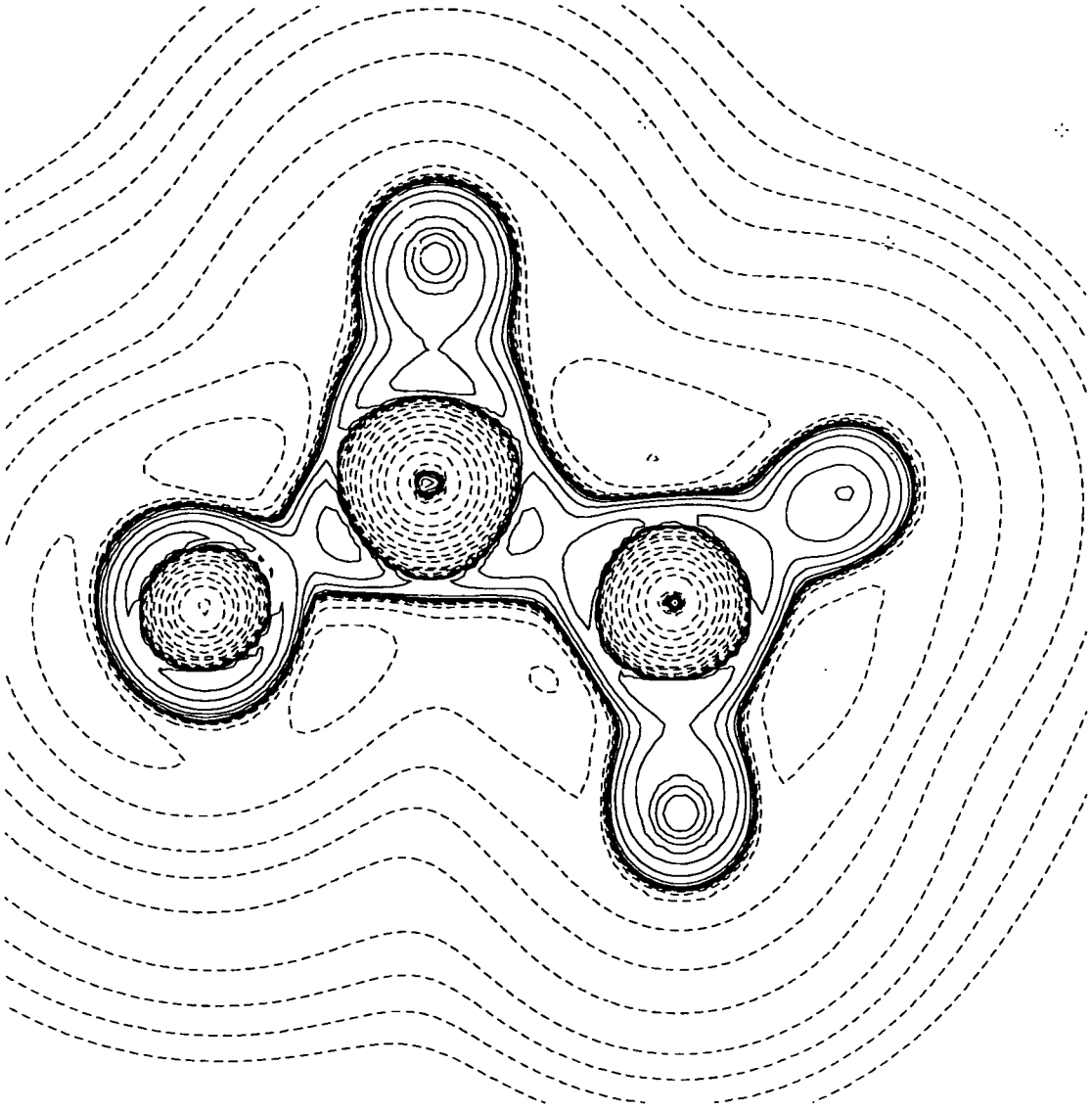

Figure 12.12 - Laplacian distribution for the 6-31G idempotent fitted matrix.

12.3.3 Normalised Fitted Matrix

The 6-31G normalised fitted matrix gives by far the best agreement factors with $\chi^2 = 3.635$ and $R = 2.508$. The scale factor is 1.004 which is the closest of all the matrices to the multipole refined value. According to the residual map, this matrix fits the data the best with no substantial residual in the oxygen lone-pair region or the carbonyl bond. This is further evidence that the 6-31G idempotent refinement has come to rest in a local rather than global minimum.

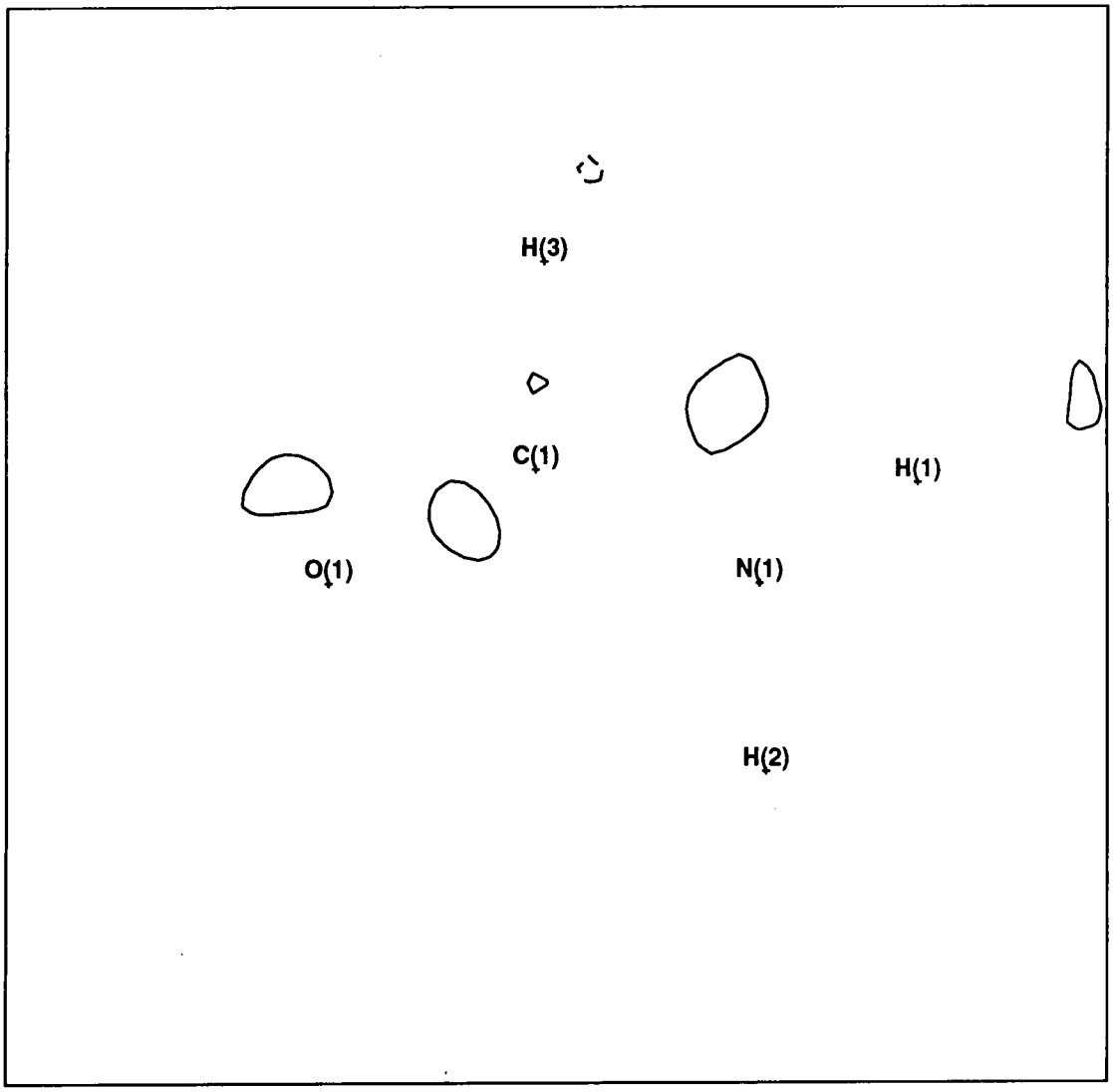

Figure 12.13 - Residual distribution for the 6-31G normalised fitted matrix.

Numerical analysis for the 6-31G normalised fit shows that the density goes slightly negative and therefore cannot be considered quantum mechanically acceptable. Of much greater interest in this case is the eigenvalue spectrum (Figure 12.14 - Note: four eigenvalues did not differ from zero in the second decimal place and are excluded from the graph). The eigenvalues of the STO-6G normalised matrix differed hugely from those of an idempotent matrix, but in this case the extra flexibility of the split-valence basis set leads to much smaller violations of the N-representability criteria. The smallest eigenvalue is -0.295 while the largest is 2.603. Of even greater interest is the shape of the eigenvalue spectrum. With no restrictions other than normalisation placed on the density matrix, the eigenvalue spectrum resembles an idempotent one. The first twelve natural orbitals have occupancies close to two, and their sum is 24.619, quite close to the idempotent value of 24.00. Of the remaining orbitals, three have small positive occupancies, seven have reasonably small negative occupancies, seven are close to zero and the remaining four effectively zero and excluded from the eigenvalue spectrum for this reason.

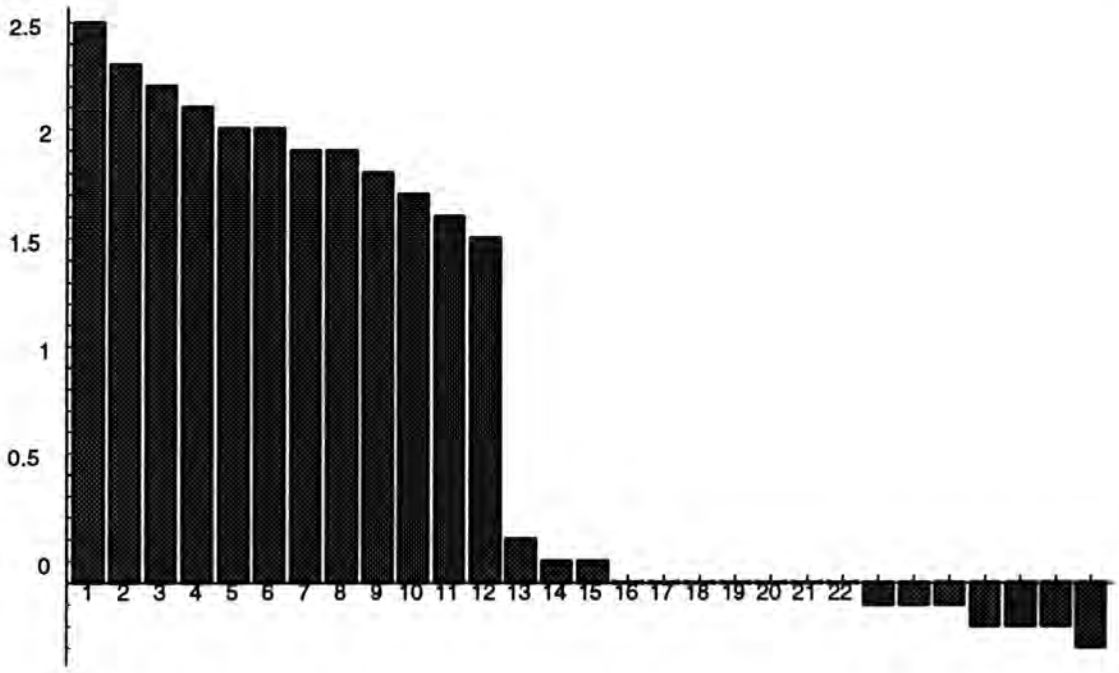

Figure 12.14 - Eigenvalue spectrum of the 6-31G normalised fitted matrix.

The shape of the eigenvalue spectrum suggests that the flexibility of the 6-31G basis set is approaching the level where an idempotent matrix will be sufficient to fully describe the density, but that a modest deviation from idempotency is still required in this basis.

The next stage of basis set expansion would conventionally be to add a set of *d* polarisation functions to carbon, oxygen and nitrogen to give the 6-31G* basis[225]. Assuming use of the set of six cartesian *d*-functions on each centre, the basis set size becomes 52 functions requiring a minimum of 480 data to provide a unique fit for the idempotent matrix and 1377 for the normalised matrix. The data to parameters ratio is unacceptable for the normalised matrix, and in any case, scattering from orbital products involving *d* functions is beyond the current program capabilities.

Another possibility would be the 6-311G extended basis set[226]. For formamide this amounts to 48 functions requiring 432 data for the idempotent fit and 1175 for the normalised fit. A possible advantage in using 6-311G is that it is "correlation-consistent", *i.e.* the radial exponents are energy optimized in a correlated calculation as opposed to STO-6G and 6-31G which are optimized at the Hartree Fock level. A disadvantage is that the extra function is a diffuse function and diffuse functions in real space project only into the lowest angle data in reciprocal space and hence will probably be poorly determined.

The Laplacian distribution (Figure 12.15) for the 6-31G normalised fitted density matrix is chemically sound, with all bonds well defined. The oxygen lone-pairs are also well defined, although smaller in extent than the theoretical equivalents, and at slightly more polar angles than usually seen in calculated maps. The only feature not convincing is the diffuseness and slightly lop-sided appearance in the region of H(3). The scattering by hydrogen is of course weak in X-ray studies and underdetermination of the orbital products involving H(3) centred functions

could be the cause.

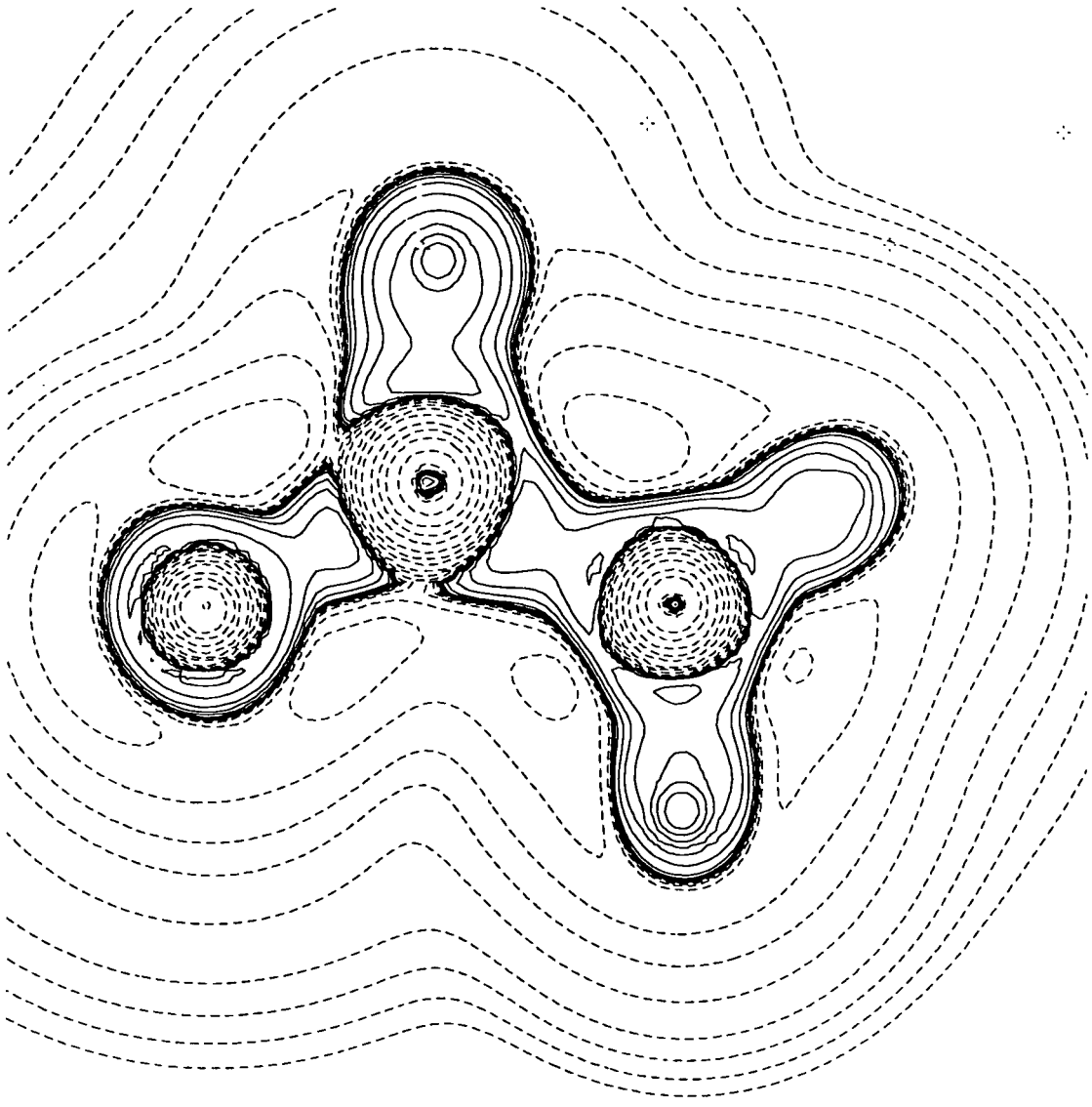

Figure 12.16 - Laplacian distribution for the 6-31G normalised fitted matrix.

12.3.4 Conclusions from 6-31G matrices

The Hartree Fock calculated density with the 6-31G basis set is in much better agreement with the experimental data than the STO-6G calculated matrix. The idempotent fitted 6-31G matrix is probably not the best idempotent 6-31G density matrix since the evidence presented suggest that the minimisation algorithm has settled into a local minimum of the χ^2 function.

The best fitted density in terms of agreement to the data is the normalised 6-31G matrix. It has the lowest agreement indices of all and a chemically informative Laplacian distribution. The eigenvalue spectrum is closer to N-representability than the corresponding STO-6G one, and in fact resembles an idempotent eigenvalue spectrum. It is known that in a sufficient basis set an idempotent matrix can describe the true density, and hence the deviation from idempotency of the fitted normalised matrix for any given basis set could be a useful indicator of basis set sufficiency.

The "best density" idea truncated at twelve terms to give an idempotent matrix with the 6-31G basis gives a reasonable Laplacian map (Figure 12.17).

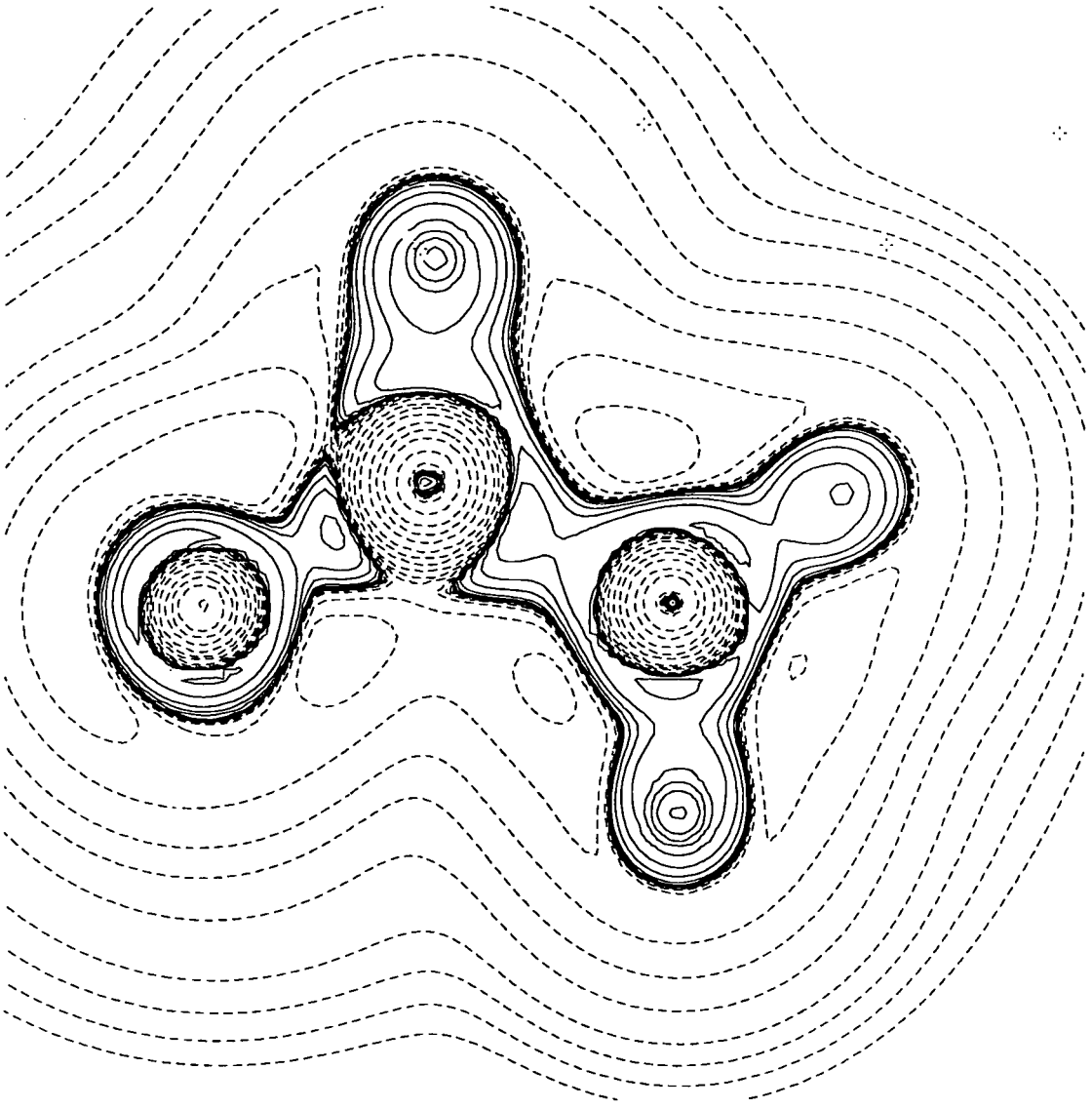

Figure 12.17 - Laplacian distribution for the "best density" idempotent matrix.

The lop-sidedness of H(3) has gone but the lone-pairs on the oxygen atom are markedly different in extent, although their positioning is consistent with the normalised matrix. Due to software limitations no values for the agreement indices are available and also there is no way currently to produce a residual map for the "best density" idempotent matrix. The similarity of the oxygen atom here compared to the normalised density matrix suggests that the residual features in this area may have been reduced but without hard evidence it is difficult to be conclusive.

Within the best density idea, there are other alternative ways of producing an N-representable matrix from the fitted normalised one. Truncating the expansion at a higher level should improve the correspondence between the two matrices. As a test, the eigenvalues of the first seven natural orbitals which are all greater than zero were set to two. Summing all of the positive eigenvalues

gives only 23.485 electrons so rescaling of some of the eigenvalues is necessary. There are 15 eigenvalues with $0.0 < n_i \leq 1.970$ so rescaling these eigenvalues to normalise the matrix will given the N-representable density matrix closest to the fitted matrix. A slight complication arises since rescaling of the largest matrix makes it greater than two, but this is overcome by setting this eigenvalue to two and rescaling the other positive eigenvalues. This natural orbital expansion has 22 terms.

An alternative would be to reset the eigenvalues greater than two to exactly two, exclude the negative eigenvalues with $n_i < -0.017$ and add an equal amount to all of the remaining eigenvalues until a normalised matrix results. This method gives 25 terms, and maximum agreement term for term with the eigenvalues of the complete normalised matrix. In practice, both methods give an imperceptibly different Laplacian distribution and therefore the former method is used.

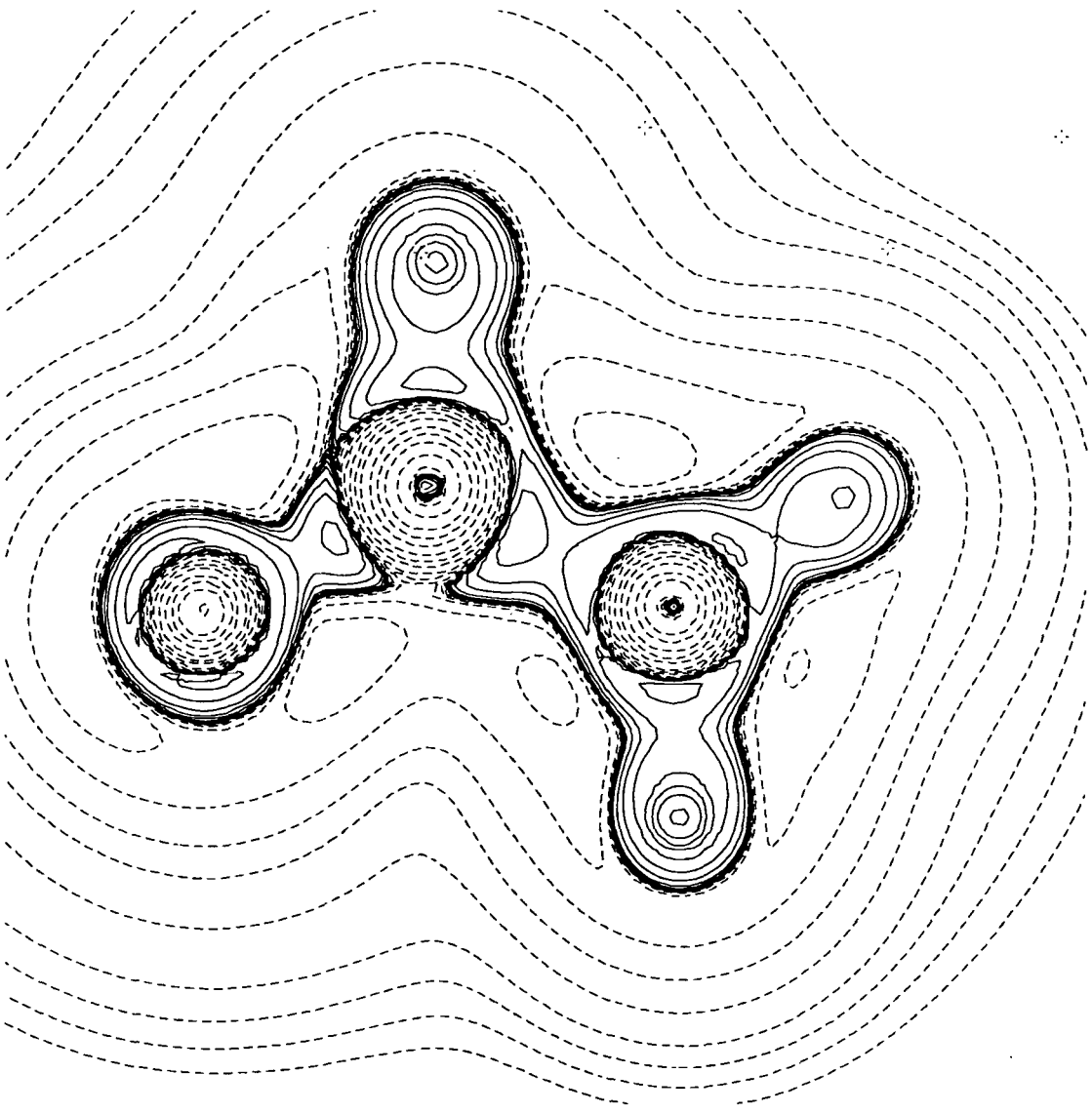

Figure 12.18 - Laplacian distribution for the "best density" matrix.

This matrix should be the best N-representable density matrix available in terms of agreement with the data. One-electron properties calculated from it should be closer to the true experimental

values than the 6-31G idempotent fitted matrix, even in the case where the idempotent method finds a true minimum.

12.4 Gradient Information and False Minima

All of the fitted matrices reported in this work were obtained by the random perturbation approach. While rather brutalist and unelegant, this method consistently returned lower χ^2 values than the gradient based techniques, which always found some local minimum less optimal than the random technique.

Assuming that the problem of false minima could be solved, the gradient based approach has the major disadvantage that $\nabla\chi^2$ needs to be evaluated in every step. In the early stages of a refinement where many of the elements of $\nabla\chi^2$ are large, big gains in χ^2 occur at each step and the efficiency of the algorithm is good. As convergence is approached far too long is spent computing $\nabla\chi^2$ for the small gains at each step, and the random method becomes more economical.

One way to improve efficiency while retaining the use of gradient information was implemented in the code. This involved optimising the value of δ by Brent's Method[227] when updating the density matrix at each step

$$P' = P - \nabla\chi^2.\delta \tag{12.2}$$

to give the greatest gain in χ^2 for that iteration. In the early stages of refinement, the steps are so big that the matrix is perturbed so far from idempotency that the McWeeny algorithm diverges, so the maximum value of δ has to be limited at the start. As convergence is approached, the elements of $\partial\chi^2/\partial P_{ij}$ become so small that they contain little useful information, and their errors are probably of similar magnitude to their values. The net effect is that the refinement moves slowly around a flat bottom and has to be terminated. For normalised density matrices, this method finds the same minimum as the random perturbation technique, but always converges on a higher minimum in the idempotent case.

A disadvantage of both methods over the conventional least-squares approach outlined in Appendix A is that no variance-covariance matrix is produced. This would be particularly useful in density matrix refinement to determine which parameters are poorly determined and which are heavily correlated. A further computational project would be to implement full least squares with inversion of the normal equations but this was outside the time limitations of the project.

12.5 Basis Set Expansion

The next step to even better fits to experimental data should be expansion of the basis set. A few difficulties become apparent though. Firstly, the "standard" basis sets in common usage are radially optimized in the sense of producing the best energy in some trial calculations on isolated gas-phase molecules. One can certainly envisage basis sets which give reasonable energies but much poorer densities, so perhaps radially optimizing basis sets with the charge density in mind as an additional criterion to the energy would be sensible. Such basis sets would obviously give better values for all one-electron properties.

A second problem is that the density of an isolated molecule is likely to be more diffuse than that of the same molecule in a crystal, where electron-electron repulsion with the charge densities of neighbouring molecules will tend to make the density more compacted and truncate the exponential decay to zero with distance. Radially optimized basis sets for molecules in crystals would likely differ from the corresponding free molecule functions for large r.

Polarisation functions of higher angular momenta, specifically a shell of d functions on the heavier atoms would be one obvious improvement to the 6-31G basis set, but increases the number of orbital products quite substantially, diminishing the data to parameters ratio. The equation given in the previous chapter for the minimum number of data to uniquely fix a density matrix with a basis set of any particular dimension assumed the data were uncorrelated and noiseless. We know that information on the valence density is carried predominantly by the low angle data, so although we have 1789 data in the refinement, the higher angle reflections will carry very little information for most of the density matrix parameters.

This problem is further exacerbated for the hydrogen atoms which scatter very weakly. A customised basis set with a single $1s$ function with suitably optimized radial exponent on the hydrogen atoms would probably eliminate some of the poorly determined orbital products, for example perhaps reducing the lop-sidedness of H(3) in the 6-31G normalised fit.

The best basis set would be one with the minimum number of parameters, all as uncorrelated as possible. For both basis sets used in this work, the normalised matrix gives better fits than the idempotent matrix in the same basis. The eigenvalue spectrum analysis suggests that the idempotent matrix will give as good a fit as the normalised one with a sufficient basis set. This agrees with the theoretical work stating that an idempotent matrix can describe any density. It is also known that the idempotency constraint acts to reduce parameter correlation in addition to substantially reducing the total number of parameters[218]. An appropriate basis set has the importance of allowing the idempotency constraint to be retained, increasing the chance of a unique, well defined matrix.

Chapter 13

References

(1) R.L. Weber, "Pioneers of Science - Nobel Prize Winners in Physics", Adam Hilger, Bristol (1988).

(2) P. Debye, *Ann. Phys.*, **46**, 809 (1915).

(3) P. Debye, P. Scherrer, *Phys. Z.*, **19**, 474 (1918).

(4) W.L. Bragg, R.W. James, C.H. Bosanquet, *Phil. Mag.*, **44**, 433 (1922).

(5) W.H. Bragg, *Proc. Roy. Soc. (London)*, **33**, 301 (1921).

(6) A. Veillard, *Chem. Rev.*, **91**, 743-766 (1991).

(7) J.K. Labonowski, J.W. Andzelm, "Density Functional Methods in Chemistry", Springer-Verlag, New York (1991).

(8) R.G. Parr, W. Yang, "Density-Functional Theory of Atoms and Molecules", Oxford University Press, New York (1989).

(9) T. Ziegler, *Chem. Rev.*, **91**, 651-667 (1991).

(10) W. Kohn, A.D. Becke, R.G. Parr, *J. Phys. Chem.*, **100**, 12974-12980 (1996).

(11) L. Szasz, "Pseudopotential Theory of Atoms and Molecules", Wiley, New York (1985).

(12) D. Feil, *Isr. J. Chem.*, **16**, 103 (1977).

(13) M. Born, *Proc. Roy. Soc. (London)*, **A179**, 69 (1941).

(14) H.M. James and G.W. Brindley, *Phil. Mag.*, **12**, 81 (1931).

(15) P. Debye, *Verh. der Deutsch. Phys. Ges.*, **xv**, 678, 738, 867 (1913).

(16) P. Debye, *Ann. der Phys.*, **xliii**, 49 (1914).

(17) M. Born, *Rep. Prog. Phys.*, **9**, 294 (1942).

(18) D.R. Hartree, *Camb. Phil. Soc. Proc.*, **xxiv**, 89 (1928).

(19) R.W. James, I. Waller and D.R. Hartree, *Proc. Roy. Soc. (London)*, **A, cxviii**, 334 (1928).

(20) L.H. Thomas, *Camb. Phil. Soc. Proc.*, **xxiii**, 542 (1927).

(21) E. Fermi, *Z. Phys.*, **xlviii**, 73 (1928).

(22) "International Tables for Crystallography", Volume IV (1974), pp. 72 and 103, Kynoch Press, Birmingham.

(23) R. McWeeny, *Acta Cryst.*, **4**, 513 (1951).

(24) H.M. James and V.A. Johnson, *Phys. Rev.*, **56**, 119 (1939).

(25) R.E. Franklin, *Acta Cryst.*, **3**, 107 (1950).

(26) G.E. Bacon, *Acta Cryst.*, **5**, 492 (1952).

(27) J.M. Foster and S.F. Boys, *Rev. Mod. Phys.*, **32**, 300 (1960).

(28) J. Pipek and P.G. Mezey, *J. Chem. Phys.*, **90**, 4916 (1989).

(29) C. Edmiston and K. Reudenberg, *Rev. Mod. Phys.*, **35**, 457 (1963).

(30) R. McWeeny, *Acta Cryst.*, **5**, 463 (1952).

(31) R.S. Mulliken, *J. Chem. Phys.*, **23**, 1833 (1955).

(32) R. McWeeny, *Acta Cryst.*, **6**, 631 (1953).

(33) R. McWeeny, *Acta Cryst.*, **7**, 180 (1954).

(34) E. Clementi and H. Popkie, *J. Chem. Phys.*, **57**, 487 (1972).

(35) B. Dawson, *Acta Cryst.*, **17**, 997 (1964).

(36) B. Dawson, *Acta Cryst.*, **17**, 990 (1964).

(37) B. Dawson, *Aust. J. Chem.*, **18**, 595 (1965).

(38) B.T.M. Willis, *Proc. Roy. Soc. (London)*, **A274**, 122 and 134 (1963).

(39) J.A.K. Duckworth, B.T.M. Willis and G.S. Pawley, *Acta Cryst.*, **A25**, 482 (1969).

(40) B. Dawson, *Proc. Roy. Soc. (London)*, **A298**, 264 (1966).

(41) F.C. von der Lage and H.A. Bethe, *Phys. Rev.*, **71**, 612 (1947).

(42) P. Coppens in *International Tables for Crystallography*, Volume B (1993), Luwer Academic Publihing, Dordrecht.

(43) R.F. Stewart, *J. Chem. Phys.*, **51**, 4569 (1969).

(44) E. Clementi, C. Roetti, *Atomic Data and Nuclear Data Tables*, **14**, 177 (1974).

(45) R.F. Stewart, *J. Chem. Phys.*, **58**, 1668 (1973).

(46) B.M. Craven, H.P. Weber and X. He, *Tech. Report TR-87-2*, Department of Crystallography, University of Pittsburgh.

(47) J. Epstein, J.R. Ruble and B.M Craven, *Acta Cryst.*, **B38**, 140 (1982).

(48) R.F. Stewart, *Acta Cryst.*, **A32**, 565 (1976).

(49) N.K. Hansen and P. Coppens, *Acta Cryst.*, **A34**, 909 (1978).

(50) T. Koritsanszky, S.T. Howard, T. Richter, P.R. Mallinson, Z. Su, N.K. Hansen, "XD - A Computer program package for multipole refinement and analysis of charge densities from X-ray diffraction data", 1995.

(51) P. Coppens, T.N. Guru Row, P. Leung, E.D. Stevens, P.J. Becker and Y.W. Yang, *Acta Cryst.*, **A35**, 63 (1979).

(52) K.L. McCormack, P.R. Mallinson, B.C. Webster and D.S. Yufit, *J. Chem. Soc., Faraday Trans.*, **92**, 1709 (1996).

(53) K. Kurki-Suonio, *Isr. J. Chem.*, **16**, 115 (1977).

(54) R.H. Blessing, *Acta. Cryst.*, **B51**, 816 (1995).

(55) R.F. Stewart, E.R. Davidson and W.T. Simpson, *J. Chem. Phys.*, **42**, 3175 (1965).

(56) F.H. Allen, O. Kennard, D.G. Watson, L. Brammer, A.G. Orpen, R. Taylor, *J. Chem. Soc., Perkin Trans. 2*, Suppl. 1 (1987).

(57) F.L. Hirshfeld, *Acta Cryst.*, **B27**, 769 (1971).

(58) F.L. Hirshfeld, *Isr. J. Chem.*, **16**, 198 (1977).

(59) B.N Figgis, P.A. Reynolds and S. Wright, *J. Am. Chem. Soc.*, **105**, 434 (1983).

(60) Newton, M.D. *J. Chem. Phys.*, **51**, 3917 (1969).

(61) B.N. Figgis, B.B. Iversen, F.K. Larsen and P.A. Reynolds, *Acta Cryst.*, **B49**, 794 (1993).

(62) B.N Figgis, P.A. Reynolds and R. Mason, *J. Am. Chem. Soc.*, **105**, 440 (1983).

(63) E.D. Stevens, P. Coppens, *Acta Cryst.*, **A35**, 536 (1979).

(64) A. Holladay, P. Leung and P. Coppens, *Acta Cryst.*, **A39**, 377 (1983).

(65) K. Tanaka, *Acta Cryst.*, **A44**, 1002 (1988).

(66) K. Tanaka, *Acta Cryst.*, **B49**, 1001 (1993).

(67) P.R. Mallinson, T. Koritsanszky, E. Elkaim, N. Li and P. Coppens, *Acta Cryst.*, **A44**, 336 (1988).

(68) F.L Hirshfeld, *Acta Cryst.*, **A32**, 239 (1976).

(69) M. Born and K. Huang, "Dynamical Theory of Crystal Lattices", pp. 406, Oxford University Press, London (1954).

(70) M. Born, J.R. Oppenheimer, it Ann. der Phys., **84**, 457 (1927).

(71) P.M. Kozlowski and L. Adamowicz, *Chem. Revs.*, **93**, 2007 (1993).

(72) S.T. Howard and P.R. Mallinson, "Experimental Electron Densities", unpublished.

(73) J. Cosier and A.M. Glazier, *J. Appl. Cryst.*, **19**, 105 (1986).

(74) M. Harel and F.L. Hirshfeld, *Acta Cryst.*, **31**, 162 (1975).

(75) P. Coppens *et al.*, *Acta Cryst.*, **A40**, 184 (1984).

(76) A. El Haouzi, N.K. Hansen, C. Le Henaff, J. Protas, *Acta Cryst.*, **A52**, 291 (1996).

(77) J.A. Ibers, *Acta Cryst.*, **22**, 604 (1967).

(78) R.H. Blessing, C. Lecomte "The Application of Charge Density Research to Chemistry and Drug Design", Plenum Press, New York (1991).

(79) R.H. Blessing, *Cryst. Rev.*, **1**, 3 (1987).

(80) L.V. Azaroff, *Acta Cryst.*, **8**, 701 (1955).

(81) G.T. DeTitta, Program ABSORB, Medical Foundation of Buffalo, USA, (1984).

(82) G.T. DeTitta, *J. Appl. Cryst.*, **18**, 75 (1985).

(83) W.R. Busing, H.A. Levy, *Acta Cryst.*, **10**, 180 (1957).

(84) P. Seiler, W.B. Schweizer, J.D. Dunitz, *Acta Cryst*, **B40**, 319 (1984).

(85) R.W. James, "The Optical Principles of Diffraction of X-rays", G. Bell and Sons, London (1948).

(86) P.J. Becker, P. Coppens, *Acta Cryst.*, **A39**, 129 (1974).

(87) P. Coppens, *Science*, **158**, 1577 (1967).

(88) W.H.E. Schwartz, K. Reudenberg, L. Mensching, *J. Am. Chem. Soc.*, **111**, 6926 (1989).

(89) L. Mensching, W. Vinniesse, P. Valtazanos, K. Reudenberg, W.H.E. Schwartz, *J. Am. Chem. Soc.*, **111**, 6933 (1989).

(90) H. Ptasiewicz-Bak, I. Olovsson, G.J. McIntyre, *Acta Cryst.*, **B49**, 192, (1993).

(91) I. Olovsson, H. Ptasiewicz-Bak, G.J. McIntyre, *Z. Nat. Sect. A - Phys. Sciences*, **48**, 3, (1993).

(92) R.F.W. Bader, "Atoms in Molecules: A Quantum Theory", Oxford University Press, Oxford (1990).

(93) D.A. Dixon, T.H. Dunning Jr., R.A.Eades, P.G. Gassman, *J. Am. Chem. Soc.*, **105**, 7014,

(1983).

(94) T. Naito, S. Nagase, H. Yamataka, *J. Am. Chem. Soc.*, **116**, 10080 (1994).

(95) A.E. Reed, R.B. Weinstock, F. Weinhold, *J. Chem. Phys.*, **83**, 735 (1985).

(96) A.E. Reed, L.A. Curtiss, F. Weinhold, *Chem Rev*, **88**, 899 (1988).

(97) A.F. Cameron, N.J. Hair, D.G. Morris, *J. Chem. Soc., Perkin 2*, 1071 (1972).

(98) S. Tsuchiya, M. Senō, *J. Phys. Chem.*, **98**, 13680 (1994).

(99) S. Inubushi, T. Ikeda, S. Tazuke, *J. Polym. Sci., A*, **25**, 137 (1987).

(100) J. Jazwinski, W. Kozminski, L. Stefaniak, G.A. Webb, *J. Mol. Struc.*, **243**, 365 (1991).

(101) S. Tsuchiya, M. Senō, *J. Org. Chem.*, **44**, 2850 (1979).

(102) S. Tsuchiya, M. Senō, *J. Chem. Soc., Perkin 2*, 887 (1983).

(103) J. Epsztajn, A.R. Katritzky, *Tet. Lett.*, **54**, 4739 (1969).

(104) S.T. Howard, M.B. Husrthouse, C.W. Lehmann, P.R. Mallinson, C.S. Frampton, *J. Chem. Phys.*, **97**, 5616 (1992).

(105) L.E. Orgel, "An Introduction to Transition-Metal Chemistry, Ligand Field Theory", Methuen, London (1960).

(106) I.A. Fallis, L.J. Farrugia, N.M. Macdonald, R.D. Peacock, *J. Chem. Soc., Dalton Trans.*, 2759-2763 (1993).

(107) G.T. Smith, P.R. Mallinson, R.D. Peacock, L.J. Farrugia, I.A. Fallis, C.S. Frampton, J.A.K. Howard, *J. Chem. Soc., Chem Commun.*, 525-526 (1996).

(108) D.S. Yufit, P.R. Mallinson, K.W. Muir, S.I. Kozhushkov, A. De Meijere, *Acta Crystallogr., Sect. B*, **52**, 668-676 (1996).

(109) S.P. Kampermann, J.R. Ruble, B.M. Craven, *Acta Crys.*, **B50**, 737-741 (1994).

(110) T. Koritsanszky, J. Buschmann, P. Luger, *J. Phys. Chem.*, **1996**, *100*, 10547-10553 (1996).

(111) J. Wang, V.H. Smith Jr., C.F. Bunge, R. Jauregui, *Acta Cryst.*, **A52**, 649-658 (1996).

(112) Z. Shi, R.J. Boyd, *J. Chem. Phys.*, **88**, 4375-4377 (1988).

(113) V.G. Tsirelson, P.F. Zou, T.-H. Tang, R.F.W. Bader *Acta Cryst.* **A51**, 143-153 (1995).

(114) F. Maseras, A. Lledos, M. Costas, J.-M. Poblet, *Organometallics*, **15**, 2947-2953 (1996).

(115) C. Bo, M. Costas, J.-M. Poblet, M.-M. Rohmer, M. Benard, *Inorg. Chem.*, **35**, 3298-3306 (1996).

(116) C. Bo, J.-P. Saraso, J.-M. Poblet, *J. Phys. Chem.*, **97**, 6362-6366 (1996).

(117) M. Costas, C. Bo, J.-M. Poblet, *Chem. Phys. Lett.*, **200**, 8-14 (1992).

(118) Z.Y. Lin, M.B. Hall, *Inorg. Chem.*, **30**, 646-651 (1991).

(119) C. Bo, J.-M. Poblet, M. Benard, *Chem. Phys. Lett.*, **169**, 89-96 (1990).

(120) R. Köstler, K.-H. Kramer and R. Liedtke, *Liebigs Ann. Chem.*, 1241 (1973).

(121) R. Huisgen, B Giese and H. Huber, *Tetrahedron Lett.*, 1883 (1967).

(122) A. M. Il'ichev, *Russ. J. Gen. Chem.*, **18**, 1121 (1948).

(123) R. E. Buckles, E. A. Hausman and N. G. Wheeler, *J. Amer. Chem. Soc.*, **72**, 2494 (1950).

(124) S. R. Naidu and S. G. Peeran, *Tetrahedron*, **31**, 465 (1975).

(125) S. G. Peeran and G. H. Reddy *Indian J. Chem., Sect B*, **29**,819 (1990).

(126) S. G. Peeran, T. H. Khan and R. Venkateswarulu, *Indian J. Chem., Sect B*, **21**, 579 (1982).

(127) M. Zh. Ovakimyan, S. K. Barsegyan, G. Ts. Gasparyan and M. G. Indzhikyan, *Arm. Khim. Zh.*, **39**, 463 (1986).

(128) J. E. Mulvaney, Z. G. Gardlund and S. L. Gardlund, *J. Amer. Chem. Soc.*, 1963, **85** 3897.

(129) T. Steiner, E.B. Starikov, A.M. Amado, J.J.C. Teixeira-Dias, *J. Chem. Soc., Perkin Trans. 2*, 1321 (1995).

(130) P. Hobza, H.L. Selzle, E.W. Schlag, *Collect. Czech. Chem. Commun*, **57**, 1186 (1992).

(131) M. Pilkington, J.D. Wallis, S. Larsen, *J. Chem. Soc., Chem Comm.*, 1499 (1995).

(132) P.A. Block, K.W. Jucks, L.G. Pedersen, R.E. Miller, *Chem. Phys.*, **139**, 15 (1989).

(133) M.-F. Fan, Z. Lin, J.E. McGrady, D.M.P. Mingos, *J. Chem. Soc., Perkin Trans. 2*, 563 (1996).

(134) C.E. Dykstra, A.J. Arduengo, T. Fukunaga, *J. Am. Chem. Soc.*, **100**, 6007 (1978).

(135) R.W. Strozier, P. Caramella, K.N. Houk, *J. Am. Chem. Soc.*, **101**, 1340 (1979).

(136) E.T. Huang, K.L. Evans, F.R. Fronczek, R.D. Gandour, *Acta Cryst.*, **C47**, 2727 (1991).

(137) E.T. Huang, K.L. Evans, F.R. Fronczek, R.D. Gandour, *Acta Cryst.*, **C48**, 763 (1992).

(138) K.L Evans, F.R. Fronczek, R.D. Gandour, *Acta Cryst.*, **C51**, 983 (1995).

(139) M. Pilkington, S. Tayyip, J.D. Wallis, *J. Chem. Soc., Perkin Trans. 2*, 2481 (1994).

(140) C.R. Rice, J.D. Wallis, *J. Chem. Soc., Chem. Comm.*, 572 (1993).

(141) M. Pilkington, J.D. Wallis, G.T. Smith, J.A.K. Howard, *J. Chem. Soc., Perkin Trans. 2*, 1849 (1996).

(142) J.D. Wallis, *personal communication.*

(143) J. Cioslowski, S.T. Mixon, W.D. Edwards, *J. Am. Chem. Soc.*, **113**, 1083 (1991).

(144) J. Cioslowski, S.T. Mixon, *J. Am. Chem. Soc.*, **114**, 4382 (1992).

(145) J. Cioslowski, S.T. Mixon, S.T. *Can. J. Chem.*, **70**, 443 (1992).

(146) J. Cioslowski, L. Edgington, B.B. Stefanov, *J. Am. Chem. Soc.*, **117**, 10381 (1995).

(147) S.C. Choi, R.J. Boyd, *Can. J. Chem.*, **64**, 2042 (1986).

(148) J.P. Ritchie, K.-Y. Lee, D.T. Cromer, E.M. Koker, D.D. Lee, *J. Org. Chem.*, **55**, 1994 (1990). (149) K.L. McCormack, P.R. Mallinson, B.C. Webster, D.S. Yufit, *J. Chem. Soc., Faraday Trans.*, **92**, 1709 (1996).

(150) R. Destro, R.E. Marsh, *Acta Crystallogr., Sect. A*, **A43**, 711 (1987).

(151) H. Ellis, ed., "Nuffield Advanced Science Book of Data", Longman (1986).

(152) M.T. Carroll, C. Chang, R.F.W. Bader, *Mol. Phys.*, **63**, 387 (1988).

(153) C.E. Shannon, *Bell Syst. Tech. J.*, **XXVII**, 379 (1948).

(154) G. Bricogne, *Acta Cryst.*, **A40**, 410 (1994).

(155) S.W. Wilkins, J.N. Varghese, M.S. Lehmann, *Acta Cryst.*, **A39**, 47 (1983).

(156) D.M. Titterington, *Astron. Astrophys.*, **144**, 381 (1985).

(157) R. Nityananda, R, Narayan, *J. Astrophys. Astr.*, **3**, 419 (1982).

(158) R. Narayan, R, Nityananda, *Ann. Rev. Astron. Astrophys.*, **24**, 127 (1986).

(159) S.F. Gull, G.J. Daniell, *Nature*, **272**, 686 (1978).

(160) R.K. Bryan, J. Skilling, *Mon. Not. R. Astr. Soc*, **191**, 69 (1980).

(161) J. Skilling, R.K. Bryan, *Mon. Not. R. Astr. Soc*, **211**, 111 (1984).

(162) A.K. Livesey, J. Skilling, *Acta Cryst.*, **A41**, 113 (1985).

(163) S.W. Wilkins, *Acta Cryst.*, **A39**, 892 (1983).

(164) E.T. Jaynes, *IEEE Trans. Syst. Sci. Cybern.*, **SSC-4**, 227 (1968).

(165) S.W. Wilkins, *Acta Cryst.*, **A39**, 896 (1983).

(166) S.W. Wilkins, D. Stuart, *Acta Cryst.*, 197 (1986).

(167) J. Navaza, *Acta Cryst.*, **A41**, 232 (1985).

(168) J. Navaza, *Acta Cryst.*, **A42**, 212 (1986).

(169) M. Sakata, M. Sato, *Acta Cryst.*, **A46**, 263 (1990).

(170) S. Kumazawa, Y. Kubota, M. Takata, M. Sakata, *J. Appl. Cryst.*, **26**, 453 (1993).

(171) T. Saka, N. Kato, *Acta Cryst.*, **A42**, 469 (1986).

(172) M. Sakata, T. Uno, M. Takata, R. Mori, *Acta Cryst.*, **B48**, 591 (1992).

(173) M. Sakata, M. Takata, H. Oshizumi, A. Goto, T. Hondoh, in "Physics and Chemistry of Ice", eds. M Maeno and T. Hondoh, Hokkaido University Press, Sapporo (1992).

(174) M. Takata, Y. Kubota, M. Sakata, *Z. Naturforsch.*, **48a**, 75 (1993).

(175) W. Jauch, A. Palmer, *Acta Cryst.*, **A49**, 590 (1993).

(176) W. Jauch, *Acta Cryst.*, **A50**, 650 (1994).

(177) R.Y. DeVries, W.J. Briels, D. Feil, *Acta Cryst.*, **A50**, 383 (1994).

(178) R.Y. DeVries, W.J. Briels, D. Feil, *Phys. Rev. Lett.*, **77**, 1719 (1996).

(179) R.Y. DeVries, W.J. Briels, D. Feil, G. Tevelde, E.J. Baerends, *Can. J. Chem.*, **74**, 1054 (1996).

(180) A. Zheludev, R.J. Papoular, E. Ressouche, J. Schweizer, *Acta Cryst.*, **A51**, 450 (1995).

(181) R.J. Papoular, Y. Vekhter, P. Coppens, *Acta Cryst.*, **A52**, 397 (1996).

(182) B. Buck and V.A. Macaulay, eds. "Maximum Entropy in Action", Oxford University Press (1992).

(183) S.F. Gull and G.J. Daniell, *Nature*, **272**, 686 (1978).

(184) G.J.H. van Nes, F. van Bolhius, *Acta Cryst.*, **B35**, 2580 (1979).

(185) R.F. Stewart, *J. Chem. Phys.*, **53**, 205 (1970).

(186) C.A. Coulson, H.C. Longuet-Higgins, *Proc. Roy. Soc. (London)*, **A191**, 32 (1947).

(187) R. McWeeny, *Proc. Roy. Soc. (London)*, **A253**, 242 (1959).

(188) R. McWeeny, "Methods of Molecular Quantum Mechanics" pp120, Academic Press, London (1989).

(189) P.-O. Löwdin, *Phys. Rev.*, **97**, 1474 (1955).

(190) P.-O. Löwdin, H. Shull, *Phys. Rev.*, **101**, 1730 (1956).

(191) H. Schmider, V.H. Smith, Jr., W, Weyrich, **Trans. ACA**, **26**, 125 (1990).

(192) A.J. Coleman, *Rev. Mod. Phys.*, **35**, 668 (1963).

(193) R. McWeeny, *Rev. Mod. Phys.*, **32**, 335 (1960).

(194) T.L. Gilbert, *Phys. Rev. B*, **12**, 2111 (1975).

(195) J.E. Harriman, *Phys. Rev. A*, **24**, 680 (1981).

(196) R. Benesch, V.H. Smith, Jr., *Acta Cryst.*, **A26**, 579 (1970).

(197) R.F. Stewart, *Isr. J. Chem.*, **16**, 111 (1977).

(198) R. Benesch, V.H. Smith, Jr., *Acta Cryst.*, **A26**, 586 (1970).

(199) W.L. Clinton, J. Nakhleh, F. Wunderlich, *Phys. Rev.*, **177**, 1 (1969).

(200) W.L. Clinton, A.J. Galli, L.J. Massa, *Phys. Rev.*, **177**, 7 (1969).

(201) W.L. Clinton, G.A. Henderson, J.V. Prestia, *Phys. Rev.*, **177**, 13 (1969).

(202) W.L. Clinton, G.B. Lamers, *Phys. Rev.*, **177**, 19 (1969).

(203) W.L Clinton, A.J. Galli, G.A. Henderson, G.B. Lamers, L.J. Massa, J. Zarur, *Phys. Rev.*, **177**, 27 (1969).

(204) P. Coppens, T.V. Willoughby, L.N. Csonka, *Acta Cryst.*, **A27**, 248 (1971).

(205) P. Coppens, D. Pautler, J.F. Griffin, *J. Am. Chem. Soc.*, **93**, 1051 (1971).

(206) D.A. Matthews, G.D. Stucky, P. Coppens, *J. Am. Chem. Soc.*, **94**, 8001 (1972).

(207) D.S. Jones, D. Pautler, P. Coppens, *Acta Cryst.*, **A28**, 635 (1972).

(208) W.L. Clinton, L.J. Massa, *Phys. Rev. Lett.*, **29**, 1363 (1972).

(209) W.L. Clinton, C.A. Frishberg, L.J. Massa, P.A. Oldfield, *Int. J. Quant. Chem., Quant. Chem. Symp.*, **7**, 505 (1973).

(210) C.A. Frishberg, L.J. Massa, *Acta Cryst.*, **A38**, 93 (1982).

(211) M.J. Goldberg, L.J. Massa, *Int. J. Quant. Chem.*, **24**, 517 (1983).

(212) F.K. Larsen, N.K. Hansen, *Acta Cryst.*, **B40**, 169 (1984).

(213) L.J. Massa, M.J. Goldberg, C.A. Frishberg, R.F. Boehme, S.J. La Placa, *Phys. Rev. B*, **55**, 622 (1985).

(214) L.M. Pecora, *Phys. Rev. B*, **33**, 5987 (1986).

(215) W.L. Clinton, C.A. Frishberg, M.J. Goldberg, L.J. Massa, P.A. Oldfield, *Int. J. Quant. Chem., Quant. Chem. Symp.*, **17**, 517 (1983).

(216) S.T. Howard, J.P. Huke, P.R. Mallinson, C.S. Frampton, *Phys. Rev. B*, **49**, 7124 (1994).

(217) V. Schoemaker, K.N. Trueblood, *Acta Cryst.*, **B24**, 63 (1968).

(218) E.D. Stevens, J. Rys, P.Coppens, *Acta Cryst.*, **A33**, 333 (1977).

(219) S.T. Howard, personal communication.

(220) W.J. Hehre, R.F. Stewart, J.A. Pople, *J. Chem. Phys.*, **51**, 2657 (1969).

(221) W.J. Hehre, R. Ditchfield, R.F. Stewart, J.A. Pople, *J. Chem. Phys.*, **52**, 2769 (1970).

(222) M.W. Schmidt, K.K. Baldridge, J.A. Boatz, S.T. Elbert, M.S. Gordon, J.J. Jensen, S. Koseki, N. Matsunaga, K.A. Nguyen, S.Su, T.L. Windus, M. Dupuis, J.A. Montgomery, *J. Comp. Chem.*, **14**, 1347 (1993).

(223) W. Kutzelnigg, V.H. Smith, Jr., *J. Chem. Phys.*, **41**, 896 (1964).

(224) W.J. Hehre, R. Ditchfield, J.A. Pople, *J. Chem. Phys.*, **56**, 2257 (1972).

(225) P.C. Hariharan, J.A. Pople, *Theoret. Chim. Acta*, **28**, 213 (1973).

(226) R. Krishnan, J.S. Binkley, R. Seeger, J.A. Pople, *J. Chem. Phys.*, **72**, 650 (1980).

(227) W.H. Press, "Numerical Recipes", Chapter 10, Cambridge University Press (1986).

(228) E. Prince, "Mathematical Techniques in Crystallography and Materials Science", Springer-Verlag, New York (1982).

(229) J.S. Rollett in "Computing Methods in Crystallography", ed. J.S. Rollett, Pergamon Press, Oxford (1965).

(230) D.W.J. Cruickshank in "Computing Methods in Crystallography", ed. J.S. Rollett, Pergamon Press, Oxford (1965).

(231) J.S. Rollett in "Computational Crystallography", ed. D. Sayre, Clarendon Press, Oxford

(1982).

Appendix A

Least Squares

A.1 Rudimentary considerations

The material in this appendix is drawn from some standard works on crystallographic least-squares analysis[228,229,230,231]. Any situation where model fitting is to be applied requires a suitable model, set of observations and knowledge of the mathematical relationship between the model and the observations. In a situation where the model has more parameters than we have observations, the situation is underdetermined and it is impossible to proceed. If we have the same number of model parameters as observations, the problem is formally exactly determinable. However in any real situation, experimental observations are subject to both statistical fluctuation and systematic error and hence even this case is underdetermined. The only case where any progress is possible is when there are many more observations than parameters and the problem is formally over-determined. For such cases the chosen method of finding the optimal model giving the best fit to the data is least-squares analysis.

A.1.1 Linear observational equations

If the relationship between the model parameters and our observations is linear, we can define a set of equations called the observational equation

$$M\mathbf{x} = \mathbf{b} \tag{A.1}$$

where A is a matrix of dimensions $m \times n$ with $m > n$, $\mathbf{x}$ is a vector representing the n model parameter values and $\mathbf{b}$ represents the m data points. For experimental observations, no exact analytical solution will occur and a residual vector may be defined as

$$\mathbf{r} = \mathbf{b} - A\mathbf{x} \tag{A.2}$$

If each observational equation is assumed to be equally precise, we can adopt minimization of $\mathbf{r}^T\mathbf{r}$, the product of the residual vector with its transpose.

The more realistic situation of variable error magnitude applies to experimental data. To approach this problem we assume we have another set of observational equations of the same order as before

$$B\mathbf{x} = \mathbf{d} \tag{A.3}$$

We now construct a matrix X with elements X_{ij} being the expectation value of the product of r_i and r_j, the residuals of equations i and j. It can be shown that X is symmetric and positive definite, and we can therefore from a lower triangular matrix of order m calling it W such that

$$WXW^T = I \tag{A.4}$$

If we then set

$$WB = A \tag{A.5}$$

we can form a set of equations for which the expectation value for the square of each residual $\mathbf{r}^T\mathbf{r}$ is unity

$$W\mathbf{d} = \mathbf{b} \tag{A.6}$$

W is of the order $m \times m$ but ignoring the correlations between members of the set of equation $W\mathbf{d} = \mathbf{b}$, both W and X become diagonal and each element of W is the reciprocal of the expectation error of the corresponding equation. Premultiplication of $B\mathbf{x} = \mathbf{d}$ by W to get $A\mathbf{x} = \mathbf{b}$ means the coefficents and right hand sides of each equation ar multiplied by a separate constant so that each equation becomes equally uncertain. The weighted $A\mathbf{x} = \mathbf{b}$ equations thus formed are called the prepared observational equations. The normal equations have solutions minimizing $\mathbf{r}^T\mathbf{r}$ and have the form

$$M = \mathbf{r}^T\mathbf{r} \tag{A.7}$$

$$= (\mathbf{b} - A\mathbf{x})^T(\mathbf{b} - A\mathbf{x}) \tag{A.8}$$

$$= \mathbf{b}^T\mathbf{b} - 2\mathbf{b}^TA\mathbf{x} + \mathbf{x}^TA^TA\mathbf{x} \tag{A.9}$$

Differentiating each element with respect to $\mathbf{x}$ in turn gives the set of equations

$$\partial M \partial \mathbf{x} = -2\mathbf{b}^TA + 2\mathbf{x}^TA^TA \tag{A.10}$$

Dividing this by 2 and transposing, bearing in mind that at the minimum of M, $\partial M/\partial \mathbf{x}$ =0 gives

$$A^TA\mathbf{x} = A^T\mathbf{b} \tag{A.11}$$

These are the normal equations. A^TA is symmetric and positive definite and can therefore be inverted provided A is of rank n, that is at least n of the m observational equations are linearly independent. This might not be the case if many of the observations in fact provide the same information as each other, or several of the unknowns to be determined are the same parameter.

A.1.2 Non-linear observational equations

In the particular case of least-squares refinement of the charge density model against experimental structure factor amplitudes, the relationship is non-linear being the Fourier transform. For our set of observations $F_o(\mathbf{H})$, we can calculate the corresponding values from our current set of model parameters $\mathbf{x}$

$$F_c(\mathbf{H}) = F_c(\mathbf{H}, \mathbf{x}) \tag{A.12}$$

If the set of $F_o(\mathbf{H})$ are independent and each has an estimated to be uncertain by $1/\sqrt{N_i}$ then minimize

$$M(\mathbf{x}) = \sum_{\mathbf{H}} w_{\mathbf{H}} ||F_o(\mathbf{H})| - |F_c(\mathbf{H},\mathbf{x})||^2 \tag{A.13}$$

$M(\mathbf{x})$ will probably be of complicated form with many local minima. If we have a reasonable good starting guess $\mathbf{x}_o$ to $\mathbf{x}$, which gives a local minimum so that $\mathbf{x} = \mathbf{x}_o + \delta\mathbf{x}$ with $\delta\mathbf{x}$ small, we can expand $M(\mathbf{x})$ as a Taylor series

$$M(\mathbf{x}) = \sum_{\mathbf{H}} w_{\mathbf{H}} ||F_o(\mathbf{H})| - [|F_c(\mathbf{H},\mathbf{x}) + \sum_{j=1}^{n} \frac{\partial F_c(\mathbf{H})}{\partial x_j}\delta x_j + 1/2 \sum_{j=1}^{n}\sum_{k=1}^{m} \frac{\partial^2 F_c(\mathbf{H},\mathbf{x})}{\partial x_j \partial x_k}\delta x_j \delta x_k + \cdots ||]|^2 \tag{A.14}$$

We have assumed that δx_j is small for all j and therefore $\delta x_j \delta x_k$ must be very small. If this assumption is valid then the second and higher derivatives may be ignored to give

$$M(\mathbf{x}) = \sum_{\mathbf{H}} w_{\mathbf{H}} ||F_o(\mathbf{H})| - |F_c(\mathbf{H},\mathbf{x}_o)| - \sum_{j=1}^{n} \frac{\partial F_c(\mathbf{H})}{\partial x_j}\delta x_j|^2 \tag{A.15}$$

This equation is of the same form as (1.8) with the substitutions $A_{ij} = \sqrt{w_{\mathbf{H}}}\partial F_c(\mathbf{H},\mathbf{x})/\partial x_j$ and $b_i = \sqrt{w_{\mathbf{H}}}||F_o(\mathbf{H})| - |F_c(\mathbf{H},\mathbf{x}_o)||$ and $x_j = \delta_{x_j}$. We therefore have linearised and prepared observational equations of the form

$$A\delta\mathbf{x} = \mathbf{b} \tag{A.16}$$

and instead of solving to obtain the parameter values, we solve to obtain the parameter shifts to be applied to the current model. The corresponding normal equations are

$$A^T A\delta\mathbf{x} = A^T\mathbf{b} \tag{A.17}$$

The elements of the $A^T A$ matrix are

$$(A^T A)_{ij} = \sum_{\mathbf{H}} w_{\mathbf{H}} \frac{\partial|F_c(\mathbf{H},\mathbf{x})|}{\partial x_i} \cdot \frac{\partial|F_c(\mathbf{H},\mathbf{x}|)}{\partial x_j} \tag{A.18}$$

and the elements of $A^T\mathbf{b}$ are

$$(A^T b)_i = \sum_{\mathbf{H}} w_{\mathbf{H}}(k|F_o(\mathbf{H})| - |F_c(\mathbf{H},\mathbf{x})|\frac{\partial|F_c(\mathbf{H},\mathbf{x})|}{\partial x_i} \tag{A.19}$$

The process is iterative and must be applied successively until the shifts are smaller than a certain value. The criteria for convergence applied is often that no parameter shift should be greater than 0.01 times that parameter's esd.

Because the evaluation of the parameter shifts involved calculations of derivatives from the current model, a poor initial model will lead to poor derivatives and hence spurious shifts. Large shifts should be damped in the initial stages of refinement to prevent the model making large changes into a neighbouring minimum.

Additional useful data produced in the least squares process are the parameter esd's and correlation coefficients. Assuming accurate standard deviations on an absolute scale on our experimental data and with a weighting scheme of $w_{\mathbf{H}} = 1/\sigma^2_{\mathbf{H}}$, the standard deviations on our parameter estimates and the correlation coefficients are given by the variance-covariance matrix C with

$$C = (A^T A) \tag{A.20}$$

Parameter variances (the squares of the esd's) are provided by the inverse of the diagonal elements of the variance covariance matrix

$$\sigma_i^2 = \frac{1}{c_{ii}} \tag{A.21}$$

The off-diagonal elements are the covariances

$$c_{ij} = p_{ij}\sigma_i\sigma_j \tag{A.22}$$

The most valuable information from the covariances are the correlation coefficients p_{ij}

$$p_{ij} = \frac{c_{ij}}{\sigma_i\sigma_j} \tag{A.23}$$

These correlation coefficients are on an absolute scale. A parameter is obviously totally correlated with itself and hence $p_{ii} = 1$. A good choice of model would have low correlations between parameters and for this reason the correlation coefficients are invaluable in deciding between alternative models. Inspection of the parameter esd's from the variance matrix is also valuable in the same context.

Appendix B

Supplementary Material for Nitrogen Ylide

B.1 Structural Parameters

B.1.1 Fractional atomic co-ordinates

atom	x/a	y/b	z/c
O(1)	0.49108(6)	0.25000	0.50075(10)
O(2)	0.37128(7)	0.25000	0.26804(9)
N(1)	0.33200(5)	0.25000	0.75775(8)
N(2)	0.30532(9)	0.25000	0.55406(11)
N(3)	0.39324(6)	0.25000	0.44379(8)
C(1)	0.21907(6)	0.25000	0.84579(10)
C(2)	0.39059(5)	0.06203(9)	0.82115(7)
H(11)	0.23118	0.25000	0.99467
H(12)	0.17801	0.11632	0.80219
H(21)	0.46935	0.05403	0.75504
H(22)	0.39531	0.06914	0.97108
H(23)	0.34150	-0.06328	0.77975

B.1.2 Mean-square atomic displacements ($Å^2$)

The form of the anisotropic temperature factor is:

$$\exp[-2\pi^2 \sum_{i=1}^{3} \sum_{j=1}^{3} U_{ij} h_i h_j a_i^* a_j^*]$$

	U_{11}	U_{22}	U_{33}	U_{12}	U_{13}	U_{23}
O(1)	0.0149(3)	0.0268(3)	0.0136(3)	0.0000	0.0035(2)	0.0000
O(2)	0.0305(4)	0.0231(3)	0.0070(2)	0.0000	0.0003(2)	0.0000
N(1)	0.0109(2)	0.0122(2)	0.0077(2)	0.0000	0.0005(2)	0.0000
N(2)	0.0129(3)	0.0164(3)	0.0083(2)	0.0000	-0.0011(2)	0.0000
N(3)	0.0172(3)	0.0137(3)	0.0076(2)	0.0000	0.0008(2)	0.0000
C(1)	0.0137(3)	0.0215(3)	0.0146(3)	0.0000	0.0040(2)	0.0000
C(2)	0.0229(2)	0.0191(2)	0.0120(2)	0.0076(2)	0.0017(1)	0.0034(2)
H(11)	0.005					
H(12)	0.009					
H(21)	0.023					
H(22)	0.021					
H(23)	0.015					

B.2 Multipole population coefficients

atom	P_v	P_{00}	P_{11}	P_{1-1}	P_{10}
O(1)	6.21(6)	-	-0.06(1)	-0.02(1)	-
O(2)	6.21(6)	-	-0.06(1)	-0.02(2)	-
N(1)	5.58(12)	-	-0.03(1)	-0.02(1)	-
N(2)	5.14(8)	-	-0.07(1)	-0.07(1)	-
N(3)	5.18(12)	-	0.02(1)	-0.01(2)	-
C(1)	4.74(8)	-	-0.19(2)	0.01(2)	-
C(2)	4.53(8)	-	-0.20(3)	0.15(3)	0.17(3)
H(11)	0.59(2)	-	0.03(1)	0.00(1)	-
H(12)	0.59(2)	-	-	-	0.03(2)
H(21)	0.68(3)	-	-	-	0.11(2)
H(22)	0.78(3)	-	-	-	0.11(2)
H(23)	0.59(3)	-	-	-	0.03(2)

atom	P_{20}	P_{21}	P_{2-1}	P_{22}	P_{2-2}
O(1)	0.02(2)	-	-	-0.09(1)	-0.01(1)
O(2)	0.02(2)	-	-	-0.09(1)	-0.01(1)
N(1)	0.03(1)	-	-	-0.07(1)	-0.01(1)
N(2)	0.05(1)	-	-	0.01(1)	0.04(1)
N(3)	-0.10(2)	-	-	0.02(1)	0.02(1)
C(1)	0.11(2)	-	-	-0.12(2)	-0.03(1)
C(2)	0.21(3)	0.01(2)	-0.04(2)	-0.16(2)	0.12(2)

atom	P_{30}	P_{31}	P_{3-1}	P_{32}	P_{3-2}	P_{33}	P_{3-3}
O(1)	-	-0.02(1)	0.01(1)	-	-	0.01(1)	0.01(1)
O(2)	-	-0.02(1)	0.01(1)	-	-	0.01(1)	0.01(1)
N(1)	-	-0.10(1)	0.14(2)	-	-	0.08(1)	0.07(1)
N(2)	-	0.00(1)	0.00(1)	-	-	0.06(1)	-0.01(1)
N(3)	-	0.00(1)	-0.01(1)	-	-	0.28(3)	0.00(1)
C(1)	-	-0.08(2)	0.18(2)	-	-	0.16(2)	0.04(2)
C(2)	0.25(3)	0.02(2)	0.04(2)	0.00(2)	0.04(2)	-0.01(2)	-0.27(2)

B.3 Definitions of local axes

ATOM	ATOMO	AX1	ATOM1	ATOM2	AX2	R/L
O(1)	N(3)	X	O(1)	O(2)	Y	R
O(2)	N(3)	X	O(2)	O(1)	Y	L
N(1)	N(2)	X	N(1)	N(3)	Y	R
N(2)	N(3)	X	N(2)	N(1)	Y	R
N(3)	O(1)	X	N(3)	O(2)	Y	R
C(1)	N(1)	X	C(1)	N(2)	Y	R
C(2)	H(23)	Z	C(2)	H(21)	Y	R
H(11)	C(1)	X	H(11)	N(1)	Y	R
H(12)	C(1)	Z	H(12)	H(11)	Y	R
H(21)	C(2)	Z	H(21)	H(23)	Y	R
H(22)	C(2)	Z	H(22)	H(23)	Y	R
H(23)	C(2)	Z	H(23)	H(21)	Y	R

B.4 κ values

κ set	κ'	κ''
O	0.998(6)	0.85(6)
N(1)	0.964(9)	0.78(4)
N(2)	0.995(7)	1.08(6)
N(3)	0.992(10)	0.75(3)
C	0.984(8)	0.77(2)
H	1.16	1.16

Appendix C

Supplementary Material for Metal Complex

C.1 Structural Parameters

C.1.1 Fractional atomic co-ordinates

atom	x/a	y/b	z/c
C(1)	0.71871(6)	0.75719(5)	0.88904(5)
C(2)	0.55247(5)	0.75260(5)	0.82903(5)
C(3)	0.53932(5)	0.64485(5)	0.83317(6)
C(4)	0.66280(6)	0.87696(5)	0.77258(5)
C(5)	0.43412(5)	0.61418(6)	0.83785(6)
C(6)	0.37606(6)	0.64553(7)	0.75107(7)
C(7)	0.38811(7)	0.64867(8)	0.93078(7)
N(1)	0.65302(4)	0.77735(4)	0.80758(5)
N(100)	0.11157(6)	0.11157	0.11157
O(1)	0.58557(5)	0.60630(5)	0.74930(6)
O(100)	0.18402(10)	0.06618(9)	0.08480(8)
F(1)	0.45801(12)	0.58917(11)	0.50388(12)
F(2)	0.45349(14)	0.49967(14)	0.36840(12)
P(1)	0.47892(1)	0.47892	0.47892
Ni(1)	0.69344(1)	0.69344	0.69344
H(O1)	0.58967	0.53552	0.75716
H(1A)	0.67818	0.75712	0.95303
H(1B)	0.76752	0.81496	0.89327
H(2A)	0.50725	0.77873	0.77424
H(2B)	0.53217	0.78181	0.89583
H(3)	0.57201	0.61859	0.89619
H(4A)	0.65996	0.92662	0.82965
H(4B)	0.60434	0.88719	0.72557
H(5)	0.43139	0.53862	0.84172
H(6A)	0.30642	0.61588	0.75168
H(6B)	0.40746	0.61804	0.68795
H(6C)	0.36676	0.72052	0.74656
H(7A)	0.31903	0.61848	0.93771
H(7B)	0.38221	0.72406	0.93079
H(7C)	0.42699	0.62805	0.99237

C.1.2 Mean-square atomic displacements (Å^2)

The form of the anisotropic temperature factor is:

$$\exp[-2\pi^2 \sum_{i=1}^{3} \sum_{j=1}^{3} U_{ij} h_i h_j a_i^* a_j^*]$$

	U_{11}	U_{22}	U_{33}	U_{12}	U_{13}	U_{23}
C(1)	0.0155(3)	0.0133(3)	0.0110(3)	0.0004(2)	-0.0006(2)	-0.0021(2)
C(2)	0.0123(3)	0.0106(3)	0.0156(3)	0.0002(2)	0.0024(2)	-0.0005(2)
C(3)	0.0114(3)	0.0116(3)	0.0140(3)	-0.0002(2)	0.0012(2)	0.0009(2)
C(4)	0.0142(3)	0.0096(3)	0.0147(3)	0.0004(2)	0.0013(3)	-0.0009(2)
C(5)	0.0127(3)	0.0136(3)	0.0180(3)	-0.0008(2)	0.0019(3)	0.0009(2)
C(6)	0.0164(3)	0.0287(4)	0.0196(4)	-0.0038(3)	-0.0030(3)	0.0008(3)
C(7)	0.0170(3)	0.0295(5)	0.0177(4)	0.0005(3)	0.0055(3)	0.0021(3)
N(1)	0.0115(2)	0.0099(2)	0.0114(2)	-0.0005(2)	-0.0001(2)	-0.0006(2)
N(100)	0.0133(2)	0.0133	0.0133	-0.0002(3)	-0.0002	-0.0002
O(1)	0.0149(3)	0.0102(3)	0.0180(3)	-0.0016(2)	0.0047(2)	-0.0025(2)
O(100)	0.0210(5)	0.0225(5)	0.0171(4)	0.0071(4)	0.0046(4)	0.0017(3)
F(1)	0.0272(6)	0.0179(5)	0.0284(6)	0.0073(5)	0.0036(5)	0.0028(5)
F(2)	0.0321(7)	0.0326(7)	0.0186(6)	0.0051(6)	-0.0009(6)	0.0060(5)
P(1)	0.0168(1)	0.0168	0.0168	0.0044(1)	0.0044	0.0044
Ni(1)	0.00906(4)	0.00906	0.00906	-0.0003(1)	-0.0003	-0.0003
H(O1)	0.028					
H(1A)	0.017					
H(1B)	0.012					
H(2A)	0.027					
H(2B)	0.015					
H(3)	0.010					
H(4A)	0.011					
H(4B)	0.006					
H(5)	0.019					
H(6A)	0.020					
H(6B)	0.024					
H(6C)	0.021					
H(7A)	0.029					
H(7B)	0.023					
H(7C)	0.029					

C.2 Multipole population coefficients

atom	P_v	P_{00}	P_{11}	P_{1-1}	P_{10}
C(1)	4.54(6)	-	0.07(3)	0.07(3)	-0.12(3)
C(2)	4.28(6)	-	0.06(3)	-0.05(3)	-0.08(3)
C(3)	4.24(5)	-	0.09(3)	-0.05(3)	0.00(3)
C(4)	4.44(6)	-	0.11(3)	-0.03(3)	-0.14(3)
C(5)	4.33(5)	-	0.04(3)	-0.01(3)	-0.09(3)
C(6)	4.58(6)	-	0.02(3)	-0.05(3)	-0.15(3)
C(7)	4.34(6)	-	-0.16(4)	0.03(4)	-0.09(3)
N(1)	5.25(8)	-	0.16(3)	-0.05(3)	-0.05(3)
N(100)	1.60(5)	-	-	-	0.01(1)
O(1)	6.45(7)	-	-0.06(2)	-0.05(2)	-0.01(2)
O(100)	6.40(5)	-	-0.01(2)	0.04(2)	-0.03(3)
F(1)	7.34(4)	-	0.03(3)	0.01(3)	0.19(3)
F(2)	7.43(4)	-	-0.11(3)	-0.18(3)	0.03(3)
P(1)	1.23(7)	-	-	-	-0.05(1)
Ni(1)	2.59(4)	0.45(6)	-	-	-0.01(1)
H(O1)	0.67(3)	-	-	-	0.14(3)
H(1A)	0.72(3)	-	-	-	0.04(2)
H(1B)	0.70(3)	-	-	-	0.04(2)
H(2A)	0.85(4)	-	-	-	0.12(2)
H(2B)	0.75(3)	-	-	-	0.02(2)
H(3)	0.80(3)	-	-	-	0.05(2)
H(4A)	0.69(3)	-	-	-	0.06(2)
H(4B)	0.70(3)	-	-	-	0.05(2)
H(5)	0.72(3)	-	-	-	0.03(2)
H(6A)	0.68(3)	-	-	-	0.09(2)
H(6B)	0.71(4)	-	-	-	0.09(2)
H(6C)	0.80(4)	-	-	-	0.05(2)
H(7A)	0.77(4)	-	-	-	0.05(3)
H(7B)	0.75(4)	-	-	-	0.03(3)
H(7C)	0.86(4)	-	-	-	0.10(2)

atom	P_{20}	P_{21}	P_{2-1}	P_{22}	P_{2-2}
C(1)	-0.12(3)	-0.02(2)	-0.05(3)	0.02(3)	-0.06(2)
C(2)	-0.07(3)	-0.06(3)	-0.01(2)	-0.00(2)	0.00(3)
C(3)	0.12(3)	-0.08(3)	0.01(2)	0.00(2)	-0.11(3)
C(4)	-0.02(3)	-0.05(2)	-0.10(3)	0.01(2)	-0.06(3)
C(5)	-0.06(3)	0.07(3)	-0.03(3)	0.04(3)	-0.06(3)
C(6)	-0.08(3)	0.01(3)	0.04(3)	0.04(4)	-0.06(3)
C(7)	0.00(3)	0.01(3)	-0.06(3)	-0.05(3)	0.02(3)
N(1)	-0.02(3)	0.01(2)	-0.04(3)	0.13(3)	0.00(2)
N(100)	-0.03(1)	-	-	-	-
O(1)	0.02(2)	-0.03(2)	0.01(2)	0.05(2)	-0.04(2)
O(100)	-0.12(3)	0.04(2)	0.00(2)	0.06(2)	-0.05(2)
F(1)	-0.01(3)	-0.01(3)	-0.02(3)	-0.03(3)	0.00(3)
F(2)	0.02(4)	0.05(3)	-0.02(3)	-0.05(4)	-0.03(4)
P(1)	0.01(1)	-	-	-	-
Ni(1)	-0.01(1)	-	-	-	-

atom	P_{30}	P_{31}	P_{3-1}	P_{32}	P_{3-2}	P_{33}	P_{3-3}
C(1)	0.31(3)	-0.03(2)	-0.14(3)	0.01(3)	-0.02(2)	0.21(3)	-0.16(2)
C(2)	0.35(3)	0.02(2)	0.01(3)	0.11(2)	0.15(3)	-0.10(2)	-0.24(3)
C(3)	0.33(3)	-0.03(3)	0.04(3)	0.09(3)	0.12(3)	-0.04(2)	-0.20(3)
C(4)	0.15(3)	-0.01(2)	0.28(3)	-0.02(3)	-0.11(2)	-0.06(3)	-0.27(3)
C(5)	0.31(3)	-0.12(3)	0.08(3)	-0.05(3)	-0.10(3)	0.01(3)	-0.29(3)
C(6)	0.32(3)	-0.06(3)	-0.13(3)	-0.01(3)	0.12(3)	0.03(2)	0.13(3)
C(7)	0.15(3)	0.00(3)	0.00(3)	0.02(3)	-0.02(3)	0.00(2)	0.24(3)
N(1)	0.24(3)	-0.06(3)	-0.04(3)	0.21(4)	0.05(3)	0.17(3)	0.00(3)
N(100)	-0.02(1)	-	-	-	-	-0.01(1)	-0.06(1)
O(1)	0.16(2)	-0.03(2)	-0.04(2)	0.13(2)	0.10(2)	0.01(2)	-0.05(2)
O(100)	0.06(2)	0.04(2)	0.02(2)	-0.08(1)	0.02(1)	0.04(1)	0.05(2)
F(1)	0.01(2)	0.07(2)	0.01(2)	-0.07(2)	0.13(2)	-0.01(2)	-0.00(2)
F(2)	0.07(2)	0.07(2)	0.01(2)	-0.05(2)	-0.16(2)	0.03(2)	0.08(2)
P(1)	-0.11(2)	-	-	-	-	0.07(1)	0.02(1)
Ni(1)	-0.19(2)	-	-	-	-	0.13(2)	-0.09(1)

atom	P_{40}	P_{43}	P_{4-3}
P(1)	-0.06(1)	-0.02(1)	-0.08(2)
Ni(1)	0.04(1)	-0.20(2)	0.08(1)

C.3 Definitions of local axes

```
ATOM    ATOMO   AX1 ATOM1   ATOM2   AX2 R/L
C(1)    N(1)    Z   C(1)    C(4)    Y   R
C(2)    N(1)    Z   C(2)    C(3)    Y   R
C(3)    C(5)    Z   C(3)    C(2)    Y   R
C(4)    C(1)    Z   C(4)    N(1)    Y   R
C(5)    C(3)    Z   C(5)    C(6)    Y   R
C(6)    C(5)    Z   C(6)    C(7)    Y   R
C(7)    C(5)    Z   C(7)    C(6)    Y   R
N(1)    C(2)    Z   N(1)    Ni(1)   X   R
N(100)  Ni(1)   Z   N(100)  O(100)  Y   R
O(1)    H(O1)   Z   O(1)    C(3)    Y   R
O(100)  N(100)  Z   O(100)  F(2)    Y   R
F(1)    P(1)    Z   F(1)    F(2)    Y   R
F(2)    P(1)    Z   F(2)    F(1)    Y   R
P(1)    Ni(1)   Z   P(1)    F(1)    Y   R
Ni(1)   DUMO    Z   Ni(1)   N(1)    X   R
H(O1)   O(1)    Z   H(O1)   C(3)    Y   R
H(1A)   C(1)    Z   H(1A)   H(1B)   Y   R
H(1B)   C(1)    Z   H(1B)   H(1A)   Y   R
H(2A)   C(2)    Z   H(2A)   H(2B)   Y   R
H(2B)   C(2)    Z   H(2B)   H(2A)   Y   R
H(3)    C(3)    Z   H(3)    O(1)    Y   R
H(4A)   C(4)    Z   H(4A)   H(4B)   Y   R
H(4B)   C(4)    Z   H(4B)   H(4A)   Y   R
H(5)    C(5)    Z   H(5)    C(7)    Y   R
H(6A)   C(6)    Z   H(6A)   H(6B)   Y   R
H(6B)   C(6)    Z   H(6B)   H(6A)   Y   R
H(6C)   C(6)    Z   H(6C)   H(6B)   Y   R
H(7A)   C(7)    Z   H(7A)   H(7C)   Y   R
H(7B)   C(7)    Z   H(7B)   H(7C)   Y   R
H(7C)   C(7)    Z   H(7C)   H(7A)   Y   R
DUMO    0.8, 0.8, 0.8
```

C.4 κ values

κ set	κ'	κ''
C	0.984(4)	0.853(7)
N(1)	0.985(7)	0.70(2)
N(100)	1.00(1)	1.00
O(1)	0.981(5)	0.78(2)
O(100)	0.974(4)	1.00
F	0.975(4)	1.00
P(1)	1.03(2)	1.00
H	1.16	1.16

	$\kappa_{0:HF}$	$\kappa_{0,2:HF}$	$\kappa_{0,1,3:ST}$
Ni(1)	1.04(1)	1.15(4)	0.44(1)

Appendix D

Supplementary Material for Diacid

D.1 Structural Parameters

D.1.1 Fractional atomic co-ordinates

atom	x/a	y/b	z/c
O(1)	0.01933(8)	0.38217(7)	0.05393(12)
O(2)	-0.10826(8)	0.44257(7)	-0.13191(12)
C(1)	-0.10587(6)	0.26669(6)	-0.08362(9)
C(2)	-0.08085(6)	0.18295(6)	0.02178(9)
C(3)	-0.12199(7)	0.08754(6)	-0.02638(10)
C(4)	-0.18899(8)	0.07544(7)	-0.17071(11)
C(5)	-0.21585(7)	0.15867(8)	-0.27167(11)
C(6)	-0.17363(7)	0.25338(7)	-0.22815(10)
C(7)	-0.05967(6)	0.36861(5)	-0.04585(9)
C(10)	-0.02155(7)	0.18981(5)	0.17983(10)
H(3)	-0.10196	0.02247	0.05211
H(4)	-0.22040	0.00060	-0.20165
H(5)	-0.26803	0.15057	-0.38480
H(6)	-0.19274	0.31806	-0.30762
H(7)	-0.07287	0.50427	-0.10008

D.1.2 Mean-square atomic displacements (Å^2)

The form of the anisotropic temperature factor is:

$$\exp[-2\pi^2 \sum_{i=1}^{3}\sum_{j=1}^{3} U_{ij} h_i h_j a_i^* a_j^*]$$

	U_{11}	U_{22}	U_{33}	U_{12}	U_{13}	U_{23}
O(1)	0.0260(4)	0.0175(3)	0.0287(4)	-0.0052(3)	-0.0151(3)	0.0054(3)
O(2)	0.0233(3)	0.0181(3)	0.0316(4)	-0.0031(3)	-0.0124(3)	0.0075(3)
C(1)	0.0153(3)	0.0169(3)	0.0148(3)	-0.0017(2)	-0.0038(2)	0.0013(2)
C(2)	0.0167(3)	0.0149(3)	0.0144(3)	-0.0011(2)	-0.0032(2)	-0.0008(2)
C(3)	0.0234(3)	0.0165(3)	0.0197(3)	-0.0027(3)	-0.0034(3)	-0.0028(3)
C(4)	0.0262(4)	0.0229(4)	0.0214(4)	-0.0062(3)	-0.0047(3)	-0.0064(3)
C(5)	0.0248(4)	0.0303(4)	0.0180(3)	-0.0064(3)	-0.0072(3)	-0.0030(3)
C(6)	0.0200(3)	0.0251(4)	0.0167(3)	-0.0037(3)	-0.0063(2)	0.0017(3)
C(7)	0.0163(3)	0.0163(3)	0.0176(3)	-0.0022(2)	-0.0041(2)	0.0030(2)
C(10)	0.0204(3)	0.0152(3)	0.0157(3)	-0.0003(2)	-0.0057(2)	0.0000(2)
H(3)	0.024					
H(4)	0.029					
H(5)	0.030					
H(6)	0.025					
H(7)	0.048					

D.2 Multipole population coefficients

atom	P_v	P_{00}	P_{11}	P_{1-1}	P_{10}
O(1)	6.38(6)	-	-0.06(2)	-0.04(2)	-0.05(3)
O(2)	6.45(6)	-	0.00(2)	0.02(3)	0.04(3)
C(1)	3.84(5)	-	0.04(2)	0.01(3)	-0.04(3)
C(2)	4.03(5)	-	0.01(2)	0.06(3)	-0.04(3)
C(3)	4.10(5)	-	-0.03(2)	0.00(3)	-0.06(3)
C(4)	4.06(5)	-	0.02(3)	0.05(4)	-0.04(4)
C(5)	4.04(5)	-	0.04(3)	0.05(3)	-0.01(4)
C(6)	4.07(5)	-	0.00(2)	-0.01(3)	-0.05(4)
C(7)	4.00(6)	-	0.00(2)	0.16(4)	-0.03(3)
C(10)	4.14(5)	-	0.00(4)	-0.05(2)	-0.14(2)
H(3)	0.79(3)	-	-	-	0.12(2)
H(4)	0.81(3)	-	-	-	0.17(2)
H(5)	0.79(3)	-	-	-	0.16(2)
H(6)	0.78(3)	-	-	-	0.14(2)
H(7)	0.72(4)	-	0.00(2)	0.04(2)	0.05(3)

atom	P_{20}	P_{21}	P_{2-1}	P_{22}	P_{2-2}
O(1)	0.00(3)	-0.05(2)	0.03(2)	-0.11(2)	0.08(2)
O(2)	-0.01(2)	0.01(2)	-0.04(2)	-0.07(2)	0.01(2)
C(1)	0.08(3)	-0.02(2)	-0.01(3)	-0.22(2)	-0.02(2)
C(2)	0.09(3)	0.00(2)	0.00(3)	-0.24(2)	0.01(2)
C(3)	0.10(3)	0.01(2)	0.02(3)	-0.22(2)	0.01(2)
C(4)	0.19(3)	0.01(3)	-0.01(3)	-0.22(3)	0.02(2)
C(5)	0.15(3)	-0.02(3)	0.02(3)	-0.22(3)	0.04(2)
C(6)	0.16(3)	-0.04(3)	-0.01(3)	-0.24(2)	0.02(2)
C(7)	0.20(3)	-0.02(2)	-0.09(3)	-0.24(3)	0.01(2)
C(10)	0.34(2)	-0.02(3)	0.02(2)	-0.02(2)	0.00(2)

atom	P_{30}	P_{31}	P_{3-1}	P_{32}	P_{3-2}	P_{33}	P_{3-3}
O(1)	0.01(2)	0.00(2)	0.00(2)	0.05(2)	-0.02(2)	-0.03(1)	0.00(1)
O(2)	0.09(2)	-0.01(2)	-0.04(2)	0.09(2)	-0.02(1)	0.01(1)	-0.01(2)
C(1)	0.27(3)	-0.01(2)	0.00(4)	0.19(2)	-0.01(3)	-0.02(2)	-0.03(2)
C(2)	0.34(3)	0.02(2)	-0.08(4)	0.25(2)	0.01(3)	-0.01(2)	-0.01(2)
C(3)	0.28(3)	0.00(2)	0.03(3)	0.20(2)	-0.02(2)	0.01(2)	0.03(2)
C(4)	0.25(3)	0.01(2)	0.02(3)	0.23(3)	0.01(2)	-0.01(2)	-0.03(2)
C(5)	0.25(3)	-0.02(3)	0.05(3)	0.26(3)	-0.04(2)	-0.03(2)	-0.03(2)
C(6)	0.29(3)	-0.02(2)	0.01(3)	0.26(3)	-0.02(2)	-0.01(2)	0.00(2)
C(7)	0.44(3)	-0.03(2)	0.04(4)	0.24(3)	-0.01(3)	-0.03(2)	0.01(2)
C(10)	0.04(2)	0.00(3)	0.02(3)	-0.01(2)	0.01(3)	-0.01(2)	0.02(2)

D.3 Definitions of local axes

ATOM	ATOMO	AX1	ATOM1	ATOM2	AX2	R/L
O(1)	C(7)	Z	O(1)	C(10)	Y	R
O(2)	C(7)	Z	O(2)	H(7)	Y	R
C(1)	C(7)	Z	C(1)	C(2)	Y	R
C(2)	C(10)	Z	C(2)	C(3)	Y	R
C(3)	C(2)	Z	C(3)	C(4)	Y	R
C(4)	C(3)	Z	C(4)	C(5)	Y	R
C(5)	C(4)	Z	C(5)	C(6)	Y	R
C(6)	C(5)	Z	C(6)	C(1)	Y	R
C(7)	C(1)	Z	C(7)	O(1)	Y	R
C(10)	C(2)	Z	C(10)	O(1)	Y	R
H(3)	C(3)	Z	H(3)	C(10)	Y	R
H(4)	C(4)	Z	H(4)	C(1)	Y	R
H(5)	C(5)	Z	H(5)	C(7)	Y	R
H(6)	C(6)	Z	H(6)	C(2)	Y	R
H(7)	O(2)	Z	H(7)	O(1)	Y	R

D.4 κ values

κ set	κ'	κ''
O	0.980(4)	0.81(6)
C	1.006(6)	0.84(1)
H	1.16	1.16

Appendix E

Courses and Conferences

E.1 External Events

The following courses and conferences were attended during the tuition period of this thesis.

- BCA CCG Autumn Meeting - Birmingham, England. 17th December 1993.
- UK Charge Density Group Meeting - Cardiff, Wales. 1st December 1993.
- Shelxl-93 Workshop - Newcastle, England. 26th-28th March 1994.
- BCA Spring Meeting - Newcastle, England. 28th-31st March 1994.
  Poster on Experimental Charge Density Study of a Nickel Complex presented
- Density Matrix Workshop - Brest, France. 5th-6th August 1994.
  Contributor to the paper presented by Sean Howard
- Sagamore XI Conference - Brest, France. 7th-12th August 1994.
  Poster on Experimental Charge Density Study of a Nickel Complex presented
- The Oxford Quantum Chemistry Summer School - Laredo, Spain. 4th-14th September 1994.
- UK Charge Density Group Meeting - Glasgow, Scotland. 10th December 1994.
  Talk given on Maximum Entropy Methods in Charge Density Analysis
- BCA Spring Meeting - Cardiff, Wales. 27th-31st March 1995.
  Poster on Experimental Charge Density Study of Weak Interactions presented
- BCA School in X-Ray Structure Analysis - Birmingham, England. 2nd-8th April 1995.
- Gordon Conference on Electron Distributions - Plymouth, New Hampshire, USA. 2nd-7th July 1995.
  2 Posters on Maximum Entropy and Experimental Charge Densities Presented.
- BCA CCG Autumn Meeting - Manchester, England. 17th November 1995.
- UK Charge Density Group Meeting - Durham, England. 14th-15th December 1995.
  Local Organiser and talk given on Density Matrix Methodology and Results
- BCA Spring Meeting - Cambridge, England. 1st-4th April 1996.

E.2 Internal Seminars

The chemistry department organises a full and varied seminar schedule, which now follows. Those talks attended by the author are prefixed with an asterisk.

- Prof. F.J. Feher, University of California, Irvine, USA. 4th October 1993*.
  Bridging the Gap Between Surfaces and Solution with Sessilquioxanes

- Dr. P. Hubbrsby, University of Nottingham, England. 14th October 1993*.
  Alkali Metals: Alchemist's Nightmare, Biochemist's Puzzle and Technologist's Dream
- Dr. P. Quayle, University of Manchester, England. 20th October 1993*.
  Aspects of Aqueous ROMP Chemistry
- Prof. R. Adams, University of South Carolina, USA. 21st October 1993.
  Chemistry of Metal Carbonyl Cluster Complexes: Development of Cluster Based Alkyne Hydrogenation Catalysts.
- Dr. R.A.L. Jones, Cavendish Laboratory, Cambridge, England. 27th October 1993*.
  Perambulating Polymers
- Prof. M.N.R. Ashfold, Universoty of Bristol, England. 10th November 1993*.
  High Resolution Photofragment Translational Spectroscopy: A New Way to Watch Photodissociation
- Dr. A. Parker, R.A.L., Didcot, England. 17th November 1993.
  Applications of Time Resolved Resonance Raman Spectroscopy to Chemical and Biochemical Problems.
- Dr. P.G. Bruce, University of St. Andrews, Scotland. 24th November 1993*.
  Structure and Properties of Inorganic Solids and Polymers.
- Dr. R.P. Wayne, Oxford University, England. 25th November 1993*.
  The Origin and Evolution of the Atmosphere
- Prof. M.A. McKervey, Queen's University, Belfast, Northern Ireland. 1st December 1993.
  Synthesis and Applications of Chemically Modified Calixarenes
- Prof. O. Meth-Cohn, University of Sunderland, England. 8th December 1993*.
  Friedel's Folly Revisited - A Super Way to Fused Pyridines.
- Prof. R.F. Hudson, University of Kent, England. 16th December 1993.
  Close Encounters of the Second Kind.
- Prof. J. Evans, University of Southampton, England. 26th January 1994*.
  Shining Light on Catalysis.
- Dr. A. Masters, University of Manchester, England. 2nd February 1994*.
  Modelling Water Without Using Pair Potentials.
- Prof. D. Young, University of Sussex, England. 9th February 1994.
  Chemical and Biological Studies on the Coenzyme Tetrahydrofolic Acid.
- Prof. K.H. Theopold, University of Delaware, USA. 16th February 1994.
  Paramagnetic Chromium Alkyls: Synthesis and Reactivity.
- Prof. P.M. Maitlis, University of Sheffield, England. 23th February 1994.
  Across the Border: Fromm Homogeneous to Heterogeneous Catalysis.
- Dr. C. Hunter, University of Sheffield, England. 2nd March 1994*.
  Noncovalent Interactions Between Aromatic Molecules.
- Prof. F. Wilkinson, Loughborough University, England. 9th March 1994*.
  Nanosecond and Picosecond Laser Flash Photolysis.
- Prof. S.V. Ley, University of Cambridge, England. 10th March 1994.
  New Methods for Organic Synthesis.
- Dr. J. Dilworth, University of Essex, England. 25th March 1994.
  Technetium and Rhenium Compounds with Applications as Imaging Agents.
- Prof. R.J. Gillespie, McMaster University, Hamilton, Canada. 28th April 1994*.
  The Molecular Structure of Some Metal Fluorides and Oxofluorides: Apparent Exceptions to the VSEPR Model.

- Prof. D.A. Humphreys, McMaster University, Hamilton, Canada. 12th May 1994.
  Bringing Knowledge to Life.
- Prof. N.L. Owen, Brigham Young University, Utah, USA. 5th October 1994.
  Determininng Molecular Structure - The Inadequate NMR Way.
- Prof N. Bartlett, University of California, USA. 19th October 1994*.
  Some Aspects of Ag(II) and Ag(III) Chemistry.
- Dr. P.G. Edwards, University of Wales, Cardiff. 2nd November 1994*.
  The Manipulation of Electronic and Structural Diversity in Metal Complexes - New Ligands.
- Prof. B.F.G. Johnson, University of Edinburgh, Scotland. 3rd November 1994.
  Arene-metal Clusters
- Dr. G. Hogarth, UCL, London, England. 9th November 1994.
  New Vistas in Metal-imido Chemistry.
- Dr. M. Block, Zeneca Pharmaceuticals, Macclesfield, England. 10th November 1994.
  Large-scale Manufacture of ZD 1542, a Thromboxane Antagonist Synthase Inhibitor.
- Prof. M. Page, Huddersfield University, England. 16th November 1994*.
  Four-membered Rings and β-Lactamase.
- Dr. J.M.J. Williams, University of Loughborough, England. 23rd November 1994*.
  New Approaches to Asymmetric Catalysis.
- Prof. D. Briggs, ICI and University of Durham, England. 7th December 1994.
  Surface Mass Spectrometry.
- Prof. P. Parsons, University of Reading, England. 11th January 1995.
  Applications of Tandem Reactions in Organic Synthesis.
- Dr. G. Rumbles, Imperial College, London, England. 18th January 1995*.
  Real or Imaginary Third Order Non-linear Optical Materials.
- Dr. D.A. Roberts, Zeneca Pharmaceuticals, Macclesfield, England. 25th January 1995.
  The Design and Synthesis of Inhibitors of the Renin-angiotensin System.
- Dr. T. Cosgrove, Bristol University, England. 1st February 1995*.
  Polymers do it at Interfaces.
- Dr. D. O'Hare, University of Oxford, England. 8th February 1995*.
  Synthesis and Solid-state Properties of Poly-, Oligo- and Multidecker Metallocenes.
- Prof. E. Schaumann, University of Clausthal. 22nd February 1995.
  Silicon and Sulphur Mediated Ring-opening Reactions of Epoxide.
- Dr. M. Rosseinsky. University of Oxford, England. 1st March 1995.
  Fullerene Intercalation Chemistry.
- Dr. M. Taylor, University of Auckland, New Zealand. 22nd March 1995*.
  Structural Methods in Main-group Chemistry.
- Dr. M. Schroder, University of Edinburgh, Scotland. 26th April 1995.
  Redox-active Macrocyclic Complexes: Rings, Stacks and Liquid Gases.
- Prof A.J. Kresge, University of Toronto, Canada. 4th May 1995.
  Reactive Intermediates: Carboxylic-acid Enols and Other Unstable Species.
- Prof. P. Luger, Free University of Berlin, Germany. 11th October 1995*.
  Low Temperature Crystallography.
- Prof. R. Schmuitzler, Universitat Braunschweig, Germany. 13th October 1995.
  Calixerane-Phosphorus Chemistry: A new Dimension in Phosphorus Chemistry.

- Prof A. Alexakis, Unicersite P. et. M. Curie, Paris, France. 18th October 1995.
  Synthesis and Analytical Uses of Chiral Diamines.
- Dr. D.M. Davies, University of Nurthumbria, Newcastle, England. 25th October 1995.
  Chemical Reactions of Organised Systems.
- Prof. W. Motherwell, UCL, London, England. 1st November 1995.
  New Reactions for Organic Synthesis.
- B. Langlois, University Claude Bernard-Lyon, France. 3rd November 1995.
  Radical Anionic and Pseudo-Cationic Trifluforomethylation.
- Dr. D. Craig, Imperial College, London, England. 8th November 1995.
  New Strategies for the Assembly of Heterocyclic Systems.
- Prof. J.P.R. Williams, University of Oxford, England. 11th November 1995*.
  Metals in Health and Disease.
- Dr. A. Andrea, UCL, London, England. 15th November 1995.
  Chemistry of Lanthanides with Polypyrazoylborate Ligands.
- Prof. D. Bergbreiter, Texas A&M University, Texas, USA. 17th November 1995*.
  Design of Smart Catalysts, Substrates and Surfaces from Simple Polymers.
- Prof. I. Souter, Lancaster University, England. 22nd November 1995.
  A Water of Glass? Luminescence Studies of Water-Soluble Polymers.
- Prof. D. Tuck, University of Windsor, Canada. 29th November 1995.
  New Indium Coordination Chemistry.
- Dr. B. Henderson, Waikato University, New Zealand. 10th January 1996*.
  Electrospray Mass Spectrometry - A New Sporting Technique.
- Dr. J.K.M. Saunders, University of Oxford, England. 11th January 1996*.
  Enzyme Mimics.
- Prof. J.W. Emsley, University of Southampton, England. 17th January 1996*.
  Liquid Crystals: More Than Meets the Eye.
- Dr. A. Armstrong, Nottingham University, England. 24th January 1996.
  Alkene Oxidation and Natural Product Synthesis.
- Dr. J. Penfold, RAL, Didcot, England. 31st January 1996.
  Soft Soap and Surfaces.
- Dr. R.B. Moody, Exeter University, England. 7th February 1996.
  Nitrosations, Nitrations and Oxidations with Nitric Acid.
- Dr. P. Pringle, University of Bristol, England. 12th February 1996.
  Catalytic Self-Replication of Phosphines on Platinum(O).
- Dr. J. Rohr, Universitat Göttingen, Germany. 15th February 1996.
  Goals and Aspects of Biosynthetic Studies on Low Molecular Weight Natural Products.
- Dr. C. Pulham, University of Edinburgh, Scotland. 21st February 1996*.
  Heavy Metal Hydrides.
- Prof E.W. Randall, QMC, London, England. 28th February 1996*.
  New Perspectives in NMR Imaging.
- Dr. R. Whitby, University of Southampton, England. 6th March 1996.
  New Approaches to Chiral Catalysts: Induction of Planar and Metal-Centred Asymmetry.
- Dr. D.S. Wright, University of Cambridge, England. 7th March 1996.
  Synthetic Applications of Me_2N-p-Block Metal Reagents.

- Prof. V. Balzani, University of Bologna, Italy. 12th March 1996*.
  Supramolecular Photochemistry.
- Prof. D. Garner, Manchster University, England. 13th March 1996.
  Mushrooming in Chemistry.
- Dr. L.D. Pettit. 30th April 1996.
  IUPAC Commision on Equilibrium Data: pH-metric Studies Using Very Small Quantities of Uncertain Purity.